The Economics of CO$_2$ Transport by Pipeline and Storage in Saline Aquifers and Oil Reservoirs

Sean T. McCoy

A Thesis Submitted in Partial Fulfillment of the
Requirements for the Degree of
Doctor of Philosophy in

Engineering & Public Policy

Carnegie Mellon University
Pittsburgh, PA

April, 2008

Revision	Description	Date
0	Original document	1/29/2008
1	Estimate for carbon content of crude oil was incorrect (see p. 198) and is corrected in this revision	4/9/2008

Acknowledgements

Abstract

Large reductions in carbon dioxide (CO_2) emissions are needed to mitigate the impacts of climate change. One method of achieving such reductions is CO_2 capture and storage (CCS). CCS requires the capture of carbon dioxide (CO_2) at a large industrial facility, such as a power plant, and its transport to a geological storage site where CO_2 is sequestered. If implemented, CCS could allow fossil fuels to be used with little or no CO_2 emissions until alternative energy sources are more widely deployed. Large volumes of CO_2 are most efficiently transported by pipeline and stored either in deep saline aquifers or in oil reservoirs, where CO_2 is used for enhanced oil recovery (EOR). This thesis describes a suite of models developed to estimate the project-specific cost of CO_2 transport and storage. Engineering-economic models of pipeline CO_2 transport, CO_2-flood EOR, and aquifer storage were developed for this purpose. The models incorporate a probabilistic analysis capability that is used to quantify the sensitivity of transport and storage cost to variability and uncertainty in the model input parameters. The cost of CO_2 pipeline transport is shown to be sensitive to the region of construction, in addition to factors such as the length and design capacity of the pipeline. The cost of CO_2 storage in saline aquifers is shown to be most sensitive to factors affecting site characterization cost. For EOR projects, CO_2 storage has traditionally been a secondary effect of oil recovery; thus, a levelized cost of CO_2 storage cannot be defined. Instead EOR projects were evaluated based on the breakeven price of CO_2 (i.e., the price of CO_2 at which the project net present value is zero). The breakeven CO_2 price is shown to be most sensitive to oil prices, losses of CO_2 outside the productive zone of the reservoir, and reservoir pressure. Future research should include collection and aggregation of more specific data

characterizing possible sites for aquifer storage and applications of these models to this

data. The implications of alternative regulations and requirements for site

characterization should also be studied to more fully assess cost impacts.

Table of Contents

List of Figures

List of Tables

Chapter 1: Carbon Capture and Storage—The Big Picture

Large reductions in carbon dioxide (CO_2) emissions from fossil fuel use will be required
to stabilize atmospheric concentrations of CO_2 [1-5]. One option to reduce CO_2 emissions
to the atmosphere from large industrial sources—particularly fossil-fuel fired power
plants—is carbon capture and storage (CCS); i.e., the capture of CO_2 directly from
anthropogenic sources and disposal of it in geological sinks for significant periods of
time [6]. CCS requires CO_2 to first be captured and compressed to high pressures, then
transported to a storage site, where it is injected into a suitable geologic formation. Each
of these steps—capture, transport, and storage—is capital and energy intensive, and will
have a significant impact on the cost of production for electricity or other industrial
commodities produced using CCS. However, with appropriate policy incentives, CCS
could act as a potential "bridging technology" that would achieve significant CO_2
emission reductions while allowing fossil fuels to be used until alternative energy sources
are more widely deployed.

This chapter is intended to be an overview of how CCS fits into a portfolio of advanced
technologies that could, if implemented, lead to reduced emissions from the electric
power sector. The chapter draws on the findings of the Intergovernmental Panel on
Climate Change (IPCC) Fourth Assessment Report (AR4) [5] to review the magnitude of
global emissions reductions required to meet various atmospheric stabilization targets.
The chapter then reviews the importance of emissions from the electric sector; available
means of mitigating these emissions, including CCS; and the challenges to CCS as an

accepted method of reducing emissions. This provides the context for a concluding

presentation of the objectives and overview of this thesis.

1.1 The Climate Change Challenge

Atmospheric concentrations of CO_2 have increased from a pre-industrial concentration of

278 ppm to a current concentration of 379 ppm. Approximately 60% of the nearly 50 Gt

per year of greenhouse gas emissions are CO_2 from fossil fuel combustion [5]. Figure 1.1,

reproduced from IPCC AR4, shows not only that CO_2 emissions from fossil fuel

emissions have been growing steadily, but that the largest single contributor to CO_2

emissions is electricity generation.
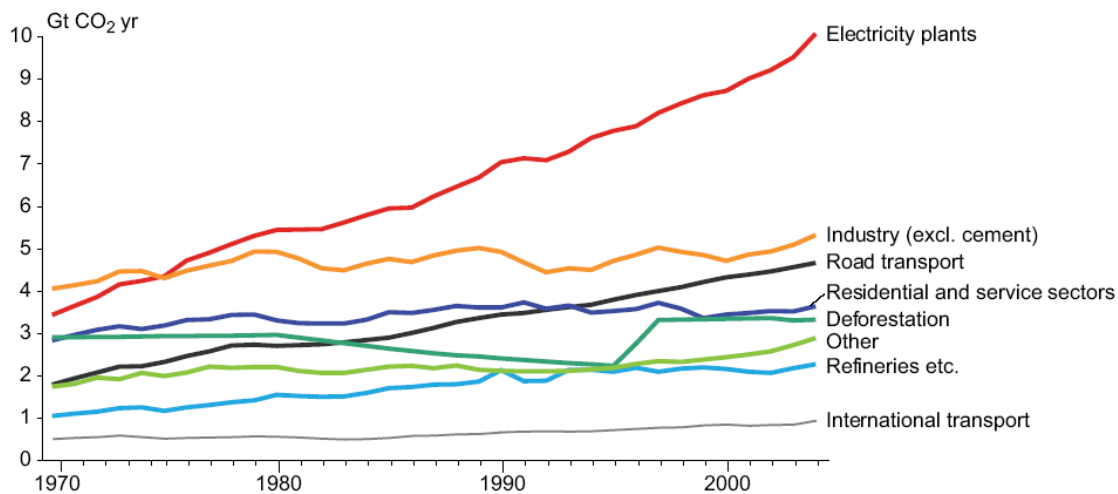
Figure 1.1. Sources of global CO_2 emissions between 1970 to 2004 by sector adapted from the IPCC AR4 [7].

Given past growth in CO_2 emissions, future growth in global population, and increasing

global average income per capita, it is almost certain that total CO_2 emissions will

continue to grow in the absence of a rapid decrease in the carbon intensity of the worlds

primary energy supply [1].

Chapter 1: Carbon Capture and Storage—The Big Picture

Table 1.1, adapted from the IPCC AR4 [5], shows the required emissions reductions to

stabilize CO_2 concentrations at various levels, the long-term (i.e., equilibrium) global

mean temperature increases associated with these concentrations, and the range of years

in which CO_2 emissions peak. In this table, the temperature rise is based on the IPCC

"best-estimate" climate sensitivity of 3^oC, which is "likely" to lie in the range of 2^oC to

4.5^oC. The emissions reduction trajectory varies between scenarios examined in the IPCC

AR4, which explains the ranges of peaking years and changes in emissions in 2050

presented in Table 1.1.

Table 1.1. A summary of emissions stabilizations scenarios showing required emissions reductions (adapted from the IPCC AR4 [5]).

Global Mean Temperature Rise $(^oC)^*$	CO_2-eq Concentration (ppm)	2050 Change Global Emissions (% of 2000)	Peaking year for CO_2 Emissions
2.0 - 2.5	445 - 490	-85 to -50	2000-2015
2.5 - 2.8	490 - 535	-60 to -30	2000-2020
2.8 - 3.3	535 - 590	-30 to +5	2010-2030
3.3 - 4.1	590 - 710	+10 to +60	2020-2060
4.1 - 4.9	710 – 855	+25 to +85	2050-2080
4.9 - 6.1	855 - 1130	+90 to +140	2060-2090

* Temperature rise above pre-industrial global mean, based on AR4 "best-estimate" climate sensitivity of 3^oC

Based on this IPCC summary, achieving the European Union (EU) target of no more than

a 2^oC temperature increase would require an emissions reduction of between 85% and

50% from 2000 levels by 2050. Achieving long term stabilization at a doubling of pre-

industrial levels (approximately 550 ppm CO_2), would require emissions to be

approximately the same as in 2000 or lower despite any growth that would otherwise

occur and would result in a warming of 2.8 to 3.3 ^oC.

The appropriate stabilization target for atmospheric concentration of CO_2 is uncertain. From the perspective of the United Nations Framework Convention on Climate Change, a stabilization target should prevent "dangerous anthropogenic interference" (DAI) with the climate system. However, what constitutes DAI and the atmospheric concentration of CO_2 at which DAI would be avoided, is unclear [7-9]. Nonetheless, achieving any significant levels of emissions reductions—or even restraining emissions growth—is a daunting task, thus will require a broad portfolio of advanced energy technologies and changes in energy consumption patterns [2-4]. Including CCS in this portfolio of technologies will allow emissions reductions targets to be met at lower costs than if CCS were not an option [10].

1.2   Mitigating Emissions from the Electricity Sector

As Figure 1.1 shows, emissions from electricity generation make up approximately one-third of global CO_2 emissions. In the US, electricity generation contributes 39% of all CO_2 emissions (i.e. approximately 2.4 Gt CO_2) [11], the majority of which come from coal combustion at large power plants. Thus, the potential exists for large CO_2 emissions reductions if the carbon intensity of electricity generation can be reduced.

There are a number of advanced technologies that can mitigate emissions from the electric sector. These advanced technologies can be generalized as efficiency improvements (both generation and end-use), decarbonization and sequestration (e.g., fuel switching and CCS), use of renewables (e.g. wind, solar, and biomass), and use of nuclear energy [2]. At the present time some of these technologies may be more desirable than others; however, the emissions reduction challenge will require more than one technology (e.g., see Pacala and Socolow [12]).

1.2.1   *The CCS Option—Capturing CO_2*

Capture of CO_2 can be accomplished via three general routes: pre-combustion CO_2 capture, where carbon is removed from the fuel prior to oxidization; post-combustion CO_2 capture, where fuel is combusted normally in a boiler or turbine, and CO_2 is removed from the exiting flue gas stream; and oxyfuel combustion, where the fuel is combusted with nearly stoichiometric amounts of oxygen in an atmosphere of CO_2. Figure 1.2 summarizes the major flows and processes in the three categories of capture processes.
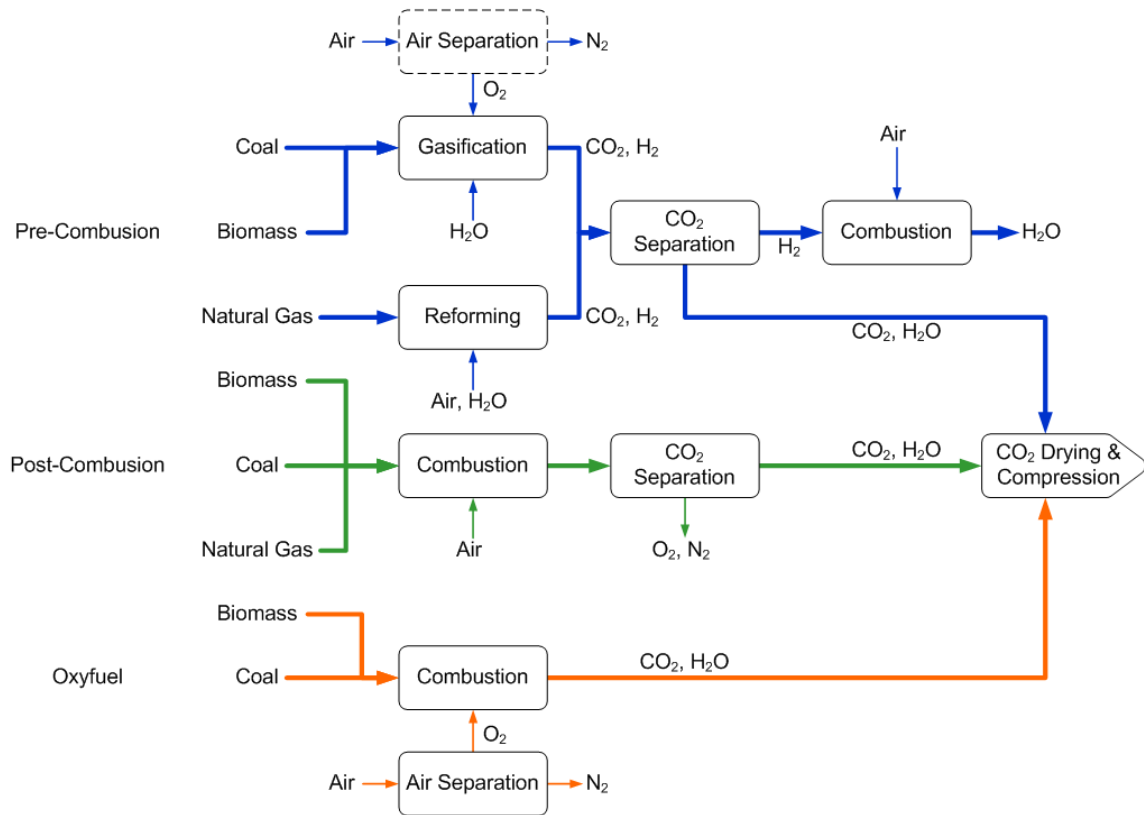
Figure 1.2. CO_2 capture processes summarized by major process steps, adapted from the IPCC Special Report on CCS [13].

All of these types of capture systems currently consume large amounts of energy, resulting in decreased plant efficiencies and reduced net power outputs when compared

against the same plants without capture systems. As a result, power plants with capture

systems will consume more fuel and water while producing more waste products (e.g.

ash, slag, and sulfur) per unit of electricity generated [14]. The decrease in energy output

coupled with the increased operating cost and increased capital cost (resulting from the

capture system) results in a higher cost of electricity (COE) for capture plants versus

those without capture. Figure 1.3, adapted from the IPCC Special Report on CCS [13],

summarizes the difference in COE and emissions rates between plants with and without

capture (including compression, but not transport or storage) for three power plant

technologies: pulverized coal (PC), integrated gasification combined cycle (IGCC), and

natural gas combined cycle (NGCC).
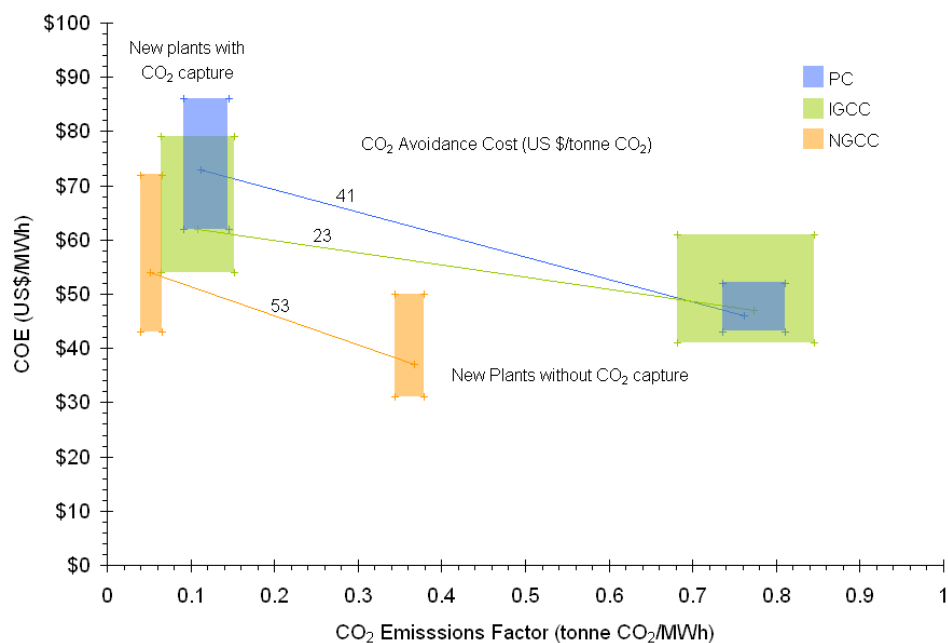
Figure 1.3. Ranges for the COE and CO_2 emissions factor for different power plant technologies with and without capture based on current technologies. Coal plants use bituminous coals, PC plants use supercritical steam cycles, and all figures are for new plants. Lines connect the IPCC "representative values" [13], and indicate the CO_2 avoidance cost *for the same type of plant*.

There are several metrics for measuring the cost of carbon capture, including the incremental COE, cost of CO_2 avoided, and cost of CO_2 captured. Figure 1.3 shows the differences in COE between plants with and without capture and the cost of CO_2 avoided *for the same plant types[1]*.

The remainder of this thesis focuses on the costs of CO_2 transport and storage expressed as cost per metric tonne of CO_2 transported or stored. The appropriate metric for comparison with capture costs is the cost of CO_2 captured, which ranges from roughly $10 to $60 per tonne of CO_2 depending on plant type and other design and operating factors [13]. In general, the cost per tonne of CO_2 captured using current technologies is highest for NGCC plants, and approximately similar for PC and IGCC plants [13].

The technological maturity of CO_2 capture systems varies from technology to technology. The recent IPCC report concludes that the components of many capture systems are well understood from a technological standpoint, but there is a lack of experience in building and operating capture systems at scale [13].

1.2.2 The CCS Option—Transport of CO_2

There are multiple options for transporting compressed CO_2 from the source to the geological sink. Practical modes of overland transport include motor carrier, rail, and pipeline. The most economic method of transport depends on the locations of capture and storage, distance from source to sink, and the quantities of CO_2 to be transported. However, the quantity to be transported is the dominant factor—on the order of 2 to 3

---

[1] The cost of CO_2 avoided is highly sensitive to the context in which it is used and types of plants being compared. For example, in a situation where the alternative to building an IGCC plant with capture is to build an NGCC plant without capture, the relevant avoidance cost should be measured between these plant types.

million metric tonnes (Mt) per year of CO_2 would need to be transported from a single

500 MW coal-fired power plant. As a result, pipeline is the only viable option for

overland transport [15, 16], and is the only method of transport considered in the thesis.

There is considerable industrial experience in the transport of CO_2 by pipeline. Upwards

of 50 Mt/y of CO_2 is transported over nearly 3100 km of pipelines primarily for use in

EOR operations [17, 18]. For comparison, this would be the amount of CO_2 produced by

about sixteen-500 MW coal fired power plants.

1.2.3   *The CCS Option—Storage of CO_2*

The theoretical capacity of geological sinks for CO_2 storage is uncertain, but likely very

large [19]. Geological sinks suitable for storing captured CO_2 include: deep saline

aquifers, depleted gas reservoirs, oil reservoirs, and coal beds. Storage of CO_2 in

producing oil reservoirs and coal beds are referred to as enhanced oil recovery (EOR) and

enhanced coal bed methane (ECBM) recovery, respectively. Table 1.2 shows the range of

capacity estimates for deep saline formations, EOR, and ECBM reported by different

authors [20-27].

Table 1.2. Summary of CO_2 storage capacity estimates for deep saline formations, EOR, and ECBM reported by several authors.

Formation	United States (Gt CO_2)	Worldwide (Gt CO_2)
Deep Saline Aquifers	10^2	10^3-10^4
EOR & Depleted Oil and Gas Fields	10^2	10^3
ECBM	10^1	10^1-10^2

On a global scale, the estimated capacity of deep saline formations is largest, followed by oil and gas reservoirs (including depleted reservoirs) and ECBM, while mined salt caverns have an estimated global storage capacity that is insignificant in comparison.

Many difference approaches have been used to make estimates of the storage capacity in the subsurface on both regional and global levels, which explains the great variation in estimates of global capacity estimates shown in Table 1.2 [19, 27]. Asides from methodological issues, such as correlating surface area of sedimentary basins with storage capacity, the range in capacity estimates can be attributed to divergent assumptions used in the various assessments, and the level of the assessment (i.e., reserves vs. resources) [19, 28].

Even at the lower end of the range of capacity estimates in Table 1.2, there is still ample global capacity to sequester large amounts of CO_2. However, the availability of storage sites is highly variable. For example, sedimentary basins[2] such as the Permian Basin (Southwest United States) and the Alberta Basin (Western Canada) will have large storage capacities in deep saline formations, and oil and gas reservoirs, whereas other areas, such as Central Canada, will have little capacity for storage owing to its location on the Precambrian Shield [29]. To effectively utilize regional storage capacities, CO_2 may have to be transported, potentially over large distances, since geological sinks further from the CO_2 source may be more suitable than nearby sinks. Suitability of geological formations for storage depends on the geological suitability of the particular

---

[2] A sedimentary basin is a depression in the earth's crust formed by movement of tectonic plates where sediments have accumulated to form sedimentary rocks. Hydrocarbons commonly occur in sedimentary basins.

sedimentary basin, the inventory of potential storage sites within the basin, the safety and long term fate of injected CO_2, and the capacity of the storage site [30].

1.3 Planned and Operating CO_2 Capture and Storage Projects

There are a number of planned CO_2 and operating storage projects. A number of these projects are relatively small-scale pilot projects (i.e., on the order of 10^5 tonnes CO_2 per year), such as the Phase III projects planned by the US Department of Energy (DOE) Carbon Sequestration Regional Partnerships [31]. However, there are also a growing number of large-scale commercial projects (i.e., 1 Mt CO_2 per year and larger). Large-scale projects currently operating or in an advanced stage of planning are summarized in Table 1.3 [27, 32, 33].

Table 1.3. A summary of operating commercial CO_2 storage projects

Project	Location	Operator	Storage Type	Injection Start Date	Annual Injection Rate	Total Planned Storage
Sleipner	North Sea	StatoilHydro	Aquifer	1996	1 Mt/y	20 Mt
Weyburn	Saskatchewan, Canada	EnCana	EOR	2000	1.2 Mt/y*	19 Mt
In Salah	Sahara, Algeria	Sonatrach, BP, StatoilHydro	Depleted Gas Reservoir	2004	1.2 Mt/y	17 Mt
Salt Creek	Wyoming, USA	Anadarko	EOR	2006	2.2 Mt/y+	27 Mt
Snohvit	Melkøya, Norway	StatoilHydro	Aquifer	2007	0.7 Mt/y	
Gorgon	Barrow Island, Australia	Chevron	Aquifer	2009§	3.2 Mt/y	>100 Mt

* Average annual delivery rate over 15 year CO_2 contract
+ Peak annual storage rate
§ Planned date

In addition to the projects listed in Table 1.3, there is a large number of operating EOR projects injecting natural CO_2 primarily for oil recovery. Chapter 3 contains an overview of operating EOR projects.

Processes analogous to those used in deep saline formation storage are used for acid gas[3] disposal in Canada. Through 2005, over 4.5 Mt of acid gas have been injected into deep saline aquifers and depleted hydrocarbon reservoirs at 48 sites, produced by 42 separate gas plants [34, 35]. Both H_2S and CO_2 are disposed of simultaneously because co-capture of the two gases is less expensive than separate capture of H_2S and CO_2. Of the total amount of acid gas injected, approximately 2.5 Mt is CO_2.

Many of these projects are being studied to better understand the processes occurring in storage, means of monitoring injected CO_2 and detecting leakage, and security of CO_2 storage in the long-term. The findings from these and other pilot projects can inform development of an integrated framework for CCS.

1.4   Challenges in CO_2 Transport and Storage

The challenges to the acceptance and widespread use of CCS as a technology to address the climate challenge are numerous. Perhaps one of the most critical is the public acceptance of CCS as a safe and effective means to reduce emissions. The issue of public perception is also tied to increasing scientific knowledge about the security of stored CO_2, its long-term fate, appropriate risk assessment, and development and

---

[3] Formally, an acid gas is any gas that can form acidic solutions when mixed with water. In this context, an acid gas is a mixture of hydrogen sulfide (H_2S) and CO_2 of varying proportions. In the petroleum industry, H_2S and CO_2 gases are obtained after a sweetening process is applied to a sour gas.

implementation of an effective regulatory system. The following three sections give a brief overview of these issues.

1.4.1 Technical Challenges in CO_2 Transport and Storage

As Table 1.2 shows, there is a wide range of capacity estimates for both the US and the world, and as noted by Bradshaw et al. [19], there are capacity estimates in the literature that report US capacities larger than world capacities estimated by others. While efforts such as the US DOE Carbon Sequestration Regional Partnerships have made estimates of storage capacity at the national level, there is still a considerable range of uncertainty in their estimates [36]. Friedmann et al. [37] argue that it is prudent for governments to quickly undertake geological assessments of CO_2 storage capacity given their low cost relative to the benefit of having accurate capacity estimates for long-term planning.

A further challenge for geological storage is to improve understanding of potential leakage processes from storage formations. Potential leakage pathways can be both natural (e.g. open faults) and man-made (e.g. abandoned wells). Faults can be identified using seismic methods and characterized as either sealing or open. Abandoned wells can also be identified. However, in a mature sedimentary basin there may be hundreds of thousands of abandoned wells that can potentially serve as conduits to the surface (e.g., see Gasda [38]). A better understanding of the processes that could lead to leakage from wells and better tools to enable risk assessment would be beneficial.

Given the volumes of CO_2 to be stored and the locations in which storage is likely to occur, it is reasonable to assume that there will be leakage from some projects, even in cases where due diligence has been exercised. In such a situation, remediation will be

required. Using natural gas storage facilities as analogs to CO_2 storage, Benson and Hepple [39] describe several pathways for leakage and possible remediation technologies. However, as both Benson and Hepple and the IPCC special report conclude [27], technologies to mitigate leakage should be further explored.

1.4.2   Regulatory Needs for CO_2 Transport and Storage

Despite the importance placed on CCS technologies by the US DOE, the US does not yet have a regulatory framework for CCS, nor does the US have a clear plan to develop an integrated regulatory framework. An integrated regulatory framework for CCS should encompass the entire lifecycle of a CSS project—from ensuring that storage sites are appropriate to verifying that CO_2 has been sequestered from the atmosphere to management of the long-term risks presented by the stored CO_2. Without an integrated regulatory framework or a clear plan forward—in addition to restrictions on CO_2 emissions—CCS will not be an option for commercial entities looking to reduce emissions.

In the US, the EPA has announced its intention to regulate geological storage of CO_2 under the Underground Injection Control (UIC) program and plans to propose draft regulations late in 2008. As pointed out by Wilson and others [40, 41], the UIC may not be an appropriate framework to regulate the lifecycle of a CCS project. An appropriate regulatory framework must balance the needs of a large number of stakeholders, accounting for the long-term liability resulting from injected CO_2 and incorporate lessons learnt from early pilot and commercial scale projects [42].

1.4.3   Pubic Perception of CO_2 Transport and Storage

Public acceptance of CCS as a safe and effective means of reducing CO_2 emissions is necessary for the technology to play a role in the future. Palmgren et al. [43] suggest that the initial public perception of CCS is not favorable in comparison with other energy technologies that could play a role in reducing emissions. In agreement, Reiner et al. [44] present survey results suggesting that the public are uncertain as to whether CCS should play a role in a portfolio of climate mitigation technologies. Of course, acceptance of CCS is also tied to acceptance of climate change as a pressing problem that requires prompt action [43, 44]. Further studies of public perception may be able to determine what aspects of CCS must be addressed, from a technological or regulatory standpoint, to improve its standing in the public arena.

1.5   Objectives and Organization of this Thesis

In addition to information on technical characteristics and risks, policy makers require methods to estimate the costs of CCS to evaluate proposed climate change mitigation strategies involving development of CCS projects. In addition, private actors also have an interest in examining the cost of CCS projects. In the last decade the understanding of CCS processes has increased greatly, as reflected by the recent IPCC Special Report [45]; however, there are still significant gaps in knowledge of the cost of integrated capture, transport, and storage processes. For example, many studies of carbon capture processes have been undertaken [13] and reasonable models linking process economics to key engineering parameters (i.e., engineering-economic models) have been developed [46], but they have not yet been linked with transport [47] and storage models to determine the economics of an integrated CCS process.

Chapter 1: Carbon Capture and Storage—The Big Picture

Current estimates of the costs of CO_2 transport and storage have by and large been based on rules-of-thumb adapted from petroleum engineering (e.g., see [48-52]). In storage, the uses of rules-of-thumb are appropriate for situations where there is limited knowledge of the geological properties of the reservoir at the scales of interest for cost calculations (i.e., over tens of km^2). For example, studies that have produced regional cost-curves for storage (i.e. the cost of storing a cumulative mass of CO_2) have typically applied these rules of thumb [51, 52]. However, when more specific geological information is available, cost estimates can be made that better reflect the specifics of the case (e.g., see [53]).

The goal of this thesis is to develop a suite of models that relate the specifics of CO_2 transport and storage projects—through both aquifer storage and EOR—to the cost of transport and geological storage. These models will: be flexible with respect to changing scenarios and assumptions; allow for probabilistic assessment; and, be relatively transparent and easy to use. The models will be used in the thesis to assess the relative importance of the input parameters, the effects of variability in the input parameters, and the relative costs of CCS for illustrative cases.

The thesis is divided into five chapters, including this introductory chapter. Chapters 2 through 4 describe the transport, EOR storage, and aquifer storage models, respectively, presenting deterministic results from application of each model to illustrative cases and results from Monte Carlo sensitivity studies using each model. The final chapter ties together the findings from the illustrative cases, and makes recommendations on the types of problems the models can be applied to solve.

1.6 References

1. Hoffert, M.I., et al., *Energy implications of future stabilization of atmospheric CO_2 content.* Nature, 1998. **395**: p. 881-884.
2. Hoffert, M.I., et al., *Advanced Technology Paths to Global Climate Stability: Energy for a Greenhouse Planet.* Science, 2002. **298**: p. 981-987.
3. Caldeira, K., A.K. Jain, and M.I. Hoffert, *Climate Sensitivity Uncertainty and the Need for Energy Without CO_2 Emission.* 2003. **299**(5615): p. 2052-2054.
4. Green, C., S. Baksi, and M. Dilmaghani, *Challenges to a climate stabilizing energy future.* Energy Policy, 2007. **35**(1): p. 616-626.
5. Fisher, B.S., et al., *Issues related to mitigation in the long term context*, in *Climate Change 2007: Mitigation. Contribution of Working Group III to the Fourth Assessment Report of the Inter-governmental Panel on Climate Change*, B. Metz, et al., Editors. 2007, Cambridge University Press: Cambridge. p. 169-250.
6. Bachu, S., *Screening and ranking of sedimentary basins for sequestration of CO_2 in geological media in response to climate change.* Environmental Geology, 2003. **44**: p. 277-289.
7. Rogner, H.-H., et al., *Introduction*, in *Climate Change 2007: Mitigation. Contribution of Working Group III to the Fourth Assessment Report of the Inter-governmental Panel on Climate Change*, B. Metz, et al., Editors. 2007, Cambridge University Press: Cambridge. p. 95-116.
8. Mastrandrea, M.D. and S.H. Schneider, *Probabilistic integrated assessment of "dangerous" climate change.* Science, 2004. **304**(5670): p. 571-575.
9. Schneider, S.H. and M.D. Mastrandrea, *Probabilistic assessment "dangerous" climate change and emissions pathways.* Proceedings of the National Academy of Sciences of the United States of America, 2005. **102**(44): p. 15728-15735.
10. Herzog, H., et al., *Cost and Economic Potential*, in *IPCC Special Report on Carbon Dioxide Capture and Storage*, B. Metz, et al., Editors. 2005, Cambridge University Press: Cambridge, U.K.
11. Environmental Protection Agency, *Inventory of US Greenhouse Gas Emissions and Sinks: 1990-2005*. 2007, US Environmental Protection Agency: Washington, D.C.
12. Pacala, S. and R. Socolow, *Stabilization wedges: Solving the climate problem for the next 50 years with current technologies.* Science, 2004. **305**(5686): p. 968-972.
13. Thambimuthu, K., et al., *Capture of CO_2*, in *IPCC Special Report on Carbon Dioxide Capture and Storage*, B. Metz, et al., Editors. 2005, Cambridge University Press: Cambridge, U.K.
14. Rubin, E.S., A.B. Rao, and C. Chen. *Comparative Assessments of Fossil Fuel Plants with CO_2 Capture and Storage*. in *7th International Conference on Greenhouse Gas Control Technologies*. 2004. Vancouver, Canada: Elsevier Science.
15. Skovholt, O., *CO_2 Transportation System.* Energy Conversion & Management, 1993. **34**(9-11): p. 1095-1103.

16. Svensson, R., et al., *Transportation systems for CO₂-application to carbon capture and storage.* Energy Conversion & Management, 2004. **45**: p. 2343-2353.

17. Gale, J. and J. Davidson, *Transmission of CO₂- Safety and Economic Considerations.* Energy, 2004. **29**: p. 1319-1328.

18. Doctor, R., et al., *Transport of CO₂*, in *IPCC Special Report on Carbon Dioxide Capture and Storage*, B. Metz, et al., Editors. 2005, Cambridge University Press: Cambridge, U.K.

19. Bradshaw, J., et al., *CO₂ storage capacity estimation: Issues and development of standards.* International Journal of Greenhouse Gas Control, 2007. **1**(1): p. 62-68.

20. Koide, H., et al., *Subterranean Containment and Long-Term Storage of Carbon Dioxide in Unused Aquifers and in Depleted Natural Gas Reservoirs.* Energy Conversion & Management, 1992. **33**(5-8): p. 619-626.

21. Bachu, S., W.D. Gunter, and E.H. Perkins, *Aquifer Disposal of CO₂: Hydrodynamic and Mineral Trapping.* Energy Conversion & Management, 1994. **35**(4): p. 269-279.

22. Hendriks, C.A. and K. Blok, *Underground storage of carbon dioxide.* Energy Conversion & Management, 1995. **36**: p. 539-542.

23. Gunter, W.D., et al., *Large CO₂ sinks: Their role in the mitigation of greenhouse gases from an international, national (Canadian) and provincial (Alberta) perspective.* Applied Energy, 1998. **61**(4): p. 209-227.

24. Holloway, S., *Storage of Fossil Fuel-Derived Carbon Dioxide Beneath the Surface of the Earth.* Annual Review of Energy & Environment, 2001. **26**: p. 145-166.

25. Stevens, S.H., et al., *CO₂ Injection and Sequestration in Depleted Oil and Gas Fields and Deep Coal Seams: Worldwide Potential and Cost.* Environmental Geosciences, 2001. **8**(3): p. 200-209.

26. Shaw, J. and S. Bachu, *Screening, evaluation, and ranking of oil reservoirs suitable for CO₂-flood EOR and carbon dioxide sequestration.* Journal of Canadian Petroleum Technology, 2002. **41**(9): p. 51-61.

27. Benson, S., et al., *Underground geological storage*, in *IPCC Special Report on Carbon Dioxide Capture and Storage*, B. Metz, et al., Editors. 2005, Cambridge University Press: Cambridge, U.K.

28. Bachu, S., et al., *CO₂ storage capacity estimation: Methodology and gaps.* International Journal of Greenhouse Gas Control, 2007. **1**(4): p. 430-443.

29. Hitchon, B., et al., *Sedimentary basins and greenhouse gases: a serendipitous association.* Energy Conversion & Management, 1999. **40**: p. 825-843.

30. Bachu, S., *Sequestration of CO₂ in geological media in response to climate change: road map for site selection using the transform of the geological space into the CO₂ phase space.* Energy Conversion & Management, 2002. **43**: p. 87-102.

31. National Energy Technology Lab. *Regional Carbon Sequestration Partnerships*. 2007 [cited 2007 December 1]; Available from: http://www.netl.doe.gov/technologies/carbon_seq/partnerships/partnerships.html.

32. Torp, T.A. and J. Gale, *Demonstrating storage of CO₂ in geological reservoirs: The Sleipner and SACS projects.* Energy, 2004. **29**: p. 1361-1369.

33.   Torp, T.A. and K.R. Brown. *CO₂ Underground Storage Costs as Experienced at Sleipner and Weyburn*. in *7th International Conference on Greenhouse Gas Control Technologies*. 2004. Vancouver, Canada: Elsevier Science.

34.   Bachu, S. and W.D. Gunter. *Overview of Acid-Gas Injection Operations in Western Canada*. in *7th International Conference on Greenhouse Gas Control Technologies*. 2004. Vancouver, Canada: Elsevier Science.

35.   Bachu, S. and K. Haug, *In-Situ Characteristics of Acid-Gas Injection Operations in the Alberta Basin, Western Canada: Demonstration of CO₂ Geological Storage*, in *The CO₂ Capture and Storage Project (CCP) for Carbon Dioxide Storage in Deep Geologic Formations for Climate Change Mitigation*, S. Benson, Editor. 2004, Elsevier Science.

36.   National Energy Technology Lab, *Carbon Sequestration Atlas of the United States and Canada*. 2007, Pittsbnurgh, PA: US Department of Energy. 86.

37.   Friedmann, S.J., et al., *The low cost of geological assessment for underground CO₂ storage: Policy and economic implications*. Energy Conversion & Management, 2006. **47**: p. 1894-1901.

38.   Gasda, S.E., S. Bachu, and M.A. Celia, *Spatial characterization of the location of potentially leaky wells penetrating a deep saline aquifer in a mature sedimentary basin*. Environmental Geology, 2004. **46**(6-7): p. 707-720.

39.   Benson, S. and R. Hepple, *Prospects for Early Detection and Options for Remediation of Leakage from CO₂ Storage Projects*, in *The CO₂ Capture and Storage Project (CCP) for Carbon Dioxide Storage in Deep Geologic Formations for Climate Change Mitigation*, S. Benson, Editor. 2005, Elsevier Science.

40.   Wilson, E.J., T.J. Johnson, and D.W. Keith, *Regulating the Ultimate Sink: Managing the Risks of Geologic CO₂ Storage*. Environmental Science & Technology, 2003. **37**: p. 3476-3483.

41.   Keith, D.W., et al., *Regulating the Underground Injection of CO₂*. Environmental Science & Technology, 2005. **39**: p. 499A-505A.

42.   Wilson, E.J., et al., *Regulating the Geological Sequestration of Carbon Dioxide*. Environmental Science & Technology. **In Press, Corrected Proof**.

43.   Palmgren, C.R., et al., *Initial Public Perceptions of Deep Geological and Oceanic Disposal of Carbon Dioxide*. Environmental Science & Technology, 2004. **38**(24): p. 6441-6450.

44.   Reiner, D.M., et al., *American exceptionalism? Similarities and differences in national attitudes toward energy policy and global warming*. Environmental Science & Technology, 2006. **40**(7): p. 2093-2098.

45.   Metz, B., et al., eds. *IPCC Special Report on Carbon Dioxide Capture and Storage*. 2005, Cambridge University Press: Cambridge, U.K. 442.

46.   Rao, A.B. and E.S. Rubin, *A technical, economic, and environmental assessment of amine-based CO₂ capture technology for power plant greenhouse gas control*. Environmental Science & Technology, 2002. **36**(20): p. 4467-4475.

47.   McCoy, S.T. and E.S. Rubin, *An engineering-economic model of pipeline transport of CO₂ with application to carbon capture and storage*. International Journal of Greenhouse Gas Control. **In Press, Corrected Proof**.

48.   Hendriks, C.F., *Carbon dioxide removal from coal fired power plants*. 1 ed. 1994: Kluwer Academic Publishers.

49.   Smith, L., et al., *Carbon Dioxide Sequestration in Saline Formations-Engineering and Economic Assessment Final Technical Report*. 2001, Battelle Memorial Institute: Columbus, OH. p. 93.

50.   Hendriks, C., et al., *Building the Cost Curves for CO_2 Storage, Part 1: Sources of CO_2*. 2002, IEA Greenhouse Gas R&D Programme: Stoke Orchard, UK.

51.   Dahowski, R., et al., *A CO_2 Storage Supply Curve for North America*. 2004, IEA Greenhouse Gas R&D Programme: Stoke Orchard, UK.

52.   Wildenborg, T., et al. *Cost Curves for CO_2 Storage: European Sector*. in *7th International Conference on Greenhouse Gas Control Technologies*. 2004. Vancouver, Canada: Elsevier Science.

53.   Bock, B., et al., *Economic Evaluation of CO_2 Storage and Sink Enhancement Options*. 2003, TVA Public Power Institute: Muscle Shoals, AL.

Chapter 2: Modeling CO$_2$ Transport by Pipeline[1]

There have been few studies that have addressed the cost of carbon dioxide (CO$_2$)

transport in detail. However, earlier work by Svensson et al. [1] identified pipeline

transport as the most practical method to move large volumes of CO$_2$ overland and other

studies have affirmed this conclusion [2]. There is considerable experience in the

transport of CO$_2$ by pipeline, as upwards of 50 million tonnes per year of CO$_2$ is

transported over nearly 3100 km of pipelines primarily for use in enhanced oil recovery

(EOR) operations [2, 3]. This chapter focuses on the cost of CO$_2$ transport via pipeline. In

1993, Skovholt [4] presented rules of thumb for sizing of CO$_2$ pipelines and estimated the

capital cost of pipeline transport. In 2002, the International Energy Agency Greenhouse

Gas Programme (IEA GHG) released a report that presented several correlations for the

cost of CO$_2$ pipelines in Europe based on detailed case study designs [5]. More recently,

an engineering-economic CO$_2$ pipeline model was developed at the Massachusetts

Institute of Technology (MIT) [6]. Results from these and similar studies were

summarized in the recent IPCC report [2]. However, none of these studies considered the

unusual physical properties of CO$_2$ at high pressures [7], the realities of available pipeline

diameters and costs, or regional differences in the cost of CO$_2$ transportation.

The objective of this chapter is to estimate the cost per tonne of transporting CO$_2$ for a

range of CO$_2$ flow rates (e.g., reflecting different power plant sizes) over a range of

distances, and to also incorporate regional cost differences within the continental US.

---

[1] Based in part on McCoy, S.T. and E.S. Rubin, *An engineering-economic model of pipeline transport of CO$_2$ with application to carbon capture and storage.* International Journal of Greenhouse Gas Control. **In Press, Corrected Proof.**

These cost estimates are embodied in an engineering-economic model that will be presented in this chapter. A probabilistic analysis is used to quantify the impact of uncertainty and variability in cost model parameters on CO_2 transport cost. This analysis also shows the range of costs associated with a given project and the probability of a given cost for a specific scenario.

2.1 Pipeline Transport Performance Model

The performance model takes as input engineering design parameters, such as pipeline length and design CO_2 mass flow and calculates the required pipe diameter. The transport performance model includes a comprehensive physical properties model for CO_2 and other fluids of interest (e.g., H_2S); accounts for the compressibility of CO_2 during transport; allows booster pumping stations and segment elevation changes; and, includes probabilistic assessment capabilities. Figure 2.1 shows the inputs and outputs from the performance model, and how the performance model interacts with the pipeline cost model (discussed in Section 2.2) and the CO_2 properties model (discussed in Appendix A).

Sections 2.1.1 through 2.1.3 present details of the performance model and illustrative results are presented in Section 2.1.4.
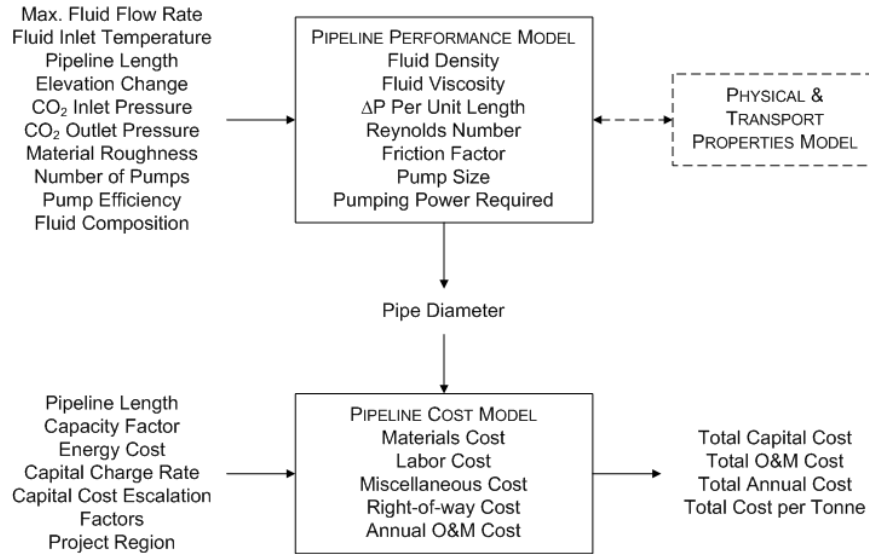
Figure 2.1. The pipeline performance model takes a series of inputs defining the design of the pipeline project and calculates the required pipe diameter, which is input to the cost model.

2.1.1   Physical Properties of Carbon Dioxide

Efficient transport of CO_2 via pipeline requires that CO_2 be compressed and cooled to the liquid state [8]. Transport at lower densities (i.e., gaseous CO_2) is inefficient because of the low density of the CO_2 and relatively high pressure drop per unit length. Moreover, by operating the pipeline at pressures greater than the CO_2 critical pressure of 7.38 MPa, temperature fluctuations along the pipeline will not result in the formation of gaseous CO_2 and the difficulties encountered with two-phase flow [9], as the phase diagram in Figure 2.2 illustrates.
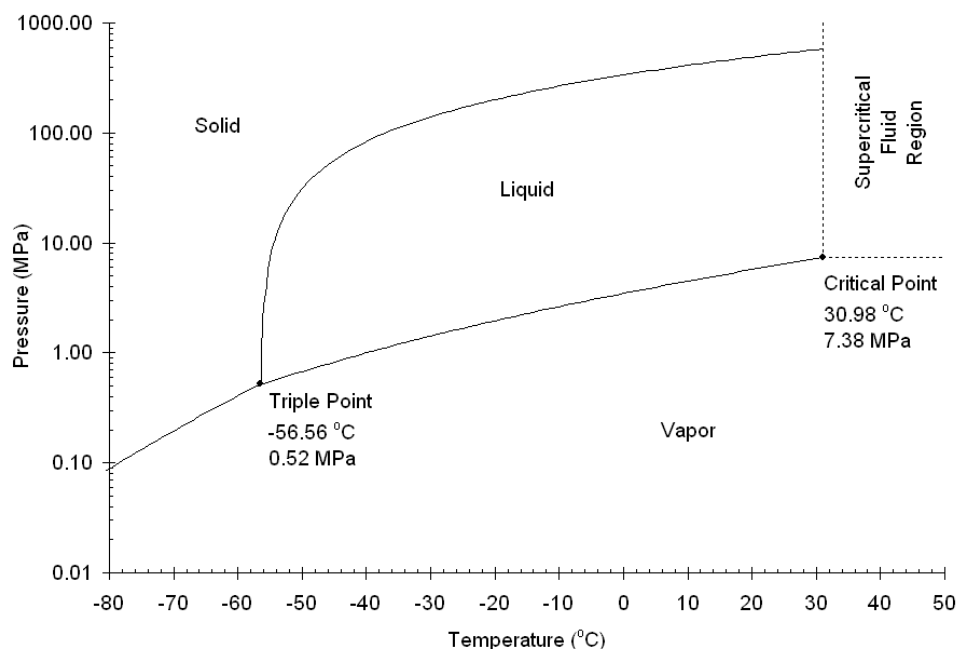
Figure 2.2. A phase diagram for CO_2, showing the triple point, critical point, and the supercritical fluid region. Transport of CO_2 should occur in the liquid phase area at pressures greater than the critical pressure.

The properties of CO_2 are considerably different from other commonly transported fluids, such as natural gas. Thus, it is necessary to use accurate representations of the phase behavior, density, and viscosity of CO_2 and CO_2-containing mixtures in the design of the pipeline. The results presented here are based on the physical properties (i.e., density and phase behavior) of CO_2 and CO_2-containing mixtures predicted using a cubic equation of state with Peng-Robinson parameters, and mixing rules employing a binary interaction parameter [10]. The transport properties of CO_2 have been estimated using the Chung et al. method [11], extended to high pressures by Reid, Prausnitz, and Poling [12]. For more information on cubic equations of state, commonly used parameterizations, and estimation methods for transport properties, see the Appendix A.

Figure 2.3 shows that the compressibility of CO_2 is non-linear in the range of pressures common for pipeline transport and is highly sensitive to any impurities, such as hydrogen sulfide (H_2S) or methane (CH_4). Figure 2.3 also shows that there is a significant difference between the compressibility of pure CO_2 and CO_2 with 10% H_2S (by volume). To reduce difficulties in design and operation, it is generally recommended that a CO_2 pipeline operate at pressures greater than 8.6 MPa where the sharp changes in compressibility of CO_2 can be avoided across a range of temperatures that may be encountered in the pipeline system [13]. Conversely, line-pipe with ASME-ANSI 900# flanges has a maximum allowable operating pressure of 15.3 MPa at 38°C [14]. Operating the pipeline at higher pressures would require flanges with a higher rating. Over the range of typical conditions shown in Figure 2.3, the density of CO_2 varies between approximately 800 kg/m^3 and 1000 kg/m^3.

Operating temperatures of CO_2 pipelines are generally dictated by the temperature of the surrounding soil. In northern latitudes, the soil temperature varies from a few degrees below zero in the winter to 6-8 ^{o}C in summer, while in tropical locations; the soil temperature may reach up to 20 ^{o}C [4]. However, at the discharge of compression stations after-cooling of compressed CO_2 may be required to ensure that the temperature of CO_2 does not exceed the allowable limits for either the pipeline coating or the flange temperature.
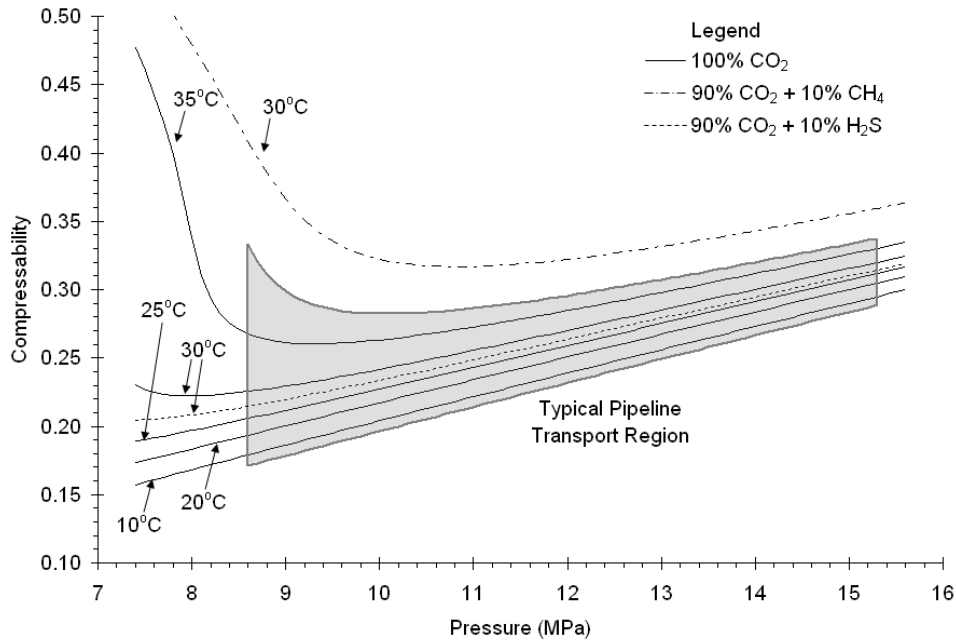
Figure 2.3. The compressibility of CO_2 as predicted by the Peng-Robinson equation of state showing the nonlinearity in the transport region and the sensitivity of compressibility to impurities such as 10% H_2S or 10% CH_4.

2.1.2   Pipe Segment Engineering and Design

While there are proven flow equations available for use with high pressure gas pipelines (e.g. AGA fully turbulent equation), these equations can introduce error into the estimation of flow rates in liquid CO_2 due to the underlying assumptions made in their development [13]. The pipeline performance model used here is based on an energy balance on the flowing CO_2, where the required pipeline diameter for a pipeline segment is calculated while holding the upstream and downstream pressures constant. A pipeline segment is defined as a length of pipeline for which the inlet pressure and minimum outlet pressure are specified (e.g., a length of pipeline lying between two compressor stations). The energy balance assumes that changes in kinetic energy of the flowing CO_2 are negligible, and that the compressibility of the CO_2 or CO_2 containing mixture can be averaged over the length of the pipeline segment. In addition, the typically long length of

26

Chapter 2: Modeling CO_2 Transport by Pipeline

a CO_2 pipeline segment coupled with the lack of insulation on buried pipelines means that it can be treated as an isothermal system, where the CO_2 is at the temperature of the earth surrounding the pipeline.

Equation 2.1 shows the differential form of this energy balance, which is integrated in following steps by making several simplifying assumptions. Equation 2.1 accounts for changes in kinetic energy, pressure-volume work, changes in potential energy, and energy loss due to skin friction in a flow system.

$$\frac{c}{g_c v} du + \frac{1}{v} dp + \frac{g}{g_c v^2} dh + \frac{2 f_F c^2}{g_c D_i} dL = 0 \qquad (2.1)$$

In Equation 2.1: c is a constant equal to the product of density, ρ, and fluid velocity, u; g is acceleration due to gravity; g_c is the conversion factor converting force units (in the SI system of units, this is equal to unity); v is the specific volume of fluid; p is pressure; h is height; f_F is the fanning friction factor; D_i is the pipeline diameter; and L is the length of the pipe segment.

Each term in Equation 2.1 has to be integrated over the length of the pipe segment between the upstream and downstream conditions, represented as points 1 and 2, respectively. The first term at left in Equation 2.1 is the kinetic energy term, which is integrated via the simple substitution:

$$\int_1^2 \frac{c}{g_c v} du = \frac{c^2}{g_c} \ln\left(\frac{u_2}{u_1}\right)$$

Integration of the pressure-volume work term in Equation 5 is somewhat more complex, and requires substitution of the compressibility for specific volume, and definition of average pressure and temperature conditions. For any fluid, compressibility is defined as:

$$Z = \frac{pvM}{RT}$$

where, R is the ideal gas constant, T is the absolute temperature of the fluid, and M is the molecular weight of the fluid. Thus, the specific volume can be rewritten in terms of the compressibility as:

$$v = \frac{ZRT}{pM}$$

Substituting the definition of specific volume above into the pressure-volume work term of Equation 2.1 results in:

$$\int_1^2 \frac{1}{v} dp = \int_1^2 \frac{pM}{ZRT} dp = \frac{M\left(p_2^2 - p_1^2\right)}{2Z_{ave}RT_{ave}}$$

Fort the case of a CO_2 pipeline modeled here, the average temperature, T_{ave}, is assumed to be constant at ground temperature so that $T_{ave} = T_{ground}$. Because pressure varies non-linearly along the pipeline, the average pressure, P_{ave}, is calculated [14]:

$$P_{ave} = \frac{2}{3}\left(p_2 + p_1 - \frac{p_2 p_1}{p_2 + p_1}\right) \tag{2.2}$$

Integration of the potential energy term is relatively simple using the definitions of average temperature and pressure, the result being:

$$\int_1^2 \frac{g}{g_c v^2}\, dh = \frac{g p_{ave}^2 M^2}{g_c Z_{ave}^2 R^2 T_{ave}^2}\left(h_2 - h_1\right)$$

The friction loss term is integrated as follows:

$$\frac{2 f_F c^2}{g_c D_i}\int_1^2 dL = \frac{2 f_F c^2}{g_c D_i} L$$

Thus, the result of integrating Equation 2.1, is then given below:

$$\frac{c^2}{g_c}\ln\!\left(\frac{u_2}{u_1}\right) + \frac{M\!\left(p_2^2 - p_1^2\right)}{2 Z_{ave} R T_{ave}} + \frac{g p_{ave}^2 M^2}{g_c Z_{ave}^2 R^2 T_{ave}^2}\left(h_2 - h_1\right) + \frac{2 f_F c^2 L}{g_c D_i} = 0 \quad (2.3)$$

where, for pipe with a circular cross section:

$$c = \frac{4\dot{m}}{\pi D_i^2}$$

Solving Equation 2.3 for the internal diameter results in the following equation:

$$D_i = \left\{ \frac{-64 Z_{ave}^2 R^2 T_{ave}^2 f_F \dot{m}^2 L}{\pi^2 \left[M Z_{ave} R T_{ave}\left(p_2^2 - p_1^2\right) + 2 g P_{ave}^2 M^2\left(h_2 - h_1\right)\right]} \right\}^{1/5} \quad (2.4)$$

where, $\dot{m}$ is the design (i.e. maximum annual) mass flow rate of CO_2.

Thus, Equation 2.4 can be used to calculate the pipe diameter required for a given pressure drop. Complicating this, however, is the Fanning friction factor, which is a function of the pipe diameter. The Fanning friction factor can not be solved for analytically, thus an explicit approximation for Fanning friction factor is given as [15]:

$$\frac{1}{2\sqrt{f_F}} = -2.0\log\left\{\frac{\varepsilon/D_i}{3.7} - \frac{5.02}{Re}\log\left[\frac{\varepsilon/D_i}{3.7} - \frac{5.02}{Re}\log\left(\frac{\varepsilon/D_i}{3.7} + \frac{13}{Re}\right)\right]\right\} \quad (2.5)$$

where ε is the roughness of the pipe, which is approximately 0.0457 mm for commercial

steel pipe [16], and *Re* is the Reynolds number. The Reynolds number is given by

Equation 18:

$$Re = \frac{4\dot{m}}{\mu\pi D_i} \tag{2.6}$$

where μ is the viscosity of the fluid. As a result, Equations 2.4, 2.5, and 2.6 must be

solved iteratively to determine the pipe diameter required for a particular application. In

the iteration scheme shown in Figure 2.4, the Reynolds number, Equation 2.6, is first

calculated using an initial estimate of pipe diameter based on a velocity of 1.36 m/s. This

initial velocity is representative of CO_2 pipeline flows, and thus minimizes the number of

iterations required over a range of model inputs for both design mass flow rate and

pipeline length. The calculated Reynolds number is then used in Equation 2.5 to estimate

the Fanning friction factor, which is then substituted into Equation 2.4. Reynolds

numbers for CO_2 pipelines are well into the turbulent regime, typically on the order of

10^6. This leads to an updated diameter, which is compared with the value at the previous

iteration. Values for the internal diameter usually converge to within 10^{-6} m in less than 5

iterations.
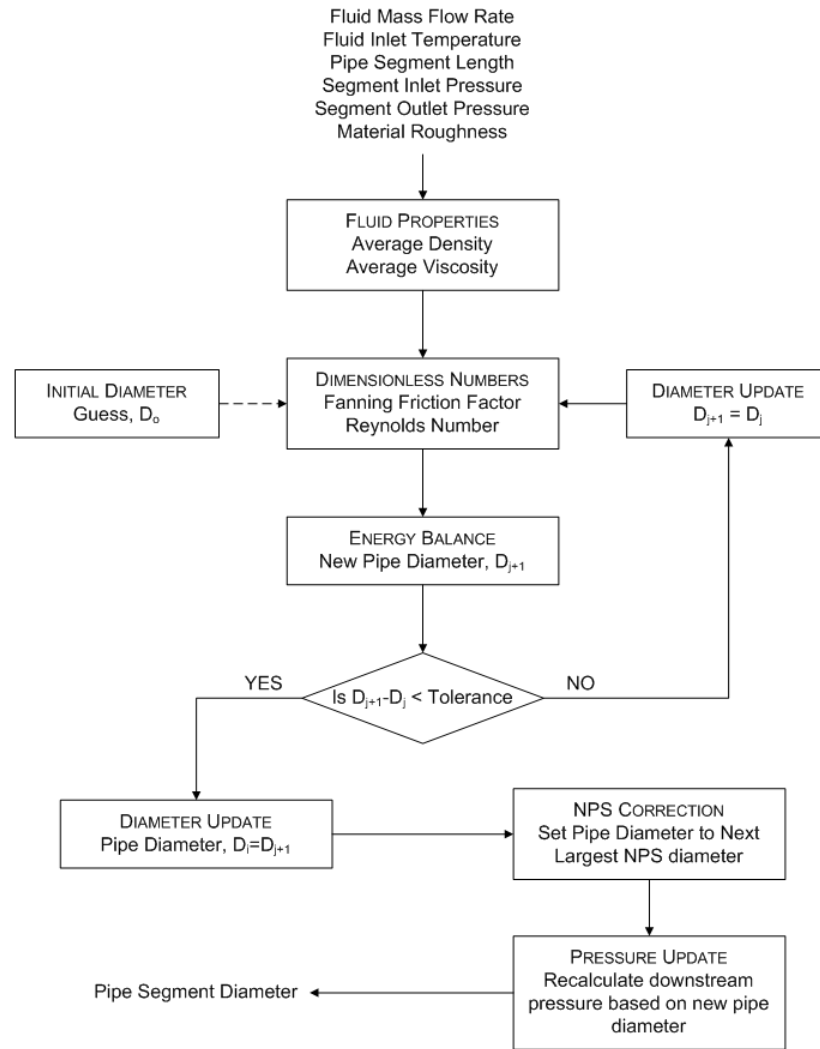
Figure 2.4. Flowchart illustrating the method used to estimate the pipeline segment diameter.

Line pipe is not available in continuous diameters. Thus the internal pipe diameter calculated must be adjusted to account for both available pipe diameters and the pipe wall thickness. A discrete size of line pipe is frequently referred to by its Nominal Pipe Size (NPS), which corresponds approximately to the outside pipe diameter measured in inches. In the model presented here, eleven NPS values between 4 and 30 are available. To determine the inside diameter, the pipe wall thickness (also known as the pipe schedule) for each NPS is estimated using the method specified in the Code of Federal

Regulations (CFR), which regulates the design, construction, and operation of CO_2 pipelines in the United States. The pipe wall thickness, t, in meters is given as [17]:

$$t = \frac{p_{mop} D_o}{2SEF}$$

where, p_{mop} is the maximum operating pressure of the pipeline (Pa), D_o is the outside pipe diameter (m), S is the specified minimum yield stress for the pipe material (Pa), E is the longitudinal joint factor (reflecting different types of longitudinal pipe welds), and F is the design factor (introduced to add a margin of safety to the wall thickness calculation). For the purposes of estimating the pipe wall thickness, the maximum operating pressure is assumed to be 15.3 MPa, the longitudinal joint factor is 1.0, and the design factor is 0.72 (as required in the CFR). The minimum yield stress is dependent on the specification and grade of line pipe selected for the pipeline. For CO_2 service, pipelines are generally constructed with materials meeting American Petroleum Institute (API) specification 5L [18]. In this case, the minimum yield stress has been specified as 483 MPa, which corresponds to API 5L X-70 line pipe.

The value of D_i calculated from Equation 2.4 is adjusted to the next larges value of D_i for an available NPS. Based on the adjusted D_i, the adjusted downstream pressure for the pipeline segment is calculated. This pressure will always be greater than the downstream pressure specified by the user since the adjusted diameter will always be greater than the optimum value calculated by Equation 2.7.

2.1.3   Booster Compression Engineering and Design

Booster compression stations may be required for longer pipeline distances, or for pipelines in mountainous or hilly regions with large increases in elevation. Additionally, in some cases the use of booster compression stations may allow a smaller pipe diameter to be used, resulting in a reduced cost of CO_2 transport.

The compression station size is developed from an energy balance on the flowing CO_2 in a manner similar to the calculation of the pipe segment diameter. If both elevation and velocity changes in the compressor are negligible, the energy balance is:

$$dH = Q + dW$$

where H is enthalpy, Q is heat, and W is work. Thus, if compression is assumed to be adiabatic and reversible (i.e., no heat is lost to the surroundings during compression and there are no losses), then:

$$Q = TdS = 0$$

where T is temperature and S is entropy. Therefore, the reversible work required is equal to the isentropic enthalpy change of the fluid being compressed:

$$W_{is} = \Delta H_{is}$$

The actual work required per unit of CO_2 compressed can then be calculated by dividing by the isentropic and mechanical efficiency:

$$W = \frac{\Delta H_{is}}{\eta_{is} \eta_{mech}} \tag{2.7}$$

The fluid enthalpy required in Equation 2.7 is determined by using thermodynamic departure functions based on the Peng-Robinson parameterization of the cubic equation of state [12] with ideal gas thermodynamic properties calculated using the method proposed by Aly and Lee [19]. Further details on the calculation of enthalpy using these methods are described in Appendix A.

In addition to calculating the work required for a compression stage, the compression algorithm calculates the outlet temperature from compression stage, which allows the required cooling duty to be determined. The general algorithm for calculating the energy requirement for a compressor station is shown in
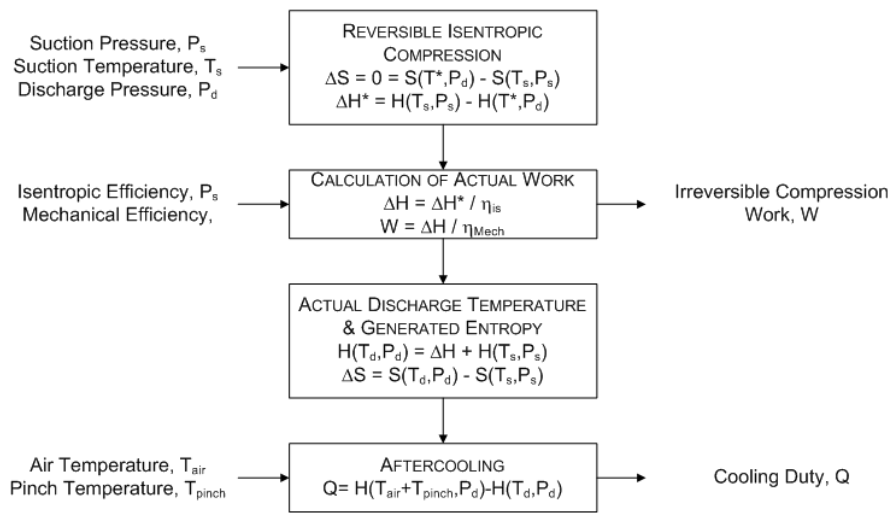
Figure 2.5. The algorithm used to estimate the compressor size and energy requirements for compression of CO_2 at booster compression stations.

Both the compressor size (i.e., brake horsepower) and pipeline diameter are calculated on the basis of the maximum design mass flow rate of CO_2, while the compression station annual power consumption is calculated on the basis of the nominal (i.e., annual average) mass flow rate of CO_2. The nominal mass flow rate of CO_2 is the product of the pipeline

load factor and the design mass flow rate of CO_2. The compressor size is required to determine the capital cost of the compressor, while the compressor station annual power requirement is required to calculate operating cost.

2.1.4 Illustrative Performance Model Results

Figure 2.6 shows the NPS of a pipeline carrying pure CO_2 as a function of the design CO_2 mass flow rate, as calculated by the iteration scheme shown in Figure 2.4. For fixed inlet pressure and minimum outlet pressure, the required pipe diameter increases with increasing design CO_2 flow rate and pipeline distance. Steps in pipeline diameter occur because of the discrete NPS available in the model. For example, the model estimates an internal diameter of 0.38 m for a pipeline spanning a distance of 100 km designed to carry 5 million tonnes per year of CO_2 at a pressure drop of 35 kPa per km. However, this is not a common line pipe size; thus, the next largest NPS is selected by the model, which has an internal diameter of about 0.39 m.
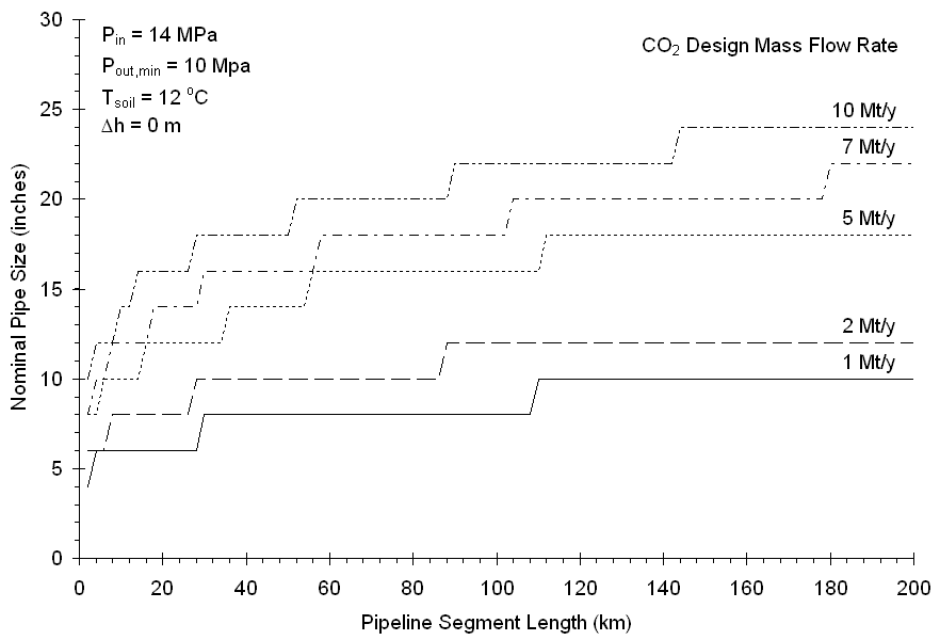
Figure 2.6. Pipeline diameter as a function of length for several flow rates in Mt/y for isothermal flow at 12°C.

Figure 2.6 also shows the economies of scale inherent in the design of the pipeline. For a 100 km long pipeline designed to carry 1 million tonnes per year of CO_2, the model calculates a diameter of 8 inches. For a pipeline with the same design parameter, except designed to handle 5 million tonnes per year, the calculated diameter is 16 inches; for 10 million tonnes per year, the diameter is 22 inches.

The illustrative results for the booster compression station are shown in Figure 2.7 show that the compressor power requirement increases linearly with mass flow rate and decreases more or less linearly with increasing isentropic efficiency. A single compressor station compressing pure CO_2 at 12 °C from approximately 10 MPa to 14 MPa requires 1.43 kWh per tonne of CO_2 that, for a design capacity of 5 million tonnes per year, CO_2 requires an 817 kW compressor.
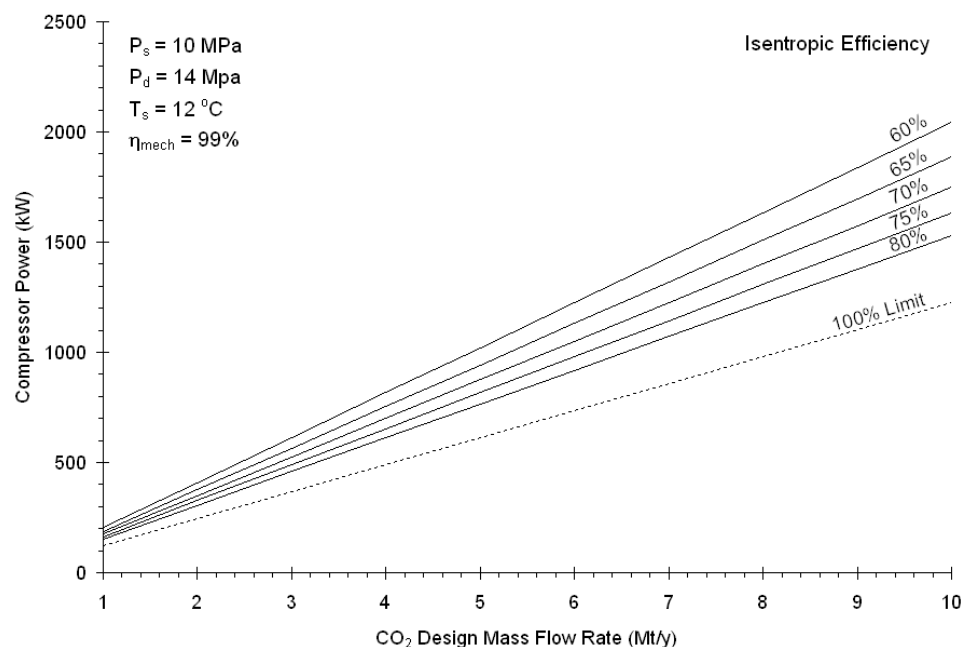
Figure 2.7. Illustrative results from the booster compression station model showing the compressor size as a function of the design mass flow rate of pure CO_2 for several different isentropic efficiencies.

2.2   Pipeline Transport Capital Cost Model

The pipeline transport economic models take output from the performance model (i.e., pipeline diameter) combined with a user-specified pipeline length and the pipeline project region to estimate the capital cost and annual operating costs of the pipeline, as shown in Figure 2.1.

Detailed construction cost data for actual CO_2 pipelines (i.e., as-built-cost including the length and diameter) are not readily available; nor have many such projects been constructed in the last decade [2]. For these reasons, the data set used to develop the pipeline capital cost models is based on natural gas pipelines. However, there are many similarities between transport of natural gas and CO_2. Both are transported at similar pressures, approximately 10 MPa and greater. Assuming the CO_2 is dry, which is a

37

common requirement for CCS, both pipelines will require similar materials. Thus, a model based on natural gas pipelines offers a reasonable approximation for a preliminary design model used in the absence of more detailed project-specific costs.

Section 2.2.1 describes the pipeline data set used to develop the capital cost model, 2.2.2 the pipeline capital cost models, and 2.2.3 provides illustrative results from the models.

2.2.1   Pipeline Data Set

The CO_2 pipeline capital cost model is based on regression analyses of natural gas pipeline project costs published between 1995 and 2005 [20-31]. These project costs are based on Federal Energy Regulatory Commission (FERC) filings from interstate gas transmission companies. The entire data set contains the "as-built" costs for 263 on-shore pipeline projects in the contiguous 48-states and excludes costs for pipelines with river or stream crossings as well as lateral pipeline projects (i.e., a pipeline of secondary significance to the mainline system, such as a tie-in between the mainline and a power plant). Costs from each year's projects have been adjusted to 2004 dollars using the Marshall and Swift equipment cost index [32].

The pipeline data set contains information on the year and location of the project and the length and diameter of the pipeline. Locations are listed by state in the data set; however, to develop the regression models presented here, the states have been grouped into six regions. The project regions used here are the same as those used by the Energy Information Administration for natural gas pipeline regions [36], and are shown in Figure 2.8.
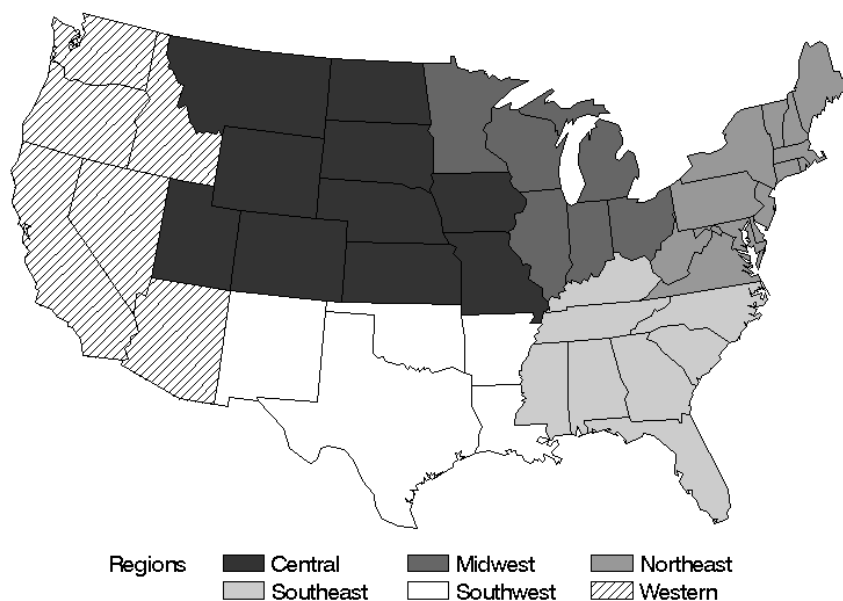
Figure 2.8. The regions used in the pipeline transport cost model.

The total construction cost for each project is broken down into four categories: materials, labor, right-of-way (ROW), and miscellaneous charges. The materials category includes the cost of line pipe, pipe coatings, and cathodic protection. Labor is the cost of pipeline construction labor. ROW covers the cost of obtaining right-of-way for the pipeline and allowance for damages to landowners' property during construction. Miscellaneous includes the costs of surveying, engineering, supervision, contingencies, telecommunications equipment, freight, taxes, allowances for funds used during construction (AFUDC), administration and overheads, and regulatory filing fees.

2.2.2 Pipeline Capital Cost Models

Separate cost models have been developed for each of the cost categories. The capital cost models take this general form:

$$\log(C) = a_0 + a_1 NE + a_2 SE + a_3 C + a_4 SW + a_5 W + a_6 \log(L) + a_7 \log(D_{nps}) \qquad (2.8)$$

where *NE*, *SE*, *CL*, *SW*, and *W* are binary variables reflecting the five geographic regions besides Midwest (i.e., Northeast, Southeast, Central, Southwest, and West, respectively) that take a value of 1 or 0 depending on the region and increase or decrease the estimated cost relative to the Midwest value. *C* is the pipeline capital cost in 2004 US dollars. The variable *L* is the total pipeline length in kilometers, and the *D* is the pipeline NPS. Regional variables exist in the cost model only if they are statistically significant predictors of the cost; thus different cost-component models include different sets of regional variables.

If the intercept and regional variables in Equation 2.8 are collected into a single term and rearranged, the cost model can be rewritten in Cobb-Douglas[2] form:

$$C = bL^{a_6} D_{nps}^{a_7}$$
$$\text{where } \log(b) = a_0 + a_1 NE + a_2 SE + a_3 C + a_4 SW + a_5 W \tag{2.9}$$

There are several properties of Cobb-Douglas functions that are interesting in the context of the cost models. If the sum of a_6 and a_7 is equal to one, the total cost exhibits constant returns to scale (i.e., cost is linear with *L* and *D*). If the sum is less than one, there are decreasing returns to scale, and if the sum is greater than one, increasing returns to scale. Moreover, the values of a_6 and a_7 represent the elasticity of cost with respect to length and diameter, respectively.

Parameter estimates for the materials, labor, miscellaneous charges, and ROW cost components are given in Table 2.1. The generalized regression model given in Equation

---

[2] In economic theory, a Cobb-Douglas production function has the form $f(K,L) = AK^a L^b$, where K and L traditionally refer to capital and labor.

2.8 accounts for a large proportion of the variation in the data set for each of the cost categories, as reflected by all of the cost component models having an adjusted-r^2 value greater than 0.81, with the exception of ROW, which has an adjusted-r^2 value of 0.67.

Table 2.1. Parameter estimates for the pipeline cost model, Equation 2.8, where standard errors are indicated in parentheses.

Coefficient Estimate	Cost Component			
	Materials	Labor	ROW	Miscellaneous
a_0	3.112** (0.067)	4.487** (0.109)	3.950** (0.244)	4.390** (0.132)
a_1	-	0.075* (0.032)	-	0.145** (0.045)
a_2	0.074** (0.021)	-	-	0.132* (0.054)
a_3	-	-0.187** (0.048)	-0.382** (0.093)	-0.369** (0.061)
a_4	-	-0.216** (0.059)	-	-
a_5	-	-	-	-0.377** (0.066)
a_6	0.901** (0.012)	0.820** (0.023)	1.049** (0.048)	0.783** (0.027)
a_7	1.590** (0.045)	0.940** (0.077)	0.403* (0.167)	0.791** (0.091)

** Significant at the 1% level
* Significant at the 5% level

Based on the regression results shown in Table 2.1, several general observations can be made. The cost of all four components exhibit increasing returns to scale, which means that multiplying both the length and diameter by a constant n multiplies the materials cost by a factor greater than n. For example, doubling both pipeline length and diameter results in a nearly 6-fold (rather than 4-fold) increase in materials cost. For the materials, labor and miscellaneous costs, the elasticity of substitution for length is less than one;

thus, a doubling in pipeline length results in less than a doubling of the cost for these components (often referred to as economies of scale). However, the elasticity of substitution for length in the ROW cost is approximately one, so that doubling the length results in a doubling of ROW cost (which is reasonable, as the ROW cost per unit of land should be approximately constant regardless of the pipeline length). The elasticity of substitution for pipeline diameter is less than one for labor, miscellaneous, and ROW costs, again indicating economies of scale; however, for materials cost it is approximately 1.6, so that doubling the pipeline diameter results in a three-fold materials cost increase. Note that this still reflects an economy of scale in the total cost of materials since doubling the diameter would quadruple the total mass of steel needed.

At least one regional variable was found to be statistically significant in all of the regression model cost categories, implying that for some regions, the cost of constructing a pipeline is higher or lower than the average for the Midwest region. For example, the labor cost regression results (Table 2.1) show that the cost intercept is approximately $6,000 greater in the Northeast than the Midwest and approximately $10,000 lower in the Central and Southwest regions. There is no statistical difference (at the 5% level) between the Midwest and West or Southeast cost intercepts.

Cost differences between regions could be caused by a combination of two types of factors: differences between regions in the average cost of materials, labor, miscellaneous costs, and land (affecting ROW cost); and, differences in other geographic factors, such as population density and terrain. Regional variation in labor and materials cost for power plant construction have been documented by the Electric Power Research Institute (EPRI) [33]. However, because the routings of pipeline projects are not reported in the

data set, it is not possible to identify how these individual factors contributed to overall cost of the projects. Thus, there are plausible circumstances where similar pipeline projects in different regions could have costs much closer to one another than to comparable projects within their respective regions (e.g. pipelines of similar length and design CO_2 mass flow in heavily populated versus unpopulated areas within the same state). Zhang et al. [34] have developed more data intensive tools to study least-cost routing of specific CO_2 pipelines which are complimentary to the use of the current screening level model.

2.2.3 Compressor Capital Cost Model

The total capital cost of a reciprocating compressor station has been estimated by the IEA for a European study involving the pipeline transmission of CO_2 [5]. This cost is given by the regression in Equation 27:

$$C = 8.35P + 0.49$$

where the result is in millions of US dollars (2004), and P is the installed booster station power in MW. This correlation yields a cost slope of $8,346 per kW of installed capacity.

2.2.4 Illustrative Capital Cost Model Results

The behavior of the capital cost models is shown in Figure 2.9, where the category cost model results are stacked to indicate the total cost of a 16 inch diameter pipeline for distances from 10 mi to 60 mi located in the Midwest. For reference, a 16 inch pipeline could transport approximately 5 million metric tonnes of CO_2 per year over a 100 km distance, which would be approximately the maximum annual emissions of a 600 MW (net) pulverized coal fired plant with 90% CO_2 capture.
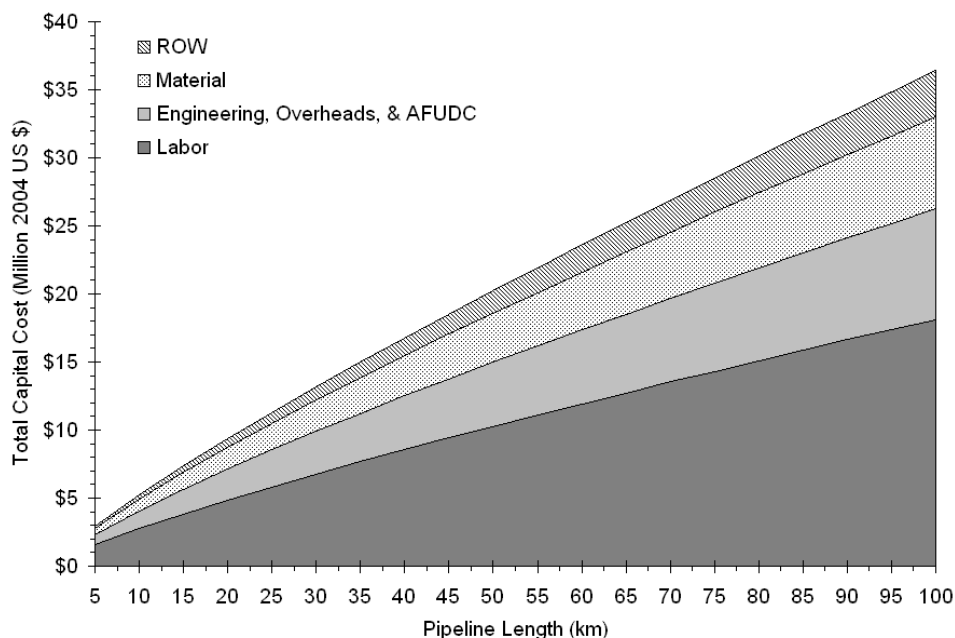
Figure 2.9. The capital cost (in millions of constant 2004 US dollars) of a 16 inch pipeline located in the Midwest over varying lengths.

Figure 2.9 shows that the labor cost accounts for over 50% of the total cost of a 16 inch pipeline across all distances between 5 km and 100 km. The next largest cost category is engineering, overheads, and AFUDC (i.e., miscellaneous), followed by materials, and ROW. However, the size breakdown shown in Figure 2.9 is dependent on the pipeline diameter. For example, the material cost increases more rapidly with pipeline diameter than the miscellaneous cost, thus for a 36 in pipeline, the materials cost is much a much larger fraction of the total cost than the miscellaneous cost.

The regional dependence of the labor, miscellaneous, and ROW models means that the predicted cost of projects in some regions will be either higher or lower than the cost of equivalent projects in other regions. The difference in cost between the Midwest and the other five regions is summarized in Table 6 for a 16 inch diameter pipeline that is 100 km long. The results in this table show that, when compared to the Midwest, pipelines in the

Northeast and Southeast are more expensive to construct, and pipelines in the Central and

Southwest are less expensive to construct.

Table 2.2. The cost of construction of a 100 km, 16 inch pipeline in the Midwest in
millions of dollars (constant 2004 US dollars), and the regional differences relative to
Midwest cost, where values in brackets are negative.

Capital Cost (Million $)	Midwest	Difference from Midwest				
		Northeast	Southeast	Southwest	West	Central
Material	6.746	0	1.244	0	0	0
Labor	18.129	3.430	0	(7.113)	0	(6.348)
Miscellaneous	8.110	3.226	2.890	0	(4.707)	(4.640)
ROW	3.417	0	0	0	0	(1.999)
Total	36.402	6.656	4.134	(7.113)	(4.707)	(12.988)

2.3   Pipeline Transport Operating & Maintenance Cost Model

In the United States, pipeline maintenance activities are regulated under Title 49 of the

Code of Federal Regulations (CFR), Section 195, subsections 400 through 452. These

regulations specify requirements for training, inspections, and repairs. Routine activities

that fall under the category of maintenance activities include:

- ROW and facilities environmental protection

- ROW and site maintenance

- Pipeline depth of cover maintenance

- Aerial inspection/patrol and leak detection

- ROW erosion control and stabilization

- Cathodic protection monitoring and maintenance

- Pipeline integrity assessment

- Pipeline repair and modifications

- Pipeline encroachment assessment

- Equipment operational test and routine maintenance

- Aesthetics and landscaping

In addition to these activities, Title 49 of the CFR, Section 195, Subpart 452, requires the operator of a CO_2 pipeline to develop and maintain an integrity management program that addresses risks along each segment of their pipeline system. This program is particularly addressed to address risks in high consequence areas (i.e., a populated place or navigable waterway).

While operating and maintenance (O&M) costs are not large in comparison to the annualized capital cost of pipeline transport, they are nonetheless significant. Bock et al. [6] report that the O&M cost of operating a 480 km CO_2 pipeline is between $40,000 and $60,000 per month. On an annual basis, this amounts to approximately $3,250 per kilometer of pipeline in 2004 dollars. Thus, for a 100 km long pipeline, transporting approximately 5 million tonnes per year of CO_2 with no booster pumping stations, the O&M cost would account for approximately 6% of the total cost per tonne of transportation.

Based on the EPRI Technical Assessment Guide [33], the O&M charges associated with the booster compression stations (in addition to energy cost) are assumed to be 1.5% of their original capital cost, annually.

2.4   Combining Performance and Cost

As Figure 2.1 shows, the cost model is dependent on the diameter of the pipeline as calculated by the performance model. Thus, the model begins by calculating the pipeline diameter for each pipeline segment using the method described in Section 2.1.2.

The number of pipeline segments is determined by the number of compressor stations specified by the user—the number of pipeline segments being one greater than the number of booster stations. For example, for a 100 km pipeline if there are two compression stations specified there are then three pipe segments. The pipeline segment length, inlet pressure, and minimum outlet pressure are all specified by the user for each pipeline segment. Thus, the calculated pipeline diameter for each pipeline segment can be different.

The capital cost for the pipeline project is estimated by summing up the capital cost for each pipeline segment and booster station. However, because the elasticity of substitution for length is less than one for materials, labor and miscellaneous capita cost (as shown by the coefficients in Table 2.1), the cost for each segment is calculated as if the entire pipeline project length were of that particular diameter, then scaled to the length of the segment. For example, the materials capital cost of a 16 inch NPS, 100 km long pipeline, is $67,459 per km; for a 100 km long pipeline with two 50 km long segments, one of which is 16 inch NPS, the materials capital cost for the shorter 16 inch NPS segment is

still $67,459. This approach is taken because it is assumed that the economies of scale for a long pipeline project with multiple segments of differing diameters would be equal to— or at least insignificantly different from—the economies of scale for a project of the same length of a single diameter.

The key results reported by the newly developed pipeline model include the total capital cost, annual O&M cost, total levelized cost, and the levelized cost per metric tonne of CO_2 transported (all in constant 2004 US dollars). The capital cost can be subject to capital cost escalation factors applied to individual categories of the capital cost (i.e., materials, labor, miscellaneous, and ROW). These escalation factors can be used to account for anticipated changes in capital cost components (e.g., in the cost of steel) or other project-specific factors that might affect capital costs relative to the regional averages discussed earlier (e.g., river crossings). Capital costs are annualized using a levelized fixed charge factor calculated for a user-specified discount rate and project life [35]. The cost per tonne CO_2 transported reflects the amount of CO_2 transported, which is the product of the design mass flow rate and the pipeline capacity factor.

2.5   Illustrative Case Study Results

Illustrative results from the pipeline model were developed using parameters representative of a typical coal-fired power plant in the Midwest region of the United States (Table 2.3). Several parameter values (e.g., capital recovery factor) are default values from the IECM software [35]. Table 2.3 includes a nominal CO_2 mass flow rate and pipeline length, but these two parameters are varied parametrically in the case study results presented here.

Table 2.3. Illustrative case study parameters for the pipeline transport model

Model Parameter	Deterministic Value	Uncertainty Distribution
Pipeline Performance Parameters		
Design Mass Flow (Mt/y)	5	Variable[§]
Pipeline Length (km)	100	Variable[§]
Elevation Change (m)	0	
Pipeline Capacity Factor (%)	100	Uniform (50, 100)
Ground Temperature (^{o}C)	12	
Inlet Pressure (MPa)	13.79	Uniform (12, 15)
Minimum Outlet Pressure (MPa)	10.3	
Pipe Roughness (mm)	0.0457	
Number of Booster Stations	0	
Economic and Financial Parameters		
Project Region	Midwest	
Capital Recovery Factor (%)	15*	Uniform (10, 20)
Annual O&M Cost ($/km/y)	3,250	Uniform (2,150, 4,350)
Escalation Factor for Materials Cost	1	Uniform (0.75, 1.25)
Escalation Factor for Labor Cost	1	Uniform (0.75, 1.25)
Escalation Factor for ROW Cost	1	Uniform (0.75, 1.25)
Escalation Factor for Miscellaneous Cost	1	Uniform (0.75, 1.25)
Escalation Factor for Compression Cost	1	

* Corresponds to a 30-year plant lifetime with a 14.8% real interest rate (or, a 20-year life with 13.9% interest rate) [§] This parameter modeled as a discrete value for sensitivity analysis

For the case study CO_2 pipeline in the Midwest, the total levelized cost of transport is estimated to be $1.16 per tonne of CO_2 transported. Table 2.4 shows the regional differences in CO_2 transport cost relative to the Midwest for a pipeline with the same parameters as in Table 2.3. In general, the model shows that the cost is greatest in the Northeast, followed (in descending order) by the Southeast, Midwest, West, Southwest, and Central U.S. This trend applies to all pipeline lengths and design mass flows. Overall, the cost category that accounts for the largest regional difference is the labor cost, which is lowest in the Southwest and highest in the Northeast.

Table 2.4. The cost of pipeline transport in the Midwest and regional differences relative to the Midwest, where bracketed values are negative (all costs in constant 2004 US dollars).

Transport Cost ($/tonne CO_2)	Midwest	Difference from Midwest				
		Northeast	Southeast	Southwest	West	Central
Materials	0.20	0	0.04	0	0	0
Labor	0.54	0.10	0	(0.21)	0	(0.19)
Miscellaneous	0.24	0.10	0.09	0	(0.14)	(0.14)
ROW	0.10	0	0	0	0	(0.06)
O&M	0.07	0	0	0	0	0
Total	1.16	0.20	0.12	(0.21)	(0.14)	(0.39)

Figure 2.10 shows results from the model as a function of pipeline distance for a project in the Midwest for four different design mass flow rates. In this example the pipeline capacity factor is assumed to be 100%, so the annual mass transported equals the design capacity of the pipeline. Figure 2.10 shows that the levelized transport cost increases with distance and decreases with increasing design capacity for a fixed distance. For a typical 500 MW power plant (emissions of approximately 2-3 million tonnes per year), transport costs could range from $0.15 per tonne for a 10 km pipeline to $4.06 per tonne for a 200 km pipeline. For an annual capacity factor of 75% (typical of existing coal-fired power plants), the levelized cost per tonne would increase to between $0.20 per tonne for the 10 km pipeline to $5.41 per tonne for 200 km pipeline. Figure 2.10 also illustrates the differences in cost between the pipelines constructed in the Northeast and Central regions. For all pipeline distances and all pipeline design capacities, the transport cost is lowest in the Central region and highest in the Northeast region.
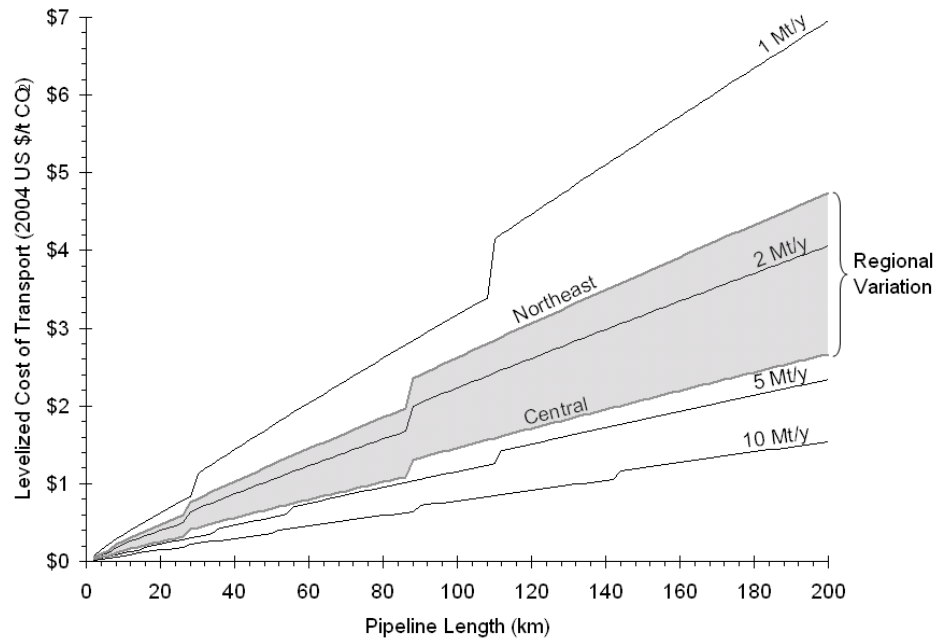
Figure 2.10. Illustrative results from the transport model showing the transport cost (in constant 2004 US dollars) over a range of pipeline design capacities and pipeline distances

2.5.1   Model Sensitivity Analysis Results

To assess the sensitivity of the model to changes in multiple design and financial parameters, uniform distributions were assigned to several parameters of interest and a series of Monte Carlo trials were used to calculate the pipeline transport cost. The uniform distribution was selected to represent uncertainty or variability because there is no prior information that would suggest choosing a more complex distribution (such as a triangular or lognormal distribution). The design parameters of interest are the ground temperature, and pipeline inlet pressure, while financial parameters include pipeline capacity factor, capital recovery factor, and annual pipeline O&M cost. Values of the input parameters for the probabilistic analysis are also shown in Table 2.3.

For this analysis 1,000 trials were conducted for each region. From these trials a cumulative distribution function (CDF) for transport cost has been generated, shown in Figure 2.11. The CDF shows that for a Midwest pipeline project transporting 5 million tonnes of CO_2 annually over 100 km, a 90% probability interval (which reflects the selection of input parameters) yields levelized costs between approximately $1.03 and $2.63 per tonne of CO_2 transported. The minimum and maximum cost predicted by the model are $0.75 and $3.56 per tonne of CO_2 transported; however, these values are very sensitive to the number of Monte Carlo simulations performed. A less sensitive measure is the median cost of transport, which is $1.65 per tonne under these conditions.
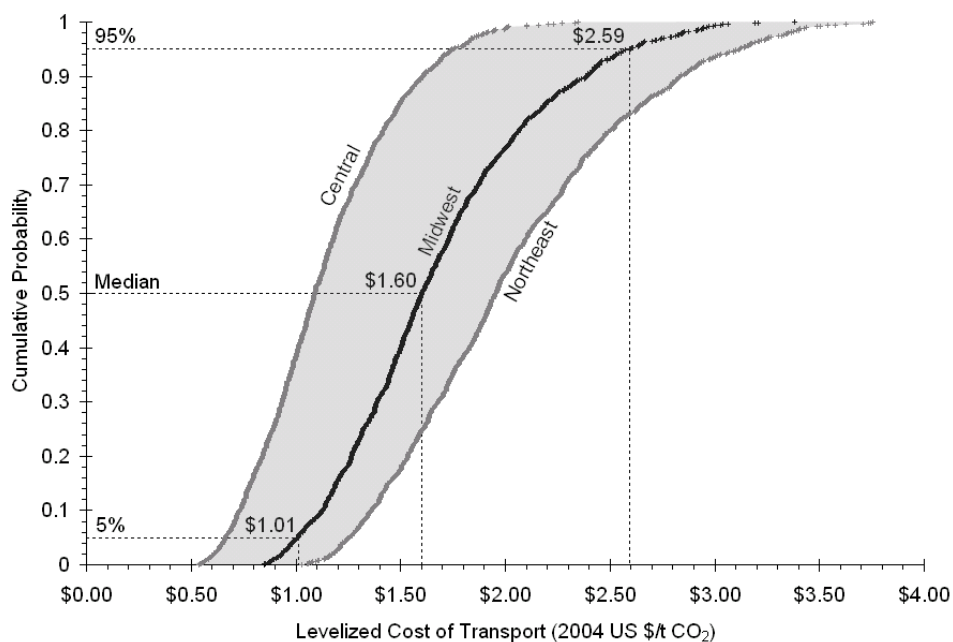
Figure 2.11. Cumulative density function generated from the Monte Carlo sensitivity analysis on the transport model.

Using the cost models for different regions changes the results of the sensitivity analysis, also shown in Figure 2.11. Thus, a project in the Central US region will have costs less than a project in the Midwest or Northeast for all combinations of input parameters. The

median cost of a project in the Central US transporting 5 million tonnes of CO_2 annually

over 100 km is $1.09 per tonne, with 90% confidence interval between $0.66 and $1.74

per tonne. In the Northeast, the project cost could approach that of the Midwest for some

combinations of input parameters. The median cost of this project in the Northeast is

$1.95 per tonne, with a 90% confidence interval between $1.26 and $3.12 per tonne.

Results of the Monte Carlo trials can also be used to assess the sensitivity of transport

cost to the model parameters having uniform distributions. The measure used to assess

the sensitivity is the Spearman rank-order correlation (r_s) [36]. Similar to the commonly

used Pearson product-moment correlation (i.e., r-value), which measures strength of a

linear relationship between variables, rank-order correlation is a measure of direction and

association between the statistical rank of variables. The value of the rank order

correlation coefficient between the transport cost and the model parameters is shown in

Figure 2.12. The dashed vertical lines to the left and the right of the axis in Figure 2.12

indicate the 5% significance level ($r_s = \pm0.07$); thus rank-order correlation coefficients

smaller than this value are not statistically significant at the 5% level. Figure 2.12 shows

the strongest correlation is between pipeline capacity factor ($r_s = -0.67$) and transport

cost, followed by capital recovery factor ($r_s = 0.65$). Following these, significant rank-

order correlation coefficients (by decreasing magnitude) are the inlet pressure, real

materials escalation rate, and elevation change. This implies that the pipeline capacity

factor and capital recovery factor are far stronger determinants of pipeline transport cost

than any of the escalation factors. For example, to double the levelized cost of transport

for the illustrative CO_2 pipeline (parameters presented in Table 2.3) the capital cost

escalation factor for pipeline materials would have to be increased 400% to 800%,

depending on the project region. By contrast, only a 50% reduction in the pipeline

capacity factor is required to double the levelized cost.
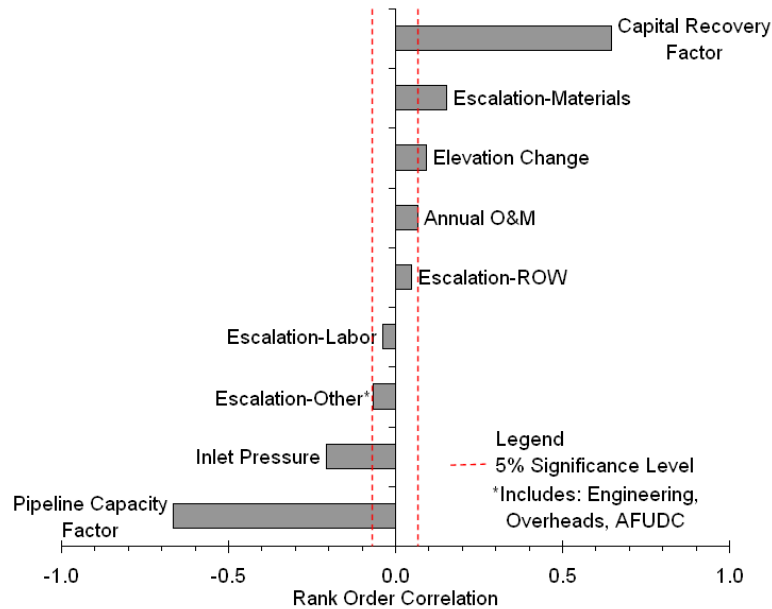
Figure 2.12. Rank-order correlation between the results of the Monte Carlo sensitivity analysis and the parameters assigned uniform distributions.

2.5.2   *Optimization of Pipeline Parameters*

While the results presented in this section are based on reasonable assumptions about

design parameters (presented in Table 2.3), the parameters may not be the optimum

parameters to minimize the cost of transport. For example, incorporating compressor

stations into the design can result in reduced capital costs. Moreover, in many cases this

will be necessary due to terrain features. Cost savings can occur with the installation of

compressor stations if the decreased capital cost resulting from a smaller diameter

pipeline offset the increased capital and operating costs from compressor stations.

Figure 2.13 shows the difference between the levelized cost of transport with and without the optimal number of compressor stations for different annual CO_2 flow rates and distances using the pipeline performance and design parameters listed in Table 2.3. The cost of energy is assumed to be $40 per MWh in this analysis. Regardless of the assumptions surrounding energy cost, however, cost savings achieved by adding booster stations decrease with increasing amounts of CO_2 handled, and increases with pipeline length. The optimum number of compressors in Figure 2.13 was arrived at through a "brute force" optimization method where the number of compressors for a given flow rate and distance is increased in integer steps from zero to find the number of compressors that minimizes cost.
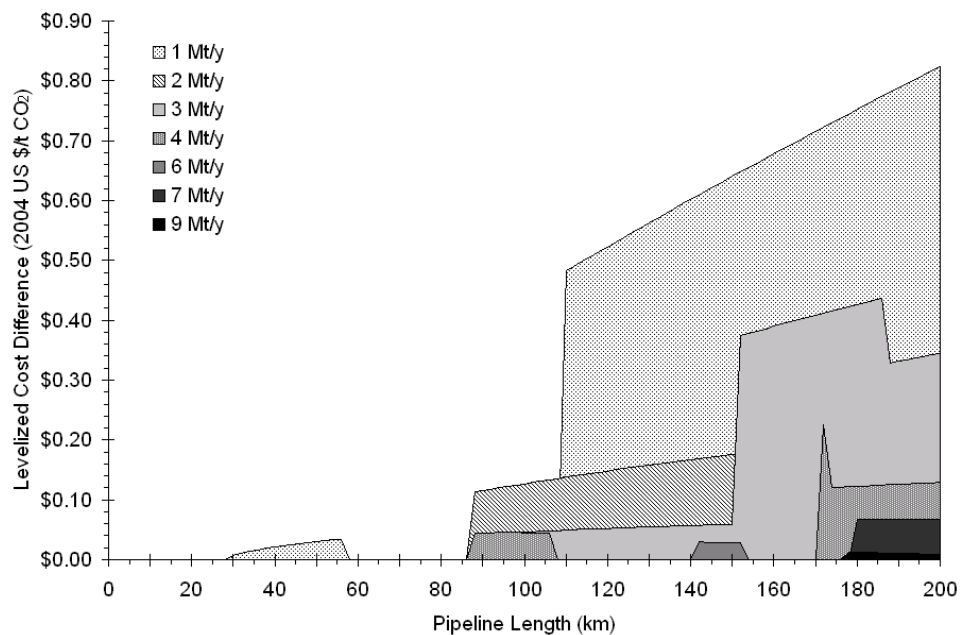
Figure 2.13. The difference (in constant 2004 US dollars) between the levelized cost of transport without compression and with the cost-minimizing number of compressors.

2.6   Comparison with Other Models

Differences between the pipeline transport model developed in this thesis and other models stem from differences in the performance model (i.e., the way the required pipeline diameter is calculated), as well as in the cost model. To better explain differences between available models, differences in the performance model, cost model, and overall results will be discussed separately.

2.6.1   Performance Model Comparison

The pipeline transport model developed in this thesis (referred to as the thesis model) is compared in Figure 2.14 with a model developed by MIT [6]. The most significant differences between the MIT model and thesis model are that: the MIT model allows for continuous pipe sizes while the thesis model only allows discrete pipe sizes corresponding with commonly available NPS; the thesis model allows for discrete pipe segments with elevation changes, while the MIT model does not; and, the MIT model does not account for the compressible nature of the flowing CO_2, while the thesis model does.

Figure 2.14 shows that for the same conditions, the thesis model tends to predict a larger pipe diameter than the MIT model. Part of the explanation for this difference is that the pipeline diameter predicted by the thesis model is the NPS pipe size, while the MIT pipeline model predicts the required internal diameter. However, the difference between the predicted diameters is larger than can be explained by wall thickness for larger distances. The primary reason for the difference, particularly at longer distances, is that the thesis model accounts for compressibility of the CO_2, resulting in a larger pipe diameter. Moreover, the MIT model calculates the properties of the flowing CO_2 at the

inlet of the pipeline, rather than averaged over the entire length of the pipeline as in the

thesis model, resulting in a smaller calculated pipe diameter.
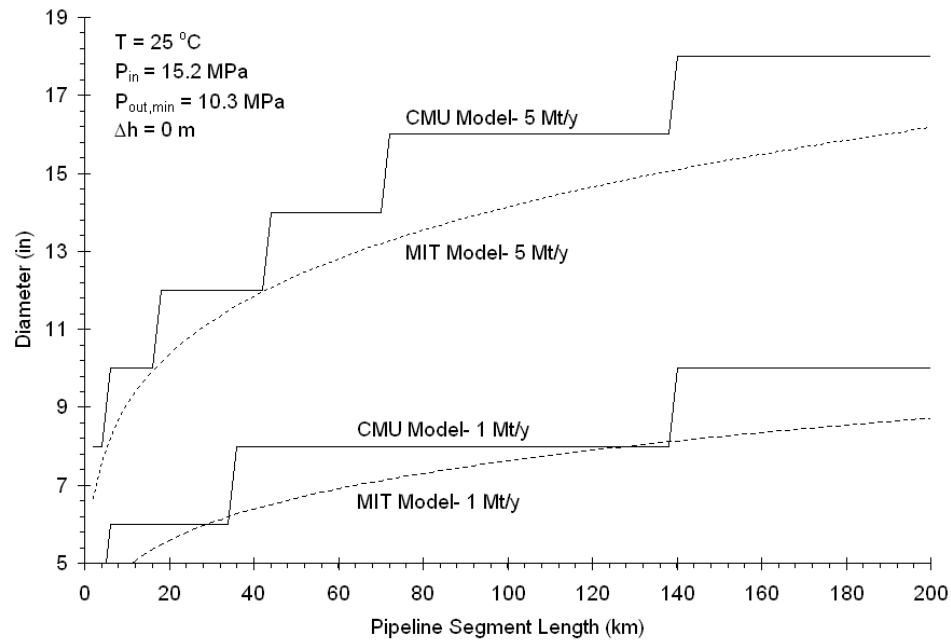
Figure 2.14. A comparison between the MIT model and the thesis model, showing that the thesis model generally predicts a larger pipe diameter for a range of flow rates (1-5 Mt/y).

A further comparison can be made with the rules-of-thumb proposed by Skovholt [4]

which are based on relatively low pressure compared to the pressures that would likely be

used in a CO_2 pipeline constructed today. The parameters used by Skovholt are presented

in Table 2.5.

Table 2.5. Parameters used by Skovholt to determine rules-of-thumb for pipe diameter

Pipeline Parameter	Value
Segment Length (km)	250
Ground Temperature (oC)	6
Maximum Pressure (MPa)	11
Minimum Pressure (MPa)	9

Using these parameters, the diameters calculated by Skovholt are compared with

diameters calculated by the thesis model for the same conditions in Table 2.6. In this

case, the diameters calculated by the thesis model are consistently larger for all mass flow

rates. Moreover, the thesis model can not accommodate the case of 110 million tonnes

per year in one pipeline. The reasons for the difference between the diameters presented

by Skovholt and those calculated by the thesis model are not clear, as Skovholt does not

describe the methods used to calculate the rules-of-thumb.

Table 2.6. Pipe diameters proposed by Skovholt compared with those calculated by the thesis model (all diameters in inches).

Design Mass Flow (Mt_{CO2}/y)	Skovholt	Thesis Model
3	16	18
20	30	36
35	40	48
110	64	N/A

2.6.2   Cost Model Comparison

The thesis cost models can be compared with the cost model from the previously

mentioned MIT study [6], cost models developed in a study for the IEA [5], and models

developed for the Midwest Geological Carbon Sequestration (MGSC) Partnership [37].

This comparison is shown in Figure 2.15 for the case of a 16-inch pipeline.

Figure 2.15 shows the total capital cost of a 16 inch NPS pipeline for a range of distances

as calculated by the MIT model, which uses a simple slope factor ($/in/km); the MGSC

model, which uses discrete slope factors ($/km) for diameters between 4 and 24 inches,

and; the IEA models, which depends on the operating pressure of the pipeline as well as

length and diameter. The IEA ANSI Class #900 model is for pipelines with an operating

pressure up to approximately 14 MPa, while the Class #1500 model is for pressures up to about 23 MPa. The figure shows that the thesis model predicts costs that are less than those predicted by the MIT model, on the low side of the MGSC model, and higher than either of the IEA models. Moreover, Figure 2.15 shows that the MIT, IEA, and MGSC models are linear in length, but the thesis model is slightly non-linear. In the thesis model, the cost per unit length decreases slightly with increasing pipeline length.
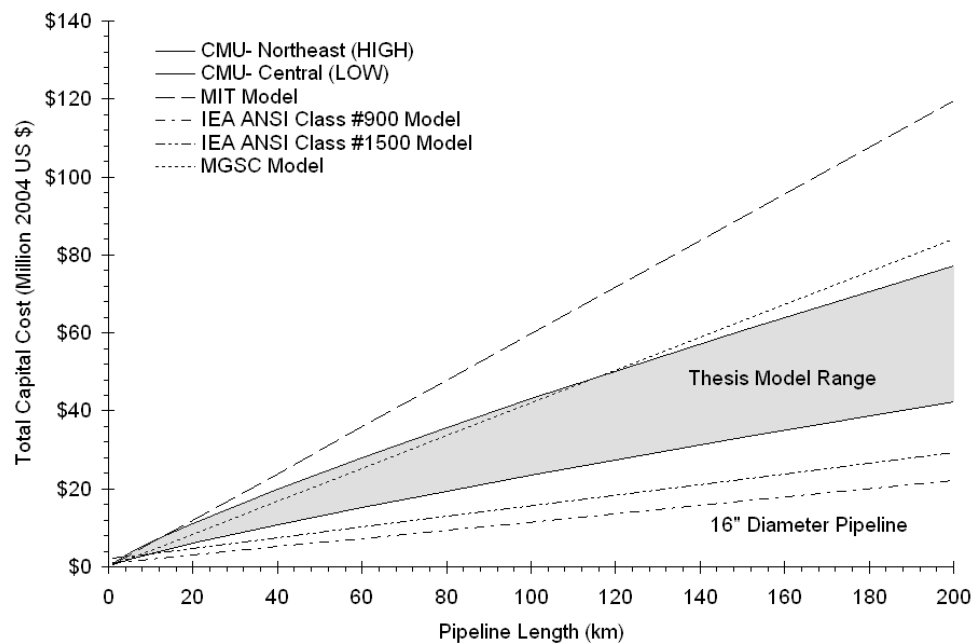
Figure 2.15. The range of capital costs possible from the thesis cost models, depending on region, compared with the capital costs possible from the MIT, IEA, and MGSC models for a 16" NPS pipeline over a range of pipeline lengths.

The differences between the thesis, MIT, IEA, and MGSC models are likely due to the differing approaches taken in their development. Both the IEA and MGSC models are based on "bottom-up" cost estimates, developed from private design studies of pipeline projects. On the other hand, the MIT model is based on similar data to the thesis model,

but with a smaller set of projects, no variation by region, and no accounting for the non-linear effects of length on cost.

2.6.3   Overall Model Comparison

Results from the MIT model and the thesis model can be compared over a range of lengths. Unfortunately, the overall results of the IEA and MGSC model can not be compared in the same way—the IEA model implementation is not amenable to sensitivity analysis, while the MGSC has not developed a design model. Figure 2.16 shows the results of the comparison between the MIT and thesis models for a fixed mass flow rate of 5 Mt/y, and a charge factor of approximately 16%.
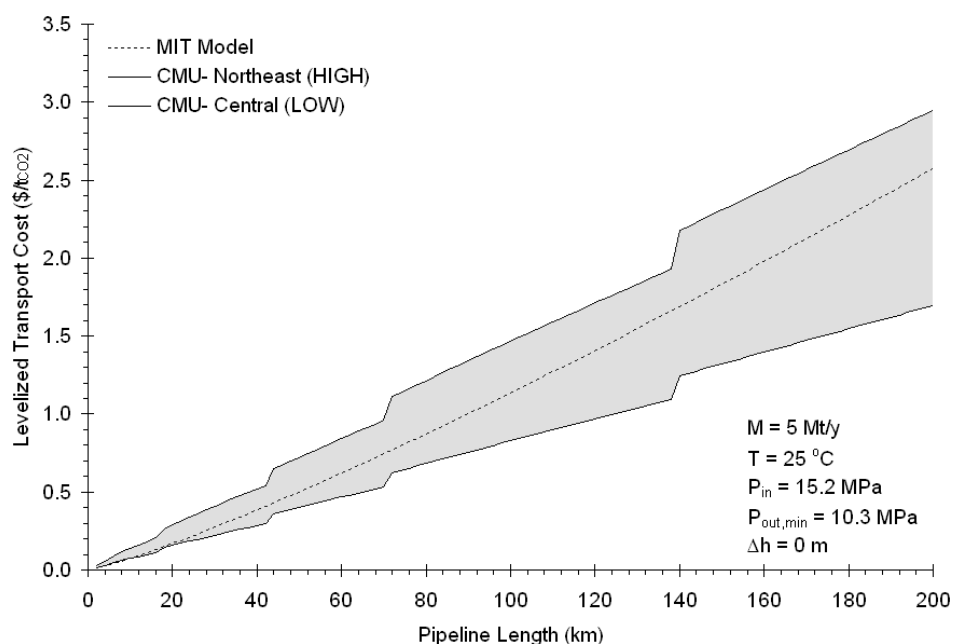
Figure 2.16. A comparison of results from the thesis pipeline transport model and the MIT pipeline transport model for a design mass flow rate of 5 million tones of CO_2 per year over a range of distances.

Figure 2.16 shows that, depending on the region selected in the thesis model, the lower costs and the larger pipe diameters predicted by the thesis transport model compared to

the MIT cost model cancel out. Nonetheless, there are significant differences between the costs predicted by the models, particularly at long lengths for pipelines in the Central, West, and Southwest, where the cost predicted by the thesis model is at least 20% less than the cost predicted by the MIT model.

The thesis model is also compared in Figure 2.17 against the results presented in the IPCC Special Report on Carbon dioxide Capture and Storage [2]. Levelized costs shown in Figure 2.17(a) generally agree with the results presented in the IPCC Special Report, repeated in Figure 2.17 (b). However, costs for projects in the central region are lower than the lower "onshore" bound in Figure 19. This may be because the results represented in the IPCC Special Report figure are not region specific. Moreover, the pipeline inlet pressure, outlet pressure, and temperature could be adjusted to change the required pipe diameter, altering the costs presented in Figure 2.17 (a).
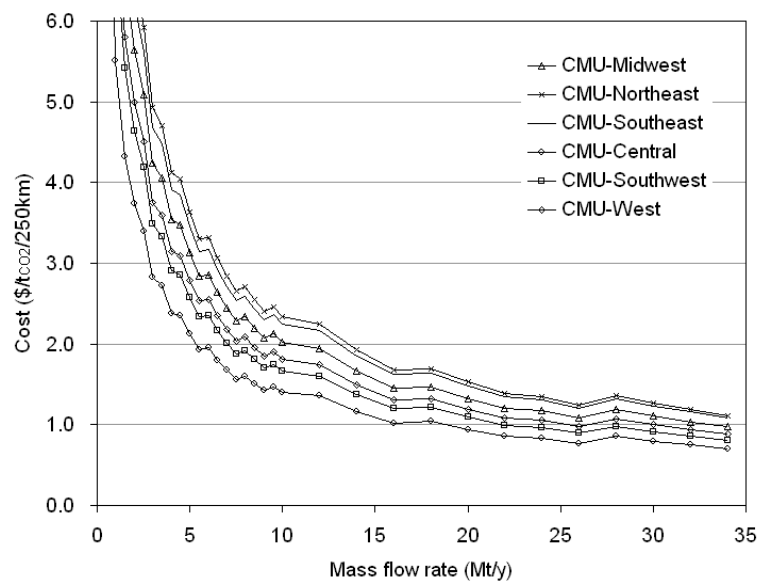
(a)
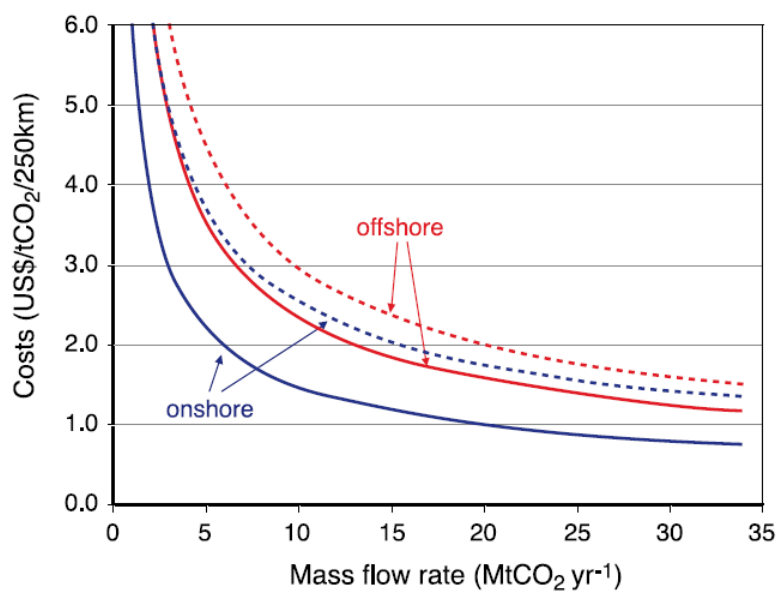
(b)

Figure 2.17. Comparison of results from the thesis model (a) and results reproduced from the IPCC Special Report [2] (b).

2.7   References

1.   Svensson, R., et al., *Transportation systems for CO$_2$-application to carbon capture and storage.* Energy Conversion & Management, 2004. **45**: p. 2343-2353.

2.   Doctor, R., et al., *Transport of CO$_2$*, in *IPCC Special Report on Carbon Dioxide Capture and Storage*, B. Metz, et al., Editors. 2005, Cambridge University Press: Cambridge, U.K.

3.   Gale, J. and J. Davidson, *Transmission of CO$_2$- Safety and Economic Considerations.* Energy, 2004. **29**: p. 1319-1328.

4.   Skovholt, O., *CO$_2$ Transportation System.* Energy Conversion & Management, 1993. **34**(9-11): p. 1095-1103.

5.   Woodhill Engineering Consultants, *Pipeline Transmission of CO$_2$ and Energy: Transmission Study - Report.* 2002, IEA Greenhouse Gas R&D Programme: Stoke Orchard, UK.

6.   Bock, B., et al., *Economic Evaluation of CO$_2$ Storage and Sink Enhancement Options.* 2003, TVA Public Power Institute: Muscle Shoals, AL.

7.   Fesmire, C.J., *531 BCF of CO$_2$ Through the CRC System.* Energy Progress, 1983. **3**(4): p. 203-206.

8.   Zhang, Z.X., et al., *Optimization of pipeline transport for CO$_2$ sequestration.* Energy Conversion & Management, 2006. **47**: p. 702-715.

9.   Recht, D.L., *Design Considerations for Carbon-Dioxide Pipe Lines. 1.* Pipe Line Industry, 1984. **61**(3): p. 53-54.

10.   Reid, R.C., J.M. Prausnitz, and B.E. Poling, *The Properties of Gases and Liquids.* 4th ed. 1987: McGraw-Hill Book Company.

11.   Chung, T.H., et al., *Generalized Multiparameter Correlation for Nonpolar and Polar Fluid Transport Properties.* Industrial & Engineering Chemistry Research, 1988. **27**: p. 671-679.

12.   Poling, B.E., J.M. Prausnitz, and J.P. O'Connell, *The Properties of Gases and Liquids.* 5 ed. 2001: McGraw-Hill Book Company.

13.   Farris, C.B., *Unusual Design Factors for Supercritical CO$_2$ Pipelines.* Energy Progress, 1983. **3**(3): p. 150-158.

14.   Mohitpour, M., H. Golshan, and A. Murray, *Pipeline Design & Construction.* 1st ed. 2003, New York, NY: ASME Press.

15.   Zigrang, D.J. and N.D. Sylvester, *Explicit Approximations to the Solution of Colebrook Friction Factor Equation.* AICHE Journal, 1982. **28**(3): p. 514-515.

16.   Boyce, M.P., *Transport and Storage of Fluids*, in *Perry's chemical engineers' handbook*, R.H. Perry, D.W. Green, and J.O. Maloney, Editors. 1997, McGraw-Hill: New York, NY.

17.   "Transportation." Title 49 <u>Code of Federal Regulations</u>, Pt. 195. 2005 ed., 170-171.

18.   American Petroleum Institute, *Spec 5L- Specification for Line Pipe.* 43rd ed. 2004, Washington, D.C.: American Petroleum Institute. 155.

19.   Aly, F.A. and L.L. Lee, *Self-consistent equations for calculating the ideal gas heat capacity, enthalpy, and entropy.* Fluid Phase Equilibria, 1981. **6**(3-4): p. 169-179.

20.   Smith, C.E., W.R. True, and J. Stell, *US gas carriers see 2004 net jump; construction plans rebound.* Oil & Gas Journal, 2005. **103**(34): p. 50-54.

21.   True, W.R., *Special Report: Pipeline Economics.* Oil & Gas Journal, 2000. **98**(36): p. 68-86.

22.   True, W.R., *Special Report: Pipeline Economics.* Oil & Gas Journal, 2003. **101**(34): p. 60-90.
23.   True, W.R., *Profitable 2000, higher demand push US natural gas construction plans.* Oil & Gas Journal, 2001. **99**(36): p. 66-80.
24.   True, W.R., *More construction, higher costs in store for US pipelines.* Oil & Gas Journal, 2000. **98**(36): p. 68-70.
25.   True, W.R., *U.S. pipelines experience another tight year, reflect merger frenzy.* Oil & Gas Journal, 1999. **97**(34): p. 13.
26.   True, W.R., *US pipeline companies solidly profitable in 2002, scale back construction plans.* Oil & Gas Journal, 2003. **101**(34): p. 60-90.
27.   True, W.R., *Fed data show solid 2001 for US pipeline companies, more gas capacity planned.* Oil & Gas Journal, 2002. **100**(38): p. 52.
28.   True, W.R., *Construction plans jump; operations skid in 1996.* Oil & Gas Journal, 1997. **95**(31): p. 37.
29.   True, W.R., *U.S. pipelines continue gains into 1996.* Oil & Gas Journal, 1996. **94**(48): p. 39.
30.   True, W.R., *U.S. interstate pipelines ran more efficiently in 1994.* Oil & Gas Journal, 1995. **93**(48): p. 39.
31.   True, W.R. and J. Stell, *US construction plans slide; pipeline companies experience flat 2003, continue mergers.* Oil & Gas Journal, 2004. **102**(32): p. 52.
32.   Chemical Engineering. *Plant Cost Index.* 2006 [cited 2006 1 June 2006]; Available from: http://www.che.com/pindex/.
33.   Electric Power Research Institute, *TAG-Technical Assessment Guide Volume 1: Electricity Supply*. 1993, Electric Power Research Institute: Palo Alto, California.
34.   Zhang, H., W. Li, and H. Herzog, *MIT CO$_2$ Pipeline Transport and Cost Model*. 2007, Massachusetts Institute of Technology: Carbon Capture and Sequestration Technologies Program: Boston, Massachusetts.
35.   Berkenpas, M.B., et al., *User Manual: Integrated Environmental Control Model*. 2004, Carnegie Mellon University: Pittsburgh, PA. p. 371.
36.   Morgan, M.G., M. Henrion, and M. Small, *Uncertainty : a guide to dealing with uncertainty in quantitative risk and policy analysis*. 1990, Cambridge: Cambridge University Press. 332.
37.   Nyman, D.J., J.S. Dracos, and R. Varagani, *Carbon Dioxide Capture and Transportation Options in the Illinois Basin--Task 3: Assess Carbon Dioxide Transportation Options in the Illinois Basin*. 2004, Midwest Geological Sequestration Partnership: Champaign, IL. p. 82.

Chapter 3: Modeling the Cost of CO_2 Storage through Enhanced Oil Recovery

The first Enhanced Oil Recovery (EOR) pilot projects employing miscible CO_2-flooding[1] began in the late 1970's. Since then, the number of these projects in the US has increased to 80 in 2006 producing close to 250,000 barrels of oil per day (BOPD), as shown in Figure 3.1. While there are CO_2-flood EOR projects operating in Turkey and Trinidad, these are immiscible CO_2-flooding projects in which oil displacement happens through a different—generally less efficient—mechanism. Production from miscible CO_2-floods accounts for slightly more than a third of the total domestic US oil production from EOR methods [1]. The large number of operating CO_2 floods has greatly contributed to understanding of the processes involved.

There are a number of methods used to model oil recovery in secondary (i.e., waterflooding) and enhanced production (i.e., CO_2-flooding, polymer injection, etc.) [2]. These methods, in order of both increasing complexity and data requirements, are: rule-of-thumb estimates [3, 4]; semi-analytical fractional-flow models [5, 6]; and, stream-tube [7] and finite difference models (e.g. ECLIPSE, GEM/STARS, UTCOMP, etc.). Investment decisions on CO_2-flooding projects are usually rely on predictions from numerical simulations performed only after a full model of the particular field has been developed and verified through a history match (i.e., matching modeled and actual production of the field over time). Without access to a history-matched model,

---

[1] CO_2-flooding processes can be categorized as miscible or immiscible; this chapter concerns the former type of CO_2-flood. Appendix B contains a brief primer on oil recovery processes which discusses the differences in between these processes.

predictions about the response of the field to enhanced recovery methods are limited to rule-of-thumb and semi-analytical results.
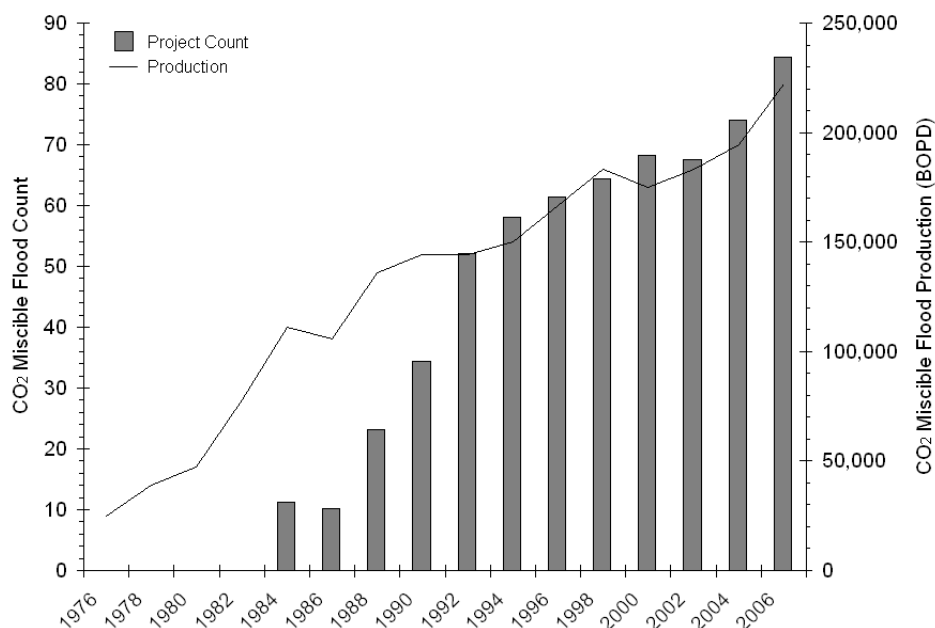
Figure 3.1. Counts of domestic US miscible CO_2 flood EOR projects and production in barrels of oil per day (BOPD) between the late 1970's and 2006 [1, 8].

A number of studies have examined the potential for production from miscible CO_2-flooding in US domestic oil reservoirs [9-11] using semi-analytical screening models relating oil production rates to CO_2 injection rates, geological properties, and assumptions on the development of an oil field. These studies, performed for Congress or a government agency, have approached the assessment from the perspective of increasing domestic oil production, but none of them examined the economics of miscible CO_2-flooding in the context of a geologic storage process.

More recently, several studies have also attempted to evaluate the economics of CO_2 storage through miscible CO_2-flooding [3, 12]. These studies have applied rules-of-thumb to estimate oil production and the cost of CO_2 storage via EOR. The Holtz et al. study

[12] used these rules of thumb to estimate incremental oil production and the resulting cost of storage for specific cases in West Texas. Similarly, the study by Massachusetts Institute of Technology (MIT) [3] used three hypothetical scenarios to illustrate a possible range of cost. There have been no studies performed to date that use a semi-analytical model to estimate the economics of CO_2-flood EOR for CO_2 storage.

The objective of this chapter is to develop and apply a semi-analytical model that can be applied to estimate the cost of geological storage of CO_2 via miscible CO_2-flood EOR[2] based on limited amount of site-specific data. The engineering-economic model will be used to assess the sensitivity of storage cost to changes in geological settings and assumptions regarding the development of the EOR. It will also show the potential range of costs that could occur and the probability associated with these costs for a given scenario.

3.1 The CO_2 Miscible-Flood Enhanced Oil Recovery Process

The CO_2 flood EOR process can be broken down into several steps, as shown in Figure 3.2. In the CO_2-flood process, CO_2 is injected through an injection well (i.e., injector) into the target reservoir; the CO_2 extracts oil from the reservoir; and, the CO_2-oil mixture, along with reservoir brine, is brought to the surface at a well (i.e. producer). These three process steps happen at the level of a well pattern (i.e., a cluster of injection and production wells) undergoing CO_2-flooding in an oil field. Depending on the size of the oil field, there may be hundreds of patterns. For example, at the SACROC field in Texas, the largest CO_2 flood (by production), there are 414 injection wells and 354 production wells [1].

---

[2] Herein the term CO_2-flooding will refer to the miscible process
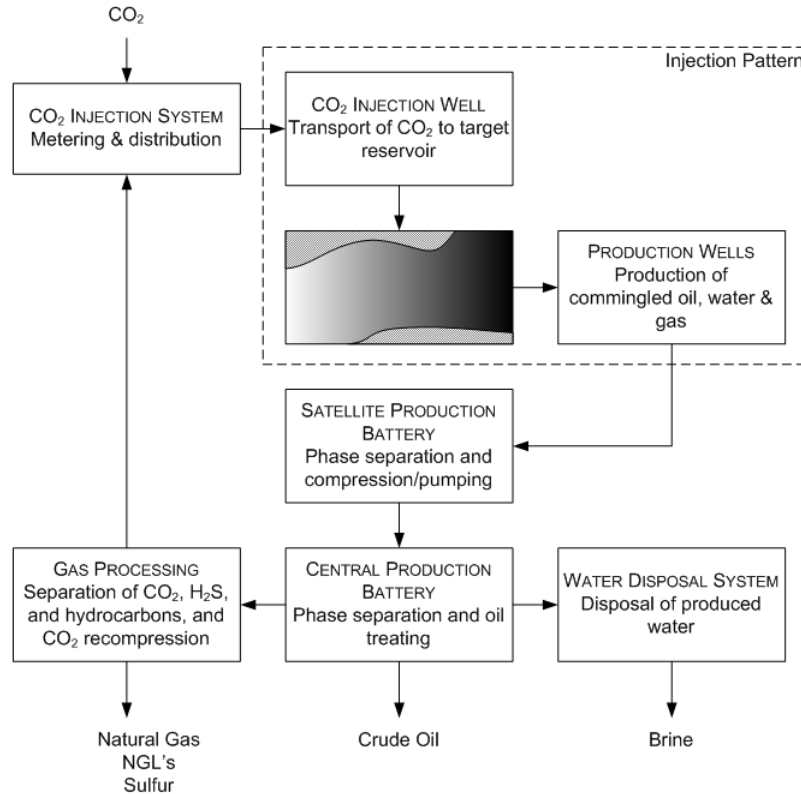
Figure 3.2. Material flows and process steps in CO_2-flooding

At the surface, the produced fluid mixture from a number of well patterns is collected, separated by phase, and the crude oil treated through the addition of chemicals such as emulsifiers to prepare it for sale. These steps happen at production batteries, and depending on the field design, may be distributed between satellite production batteries, handling fluids from a small number of patterns, and a central production battery, handling fluids from the entire field.

Traditional CO_2-flood projects are designed to minimize the amount of CO_2 that must be purchased; thus, CO_2 separated from the produced oil is compressed and recycled to the injector. The gaseous stream separated from the produced oil typically also contains

hydrogen sulfide gas (H_2S), methane, ethane, and natural gas liquids[3] (NGLs), which may be separated from the CO_2 recycle, depending on purity requirements for the injected CO_2, safety requirements for dealing with H_2S, and process economics.

CO_2-flood projects explicitly intended to be operated as CO_2 storage operations may be designed somewhat differently than traditional CO_2 floods. For example, with an economic incentive to store as much CO_2 as possible, it may be desirable to eliminate CO_2 recycle (and potentially H_2S separation) from the CO_2-flood operation, and integrate the CO_2 flood with acid-gas injection,[4] maximizing the amount of CO_2 stored by the project while recovering a comparable amount of oil to a traditional EOR project [13, 14]. In addition, it may be possible to optimize operation and design of injection patterns to maximize both oil recovery and CO_2 storage. For example, design of well completions to create "favorable" CO_2 injection profiles, changes in the composition of the injected solvent stream over time, and shut-in of production wells to minimize the ratio of gas-to-oil (GOR) produced can all increase the amount of CO_2 that remains trapped in the subsurface while increasing oil recovery rates [15, 16].

3.2 Enhanced Oil Recovery Performance Model

The model of the EOR process developed here can be separated into two parts: a performance model, and a economics model. As shown in Figure 3.3, the performance model takes inputs that describe reservoir and oil properties, and the operating strategy (field properties). From these inputs the model estimates the oil recovery rate as a function of the amount of CO_2 injected, the required wellhead pressure to achieve the

---

[3] NGLs are natural gas components that are liquids under ambient conditions, such as propane and butane.
[4] Formally, an acid gas is any gas that can form acidic solutions when mixed with water. In the petroleum industry, acid gas refers to a mixture of H_2S and CO_2.

desired injection rate, and the total amount of oil recovered from the project at the end of its economic life.
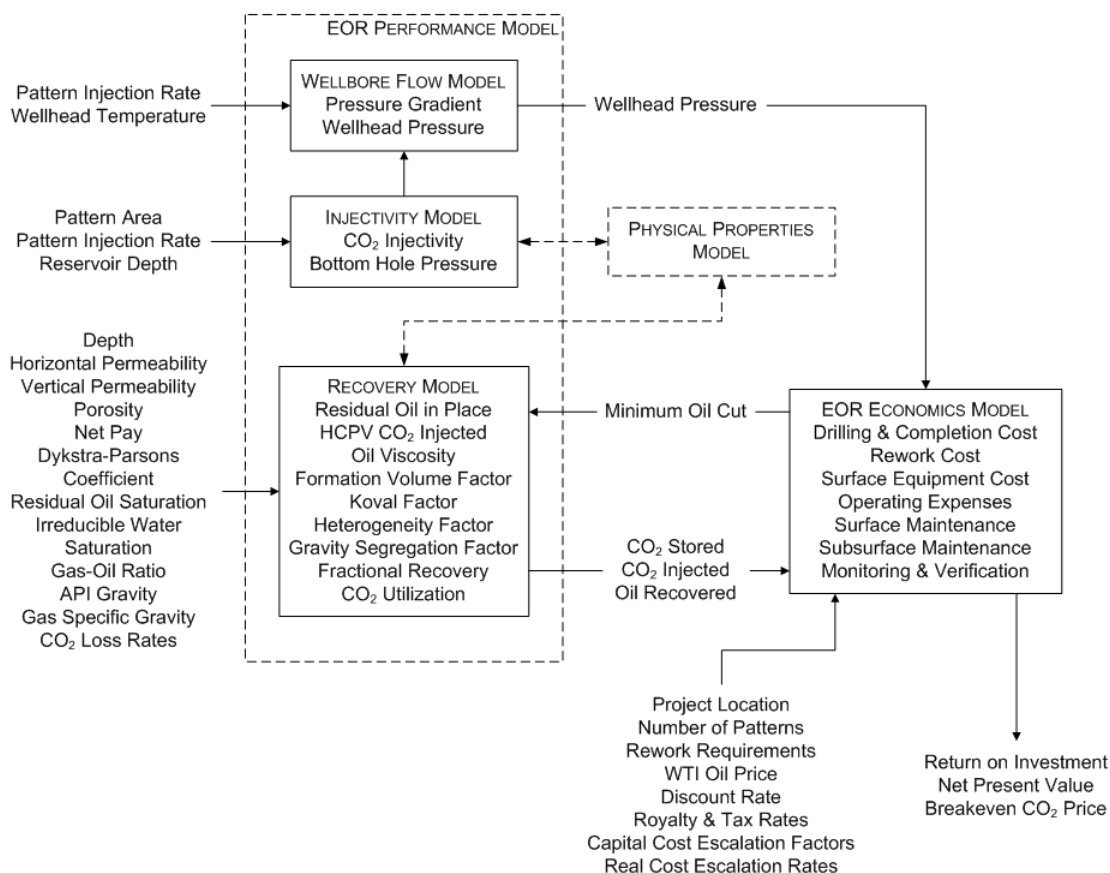
Figure 3.3. The CO_2-flood EOR engineering-economic model developed here.

3.2.1   Establishing the Bottom Hole Injection Pressure—Modeling Injectivity

The rate at which CO_2 can be injected into the oil reservoir is determined by the injectivity of the system. Injectivity is defined as the injection rate divided by the excess pressure above reservoir equilibrium pressure driving injection [17]:

$$I = \frac{q}{p_{wb} - p_e} \qquad (3.1)$$

Thus, given an injection rate, q, and reservoir equilibrium pressure, p_e, the pressure at the well bottom, p_{wb}, can be calculated if the injectivity is known.

For an isolated injection pattern, the injectivity can be calculated analytically. Figure 3.4 shows the geometry of a typical isolated inverted 5-spot injection pattern and the nomenclature used in the derivation.
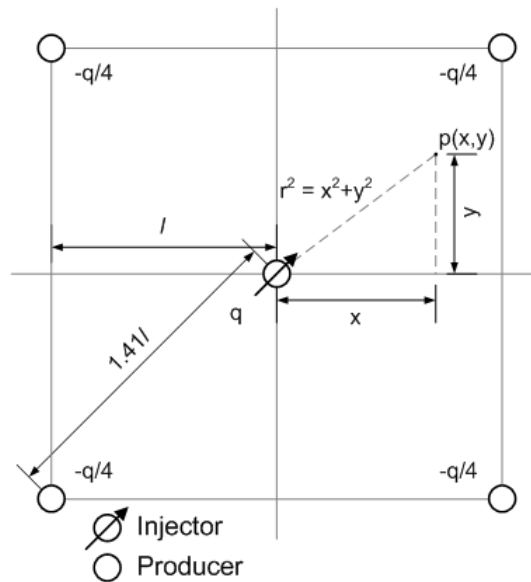
Figure 3.4. An inverted 5-spot pattern, where CO_2 is injected through the well at center, and fluid is produced at the four surrounding wells, showing nomenclature used in derivation of the injectivity equation.

An analytical solution for pressure at any point in the system can be written if several assumptions are made, which are: the system is at steady state; the reservoir fluid and injected fluids are the same and incompressible; the reservoir permeability is homogeneous and isotropic; and, full completion of all five wells through the net pay. The solution is derived by superposition of the effects of each of the individual wells as [18]:

$$\frac{4\pi kh[p(x,y)-p_e]}{q\mu} = \ln\left\{\frac{\left[\left((l+x)^2+(l-y)^2\right)\left((l-x)^2+(l-y)^2\right)\left((l-x)^2+(l+y)^2\right)\left((l+x)^2+(l+y)^2\right)\right]^{1/4}}{\left(x^2+y^2\right)}\right\}$$

where, k is permeability, h is reservoir thickness (i.e., net pay), q is the CO_2 injection rate, μ is viscosity of the CO_2, and l is the producer-injector spacing.

Solving the above equation for pressure at x equals the wellbore radius, r_w, where r_w is small (i.e., $r_w << l$), and y is equal to zero, then rearranging for injectivity results in Equation 3.2.

$$I = \frac{q}{p_{wb}-p_e} = \frac{4\pi kh}{\mu\ln\left\{\frac{\left[(l+r_w)^2+l^2\right]^{1/2}\left[(l-r_w)^2+l^2\right]^{1/2}}{r_w^2}\right\}} \qquad (3.2)$$

Equation 3.2 will likely overestimate the injectivity of CO_2 in a tertiary-flooding situation (i.e., where CO_2 flooding is occurring after waterflooding) as it is derived on the basis of a single flowing fluid. In such a situation, the effects of multi-phase flow, fluid mixing, and permeability heterogeneity will result in reduced injectivity compared to the value predicted by Equation 3.2 [19, 20]. Other analytical models for 5-spot injectivity, such as that for a 5-spot flooding network [21], are derived based on similar assumptions and also overestimate injectivity.

Equation 3.2 is thus used in the model to estimate the required well bottom pressure (bottomhole injection pressure or BHIP) for the injection rate supplied to the model. In addition to the injection rate, the pattern area and reservoir equilibrium pressure are required. The producer-injector distance, l, is calculated on the basis of pattern area, where (as can be seen from Figure 3.4) one-half the square-root of pattern area is equal to

the producer-injector distance. The reservoir equilibrium pressure can be calculated from the hydrostatic pressure gradient and depth [22]:

$$p_e = Gd \tag{3.3}$$

where G is the pressure gradient, typically ranging from 10.5 kPa/m to 12.4 kPa/m [23].

It is undesirable to cause uncontrolled fractures in a reservoir undergoing CO_2 flooding, thus the upper limit on injection pressure is the fracture pressure of the reservoir rock. In absence of field data, this can be estimated from a correlation presented by Heller and Taber [24]:

$$
\begin{aligned}
G_f &= \gamma - \beta e^{-\alpha d} \\
p_f &= G_f d
\end{aligned} \tag{3.4}
$$

where, P_f is the fracture pressure at depth (Pa), G_f is the fracture gradient (Pa/m), and α, β and γ are coefficients with the values: 4.36×10^{-4} m^{-1}, 9.24 kPa/m, and 22.62 kPa/m.

3.2.2   *From the Surface to the Reservoir—Modeling the Wellbore Environment*

As shown by Equation 3.1, injectivity is proportional to the difference between the reservoir pressure and the pressure at the well bottom (BHIP). Thus, estimating the injection rate for a given wellhead pressure (or vice versa) requires estimation of the pressure change through the well.

BHIP is frequently estimated by assuming it is equal to the hydrostatic pressure exerted by a static column of fluid (e.g., Hendriks [23]). However, this is only an approximation valid at low flow rates, as the loss of pressure due to friction between the flowing fluid and the surrounding rock counteracts the pressure increase due to hydrostatic pressure.

For a high capacity well, such as that found in the Norwegian Sleipner project, pressure losses due to friction will not be negligible. Moreover, heat transfer between the surrounding rock and the wellbore also affects the pressure and temperature distribution in the well [25, 26].

Figure 3.5 shows a typical vertical injection well completion. For simplicity, this figure does not show the conductor pipe or differentiate between the intermediate and production casing strings. The annulus between the production casing and the production tubing is generally filled with a fluid, such as a brine or hydrocarbon. The injectant flows from the surface to the reservoir through the production tubing and enters the reservoir through perforations in the production tubing.

A full numerical model of the wellbore allows sensitivity of BHIP and bottomhole temperature to changes in a variety of input parameters to be estimated. Appendix C describes a numerical model that can be used to calculate the pressure gradient in a CO_2 injection well considering pressure changes due to hydrostatic head, friction losses, and heat transfer. However, the complexity of such a model is unnecessary in the context of the EOR performance model. Thus, a response surface model based on the full numerical model (described in Appendix C) is used to estimate BHIP in the EOR performance model.
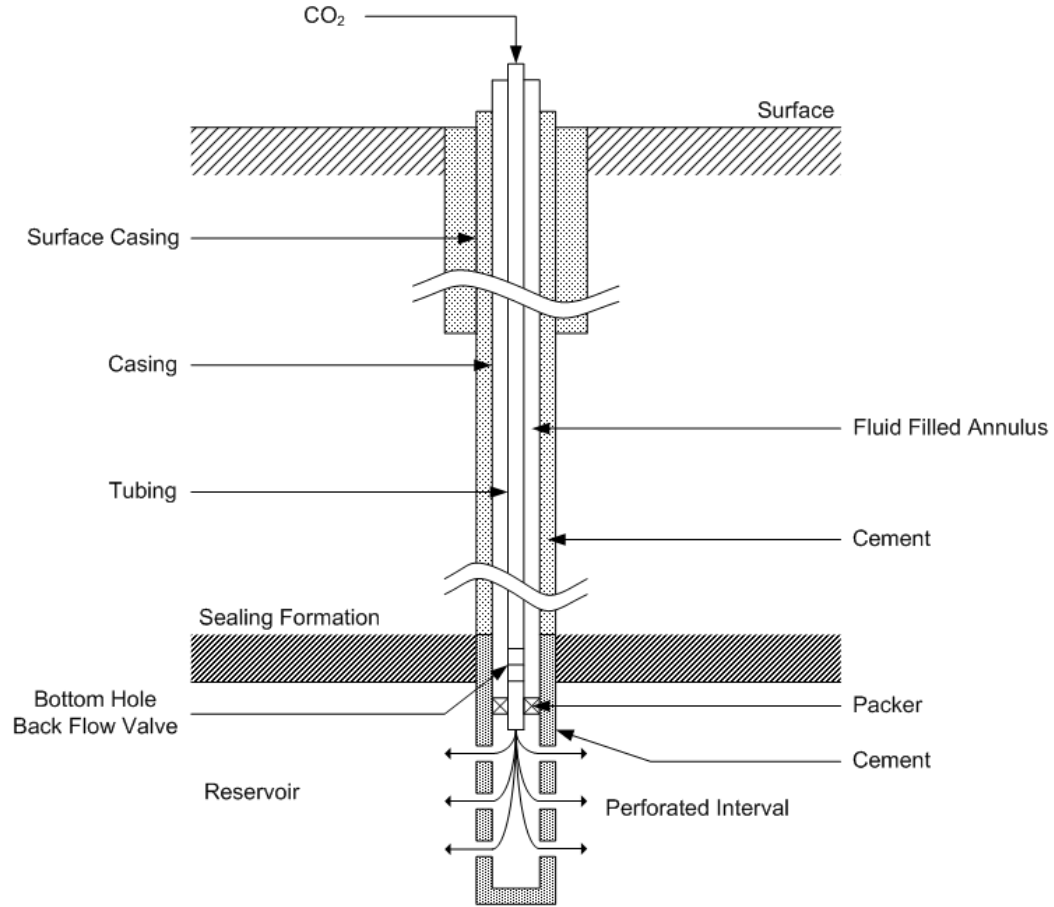
Figure 3.5. A typical well completion, showing components relevant to modeling flow in the wellbore.

The response surface model assumes that the pressure gradient in the wellbore is a linear function of depth and, thus, that the BHIP can be written as:

$$p_{wb} = \frac{\Delta P}{\Delta L} L + p_{wh} \qquad (3.5)$$

where, p_{wb} is the BHIP pressure, p_{wh} is the wellhead pressure, and L is the wellbore length.

Results from the numerical model show that the pressure gradient in the well becomes non-linear at high flow rates. Because Equation 3.5 can only represent pressure gradients

linear in depth, it is valid only for flow rates below approximately 1 Mt CO_2 per year at

temperatures less than 30°C and wellhead pressures greater than 8 MPa for the 3-inch

(0.076 m) inside diameter tubing modeled (Table C.1 describes the other parameters used

in the numerical model). The form of the regression equation for pressure gradient is:

$$\frac{\Delta P}{\Delta L} = a_1 q^2 + a_2 \log(p_{wh})^2 \tag{3.6}$$

where, P_{wh} is the wellhead pressure (Pa), and q is the volumetric flow rate (m³/d) at

wellhead conditions.

Parameter estimates for the regression coefficients are given in Table 3.1. The regression

model given in Equation 3.6 accounts for a large proportion of the variation in the set of

2895 data points generated by the numerical model, reflected by an adjusted-r^2 value of

0.99.

Table 3.1. Regression coefficient estimates for the pressure drop correlation, Equation
3.6, where standard errors are reported in parentheses.

Coefficient	Value
a_1	-7.008×10^{-4} ** (3.100×10^{-6})
a_2	1.812×10^{2} ** (2.692×10^{-1})

** Significant at the 1% level

The regression coefficients in Table 3.1 show that the wellbore pressure gradient is

negatively correlated with the volumetric flow rate, and positively correlated with the

square of the base-ten logarithm of pressure. In addition, wellhead temperature influences

the pressure gradient predicted by Equation 3.6 through its effect on volumetric flow rate.

Figure 3.6 shows the pressure gradient predicted by Equation 3.6 using the coefficients listed in Table 3.1.
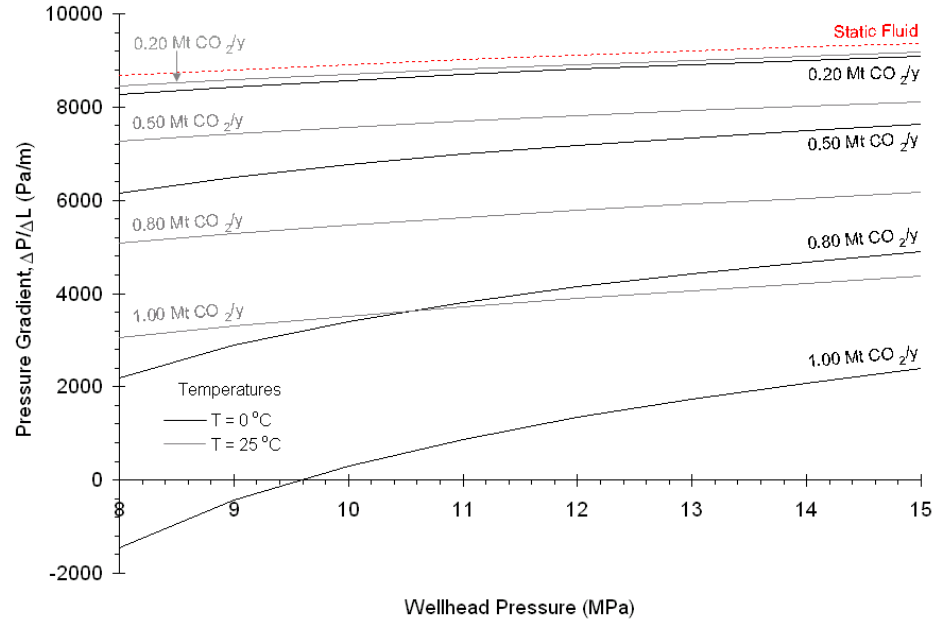
Figure 3.6. Pressure gradients predicted by the reduced form wellbore pressure model for mass flow rates between 0.2 and 1.0 Mt CO_2 per year at two different wellhead temperatures and for a static column of CO_2.

The difference between the lines of constant mass flow at 25 ^{o}C and 0 ^{o}C in Figure 3.6 shows that the pressure gradient is negatively correlated with wellhead temperature. However, in the limit as volumetric flow rate approaches zero, Equation 3.6 reduces to a strictly pressure dependent function, shown by the single dashed line in Figure 3.6. Nonetheless, Equation 3.6 can be used to estimate the hydrostatic pressure gradient for a static column of CO_2 within the limits of the regression equation.

3.2.3   Estimating Recovery of Oil

Recovery of oil and gas in miscible CO_2-flooding (or any other EOR process) can be characterized by the overall recovery efficiency, E_r. The overall recovery efficiency is the product of a number of factors:

$$E_r = E_m \cdot E_d \cdot E_a \cdot E_v \qquad (3.7)$$

where, E_m is the mobilization efficiency, E_d is (linear) displacement efficiency, E_a is areal (horizontal) sweep efficiency, and E_v is vertical sweep efficiency [27, 28]. The product of the overall recovery efficiency and the volume of oil in place prior to the commencement of the recovery operation, V_{pd}, is the volume of oil produced.

Mobilization efficiency is the ultimate fraction of oil that can be recovered at the microscopic level from a differential volume of reservoir rock [27]. This is written as:

$$E_m = \frac{S_{oi} - S_{or}}{S_{oi}} \qquad (3.8)$$

Where, S_{oi} and S_{or} are the phase saturation for the oil phase initially (before CO_2-flooding) and residual to the CO_2 flood, respectively. The residual oil saturation reflects the effects of interfacial tension between the fluids in the rock and ratios of viscous to capillary forces [28].

In miscible displacement, the injected solvent (CO_2 or otherwise) becomes completely miscible with the reservoir oil. For a given solvent-oil pair, miscibility is a function of reservoir temperature and pressure, and is characterized by the minimum miscibility

Chapter 3: Modeling the Cost of CO_2 Storage through Enhanced Oil Recovery

pressure (MMP)[5]. At pressures greater than MMP, CO_2 in contact with reservoir oil

extracts low and intermediate molecular weight hydrocarbons from the oil, and after

multiple contacts with the crude oil, this CO_2-rich phase becomes completely miscible

with the reservoir oil [29-31]. This is described in the EOR literature as multi-contact

miscibility (MCM) [28].

Under miscible conditions, interfacial tension between the oil and CO_2 is effectively zero.

Consequently, S_{or} is assumed to be zero, and Equation 3.8 reduces to 100% mobilization

efficiency.

Displacement efficiency is a measure of the fraction of the oil swept from the reservoir in

a linear displacement, and is a function of the volume of CO_2 injected, V_{pi}. Displacement

efficiency is defined as [27]:

$$E_d = \frac{S_{oi} - S_o(V_{pi})}{S_{oi} - S_{or}}$$

In this equation, the initial and residual oil saturation are assumed to be known

parameters; however, oil saturation as a function of the injected volume of CO_2 must be

calculated.

Saturation of fluid at a point in the reservoir as a function of the volume of injected

solvent can be estimated from a fractional-flow based model. In a reservoir undergoing

CO_2-flooding, there are at least three flowing phases: a water phase, CO_2-rich phase, and

an oil-rich phase. Moreover, because of the differences in viscosity between the flowing

---

[5] See Appendix B for a brief discussion of MMP and miscible CO_2-flood screening criteria

phases, each phase travels at a different velocity, resulting in viscous fingering

(illustrated in Figure 3.7).
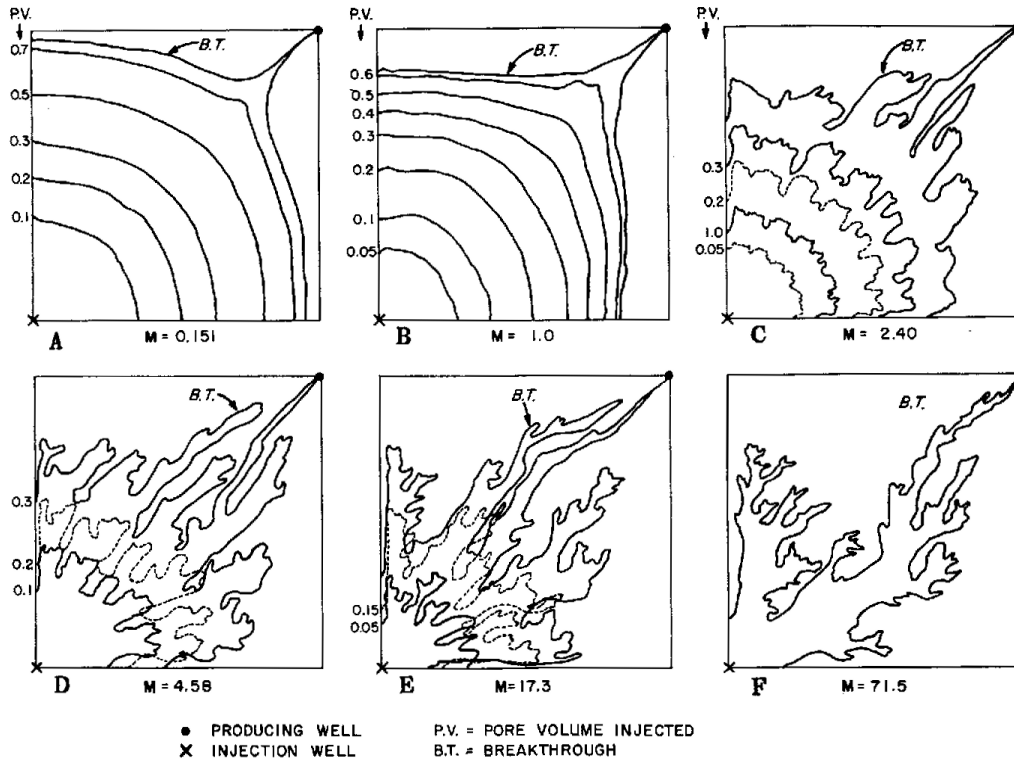
Figure 3.7. Displacement fronts in a quarter of an inverted five-spot pattern, for different mobility ratios, showing the effect of viscous fingering reproduced from Habermann (© 1960 Society of Petroleum Engineers) [32].

While there have been great improvements made in analyzing multiphase miscible

systems with viscous fingering [33, 34], it is still difficult to solve the system of

equations analytically for fractional flow. Consequently, the model presented here is a

two-phase, semi-empirical model of unstable displacement, similar to other models used

at the screening level to estimate oil recovery in CO_2-flooding [5, 10, 35, 36].

The equations used to estimate displacement efficiency in the CO_2-flooding case are

based on the analogous case of immiscible displacement [6]. In an immiscible

Chapter 3: Modeling the Cost of CO_2 Storage through Enhanced Oil Recovery

displacement (e.g. a waterflood), where one phase is displacing another immiscible phase, neglecting capillary pressure in a horizontal reservoir, the fractional flow of the displacing fluid, f_d, can be written [27]:

$$f_d = \frac{1}{1 + \left(\dfrac{\mu_d k_{ro}}{\mu_o k_{rd}} \right)}$$

(3.9)

where: μ refers to the viscosity of the displacing fluid, d, and oil o; and k_r is the relative permeability of the rock with respect to oil, o, and the displacing fluid, d.

Assuming that the relative permeability of the rock to the flowing phases is a linear function of the displacing fluid saturation, S_d, we can write:

$$\frac{k_{ro}}{k_{rd}} = \frac{1 - S_d}{S_d}$$

Then, if the mobility ratio is defined as,

$$M = \frac{\mu_o}{\mu_d}$$

(3.10)

Equation 3.9 can be written:

$$f_d = \frac{1}{1 + \left(\dfrac{1 - S_d}{S_d} \right)\left(\dfrac{1}{M} \right)}$$

(3.11)

This derivation only applies for a stable displacement, where the mobility ratio is less than or equal to one. In this situation, the oil is capable of traveling at the same velocity as the displacing fluid under an imposed pressure gradient. When the mobility ratio is

greater than one, the displacing fluid will bypass the oil, leaving regions of the reservoir unswept by the displacing fluid, and thus reducing oil recovery.

In the CO_2-flooding process, the displacing fluid, CO_2, is miscible with oil and the mobility ratio is on the order of 10-100; thus, without modification Equation 3.11 is unsuitable for determining fractional flow. Koval [6] suggested, however, that this immiscible displacement equation can be used to model miscible displacement if the mobility ratio, M, is replaced with an effective mobility ratio, K. Koval originally intended that this factor would account for mixing between CO_2 and oil, viscous fingering, and effects of reservoir heterogeneity. Further development of the Koval model has extended it to account for vertical sweep.

Vertical sweep efficiency is the fraction of the reservoir that has been swept by the displacing fluid [27]. In the CO_2 flooding process, the injected CO_2 tends to be less dense than the reservoir oil; thus, CO_2 tends to migrate towards the top of the reservoir leaving lower portions of the reservoir unswept.

Paul and Lake [36] recognized that Koval's definition of K could be adjusted for vertical sweep, by including a gravity segregation factor. Thus, as used here K is defined as [36]:

$$K = EHG \tag{3.12}$$

where: E is effective mobility, accounting for miscibility of CO_2 and oil, and viscous fingering [6]; H is the heterogeneity factor, accounting for effects of dispersion and channeling [37]; and, G is the gravity segregation factor [36].

The factors in Equation 3.12 are defined as:

82

Chapter 3: Modeling the Cost of CO_2 Storage through Enhanced Oil Recovery

$$E = \left(0.78 + 0.22M^{\frac{1}{4}} \right)^{4} \tag{3.13}$$

$$\log H = \left[\frac{V_{DP}}{\left(1 - V_{Dp}\right)^{0.2}} \right] \tag{3.14}$$

$$G = 0.565 \log\left(\frac{t_h}{t_v} \right) + 0.870 \text{ , where } \frac{t_h}{t_v} = 2.5271 k_v A \frac{\Delta\rho}{q\mu_s} \tag{3.15}$$

In Equation 3.14, V_{DP} is the Dykstra-Parsons coefficient, which is a measure characterizing the permeability distribution of the reservoir. In Equation 3.15, k_v is the reservoir permeability in the vertical direction (md), A is the pattern area (acres), q is the gross injection rate of CO_2 (RB/day), and $\Delta\rho$ is the density difference between CO_2 and oil (kg/m^3).

Determining the relationship between fractional flow and fluid saturation requires the equation of Buckley and Leverett [6]. The Buckley-Leverett equation describes displacement of one immiscible fluid by another, relating the velocity of the displacing-fluid front in the reservoir to the derivative of the fractional flow equation [38]. Thus, the integrated form of the Buckley-Leverett equation, relates the distance of a plane of fluid saturation to distance in the reservoir:

$$x(S_d) = \frac{V_i}{A\phi} \frac{df_d}{dS_d}\bigg|_{S_d}$$

where: x is the distance in the reservoir, V_i is the volume of injected fluid, A is the cross sectional area of the reservoir, and φ is reservoir porosity.

At the production well, where x equals L, the Buckley-Leverett equation can be solved to yield:

$$V_{i,pv} = \frac{V_i}{LA\phi} = \frac{1}{\frac{df_d}{dS_d}\bigg|_{S_d}} \qquad (3.16)$$

In Equation 3.16, $V_{i,pv}$ refers to the dimensionless pore volume of fluid injected into the reservoir. The denominator of Equation 1.16 is shown for simplicity as the product of length, area, and porosity; however, the pore volume available for flow is reduced by the presence of immobile water (i.e., $1-S_w$).

Substituting for K and taking the derivative of Equation 3.11 yields the expression for the derivative of fractional flow required in Equation 3.16:

$$\frac{df_d}{dS_d} = \frac{K}{[1+S_d(K-1)]^2} \qquad (3.17)$$

Thus, substituting Equation 3.17 into 3.16, and solving for f_d we arrive at an equation for the fractional flow of the displacing fluid (CO_2) at the producing well in the linear system after breakthrough (i.e., the time at which CO_2 reaches the production well):

$$f_d = \frac{K - \sqrt{K/V_{i,PV}}}{(K-1)} \qquad (3.18)$$

where, f_d is referred to as the "cut" of the displacing fluid (e.g., f_c is referred to as the CO_2 cut). Breakthrough occurs after the injection of $1/K$ pore volumes of CO_2 based on the solution of Equation 3.18 with f_d equal to zero.

To arrive at the pore volume of oil produced from the linear reservoir, equivalent to E_dE_v, Equation 3.18 must be integrated and added to the pore volumes produced prior to breakthrough.

Chapter 3: Modeling the Cost of CO_2 Storage through Enhanced Oil Recovery

$$E_d E_v = V_{i,PV}\Big|_{bt} + \int_{V_{i,PV}|_{bt}}^{V_{i,PV}} \left[1 - \frac{K - \sqrt{K/V_{i,PV}}}{(K-1)} \right] dV_{i,PV}$$

$$= \frac{1}{K} + \int_{V_{i,PV}|_{bt}}^{V_{i,PV}} \left[1 - \frac{K - \sqrt{K/V_{i,PV}}}{(K-1)} \right] dV_{i,PV} \qquad (3.19)$$

$$= \frac{2\sqrt{KV_{i,PV}} - V_{i,PV} - 1}{(K-1)}$$

Thus, after CO_2 breakthrough, the product of displacement efficiency and vertical sweep efficiency in a linear flood is given by Equation 3.19.

Areal sweep, E_a in Equation 3.7, is the fraction of the well pattern swept by the displacing fluid. To estimate areal sweep, the model uses Claridge's modification of Koval's method [5]. Claridge's method estimates the areal sweep for a 5-spot well pattern (or inverted 5-spot, shown in Figure 3.1) and is based on the concept of apparent pore volumes injected. Claridge defines apparent pore volumes injected, $V_{a,PV}$, as:

$$V_{a,PV} = \frac{V_{i,PV}}{E_d E_v} \qquad (3.20)$$

Where the product, $E_v E_d$, is calculated using Equation 3.19, using the pore volumes of fluid injected relative to the volume fraction swept by the injected fluid, $V_{d,PV}$, in place of $V_{i,PV}$:

$$V_{d,PV} = \frac{V_{i,PV}}{E_A} = \left(\frac{E_v E_d}{E_A} \right) V_{a,PV} \qquad (3.21)$$

Areal sweep in Equation 3.21 is calculated based on the set of equations given below as Equation 3.22.

$$E_{a,bt} = \begin{cases} V_{a,PV}, & V_{a,PV} \leq 1 \\ 1.0, & V_{a,PV} > 1 \end{cases}$$

$$M_{bt} = \frac{1 - E_{a,bt}}{E_{a,bt} - 0.4}$$

$$E_a = \frac{E_{a,bt} + 0.4M'}{1 + M''} \qquad\qquad (3.22)$$

$$M' = 25 \frac{M_{bt}^{5/6} + 0.3 + 2.3(V_{a,PV} - 1)}{V_{a,PV} + 1}$$

$$M'' = \frac{M - M_{bt}}{(M' - M_{bt})^{(0.85 - 0.55 E_{a,bt} + 0.25 V_{a,PV})}}$$

Equations 3.19, 3.20, 3.21 and 3.22, can be used to estimate the fraction of total oil recovered, i.e., E_r, as a function of the fraction of CO_2 in the produced fluid, f_d. Unfortunately, there is no analytical solution to calculate E_a and $E_v E_d$ as a function of f_d (or V_{pvi}) using these equations. Thus, the model uses the iteration scheme presented in Figure 3.8 to arrive at the values of $E_v E_d$, E_a, and V_{pvi}.
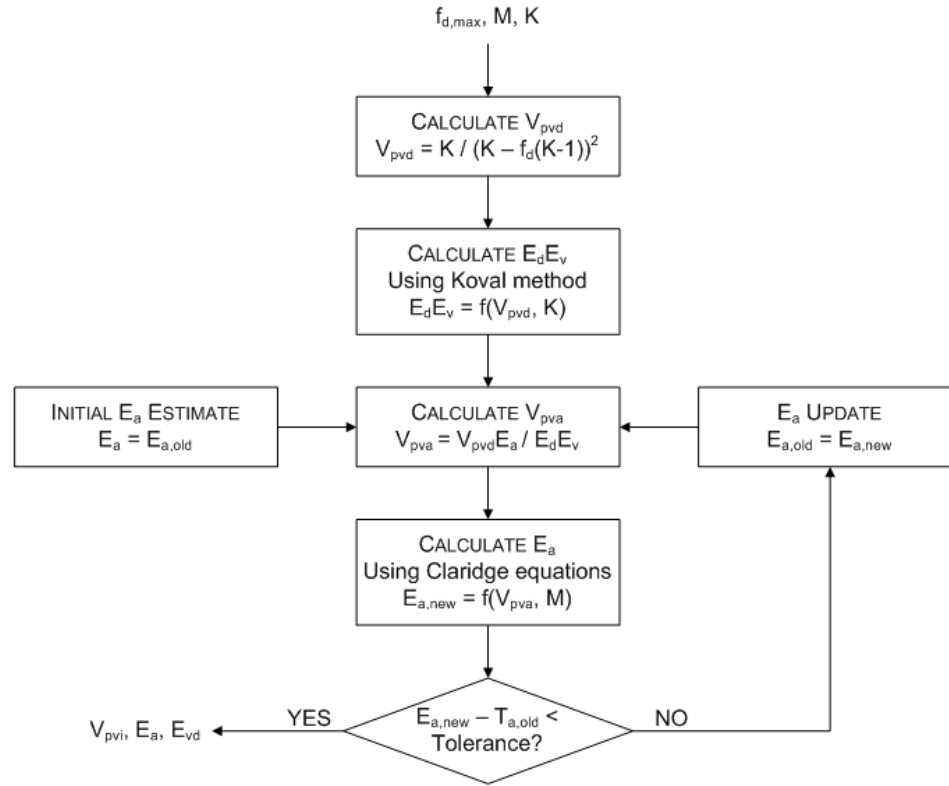
Figure 3.8. The iteration scheme used to calculate E_a and $E_v E_d$

3.2.4   Estimating Net CO_2 Injected—The CO_2 Mass Balance

The amount of CO_2 injected (i.e., gross CO_2 injected) in traditional CO_2-flooding is many times greater than the actual amount of CO_2 stored (i.e., net CO_2 injected minus any leakage to the atmosphere) because CO_2 produced with oil is traditionally recycled and re-injected. The amount of CO_2 stored at the end of the economic life of the field must be estimated from a mass balance on CO_2 in the system. In this case, we consider pressure and temperatures to be constant, thus the mass balance can be written in terms of volume. Figure 3.9 shows the process streams required for a volumetric balance.
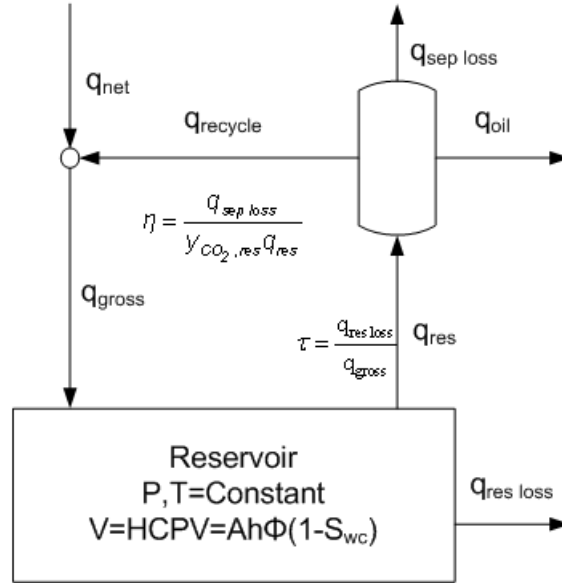
Figure 3.9. The process streams required for the mass balance, where q indicates the cumulative volume.

All of the volumetric flow rates in the following equations are written in terms of volumes at reservoir conditions (e.g., reservoir barrels, denoted RB). Conversions between reservoir volumes and surface volumes (e.g., stock-tank barrels, denoted STB) can be made by using the formation volume factor, defined for fluid x (i.e. oil or CO_2) as:

$$B_x = \frac{\rho_x(T_{res}, P_{res})}{\rho_x(T_{std}, P_{std})} \tag{3.23}$$

where the density is measured at petroleum industry standard conditions, which are 60 °F (289 K) and 1 atm (101 kPa).

The EOR performance model requires the gross injection rate, q_{gross}, be specified. Thus from Figure 3.9 flow rates for the process streams of interest can be written:

Chapter 3: Modeling the Cost of CO_2 Storage through Enhanced Oil Recovery

$$q_{prod} = q_{gross}(1-\tau)$$
$$q_{rcy} = q_{gross} f_d (1-\tau)(1-\eta)$$
$$q_{net} = q_{gross}[1 - f_d(1-\tau)(1-\eta)]$$

(3.24)

where τ specifies the rate of CO_2 escaping from the pattern, and η specifies the rate with which CO_2 is lost to the atmosphere from the separator.

Note that both loss rates imply that CO_2 leaves the process through some mechanism; however, only the loss rate to the atmosphere reduces the greenhouse gas mitigation efficiency of CO_2-flooding. Losses of CO_2 in the reservoir may result from poor injection well conformance, i.e., where injected fluids, in this case CO_2, that do not enter the intended zone in the reservoir [39]. In addition, some of the injected CO_2 will dissolve in residual water and oil, or escape into adjacent non-productive zones of the reservoir. This lost CO_2, the flow rate of which is represented by q_{loss}, is assumed to remain in the reservoir and not reach the atmosphere.

The fraction of CO_2 produced at the surface that escapes from processing facilities (the stream q_{atm}) is specified by η—the efficiency of surface processing. Emissions in this stream are fugitive emissions from the surface processing steps, occurring due to leaks in valves and flanges and the imperfect separation of CO_2 from produced oil and water.

To estimate the net CO_2 stored, the mass balance equations (3.24) must be rewritten in terms of cumulative volumes of CO_2. Following the nomenclature established in Figure 3.9, the gross volume of CO_2 injected is:

$$V_{gross} = \frac{V_{prod}}{(1-l)}$$

(3.25)

The produced volume, V_{prod}, is the sum of the volumes of oil produced and CO_2 produced, V_{CO2}:

$$V_{prod} = V_{pvi} Ah\phi(1 - S_w) = E_a E_v E_d Ah\phi(1 - S_w) + V_{CO2}$$

where, A is the pattern area, h is net pay, φ is the reservoir porosity, and S_w is the average water saturation in the reservoir (i.e. the fraction of the pore space saturated with water).

The displaceable pore volumes[6] of CO_2 produced after breakthrough, V_{pvd}, is calculated by integrating Equation 3.18:

$$V_{pvd,CO2} = \int_{V_{pvd,bt}}^{V_{pvd}} \frac{K - \sqrt{K/V_{i,PV}}}{(K - 1)} dV_{i,PV}$$
$$= \frac{KV_{pvd} - 2\sqrt{KV_{pvd}} + 1}{K - 1}$$

Thus, the actual pore volumes of CO_2 injected can be written (via Equation 3.21) as:

$$V_{CO2} = E_a Ah\phi(1 - S_w)V_{pvd,CO2}$$

Now the remaining equations required for the mass balance can be written:

$$V_{rcy} = V_{CO2}(1 - \eta)$$
$$V_{net} = \frac{V_{prod}}{(1 - l)} - V_{CO2}(1 - \eta) \tag{3.26}$$

3.2.5   Recovery of CO_2—Surface Facility Engineering

The prior production history of an oil field significantly influences all aspects of a CO_2 flood, including changes to surface facilities. The equipment already in place at the field

---

[6] The displaceable pore volume is the fraction of the total hydrocarbon pore volume (HCPV) that can be displaced by CO_2-flooding. The actual pore volume is just that, i.e. the hydrocarbon pore volume.

determines what new equipment will be needed and generally depends on whether CO_2-flooding is being used as a secondary or tertiary recovery method. Equipment already in place and adopted for use in CO_2-flooding will have performance that is different from that which is new. Table 3.2, modified from Jarrell et al. [39], summarizes the categories of surface facilities required for a CO_2 flood and whether equipment already in place is required and can be used as is, or modified for use in CO_2-flooding, or if new equipment is required.

Table 3.2. Surface facility categories and changes required for CO_2-flooding depending on production stage, where "NC" indicates no change, and "NR" indicates not required.

Equipment Category	Secondary Recovery	Tertiary Recovery
Gas Processing Plant		
Dehydration/compression	New	New
CO_2 removal	New	New
H_2S removal	New	New
NGL separation	New	New
Production Facilities		
Central tank battery	NC	Upsize
Satellite batteries	Upsize	Upsize
Fluid gathering	NC	Upsize
Gas gathering	Upsize	Upsize
Water Injection Facilities		
Makeup water	NR	Downsize
Disposal	NC	New
Distribution system	NC	NC[*]
CO_2 Injection System		
Injection skids	New	NR[*]
Distribution lines	New	NR[*]
Production Wells		
Wellhead	Upsize/NC	Upsize/NC
Lift equipment	NC[+]	Downsize[§]
Injection Wells		
Wellhead	New	Upsize/NC
Downhole equipment	New	Upsize/NC

[*] Assumes existing water distribution system and water injection wells can be converted to CO_2 injectors
[+] Gas production increase
[§] Water production decrease—gas production increase

The most significant differences between CO_2-flooding (and specifically continuous CO_2-injection) applied as secondary and tertiary recovery methods are changes in water production and requirements for well workover[7]. In secondary production, produced water rates should not significantly increase; thus, changes to water disposal facilities are not required. Conversely, in tertiary CO_2 flooding, produced water that would otherwise have been re-injected in the waterflood must now be disposed. Additionally, because water injection wells have already been drilled and completed during waterflooding, they will likely only require minor modifications, such as a new wellhead, for CO_2 injection [39].

Regardless of the previous history of the field, gas processing facilities will be required. Moreover, these are the most costly facilities in the CO_2 flood [39]. The gas processing facilities must, at a bare minimum dehydrate and compress the produced CO_2 for re-injection; however, there are many other processes that can be incorporated, such as removal of H_2S and separation of NGLs prior to re-injection [39, 40]. The design of the gas processing plant depends on purity requirements for the injected gas (based on the effect of impurities on MMP), regulatory requirements, and markets for byproducts (e.g. sulfur and NGLs).

Ideally a performance model would estimate sizes of separator vessels, absorption columns, pumps, and compressors, allowing both capital and operating costs (as well as energy requirements and the associated CO_2 emissions) to be estimated. However, the dependence of surface facilities requirements on the prior production history of the field,

---

[7] A workover is maintenance on a well where the tubing string may be pulled and replaced.

and the variety and complexity of options for surface facilities means that it is difficult to develop a generic performance model for surface facilities. For example, in the case of the gas processing facilities, there are at least two broad classes of processes for gas dehydration in use, three for H_2S removal, and four for NGL separation [40].

The EOR performance model must, however, estimate the energy requirements for CO_2 compression, as this is an energy intensive process common to all CO_2 floods. The compression energy requirement is based on compressing the recycle stream of CO_2 from atmospheric pressure to the required wellhead pressure. The energy requirement is calculated based on the method discussed in Chapter 2.

3.2.6   *Illustrative Performance Model Results*

Performance model results have been generated for four illustrative case study reservoirs, selected from successful projects that currently are (or were) operating and have published reservoir descriptions [41-46]. These four reservoirs cover a range of performance parameter values—*kh* from 1,500 to 5200 md·ft and pattern areas from 40 acres to 160 acres—and two lithologies—sandstone and limestone. The model performance inputs and other pertinent data are shown in Table 3.3.

Each of the case studies was evaluated at a constant injection rate of 600 mscf (thousand standard cubic feet) per CO_2 per day per pattern (32 tonnes CO_2 per day) with the exception of the Joffre-Viking, where injection was modeled at a constant 300 mscf CO_2 per day (16 tonnes per day) due to the extremely high permeability of the Viking pool. Injection rates on the order of hundreds of mscf per day per pattern are typical of current practice [1] and, for comparison, are 200 times smaller than the amount of CO_2 captured

from a 500 MW pulverized coal power plant. The cumulative oil production as a percent

of the original oil in place (OOIP) over time for a single typical pattern in each of the four

CO_2 floods is shown in Figure 3.10.

Table 3.3. Key performance model parameters for the four case study reservoirs as well as residual oil in place (ROIP) prior to CO_2-flooding and the original oil in place (OOIP) at discovery [41-46].

Parameter	Northeast Purdy Unit	SACROC Unit, Kelly-Snyder Field	Ford Geraldine Unit	Joffre Viking Unit
Location	Oklahoma	Texas	Texas	Alberta
Reservoir	Purdy Springer A	Canyon Reef	Ramsey	Viking
Lithology	Sandstone	Limestone	Sandstone	Sandstone
Previous Recovery	Primary & Waterflood	Primary & Waterflood	Primary & Waterflood	Primary & Waterflood
Productive Area (acres)	9,177	49,900	5,280	16,611
Number of Patterns	229	1,248	132	208
Pattern Area (acres)	80	40	40	80
Depth (m)	2,499	2,042	2,680	1,500
p_{res} (MPa)	20.7	18.6	9.7	14.0
MMP (MPa)	14.5	11.0	6.2	
T_{res} (K)	338	328	301	329
Net Pay (m)	12.2	81.7	7.6	3.0
k_h (md)	44	19	60	507
k_v/k_h	0.18	0.40	0.10*	0.10
ϕ (%)	13.0	3.9	23.3	13.0
V_{DP}	0.80	0.68	0.70*	0.70*
S_{orw} (%)	47	42	41	35
γ_{API} (°API)	35	41	40	42
μ_o (cp)	1.4	0.4	1.4	1.0
B_o (RB/STB)	1.2	1.5	1.3	1.2
R_s (scf/STB)	400	1,000	575	264
p_b (MPa)	19.3	12.8	9.5	-
γ_g (air = 1)	-	1.03	-	-
ROIP (MMSTB)	146	1,163	76	47
OOIP (MMSTB)	220	2,163	97	93

* Estimated parameter value
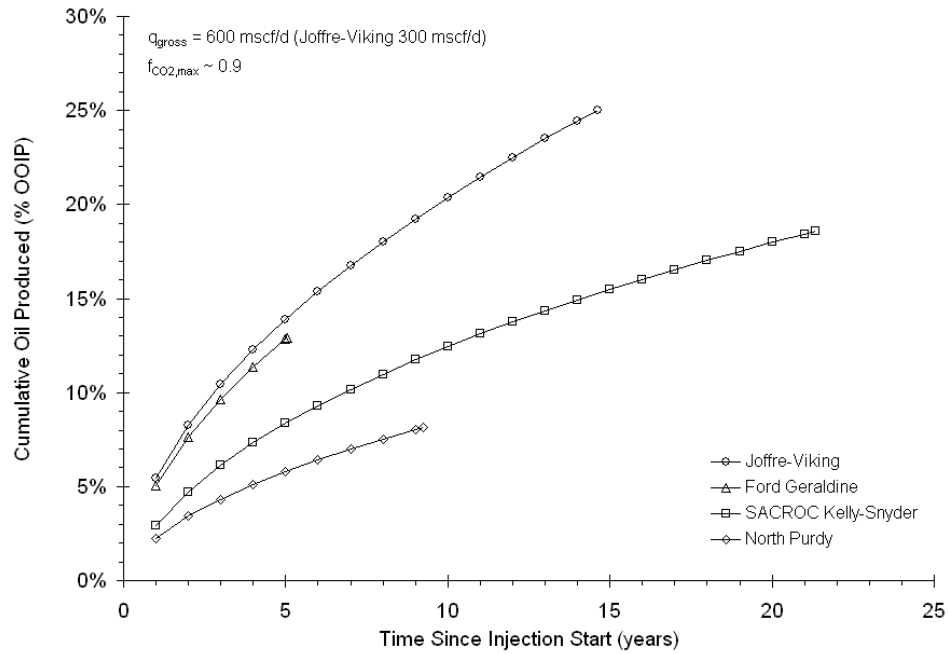
Figure 3.10. Cumulative oil recovery as a fraction of OOIP for a typical pattern in the four illustrative case studies listed in Table 3.3.

Figure 3.10 shows that, of the four illustrative cases, a typical pattern in the Joffre-Viking field could be expected to have the highest incremental recovery under CO_2-flooding, followed by Ford Geraldine, SACROC Kelly-Snyder, and North Purdy cases. In addition, the life of a typical pattern in each case was set by specifying a maximum CO_2 cut, $f_{c, max}$, of approximately 0.9 (see Equation 3.18). The CO_2 cut over time is given in Figure 3.11.
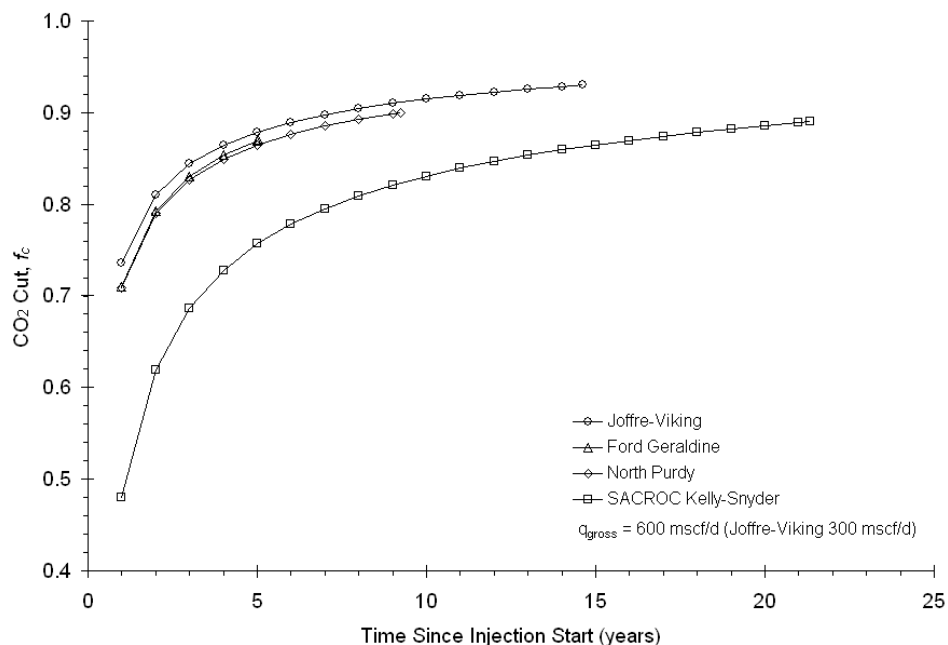
Figure 3.11. The CO_2 cut for a typical pattern in the four illustrative case studies listed in Table 3.3.

Summary results for typical patterns in each of the four case studies are shown in Table 3.12. The results from the four case studies are considerably different from one another. In general, the gross utilization of CO_2 is somewhat higher than the typical rule-of-thumb for West-Texas (i.e., 7-10 mscf/STB [47]); however, the estimated net CO_2 utilization does agree with numbers predicted for operating CO_2 floods, summarized in Table 3.5 [46-48]. Note that changing the CO_2 cut will change both oil recovery and CO_2 utilization; thus, reported CO_2 utilizations are a function of the expected life the field. Because of this, caution must be exercised in comparing the model results in Table 3.4 and predicted values in Table 3.5 as *they are not be directly comparable.*

Table 3.4. End-of-life summary results from the EOR performance model for a typical pattern in the four illustrative case studies listed in Table 3.3.

Parameter	Northeast Purdy Unit	SACROC Unit, Kelly-Snyder Field	Ford Geraldine Unit	Joffre Viking Unit
Pattern Life (years)	9.24	21.35	5.04	14.62
Oil Recovery (10^3 STB)	157	322	95	112
Recovery (% OOIP)	8	19	13	25
Gross Utilization (mscf/STB)	13	15	12	14
Net Utilization (mscf/STB)	3	4	4	3
CO_2 Stored (kt)	25	67	17	16
CO_2 Storage Rate (tonne/STB)	0.16	0.21	0.18	0.14

Table 3.5. Predicted ultimate net utilization and gross utilization of CO_2 and the incremental oil recovery reported in the literature for the four case study fields and eight other projects [46-48].

Field Name	Net Utilization (mscf/STB)	Gross Utilization (mscf/STB)	Incremental Oil (% OOIP)
Case Studies			
Northeast Purdy Unit	4.6	6.5	7.5
SACROC-4PA & 17PA	3.2-6.5	9.5-9.7	7.5
Ford Geraldine	5	9	17
Joffre Viking	5.4-6.9		14-18
Other Reported Values			
Dollarhide Devonian	2.4		14
East Vacuum Grayburg-San Andres	6.3	11.1	
Means San Andres		15	9.2
North Cross	7-8	18	22
Rangely Weber	4-6	9.2	7.5
Twofreds	8		15.6
Wertz		13-15	
Wasson-Denver	5.3		16.6

The sensitivity of the cumulative oil recovery at the pattern end-of-life to changes in

model parameters using the SACROC Kelly-Snyder case is illustrated in Figure 3.12. The

parameters varied in this single-parameter sensitivity analysis are the reservoir

temperature, pressure, permeability, Dystra-Parsons coefficient, oil viscosity, and oil API

gravity. Because the pattern area, reservoir net pay, porosity, initial oil saturation and formation volume factor were not changed, the ROIP at the beginning of the CO_2 flood remains constant. Thus, changes in the cumulative oil produced shown in Figure 3.12 are directly proportional to changes in displacement efficiency.
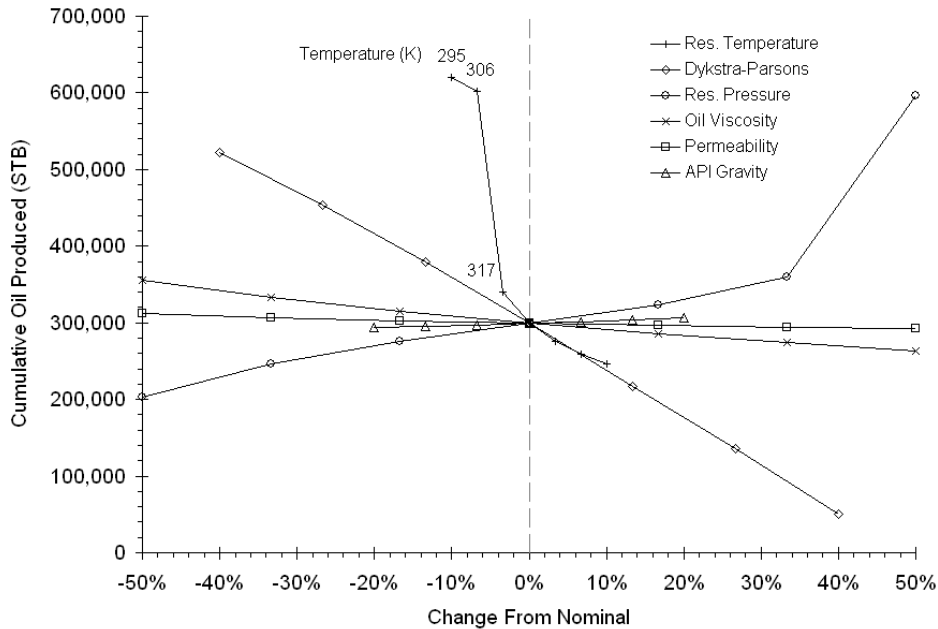
Figure 3.12. Sensitivity of cumulative oil recovery at the pattern end-of-life using the SACROC Kelly-Snyder parameter values as defined in Table 3.3, highlighting the temperatures over which oil production changes rapidly.

The strong sensitivity of the cumulative oil production to decreases in reservoir temperature is because CO_2 density and viscosity undergo rapid changes in the vicinity of the critical temperature of CO_2 (304 K). The net CO_2 utilization also exhibits the same strong sensitivity to small changes in temperature, as shown in Figure 3.13; however, unlike oil recovery, net CO_2 utilization is insensitive to changes in reservoir permeability, Dykstra-Parsons coefficient, oil viscosity, and API gravity.
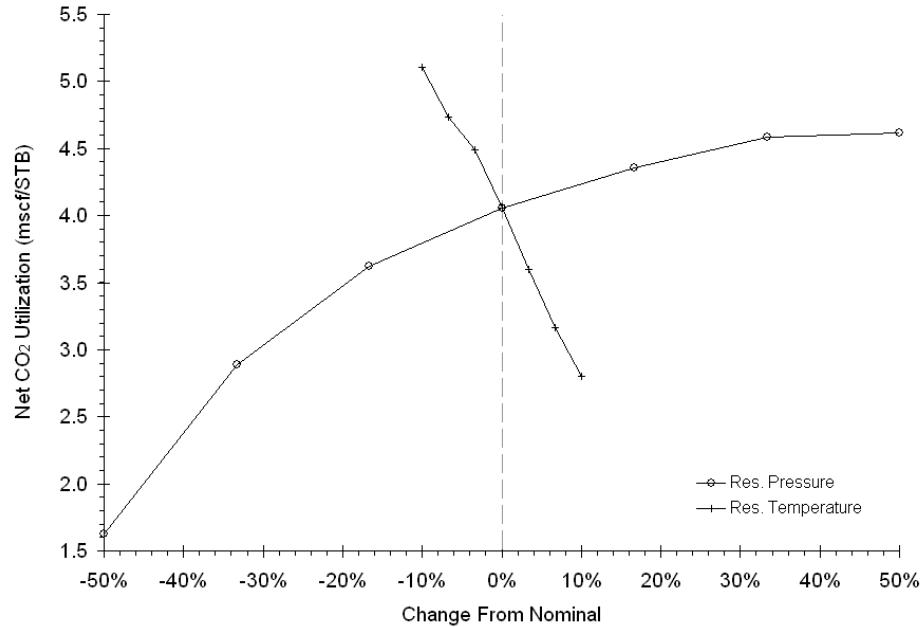
Figure 3.13. Sensitivity of net CO_2 utilization at the pattern end-of-life using the SACROC Kelly-Snyder parameter values as defined in Table 3.3

3.3   Enhanced Oil Recovery Economics Model

The economics model developed for EOR storage of CO_2 takes a number of inputs (shown in Figure 3.3), along with the performance model results, to estimate the profitability of the CO_2 flood, measured by net present value (NPV) and return on investment (ROI). The model estimates NPV and ROI by performing a discounted cash flow analysis using the oil production rates and CO_2 consumption rates from the performance model.

The model estimates the annual revenues and costs from the field from both oil production and (if applicable) CO_2 storage. The revenues from oil production are subject to royalties, severance taxes, and *ad valorem* taxes specified by the user. Expenses are incurred for normal field operating and maintenance costs, as well as fluid lifting, and processing of recycled CO_2.

The capital cost of the project is estimated based on the requirements for field production equipment, field CO_2 processing equipment, new pattern injection and production equipment, drilling and completion costs for new wells, and workovers for existing wells. These capital costs are amortized over the life of the field using the project discount rate.

The following sections describe how capital, O&M, fluid lifting, and CO_2 processing costs are estimated. In addition, the relationship used to estimate the first purchase price of crude oil based on market standard oil prices (e.g., the West Texas Intermediate) is described.

3.3.1 Lease Equipment Capital Cost

Converting a producing lease[8] to CO_2-flooding requires a number of changes to existing equipment, as shown in Table 3.2. Lewin & Associates developed a regression equation to estimate the costs of lease equipment for 12 regions of the United States in 1981 [49]. The lease equipment category covers the costs of adding or modifying production equipment for CO_2 service. When updated to 2004 dollars using the EIA Oil and Gas Lease Equipment and Operating Cost index [50], cost predicted by the Lewin & Associates regressions compare well with cost estimates in more recent reports (e.g., see [51]).

The Lewin & Associates cost regressions take the form:

$$C = a_1 e^{a_2 d} \tag{3.27}$$

---

[8] In this context, a parcel of land—including underlying mineral rights—that the operator leases for oil production, usually consisting of more than one pattern.

where C represents cost and d is depth in ft. The regression coefficients (where the a_1

parameter values have been updated to 2004 dollars) are listed by region in Table 3.6.

Table 3.6. Regression coefficients for lease equipment from Lewin and Associates [49]
updated to 2004 dollars for use in Equation 3.27.

Region	States	a_1	a_2
1	AK	50362	3×10^{-5}
2	CA, OR, WA	50362	3×10^{-5}
2A	Pacific Coast-Offshore, ID, NV, UT	50362	3×10^{-5}
3	CO, AZ, NM-West	34774	3×10^{-5}
4	WY, MT, ND, SD	34774	3×10^{-5}
5	TX-West, NM-East	29211	4×10^{-5}
6	TX-East, AR, LA, MS, AL	29211	4×10^{-5}
6A	Gulf Cost-Offshore	29211	4×10^{-5}
7	OK, KS, NE, MO, IA, MN	29211	4×10^{-5}
8	MI, WI	29211	4×10^{-5}
9	IL, IN, KY, TN	29211	4×10^{-5}
10	OH, PA, WV, NY, VA, NC	29211	4×10^{-5}
11A	SC, GA, FL	29211	4×10^{-5}

The costs for CO_2 processing equipment—also considered as lease equipment, but not

included in the Lewin & Associates regression—vary widely depending on the type of

processing required. The capital cost is generally lower for simple compression and

dehydration equipment than for more complex facilities incorporating NGL separation.

For simple compression and dehydration systems, a regression has been developed based

on 12 point estimates presented in the literature [3, 10, 27, 39, 51]. The regression

equation takes the form:

$$\log(C_{CPE}) = a_0 + a_1 \log(N_p q_{rcy,\max}) \qquad (3.28)$$

where C_{CPE} is the capital cost of CO_2 processing equipment, N_p is the number of patterns,

and $q_{rcy,max}$ is the pattern recycle rate (at the maximum CO_2 cut) in mmscf (million

standard cubic feet) per day. If construction is staggered (e.g., 10 patterns in year zero, 12

patterns in year 1), N_p would in this case be equal to the maximum number of patterns constructed in a given year (i.e., 12).

Parameter estimates for the coefficients in the CO_2 processing equipment cost correlation are given in Table 3.7. The generalized regression model given in Equation 3.28 accounts for a large proportion of the variation in the data set as reflected by an adjusted-r^2 value of 0.72.

Table 3.7. Regression coefficient estimates for the CO_2 processing equipment cost correlation, Equation 3.28, where standard errors are reported in parentheses.

Coefficient	Value
a_0	9.374×10^{-1} ** (1.855×10^{-1})
a_1	5.851×10^{0} ** (3.109×10^{-1})

** Significant at the 1% level

Use of the regression coefficients presented in Table 3.7 in Equation 3.28 results in costs ranging from $6,187,000 for compression and dehydration train handling 10 mmscf per day to $53,570,000 for a train handling 100 mmscf per day.

3.3.2 Pattern Equipment Capital Cost

Pattern equipment includes both production related-equipment (e.g., rods, pumps, wellheads, etc.) and injection-related equipment (e.g., injection skids, wellheads, etc.). This category does not include the drilling and completion (i.e., installation of tubing and downhole equipment) of new injection or production wells, which is treated in Section 3.3.3.

Chapter 3: Modeling the Cost of CO_2 Storage through Enhanced Oil Recovery

The cost models for production equipment and injection equipment associated with new wells are taken from the Lewin & Associates [49], and updated to 2004 dollars using the EIA Oil and Gas Lease Equipment and Operating Cost index [50]. The form of the Lewin & Associates cost model is presented in Equation 3.27, and the regression coefficients are listed by region in Table 3.8 (where the a_1 parameter values have been updated to 2004 dollars).

Table 3.8. Regression coefficients for production equipment and injection equipment from Lewin and Associates [49] updated to 2004 dollars for use in Equation 3.27.

Region	States	Production Equipment		Injection Equipment	
		a_1	a_2	a_1	a_2
1	AK	48328	1.1×10^{-4}	33132	9.0×10^{-5}
2	CA, OR, WA	48328	1.1×10^{-4}	33132	9.0×10^{-5}
2A	Pacific Coast-Offshore, ID, NV, UT	48328	1.1×10^{-4}	33132	9.0×10^{-5}
3	CO, AZ, NM-West	31130	1.5×10^{-4}	33132	9.0×10^{-5}
4	WY, MT, ND, SD	31130	1.5×10^{-4}	33132	9.0×10^{-5}
5	TX-West, NM-East	36049	1.5×10^{-4}	33132	9.0×10^{-5}
6	TX-East, AR, LA, MS, AL	36049	1.4×10^{-4}	33132	9.0×10^{-5}
6A	Gulf Cost-Offshore	36049	1.4×10^{-4}	33132	9.0×10^{-5}
7	OK, KS, NE, MO, IA, MN	36049	1.4×10^{-4}	33132	9.0×10^{-5}
8	MI, WI	36049	1.4×10^{-4}	33132	9.0×10^{-5}
9	IL, IN, KY, TN	36049	1.4×10^{-4}	33132	9.0×10^{-5}
10	OH, PA, WV, NY, VA, NC	36049	1.4×10^{-4}	33132	9.0×10^{-5}
11A	SC, GA, FL	36049	1.4×10^{-4}	33132	9.0×10^{-5}

For wells that are already in place and only require a well workover (i.e., tubing and downhole equipment replacement) prior to CO_2-flooding, the cost is expressed as a sum of a fraction of the production or injection equipment cost (depending on whether the well is a producer or injector) and the drilling and completion cost (Section 3.3.3). The expression for workover cost is [49]:

$$C_{WO} = 0.48 C_{D\&C} + 0.50 C_{PE} \qquad (3.29)$$

where $C_{D\&C}$ are the drilling and completion capital cost (discussed in the following section) and C_{PE} is the cost of production equipment.

3.3.3   *Drilling and Completion Capital Cost*

Drilling and completion (D&C) costs include the cost of physically drilling an injection well, running casing, hanging tubing, and installing any downhole equipment (e.g., chokes and packers). D&C costs are well documented by the annual Joint Association Survey (JAS) on Well Drilling Costs [52], which lists the average cost of wells drilled and completed each year by depth interval and state. A regression based on these costs was also developed by Lewin & Associates [49] in 1981, and has been updated to 2004 dollars using the using the EIA Oil and Gas Lease Equipment and Operating Cost index [50]. The form of the Lewin & Associates cost model is presented in Equation 3.27, and the regression coefficients are listed by region in Table 3.9 (with the a_1 parameter values updated to 2004 dollars).

Table 3.9. Regression coefficients for well drilling and completion from Lewin and Associates [49] updated to 2004 dollars for use in Equation 3.27.

Region	States	a_1	a_2
1	AK		
2	CA, OR, WA	70123	3.2×10^{-4}
2A	Pacific Coast-Offshore, ID, NV, UT	185819	3.2×10^{-4}
3	CO, AZ, NM-West	80086	2.7×10^{-4}
4	WY, MT, ND, SD	74808	2.8×10^{-4}
5	TX-West, NM-East	43986	3.4×10^{-4}
6	TX-East, AR, LA, MS, AL	44041	3.5×10^{-4}
6A	Gulf Cost-Offshore	996487	1.1×10^{-4}
7	OK, KS, NE, MO, IA, MN	42493	3.5×10^{-4}
8	MI, WI	65370	3.8×10^{-4}
9	IL, IN, KY, TN	34362	3.9×10^{-4}
10	OH, PA, WV, NY, VA, NC	23529	5.1×10^{-4}
11A	SC, GA, FL	216124	3.0×10^{-4}

Note that recent increases oil price have spurred a large increase in drilling activity. Thus, similar to increases in lease, production, and injection equipment costs (driven by materials cost increases), D&C costs in years after 2004 can be expected to be considerably higher. The EIA Oil and Gas Lease Equipment and Operating Cost index [50] can be used to update these costs for future periods.

3.3.4   Operating & Maintenance Cost Model

Operating and maintenance (O&M) costs for CO_2-flooding includes operating expenses for labor, consumables, surface equipment maintenance, and subsurface equipment maintenance, including periodic well workovers. Lewin & Associates [49] have estimated O&M costs as a function of well depth and region and these costs have been updated to 2004 dollars using the EIA Oil and Gas Lease Equipment and Operating Cost index [50]. The form of the Lewin & Associates cost model is presented in Equation

Chapter 3: Modeling the Cost of CO_2 Storage through Enhanced Oil Recovery

3.27, and the regression coefficients are listed by region in Table 3.10 (with the a_1

parameter values updated to 2004 dollars).

Table 3.10. Regression coefficients for O&M costs from Lewin and Associates [49]
updated to 2004 dollars for use in Equation 3.27.

Region	States	a_1	a_2
1	AK	28577	1.3×10^{-4}
2	CA, OR, WA	28577	1.3×10^{-4}
2A	Pacific Coast-Offshore, ID, NV, UT	28577	1.3×10^{-4}
3	CO, AZ, NM-West	26847	1.1×10^{-4}
4	WY, MT, ND, SD	26847	1.1×10^{-4}
5	TX-West, NM-East	26878	1.1×10^{-4}
6	TX-East, AR, LA, MS, AL	26878	1.1×10^{-4}
6A	Gulf Cost-Offshore	26878	1.1×10^{-4}
7	OK, KS, NE, MO, IA, MN	26878	1.1×10^{-4}
8	MI, WI	26878	1.1×10^{-4}
9	IL, IN, KY, TN	26878	1.1×10^{-4}
10	OH, PA, WV, NY, VA, NC	26878	1.1×10^{-4}
11A	SC, GA, FL	26878	1.1×10^{-4}

3.3.5   *Fluid Pumping and CO_2 Processing Cost*

The unit cost of lifting liquids to the surface and processing recycled CO_2 (i.e.

dehydration and compression) are model parameters provided by the user. Default values

are Advanced Resources International estimates, which are $0.25 per STB of fluid for

lifting and 1% of the oil price [51] per mscf CO_2 for processing.

3.3.6   *Illustrative Economics Model Capital and O&M Cost Results*

Results from the economics model for the capital cost of an inverted 5-sport injection

pattern are illustrated in Figure 3.14. This figure shows the capital cost of pattern

equipment for a project in West Texas or Eastern New Mexico (i.e., model region 5) for

three separate cases: no new wells required to convert a pattern to a CO_2-flood; four new

producers drilled and completed to develop a flooding-pattern; and, four new producers

and a new injector drilled and completed. As indicated by Equation 3.27, the cost is an exponential function of depth.
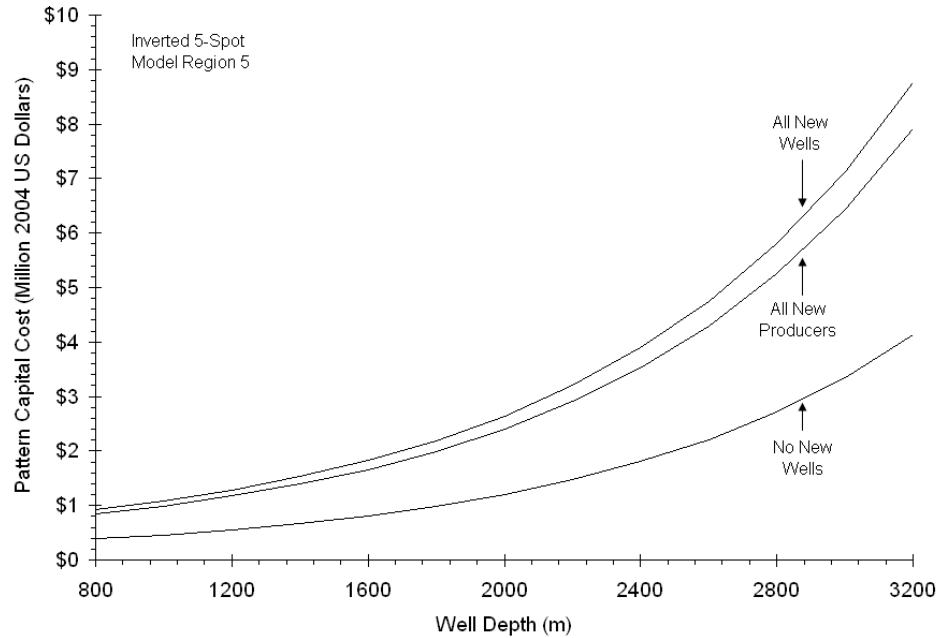
Figure 3.14. Cost of completing one inverted five-spot pattern in West Texas or Eastern New Mexico for three different cases.

The lease equipment cost for a field in West Texas or Eastern New Mexico (i.e., model region 5) as a function of the maximum CO_2 recycle rate and number of injection patterns is shown in Figure 3.15. The lease equipment cost is not highly sensitive to reservoir depth because the depth-dependent capital cost of production equipment is only a small fraction of the non-depth dependent lease equipment cost. The majority of the lease equipment cost is the cost of CO_2 processing equipment, which a function of the maximum CO_2 recycle rate.
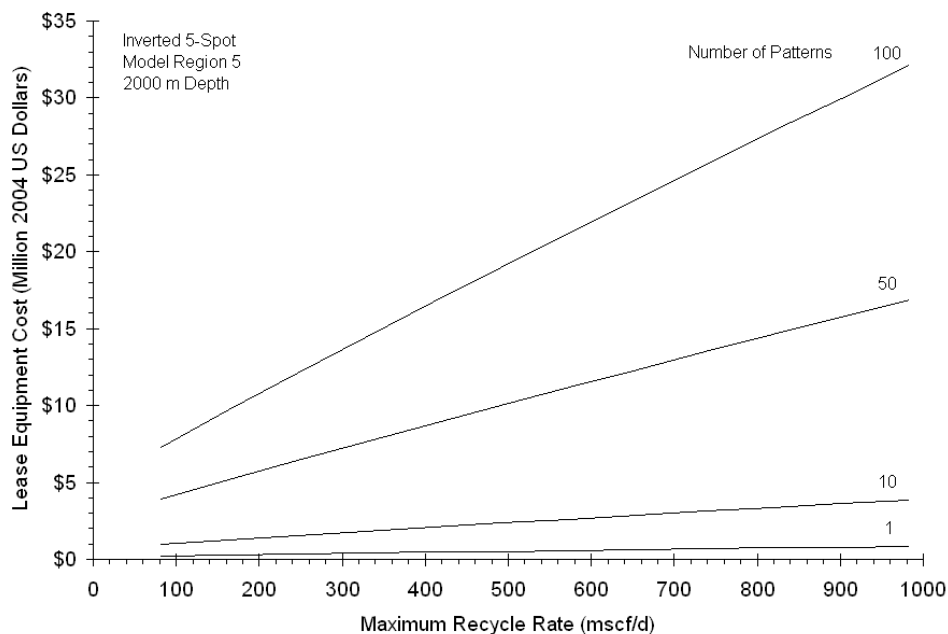
Figure 3.15. Lease equipment capital cost in West Texas or Eastern New Mexico as a function of CO_2 recycle rate for differing numbers of patterns.

Similar to pattern cost, O&M cost is an exponential function of depth, as shown in Figure

3.16 for a field in West Texas or Eastern New Mexico (i.e., model region 5).
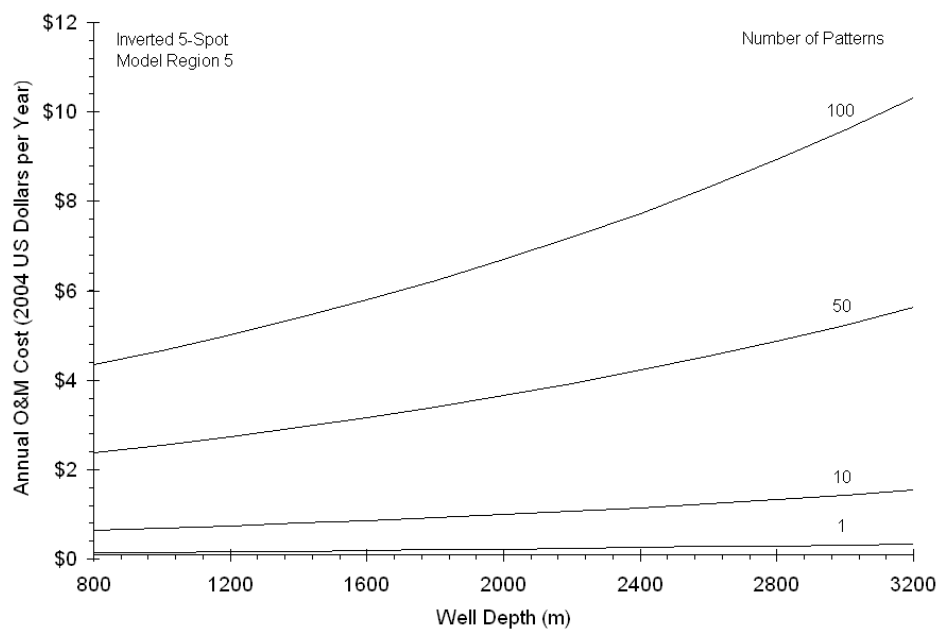
Figure 3.16. Field O&M cost in West Texas or Eastern New Mexico as a function of well depth for differing numbers of patterns.

The total pattern capital cost is the cost for one pattern (shown in Figure 3.14) multiplied

by the number of patterns; thus, it scales linearly with number of patterns. The annual

O&M cost also scales linearly with the number of patterns. Conversely, the lease capital

cost does not scale linearly with the number of patterns because the dominant component

of the lease capital cost is the CO_2 processing equipment cost (Equation 3.28), which is a

non-linear function of the maximum CO_2 recycle rate. In addition, the maximum recycle

rate for the project can be decreased by spreading pattern construction out over a number

of years. Table 3.11 shows the breakdown of capital costs associated with the

development of a 50 pattern CO_2 flood, with a maximum recycle rate of 500 mscf per

pattern and a 2000 m deep reservoir for two extreme cases: no wells initially present, and

all required wells (and associated production equipment) present.

Table 3.11. The capital and O&M cost in 2004 US dollars for a lease with 50 injection patterns where all wells are new—corresponding to a greenfield development—and all wells are already in place—corresponding to tertiary recovery.

Cost Item	All New Wells	No New Wells
Pattern Capital Cost		
Well Drilling & Completion ($)	$47,000,000	$0
Production Well Equipment ($)	$9,000,000	$0
Injection Well Equipment ($)	$3,000,000	$0
Production Well Workovers ($)	$0	$16,000,000
Injection Well Workovers ($)	$0	$11,000,000
Producer-Injector Conversions ($)	$0	$0
Subtotal ($)	$59,000,000	$27,000,000
Lease Equipment		
Production Lease Equipment ($)	$3,000,000	$0
CO_2 Processing Equipment ($)	$8,000,000	$8,000,000
Subtotal ($)	$10,000,000	$8,000,000
Total Cost		
O&M Cost		
Annual O&M Cost ($/year)	$4,000,000	$4,000,000

3.3.7   Oil Purchase Price Adjustment

The price in dollars per barrel a lease owner receives for the crude oil produced from

their lease, including CO_2-flooding projects, is known as the "first purchase price." This

price is a function of the oil stream (i.e., the type of oil categorized by reservoir or

general area) and is corrected for oil gravity, where heavier oils (i.e. those with lower API

gravities) have correspondingly lower first purchase prices. Generally, gravity corrections

only apply to oils below 40.0° API.

Estimating revenues from crude oil production requires a relationship between a

commonly used benchmark oil price and the first purchase price. This relationship has

been developed using a dataset containing the first purchase price of domestic crude oil,

binned by API gravity, between January 1993 and November 2006 and a second dataset

containing the West Texas Intermediate (WTI) price over the same period. West Texas

Intermediate is a 39.6° API oil, with 0.24% sulfur, priced free on board at Cushing,

Oklahoma. Both of these datasets were collected and published by the Energy

Information Administration (EIA). The fitted correlation takes the form:

$$P_{FPP} = a_o + a_1 P_{WTI} + a_2 G_{20} + a_3 G_{25} + a_4 G_{30} + a_5 G_{35} + a_6 G_{40} \qquad (3.30)$$

where: P_{FPP} is the first purchase price of crude oil, P_{WTI} is the WTI price, and G_{20} through

G_{40} are binary variables indicating API gravity. The binary variables take the value of one

for oil with API gravities in the ranges shown in Table 3.12, and zero otherwise. For

example, for a 32.0° API oil, the variable G_{35} takes the value of one, while all the other

binary variables take the value of zero.

Table 3.12. API gravity ranges corresponding to the binary variables in Equation 3.30

Binary Variable	API Gravity (γ_{API}) Range
G_{20}	$\gamma_{API} \leq 20.0$
G_{25}	$20.0 < \gamma_{API} \leq 25.0$
G_{30}	$25.0 < \gamma_{API} \leq 30.0$
G_{35}	$30.0 < \gamma_{API} \leq 35.0$
G_{40}	$40.0 \leq \gamma_{API}$

Parameter estimates for the coefficients in the first purchase price correlation are given in Table 3.13. The regression model given in Equation 3.30 accounts for a large proportion of the variation in the data set as reflected by having an adjusted-r^2 value greater than 0.99.

Table 3.13. Regression coefficient estimates for the first purchase price correlation, Equation 3.30, where standard errors are reported in parentheses.

Coefficient	Value
a_0	-4.754×10^{-1} ** (9.756×10^{-2})
a_1	0.954×10^{-1} ** (2.190×10^{-3})
a_2	-4.842×10^{0} ** (1.007×10^{-1})
a_3	-3.643×10^{0} ** (1.003×10^{-1})
a_4	-5.986×10^{0} ** (9.921×10^{-2})
a_5	-1.152×10^{0} ** (9.856×10^{-2})
a_6	-6.309×10^{-1} ** (9.824×10^{-2})

** Significant at the 1% level

The results of the first purchase price correlation for a range of WTI prices and API gravity ranges is shown in Figure 3.17. For example, for a WTI price of 75$ per barrel, a

lease owner can expect to receive $70/bbl for the 37° API oil produced from their lease, while an owner with a lease producing 66° API oil can expect to receive $65/bbl.
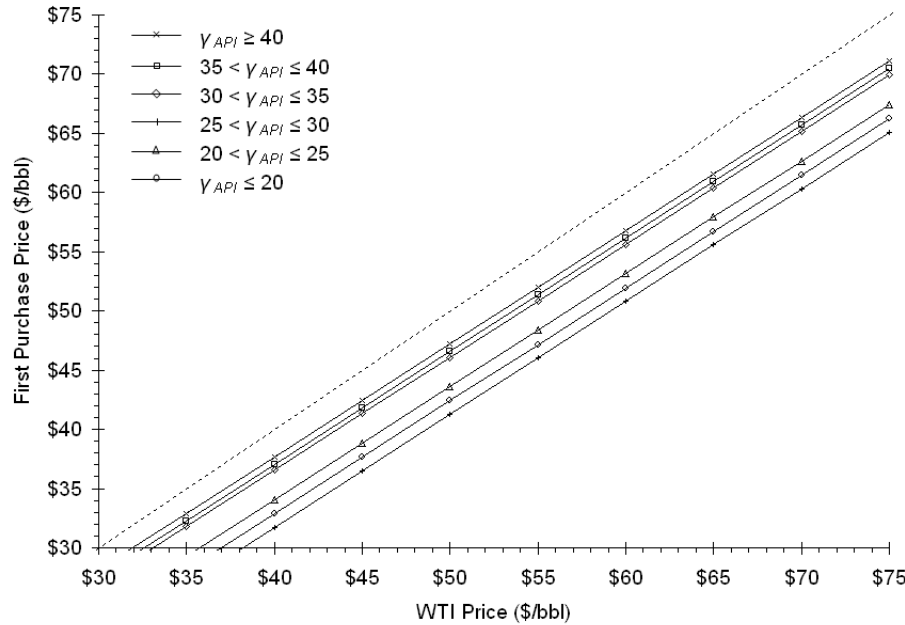
Figure 3.17. The first purchase price for crude oil as a function of the WTI price and the API gravity range.

3.4   Combining Performance and Cost

As shown in Figure 3.3, the maximum CO_2 cut, $f_{CO2,max}$, is specified in the economics model. The performance model uses this CO_2 cut to determine the pattern life, which defines the ultimate amount of oil recovered and CO_2 stored for a pattern. The performance of a single pattern is then multiplied by the total number of patterns completed and operating (allowing for staged construction) to arrive at the overall field performance.

The annual cash flow (in real dollars) is estimated by subtracting costs from annual oil revenues, which are calculated as the annual oil production estimated by the performance model multiplied by the real first purchase price (inflated using the real cost escalation

rate for the oil price specified by the user). This real cash flow is discounted using the project discount rate to arrive at the NPV and ROI for the project. The costs considered by the model are:

- royalties and taxes, the rates for both of which are user specified and subject to escalation rates;

- the annual cost of purchasing CO_2, calculated by multiplying the annual CO_2 requirement calculated by the performance model and the specified CO_2 price (subject to the real cost escalation rate for CO_2);

- the O&M cost, calculated by the methods discussed in Section 3.3.4 and subject to a real cost escalation rate;

- CO_2 processing cost and fluid lifting cost, calculated as discussed in Section 3.3.5, and subject to real cost escalation rates;

- M&V cost, which is a user supplied value in real dollars and subject to real escalation rates;

- Capital costs as discussed in Sections 3.3.1 to 3.3.3, and are subject to capital cost escalation factors that can be used to scale the capital costs predicted by the model; and,

- Debt service on capital expenditures, calculated based on the project discount rate.

3.5   Illustrative Case Studies

The performance model parameters for the four illustrative cases were given in Table 3.3 and were previously used to illustrate the behavior of the performance model. Economics model parameter values used in the case studies are listed in Table 3.14 and are the same for each case, making comparisons among the four cases simpler. The WTI oil price is varied parametrically in the estimation of the breakeven cost for CO_2. The breakeven cost for CO_2 is the CO_2 purchase price at which the project net present value (NPV) equals zero.

The pattern construction schedule used for all of the cases assumes 50% of the patterns built in the year prior to the start of injection (year zero); 30% of the patterns built in the first year; and, 20% of the patterns built in the second year. Using this pattern schedule, the performance parameters in Table 3.3, and economics parameter values in Table 3.14, results in the CO_2-flood performance summarized in Table 3.15.

Table 3.14. Economics model parameter values used in the four case studies

Project Parameter	Deterministic Value
WTI Oil Price ($/STB)	50.00
CO_2 Purchase Price ($/mscf)[†]	2.00
Real Discount Rate (%)	12
CO_2 Processing O&M Cost ($/mscf)[†]	0.50
Lifting O&M Cost ($/STB)	0.60
Operating Monitoring & Verification ($/y)	0
Closure Cost ($)	0
Taxes & Royalties	
Royalty Rate (%)	12.5
Severance Tax Rate (%)	5.0
Ad Valorium Tax Rate (%)	2.0
CO_2 Tax ($/tonne)	0.00
Real Escalation Rates	
Oil Price (%/year)	1
CO_2 Tax (%/year)	1
CO_2 Cost (%/year)	1
CO_2 Processing O&M Cost (%/year)	1
Lifting O&M Cost (%/year)	1
M&V Cost (%/year)	1
Lease O&M Cost (%/year)	1
Capital Cost Escalation Factors	
Drilling & Completion	1
Production Well Equipment	1
Injection Well Equipment	1
Production Lease Equipment	1
CO_2 Processing Equipment	1
Producer Breakdown	
Existing Producers	n[‡]
New Producers	0
Producer Workovers	n[‡]
Injector Breakdown	
Existing Injectors	$n + \left\lfloor \sqrt{4n-3} \right\rfloor + 2$ [*]
Producer-Injector Conversions	0
New Injectors	0
Injector Workovers	$n + \left\lfloor \sqrt{4n-3} \right\rfloor + 2$ [*]

[†] Appendix E lists price conversions from $/mscf to $/tonne
[‡] n is the number of patterns, thus there is one injector per pattern
[*] Number of production wells in a five-spot flooding network

Table 3.15. Results for the four illustrative cases described in Table 3.3

Parameter	Northeast Purdy Unit	SACROC Unit, Kelly-Snyder Field	Ford Geraldine Unit	Joffre Viking Pool
$f_{c,max}$	0.90	0.88	0.87	0.93
Oil Produced (MMSTB)	36	402	13	23
CO_2 Stored (Mt)	5.8	83.3	2.3	3.3
Capital Cost (million 2004 US Dollars)	$231	$787	$155	$80
NPV (million 2004 US Dollars)	$175	$3,247	-$7	$162
ROI	53%	162%	7%	110%

As previously noted, the $f_{c,max}$ values shown in Table 3.13 maximize the NPV for each project and were isolated using parabolic interpolation and refined with bisection [53]. Increasing the value of the maximum CO_2-cut increases the project life, increasing the payback time for the project capital; however, this may also result in negative cash-flows towards the end of the project. The effect of changing the maximum CO_2 cut on NPV is shown for the Northeast Purdy and Ford Geraldine Units in Figure 3.18. This figure shows that values of f_c of approximately 0.90 and 0.88 maximize the NPV of the respective projects, correspond to project lifetimes of 12 years and 8 years, respectively, under the case study assumptions.
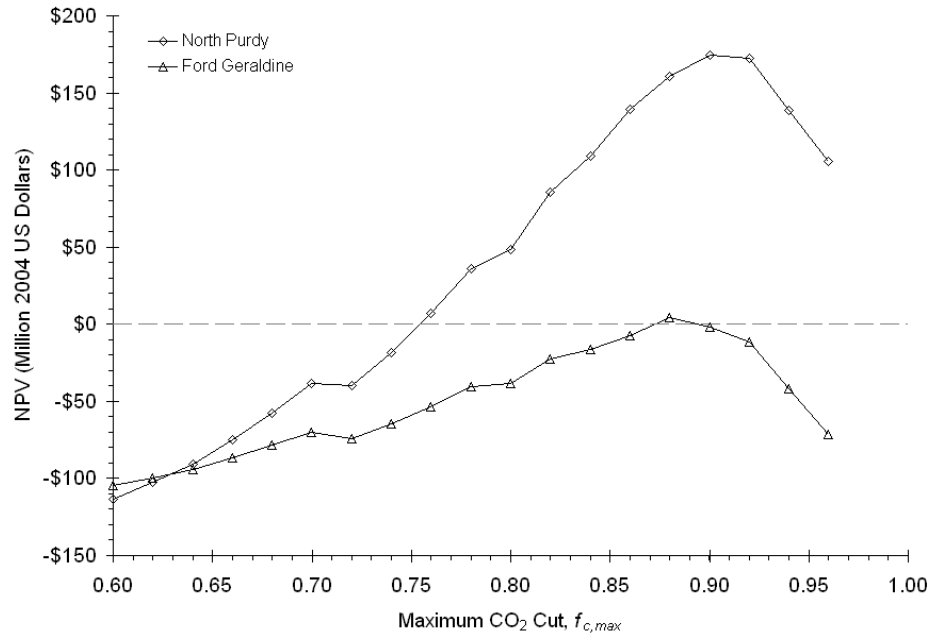
Figure 3.18. NPV as a function of changing maximum CO_2 cut for the Northeast Purdy Unit and the Ford Geraldine Units

The results in Table 3.15 show that, from the standpoint of large-scale CO_2 sequestration, projects similar to Northeast Purdy, Ford Geraldine or Joffre Viking would be of limited value as stand-alone projects, as they store small amounts of CO_2 relative to the amount of CO_2 produced from a large point source such as a power plant over its lifetime of operation (e.g. 500 MW coal fired plant over 30 years produces emissions of 90 Mt). Moreover, the rate at which these three projects store CO_2 is much lower than the rate that a large point source produces CO_2 (e.g. 500 MW coal fired plant produces emissions of 2-3 Mt per year), as illustrated in Figure 3.19. Conversely, a large field similar to the SACROC Kelly-Snyder field in Texas (developed rapidly, as in the case study) could sequester large amounts of CO_2 at rates compatible with a large point source.
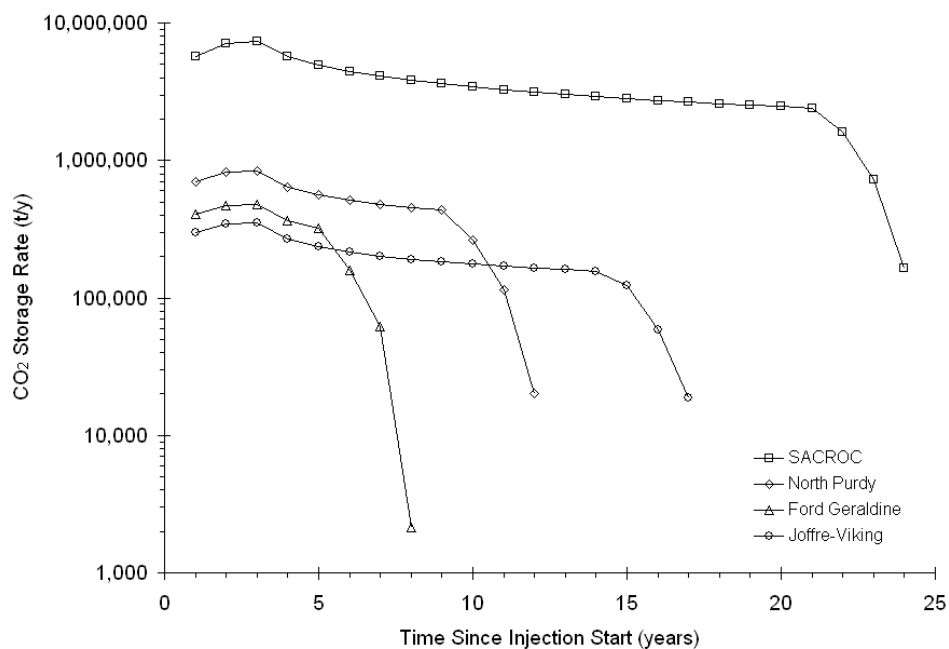
Figure 3.19. CO_2 storage rates for the four illustrative cases.

The breakeven CO_2 price can also be calculated by the model, as shown in Figure 3.20. The breakeven CO_2 price can be interpreted as the highest price a CO_2-flood developer would be willing to pay for CO_2 delivered to the site, based on the assumed benchmark oil price (and numerous other factors).
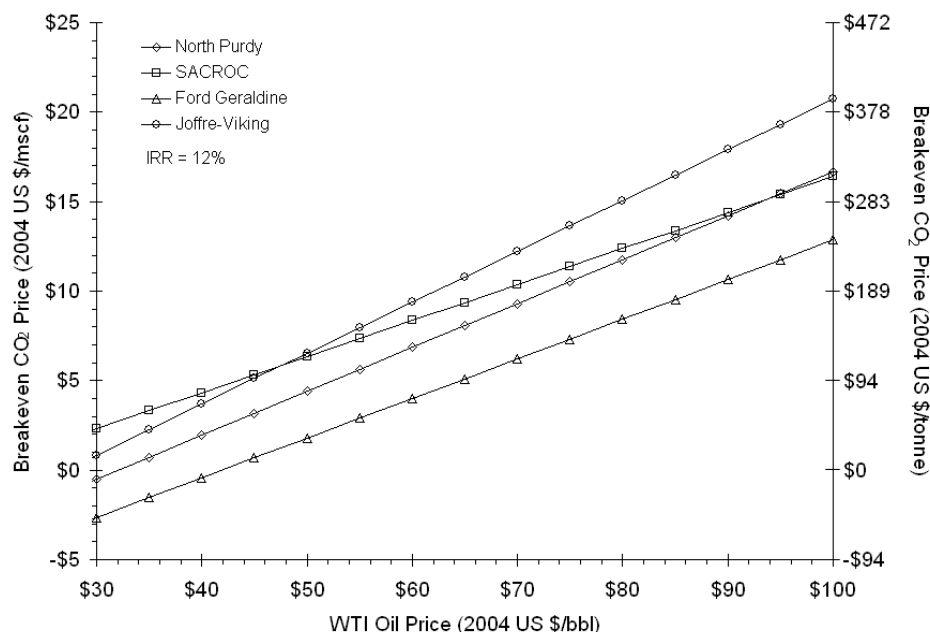
Figure 3.20. The breakeven CO_2 price for the four illustrative cases.

As would be expected based on pattern performance, there is considerable variation between breakeven costs for each case. However, at recent oil prices (i.e., greater than $50/bbl) all of the case study projects would be able to breakeven paying at least $1 per mscf CO_2 ($19 per tonne CO_2). The breakeven costs shown in Figure 3.20 are somewhat more pessimistic than those estimated in the literature [54] for generic sandstone and carbonate west-Texas reservoirs, but this may be the result of a number of factors: the model here uses higher capital costs compared to earlier studies; operation of the field can increase recovery (and the amount of CO_2 stored [55]) for example, by "shutting-in" patterns, drilling additional wells, and inverting injection patterns; and, improved mobility control in traditional water alternating gas (WAG) CO_2-floods results in lower CO_2 utilization rates. Both the addition of a third mobile phase to the reservoir (as occurs in WAG CO_2-floods) and the effects of operational decisions can not modeled analytically.

3.5.1   Model Sensitivity Analysis Results

To assess the sensitivity of the model to changes in multiple performance and economic parameters, uniform distributions were assigned to a number of parameters and the model was used to estimate the breakeven price for CO_2 over a series of Monte Carlo trials for the SACROC Kelly-Snyder case. The uniform distribution was selected to represent uncertainty or variability because there is no prior information that would suggest choosing a more complex distribution (such as a triangular or lognormal distribution). Twelve performance model parameters and seven economic model parameters were assigned distributions; both the parameters and the distributions for the parameter values are listed in Table 3.16.

Table 3.16. Assumed uncertainty distributions for parameters considered in the sensitivity analysis of the SACROC Kelly-Snyder case.

Model Parameter	Uncertainty Distribution
Performance Model Parameters	
Gross CO_2 Injection Rate, q_{gross} (mscf/d)	Uniform (450, 750)[a]
Reservoir Pressure, p_{res} (MPa)	Uniform (14, 23.3)[a]
Reservoir Temperature, T_{res} (K)	Uniform (320, 335)[b]
Net Pay, h (m)	Uniform (74, 90)[b]
Horizontal Permeability, k_h (md)	Uniform (17, 21)[b]
Permeability Anisotropy, k_v/k_h	Uniform (0.3, 0.5)[a]
Porosity, ϕ (%)	Uniform (3.5, 4.3)[b]
Dykstra-Parsons Coefficient, V_{DP}	Uniform (0.61, 0.75)[b]
Initial Oil Saturation, S_{orw} (%)	Uniform (38, 46)[b]
Oil Viscosity, μ_o (cp)	Uniform (0.32, 0.39)[b]
Reservoir Loss Fraction, η (%)	Uniform (0, 10)[c]
Surface Processing Loss Fraction, τ (%)	Uniform (0, 4)[c]
Economics Model Parameters	
CO_2 Processing O&M Cost ($/mscf)	Uniform (0.40, 0.60)[e]
Real Discount Rate (%)	Uniform (10, 15)
Lifting O&M Cost ($/STB)	Uniform (0.50, 0.70)
Oil Price Real Escalation Rate (%/year)	Uniform (-1, 2)[e]
Capital Cost Escalation Factors	
Production Well Equipment	Uniform (0.75, 1.00)
Injection Well Equipment	Uniform (0.75, 1.00)
Production Lease Equipment	Uniform (0.75, 1.00)
CO_2 Processing Equipment	Uniform (0.75, 1.00)

[a] Distribution bounds 25% above and below deterministic value (see Table 3.3)
[b] Distribution bounds 10% above and below deterministic value (see Table 3.3)
[c] Distribution bounds 100% above and below deterministic value (see Table 3.3)
[d] Distribution bounds 20% above and below deterministic value (see Table 3.14)
[e] Starting with an oil price of $50/bbl in 2006, real escalation rates between -1% and 2% per year result in 2004 constant dollar oil prices between $40/bbl and $80/bbl in 2030. For reference, the most recent EIA Annual Energy Outlook projects oil prices of approximately $30/bbl (low price case) and $90/bbl (high price case) in 2030 (2004 constant dollars) [56].

Of all the performance parameters in the model, those in Table 3.16 were selected

because they are parameters that are likely to vary over a large reservoir such as the

Kelly-Snyder Canyon Reef. Parameters that directly affect the amount of oil in place at

the beginning of the project were assumed to vary less from their deterministic values

than those that vary considerably over the life of the project (e.g. reservoir pressure), or

those that are largely speculative (i.e., loss fractions), because the amount of oil in place would likely be quite well known at the beginning of a tertiary CO_2-flood. All performance and economic model parameters not listed in Table 3.16 were treated as constants (with the values listed in Table 3.3 and Table 3.14) and the optimum NPV-maximizing CO_2 cut of 0.89 for the SACROC Kelly-Snyder deterministic case was used. For this analysis, 1,000 trials were conducted. From these trials, three cumulative distribution functions (CDF) were generated showing the breakeven CO_2 price, the net CO_2 utilization, and the cumulative mass of CO_2 stored.

Figure 3.21 shows the CDF for the breakeven CO_2 price based on an oil price of $50/bbl with the uncertain real price escalation rate given in Table 3.16. The median breakeven price of CO_2 from the sensitivity analysis is $6.39 per mscf CO_2 ($121 per tonne CO_2), with a 90% confidence interval of $4.78 to $8.60 per mscf CO_2 ($90 to $163 per tonne CO_2, respectively).
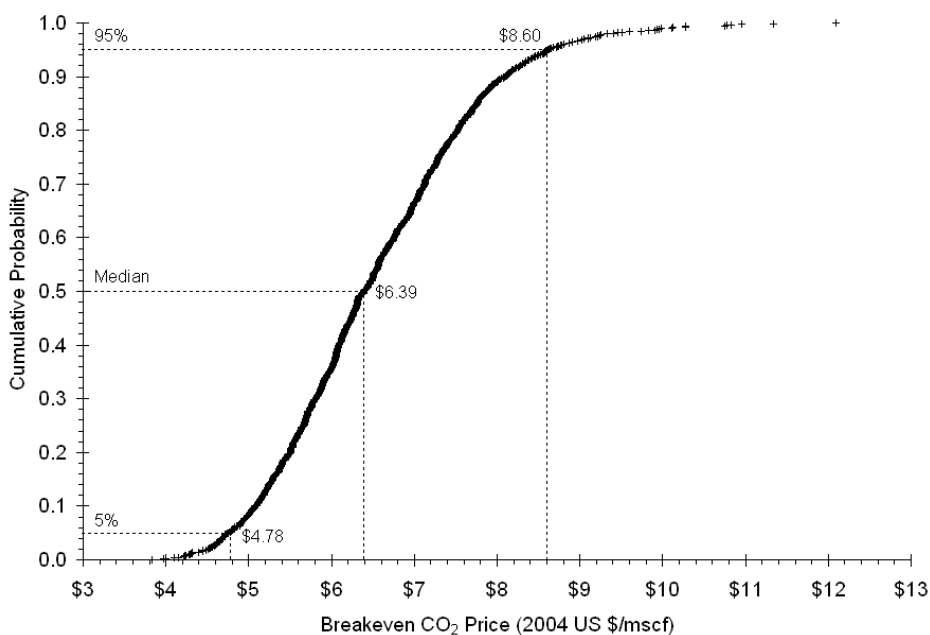
Figure 3.21. CDF for the breakeven CO_2 price for the SACROC Kelly-Snyder case

Results of the Monte Carlo trials can also be used to assess the sensitivity of breakeven cost to the model parameters having uniform distributions. The measure used to assess the sensitivity is the Spearman rank-order correlation (r_s) [57]. The value of the rank order correlation coefficient between the breakeven CO_2 price and the model parameters assigned distributions is shown in Figure 3.23. The dashed vertical lines to the left and the right of the axis in Figure 3.23 indicate the 5% significance level (rs = ±0.07); thus rank-order correlation coefficients smaller than this value are not statistically significant at the 5% level. Figure 3.23 shows the strongest correlation is between the oil price escalation rate ($r_s = 0.57$)—a proxy for oil price—and breakeven CO_2 price, followed by reservoir loss fraction ($r_s = -0.53$) and reservoir pressure ($r_s = -0.41$). Following these, significant rank-order correlation coefficients (by decreasing magnitude) are the: reservoir temperature, Dykstra-Parsons coefficient (representing permeability heterogeneity), surface loss rate, gross injection rate, initial oil saturation, porosity, CO_2 processing O&M cost, and escalation in drilling and completion cost.
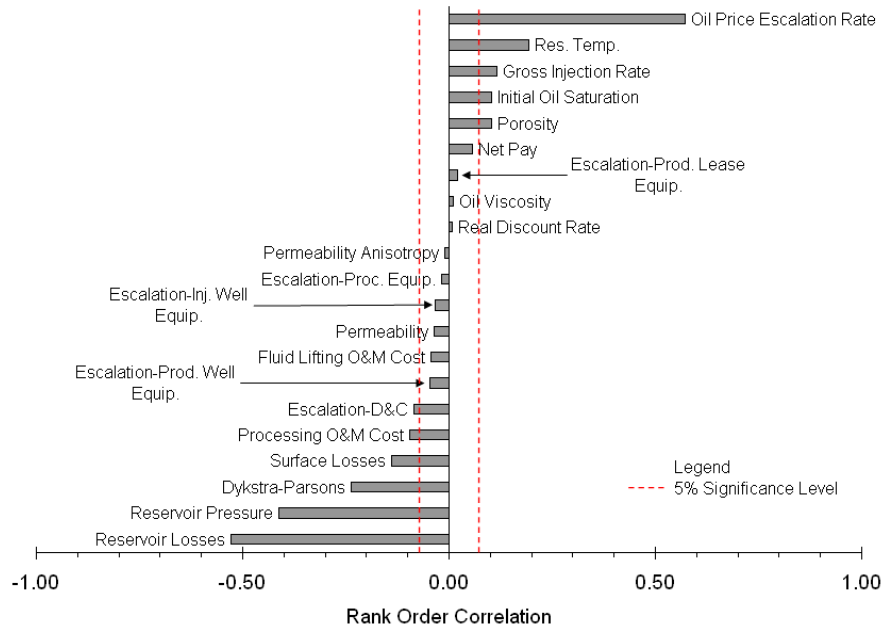
Figure 3.22. Rank-order correlation between the results of the Monte Carlo sensitivity analysis and the parameters assigned uniform distributions.

These results show that the breakeven CO_2 price is highly sensitive to a number of factors. In practice, however, the uncertainty around these parameters should be relatively small. While factors such as reservoir pressure, temperature, and initial oil saturation (i.e., residual to waterflooding) may vary from area to area within the field, they will be well characterized by the time tertiary CO_2 flooding is being planned. Moreover, reservoir pressure and reservoir loss rates can be controlled to some extent. In contrast, the uncertainty associated surrounding future oil prices over the operating life of the field is far and away the most difficult parameter to estimate. In this analysis the real oil price at the start of the CO_2-flood has been assumed to be well known compared to the nominal oil price in some future year of operation; thus, the real oil price escalation rate has been assigned uncertainty.

The CDF for net CO_2 utilization for the SACROC Kelly-Snyder case is shown in Figure 3.23. The median value is 4 mscf CO_2 per STB (0.21 tonnes CO_2 per STB), with a 90% confidence interval between 3 and 5 mscf CO_2 per STB (0.16 and 0.26 tonnes CO_2 per STB). The CO_2 utilization is most sensitive to the reservoir loss rate ($r_s = 0.77$), reservoir pressure ($r_s = 0.54$), reservoir temperature ($r_s = -0.27$), and the surface loss rate ($r_s = 0.21$). The net CO_2 utilization is strictly a function of the performance model and is unaffected by factors such as oil price (at a constant maximum CO_2 cut).
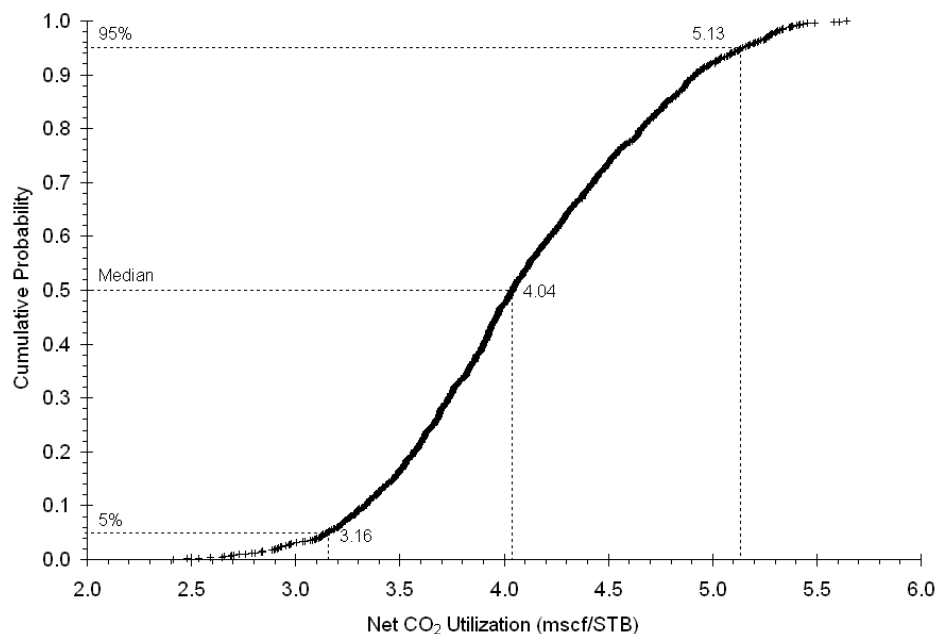
Figure 3.23. CDF for net CO_2 utilization

The CDF for the net CO_2 stored (i.e. the net mass CO_2 injected minus losses to the atmosphere) resulting from the sensitivity analysis is shown in Figure 3.24. The median amount of CO_2 stored is 81 Mt of CO_2, with a 90% confidence interval between 54 and 126 Mt of CO_2 stored. For a fixed maximum CO_2 cut, the amount of CO_2 stored is most sensitive to reservoir pressure ($r_s = 0.57$), reservoir loss rate ($r_s = 0.45$), Dykstra-Parsons

coefficient (r_s = -0.39), reservoir temperature (r_s = -0.32), and reservoir porosity (r_s = 0.21).
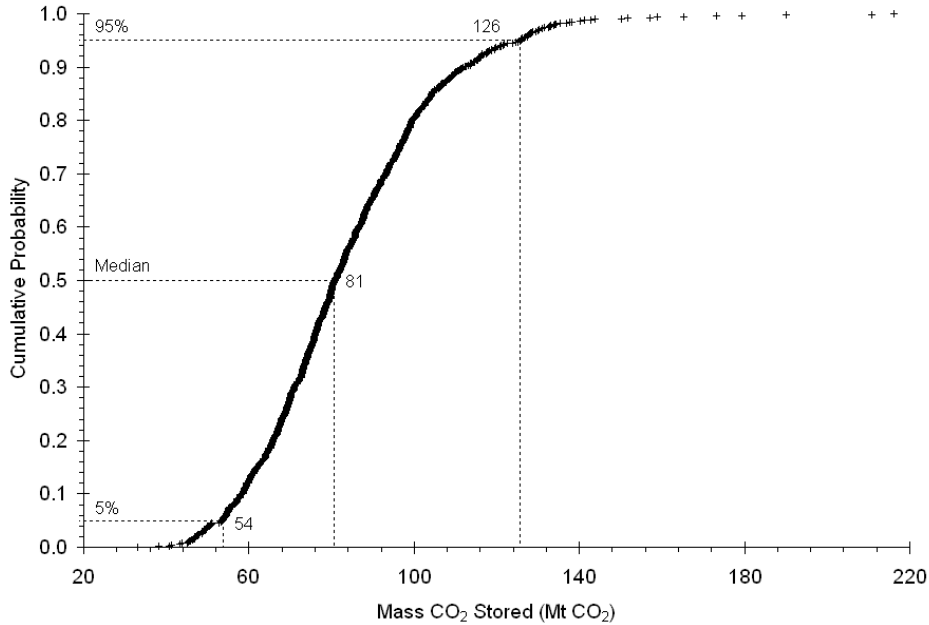
Figure 3.24. CDF for the net mass of CO_2 stored at the field end-of-life

The rank-order correlation results show (for this case) that the reservoir pressure, reservoir temperature and the reservoir loss rate are consistently have a strong impact on the breakeven CO_2 price, the net CO_2 utilization, and the amount of CO_2 stored. In addition, the results appear to be more sensitive to permeability variations than absolute permeability. Both the breakeven CO_2 price and the amount of CO_2 stored are also impacted by CO_2 losses from surface processing. Unlike the reservoir parameters, which are to a large extent unchangeable for a given reservoir, losses from surface processing equipment could be minimized though design decisions and maintenance. However, because CO_2 has traditionally been a commodity in EOR, it would stand to reason that losses to the atmosphere are currently monitored. Unfortunately this data is not reported in the literature.

3.6   Comparison with Other Models

It is difficult to quantitatively compare the model developed here with other EOR

screening models discussed earlier such as the DOE sponsored CO_2-PM [36] or CO_2-

Prophet [7] models for a number of reasons. While both of these models are designed to

be "screening" models, they take different approaches, require different sets of input

parameters, have been presented in the literature using different cases, and are meant for

different groups of users (i.e. reservoir engineers versus strategic planners) than the

model developed here.

The CO_2-PM model is based on the same correlations for vertical and aerial sweep

efficiency as used here; however the CO_2-PM displacement efficiency calculations

account for three flowing phases (oil, water, and CO_2) and thus requires input

characterizing the relative permeability curves for each of the flowing phases which at a

screening level would likely be unavailable to the user. The CO_2-Prophet model is a

stream tube model, allowing the model to account for irregular injection patterns and

varying production rates from each well in the pattern but does not perform any economic

analysis. Like CO_2-PM, CO_2-Prophet requires inputs for the relative permeability curves

for each of the flowing phases (i.e., for CO_2-Prophet, this is a set of 14 parameters [7])

that would likely be unavailable to the user.

Despite the differences in the level of detail (e.g., the model presented here doesn't treat

water as a mobile phase), the relative shape of the oil recovery curves generated by the

model presented here and the CO_2-PM and CO_2-Prophet models are similar. Moreover,

they reach similar endpoint recoveries at roughly similar pore volumes (see Paul et al.

[36] for CO_2-PM example results and Dobitz and Preiditis [7] for CO_2-Prophet example results).

Kinder Morgan (KM) has also developed a public CO_2-flood scoping model based on typical WAG CO_2-flooding performance from the San Andres formation in the Permian Basin (see [39]). The core of the KM model is a set of dimensionless curves that are scaled based on user inputs to provide results for a specific case. As illustrated by the sensitivity analysis shown earlier, and acknowledged by KM[9], this approach does not consider a number of important factors that are reservoir specific. Nonetheless, the KM dimensionless curves are compared to results for both dimensionless oil production and CO_2 production generated by the model presented here in Figure 3.25 and Figure 3.26.

Figure 3.25 shows that compared to the KM-WAG curve, the model developed here reaches similar oil recoveries at similar volumes of CO_2 injected for the Joffre-Viking and Ford Geraldine cases. The smaller area under the KM-WAG curve than the illustrative case curves in Figure 3.26 implies that the KM-WAG model recycles less CO_2 of the life of the project compared to the model developed here. Thus, the KM-WAG model would predict lower gross CO_2 utilizations, which translates into lower operating costs over the life of the field. However, as both figures show, the KM-WAG curves end at 0.75 HCPV of CO_2 injected while two of the illustrative cases inject almost twice as much.

---

[9] The KM model is provided with the disclaimer that "the data and processes contained hereon are intended to provide example results for data only and should not be relied on for any specific case or application. Results may vary depending on numerous variables."
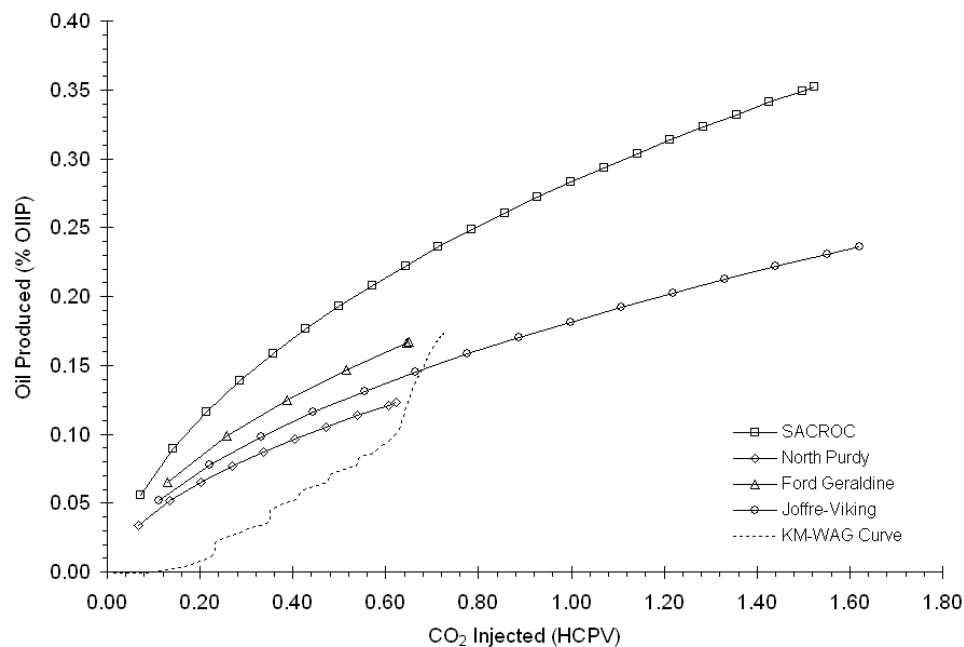
Figure 3.25. A comparison of dimensionless results for oil production obtained from the four cases presented here and the KM-WAG curve.
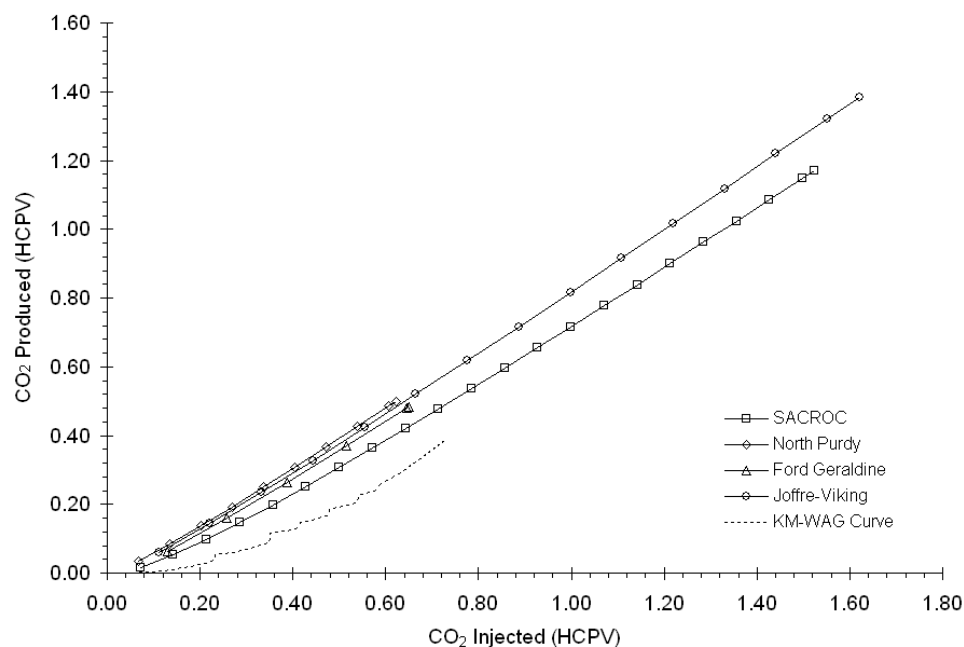
Figure 3.26. A comparison of dimensionless results for CO_2 production obtained from the four cases presented here and the KM-WAG curve.

3.7   References

1.   Moritis, G., *CO_2 injection gains momentum.* Oil & Gas Journal, 2006. **104**(15): p. 37-41.
2.   Gerritsen, M.G. and L.J. Durlofsky, *Modeling fluid flow in oil reservoirs.* Annual Review of Fluid Mechanics, 2005. **37**: p. 211-238.
3.   Bock, B., et al., *Economic Evaluation of CO_2 Storage and Sink Enhancement Options*. 2003, TVA Public Power Institute: Muscle Shoals, AL.
4.   Amyx, J.W. and D.M. Bass, *Estimating Secondary Reserves*, in *Petroleum Economics and Valuation Symposium*. 1962, Society of Petroleum Engineers: Dallas, TX.
5.   Claridge, E.L., *Prediction of Recovery in Unstable Miscible Flooding.* SPE Journal, 1972. **12**(2): p. 143-155.
6.   Koval, E.J., *A Method for Predicting the Performance of Unstable Miscible Displacement in Hetrogeneous Media.* SPE Journal, 1963. **3**(6): p. 145-154.
7.   Dobitz, J.K. and J. Prieditis, *A Stream Tube Model for the PC*, in *SPE/DOE Ninth Symposium on Improved Oil Recovery*. 1994, Society of Petroleum Engineers: Tulsa, OK.
8.   Moritis, G., *EOR oil production up slightly.* Oil & Gas Journal, 1998. **96**(16): p. 49-50.
9.   Office of Technical Assessment, *Enhanced Oil Recovery Potential in the United States*. 1978, Office of Technical Assessment: Washington, DC. p. 238.
10.   National Petroleum Council, *Enhanced Oil Recovery*. 1984.
11.   Interstate Oil and Gas Compact Commission, *An Evaluation of Known Remaining Oil Resources in the United States: Project on Advanced Oil Recovery and the States*. 1993, Interstate Oil & Gas Compact Comission: Oklahoma City, OK.
12.   Holtz, M.H., P.K. Nance, and R.J. Finley, *Reduction of Greenhouse Gas Emissions through CO_2 EOR in Texas.* Environmental Geosciences, 2000. **8**(3): p. 187-199.
13.   Bachu, S. and W.D. Gunter. *Overview of Acid-Gas Injection Operations in Western Canada*. in *7th International Conference on Greenhouse Gas Control Technologies*. 2004. Vancouver, Canada: Elsevier Science.
14.   Bachu, S. and K. Haug, *In-Situ Characteristics of Acid-Gas Injection Operations in the Alberta Basin, Western Canada: Demonstration of CO_2 Geological Storage*, in *The CO_2 Capture and Storage Project (CCP) for Carbon Dioxide Storage in Deep Geologic Formations for Climate Change Mitigation*, S. Benson, Editor. 2004, Elsevier Science.
15.   Kovscek, A.R. and Y. Wang, *Geologic storage of carbon dioxide and enhanced oil recovery. I. Uncertainty quantification employing a streamline based proxy for reservoir flow simulation.* Energy Conversion & Management, 2005. **46**: p. 1920-1940.
16.   Kovscek, A.R. and M.D. Cakici, *Geologic storage of carbon dioxide and enhanced oil recovery. II. Cooptmization of storage and recovery.* Energy Conversion & Management, 2005. **46**: p. 1941-1956.

17.   Craft, B. and M. Hawkins, *Applied Petroleum Reservoir Engineering*. 1st ed. Prentice-Hall Chemical Engineering Series. 1959, Englewood Cliffs, NJ: Prentice-Hall. 437.

18.   Brigham, W., *Doublets and Other Allied Well Patterns*. 2000, Stanford University Petroleum Research Institute: Stanford, CA.

19.   Roper Jr., M.K., K. Sepehrnoori, and G.A. Pope, *Analysis of Teritary Injectivity of Carbon Dioxide*, in *SPE Permian Basin Oil and Gas Recovery Conference*. 1992, Society of Petroleum Engineers: Midland, TX.

20.   Pizarro, J.O.S. and L.W. Lake, *Understanding Injectivity in Heterogeneous Reservoirs*, in *SPE/DOE Improved Oil Recovery Symposium*. 1998, Society of Petroleum Engineers: Tulsa, OK.

21.   Muscat, M., *Flow of Homogeneous Fluids*. 1st ed. 1937, New York: McGraw-Hill. 763.

22.   Bachu, S., *Sequestration of CO₂ in geological media in response to climate change: road map for site selection using the transform of the geological space into the CO₂ phase space.* Energy Conversion & Management, 2002. **43**: p. 87-102.

23.   Hendriks, C.F., *Carbon dioxide removal from coal fired power plants*. 1 ed. 1994: Kluwer Academic Publishers.

24.   Heller, J.P. and J.J. Taber, *Influence of Reservoir Depth on Enhanced Oil Recovery by CO₂ Flooding*, in *Permian Basin Oil & Gas Recovery Conference of the Society of Petroleum Engineers*. 1986, Society of Petroleum Engineers: Midland. TX.

25.   Tek, R.M. and D.L. Katz, *Temperature and Pressure Gradients in Gas Wells*, in *53rd Annual Fall Technical Conference and Exhibition of the Society of Petroleum Engineers of AIME*. 1978, Society of Petroleum Engineers: Houston, TX.

26.   Ramey, H.J., *Wellbore Heat Transmission.* Journal of Petroleum Technology, 1962(April): p. 427-435.

27.   Klins, M.A., *Carbon Dioxide Flooding-Basic Mechanisms and Project Design*. 1984, Boston: International Human Resources Development Corporation. 267.

28.   Green, D.W. and G.P. Willhite, *Enhanced Oil Recovery*. SPE Textbook Series. 1998, Richardson, TX: Society of Petroleum Engineers. 545.

29.   Holm, L.W. and V.A. Josendal, *Mechanisms of Oil Displacement by Carbon Dioxide.* Journal of Petroleum Technology, 1974(December): p. 1427-1438.

30.   Stalkup Jr., F.I., *Miscible Displacement*. 1983, Dallas: Society of Petroleum Engineers. 204.

31.   Orr, F.M., B. Dindoruk, and R.T. Johns, *Theory of Multicomponent Gas/Oil Displacements.* Industrial & Engineering Chemistry Research, 1995. **34**: p. 2661-2669.

32.   Habermann, B., *The Efficiency of Miscible Displacement as a Function of Mobility Ratio.* Transactions of AIME, 1960. **219**: p. 264-272.

33.   Jessen, K., et al., *Fast, approximate solutions for 1D multicomponent gas-injection problems.* SPE Journal, 2001. **6**(4): p. 442-451.

34.   Juanes, R. and M.J. Blunt, *Analytical solutions to multiphase first-contact miscible models with viscous fingering.* Transport in Porous Media, 2006. **64**(3): p. 339-373.

35.   Shaw, J. and S. Bachu, *Screening, evaluation, and ranking of oil reservoirs suitable for CO_2-flood EOR and carbon dioxide sequestration.* Journal of Canadian Petroleum Technology, 2002. **41**(9): p. 51-61.

36.   Paul, G.W., L.W. Lake, and T.L. Gould, *A Simplified Predictive Model for CO2 Miscible Flooding*, in *59th Annual Technical Conference and Exhibition of the Society of Petroleum Engineers.* 1984, Society of Petroleum Engineers: Houston, TX.

37.   Lake, L.W., *Enhanced Oil Recovery.* 1996, Upper Saddle River, NJ: Prentice Hall.

38.   Dake, L.P., *Fundamentals of reservoir engineering.* 1 ed. 1978: Elsevier.

39.   Jarrell, P.M., et al., *Practical Aspects of CO_2 Flooding.* SPE Monograph Series. 2002, Richardson, TX: Society of Petroleum Engineers. 220.

40.   Ormiston, R.M. and M.C. Luce, *Surface Processing of Carbon Dioxide.* Journal of Petroleum Technology, 1986(August): p. 823-828.

41.   Simlote, V.N. and E.M. Withjack, *Estimation of Tertiary Recovery by CO_2 Injection--Springer A Sand, Northeast Purdy Unit.* Journal of Petroleum Technology, 1981(May): p. 808-818.

42.   Dicharry, R.M., T.L. Perryman, and J.D. Ronquille, *Evaluation and Design of a CO_2 Miscible Flood Project-SACROC Unit, Kelly-Snyder Field.* Journal of Petroleum Technology, 1973(November): p. 1309-1318.

43.   Langston, M.V., S.F. Hoadley, and D.N. Young, *Definitive CO_2 Flooding Response in the SACROC Unit*, in *SPE/DOE Enhanced Oil Recovery Symposium.* 1988, Society of Petroleum Engineers: Tulsa, OK.

44.   Kane, A.V., *Performance Review of a Large-Scale CO_2-WAG Enhanced Recovery Project, SACROC Unit--Kelly-Snyder Field.* Journal of Petroleum Technology, 1979(February): p. 217-231.

45.   Phillips, L.A., J.L. McPherson, and R.J. Leibrecht, *CO_2 Flood: Design and Initial Operations, Ford Geraldine (Delaware Sand) Unit*, in *58th Annual Technical Conference and Exhibition.* 1983, Society of Petroleum Engineers: San Francisco, CA.

46.   Stephenson, D.J., A.G. Graham, and R.W. Luhning, *Mobility Control Experience in the Joffre Viking Miscible CO_2 Flood.* SPE Reservoir Engineering, 1993(August): p. 183-188.

47.   EPRI, *Enhanced Oil Recovery Scoping Study.* 1999, Electric Power Research Institute: Palo Alto, CA. p. 148.

48.   Brock, W.R. and L.A. Bryan, *Summary Results of CO_2 EOR Field Tests, 1972-1987*, in *SPE Joint Rocy Mountain Regional\Low Permeability Reservoirs Symposium and Exhibition.* 1989, Society of Petroleum Engineers: Denver, CO.

49.   Lewin & Associates Inc., *Economics of Enhanced Oil Recovery.* 1981, Department of Energy: Washington, DC. p. 123.

50.   Energy Information Administration. *Oil and Gas Lease Equipment and Operating Costs 1988 Through 2006.* 18 June 2007 [cited 26 September 2007]; Available from:

http://www.eia.doe.gov/pub/oil_gas/natural_gas/data_publications/cost_indices_equipment_production/current/coststudy.html.

51.   Advanced Resources International, *Basin Oriented Strategies for CO₂ Enhanced Oil Recovery: Permian Basin*. 2006, US Department of Energy: Arlington, VA. p. 117.

52.   American Petroleum Institute, *Joint Association Survey on Drilling Costs*. 2002, American Petroleum Institute: Washington, DC. p. 111.

53.   Press, W.H., *Numerical recipes in C : the art of scientific computing*. 2nd ed. 1992, Cambridge; New York: Cambridge University Press. xxvi, 994 p.

54.   Wolsky, A.M. and D.J. Jankowski, *The Value of CO₂: Framework and Results*. Journal of Petroleum Technology, 1986(September): p. 987-994.

55.   Jessen, K., A.R. Kovscek, and F.M. Orr, *Increasing CO₂ Storage in Oil Recovery*. Energy Conversion & Management, 2005. **46**: p. 293-311.

56.   Energy Information Administration, *Annual Energy Outlook 2007*. 2007, US Department of Energy: Washington, D.C. p. 229.

57.   Morgan, M.G., M. Henrion, and M. Small, *Uncertainty : a guide to dealing with uncertainty in quantitative risk and policy analysis*. 1990, Cambridge: Cambridge University Press. 332.

Chapter 4: Modeling CO_2 Storage in Saline Aquifers

A saline aquifer is a geologic formation with sufficient porosity and permeability to transmit significant quantities of water with a dissolved solids content that makes the water unfit for consumption, agricultural, or industrial uses, and is referred to as "brine" or "formation water". Moreover, this formation should be of sufficient depth to ensure that injected CO_2 remains in the supercritical phase [1]. As of late 2007, there are three planned or operating projects injecting CO_2 into saline aquifers and one other project injecting CO_2 into the water leg of a hydrocarbon reservoir for the purpose of CO_2 storage (see Table 1.3).

While there are many analogues to CO_2 storage, such as acid gas injection [2, 3], natural gas storage [4, 5], disposal of treated wastewater [5, 6], and disposal of hazardous waste [5], there are still many gaps in our understanding of CO_2 storage processes, including the cost of storage [7]. The objective of this chapter is to present the development of a model that will allow the cost of CO_2 storage to be estimated given the specifics of a storage site.

A limited number of studies have examined the cost of aquifer storage [8-10]. None of these studies have developed a comprehensive model that estimates performance of a storage project from wellhead to subsurface and bases cost on the project performance. The earliest study by Hendriks [8] estimated costs based on petroleum engineering rules-of-thumb for a hypothetical aquifer and performed single parameter sensitivity analysis on the depth. Bock et al. [9] performed a cost analysis on three hypothetical cases using a correlation for single-well injectivity developed by Law [11] and costs based on data

from secondary oil production. The work by Bock et al. also contained a sensitivity analysis on four parameters [9]. Studies have also been performed for the IEA Greenhouse Gas Programme (e.g., see [12]) that have applied relatively crude rules-of-thumb to estimate costs for a large number of aquifers.

In this chapter, an analytical model is developed to estimate the cost of geological storage of CO_2 in aquifers for a range of geological settings and CO_2 injection rates. The cost estimates for CO_2 storage are embodied in an engineering-economic that is used to assess the sensitivity of storage cost to changes in geological settings and other assumptions. This analysis will also show the potential range of costs that could occur and the probability associated with these costs for a given scenario.

4.1   The Aquifer Storage Process

The aquifer storage process, the steps of which are shown in Figure 4.1, is considerably simpler than the EOR process modeled in Chapter 3. In the aquifer storage process, CO_2 is received at the storage site and compressed if the pressure is not high enough for injection. Following recompression (if necessary), CO_2 is distributed to the injection wells which transport it to the target formation.
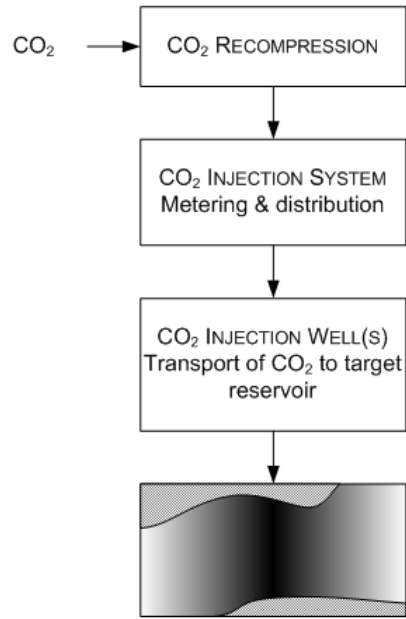
Figure 4.1. Material flows and process steps in aquifer storage of CO_2

In the aquifer injected CO_2 will spread radially away from the wellbore under the imposed pressure gradient. The rate at which CO_2 moves away from the wellbore is given by Darcy's law [13, 14], in which the fluid flux is proportional to the permeability of the formation to CO_2, k. On a larger scale (both spatially and temporally), to avoid the release of CO_2 to the atmosphere, the injected fluid must be trapped in the formation. Trapping mechanisms can be either physical, where CO_2 remains as a separate phase, or chemical, in which CO_2 dissolves into the formation water and may react with minerals present in the formation to become immobilized—processes typically occurring on a scale of decades to centuries [7, 15]. Thus, in the short term, the rate at which CO_2 can be injected as well as the storage site capacity are functions of the imposed pressure gradient and aquifer permeability. Conversely, the security of CO_2 storage with respect to leakage and the long term capacity of the aquifer are functions of fluid trapping mechanisms.

The aquifer storage model developed here can be applied to any aquifer; however, the capacity of that aquifer to accept CO_2 may be less than implied by the model should the aquifer not meet certain technical constraints, such as caprock integrity or continuity. Figure 4.2 shows the reserve-resource pyramid developed by the Carbon Sequestration Leadership Forum (CSLF) [15], where the available storage capacity decreases as constraints are applied to the physical storage capacity of the geological system (i.e. theoretical capacity). Following this nomenclature, the model developed here is a tool that can be used to estimate the practical, or economic, capacity of a system [15].
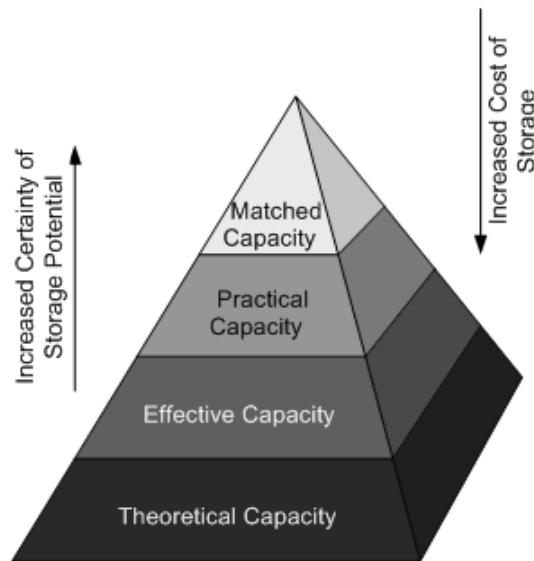
Figure 4.2. The resource-reserve pyramid for geological storage of CO_2 developed by the CSLF [15].

4.2   Aquifer Storage Performance Model

The model of the aquifer storage process presented here can be separated into two parts: a performance model, and a cost model. As shown in Figure 4.3, the performance model takes inputs that describe reservoir and brine properties, the development of the storage field, and the time horizon of interest. From these inputs the model estimates the number

of wells required to achieve the desired injection over the planning horizon, the required

wellhead pressure to achieve this rate, and the additional compression energy required (if

any) to meet this wellhead pressure.
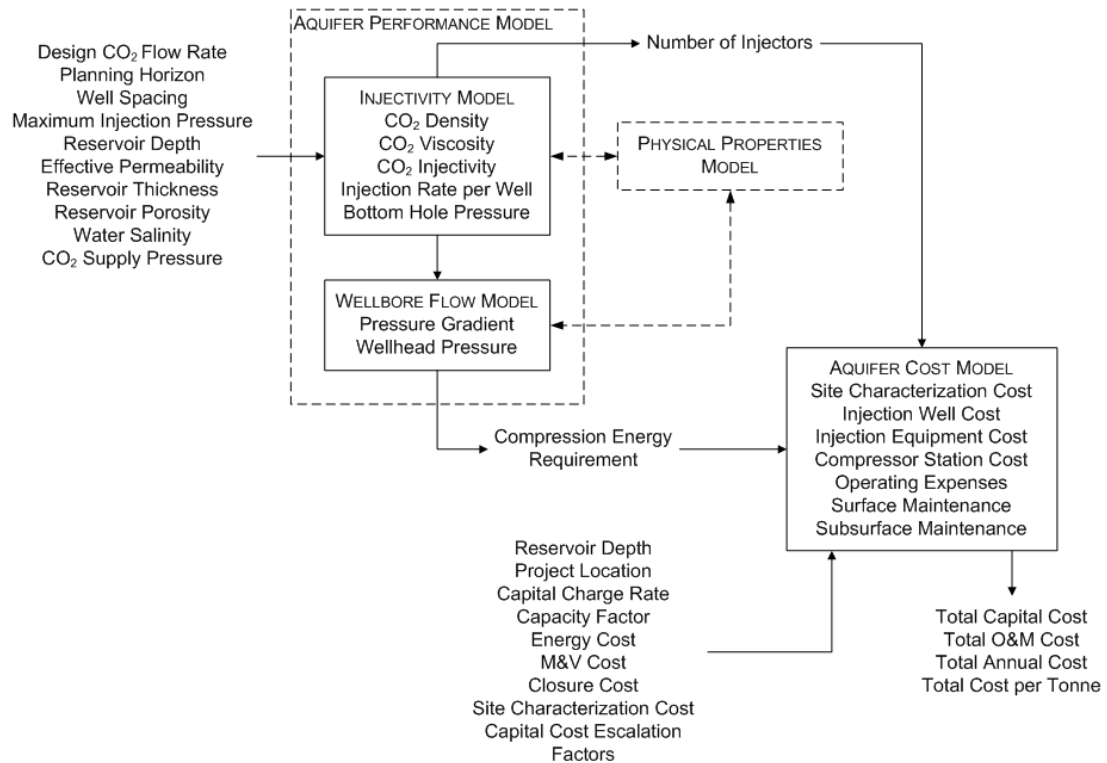
Figure 4.3. Schematic of the Aquifer storage engineering-economic model parameters.

In Sections 4.2.1 to 4.2.4 the approximate solution to injectivity for a doublet system is

developed, extended to a multi-well system, and sensitivity of the multi-well system to

boundary conditions is examined. This analysis is followed by development of a wellbore

flow model for CO_2 (Section 4.2.5), treatment of reservoir heterogeneity (Section 4.2.6),

generation of a generic multi-well geometry (Section 4.2.7), and concludes with

illustrative results (Section 4.2.8).

4.2.1   Approximate Solution to Injectivity of a Doublet System

Injection of millions of tonnes per year of CO_2 into an aquifer will require multiple

injection wells in many cases. For example, the developers of the Australian Gorgon

project (which is summarized in Table 1.3) estimate that seven injection wells will be

required to handle a cumulative injection rate of more than 3 million metric tonnes (Mt)

per year CO_2 [16]. A scenario with multiple injection wells (i.e. injectors) is more

complex than a similar scenario with only one injector because the pressure field

generated by any well will interact with the pressure field of every other injector. Thus,

the interactions between multiple injection wells injecting CO_2 into the same confined

aquifer must be considered when estimating the injectivity of the injection well system.

Injectivity, *I*, is the injection rate of fluid normalized to the difference between the

bottom-hole injection pressure (BHIP) and a reference pressure—usually the initial

aquifer pressure. The behavior of a multi-well system can be derived from the behavior

of a two-well system, referred to as a doublet [17].

For a single injection well, the governing equation is given as Equation 4.1, written in

terms of radial coordinates and pressure (as opposed to fluid head) [14]:

$$\frac{\partial^2 p}{\partial r^2} + \frac{1}{r}\frac{\partial p}{\partial r} = \frac{c\mu}{k_{h,eff}\, b}\frac{\partial p}{\partial t} \tag{4.1}$$

where, *p* refers to pressure (Pa), *r* refers to radial distance from the injection well (m), *c* is

compressibility of the rock-fluid system $(1/\text{Pa})^1$, μ is viscosity (Pa·s), $k_{h,eff}$ is effective

---

[1] Note that this compressibility, *c*, is different from the unitless compressibility factor, *z*. In this context, *c*
equals $1/v \cdot \partial v / \partial p$, where v is specific volume.

permeability in the horizontal direction (m^2), b is thickness of the aquifer (m), and t is

time (s).

For a confined homogeneous aquifer—an aquifer confined between two aquitards (i.e.,

formations that do not permit flow of water) with spatially invariant permeability—

Equation 4.1 was solved by Thies (see, for example [14]) to give:

$$p(X,t) - p_i = \frac{q\mu}{4\pi k_{h,eff} b} W(u) \tag{4.2}$$

where $W(u)$ is the well function evaluated at u for a confined aquifer and $p(X, t)$ is the

pressure at time t, and point $X(x,y)$. The well function is the exponential integral, and is

tabulated in many textbooks (e.g., [14], [13]) or can be calculated from the evaluation of

a power series expansion [18]. The variable u is defined in Equation 4.3, where r refers to

the distance between X and the injector:

$$u = \frac{r^2 c \mu}{4 k_{h,eff} t} \tag{4.3}$$

Using Equation 4.2 the pressure at any point in the system can be estimated as a function

of time. Moreover, the applicability of Equation 4.2 can be expanded to a multi-well

system by writing:

$$\frac{4\pi k_{h,eff} b}{\mu} [p(X,t) - p_i] = \sum_{i=1}^{n} q_i W(u_i) \tag{4.4}$$

where the right hand side of Equation 4.4 is the superposition of the well effects from n

wells on the pressure at point X.

However, for the purpose of the performance model, the steady state solution for

injection rates as a function of system geometry, well pressure, and reservoir pressure is

desirable. To arrive at a steady state solution for Equation 4.1, terms from the power

series expansion for $W(u)$ can be used. The first few terms from the expansion are [19]:

$$W(u) = -0.5772 - \ln u + u - \frac{1}{4}u^2 + \frac{1}{18}u^3 - \frac{1}{96}u^4 + \frac{1}{600}u^5 + ... \quad (4.5)$$

The values of the well function corresponding to the truncated power series using the first

two (i.e., -0.5772-ln u) to six terms is given in Figure 4.4.

Given typical ranges for permeability (10^{-14} to 10^{-16} m^2), compressibility (10^{-9} to 10^{-10} Pa^{-1}), and viscosity (10^{-3} to 10^{-5} cP), the values for u of practical interest for the CO_2

injection problem (i.e., where t is on the order of years and r on the order of kilometers)

will usually be less than 0.1. Only at very large distances and short times will the values

of u be on the order of 1. Thus, use of only the first two terms of the power series

expansion are adequate for this analysis and will result in a steady state solution for the

incompressible system on a finite but expanding spatial domain, as described by

Nordbotten et al. [20] (for an analogous problem).
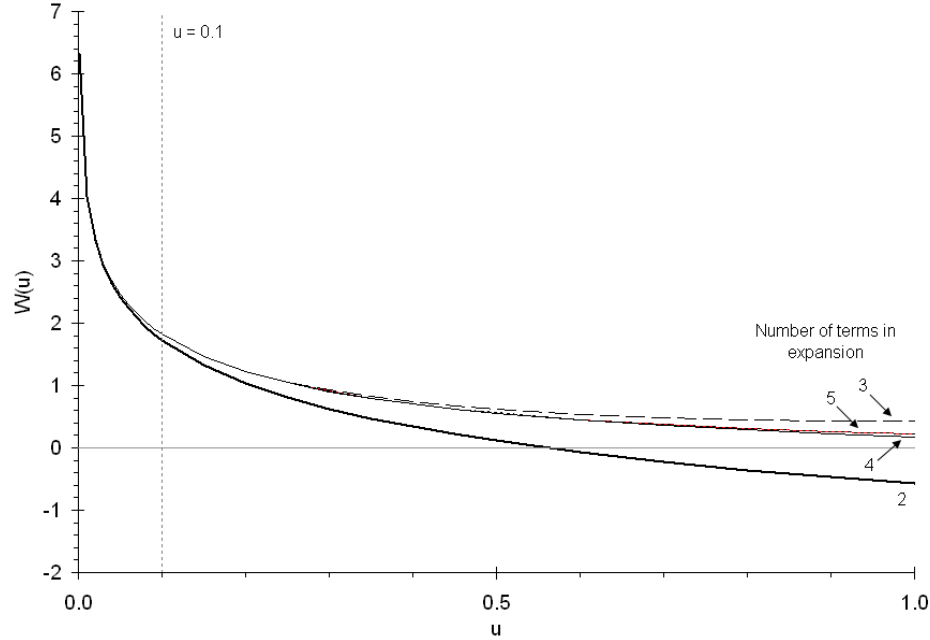
Figure 4.4. Values of the well function, *W(u)*, corresponding to different numbers of terms used in the power series expansion.

Using this approximation in Equation 4.4 for a two well system (*n* = 2) results in:

$$\frac{4\pi k_{h,eff} b}{\mu}[p(X,t) - p_i] = q_1\left[-0.5772 - \ln\left(\frac{r_{X,1}^2 c\mu}{4k_{h,eff}t}\right)\right] + q_2\left[-0.5772 - \ln\left(\frac{r_{X,2}^2 c\mu}{4k_{h,eff}t}\right)\right]$$

To arrive at a steady state solution for this equation, one well must be an injector and the other must be a producer, and the flow rates in the two wells must be equal. This generic type of two well system is referred to as a doublet system [17]. With these conditions met, the equation for the system can be reduced to:

$$\frac{4\pi k_{h,eff} b}{q\mu}[p(X,t) - p_i] = \ln\left(\frac{r_{X,2}^2}{r_{X,1}^2}\right) = \ln(K) \qquad (4.6)$$

Thus, Equation 4.6 is the steady state solution for the pressure at any point *X* in the doublet system. The logarithmic term on the right hand side is a constant, *K*, and thus the locus of points where *p* = *p(X, t)* form circles of constant pressure [17].

4.2.2   Extending the Doublet Solution to a Two Injector System

The solution presented in Equation 4.6 is only for a doublet system—one producer and one injector—not a system of multiple injectors. To arrive at a solution for a system with multiple wells where the pressure is defined as a constant at a given radius, several additional steps must be taken. These steps are summarized following the approach taken by Brigham [17].

The first step in the solution is to define the relationship for a single well near a constant pressure boundary, shown in Figure 4.5.
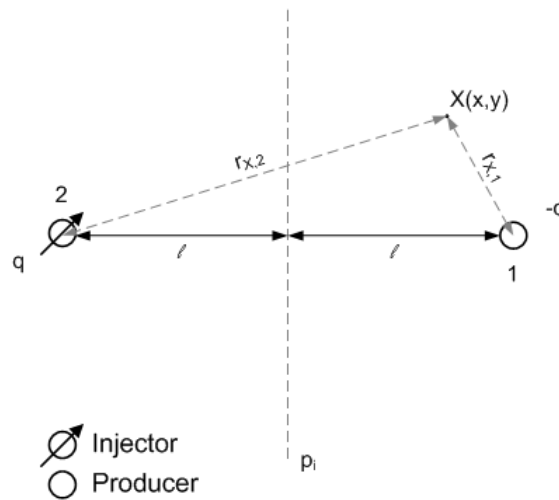
Figure 4.5. The doublet system used to derive the pressure-flow relationship for pressure at an injection or production well near a constant pressure boundary, where $p = p_e$, modified from Brigham [17].

Writing the equations in terms of the pressure at well 1, the distance from well 1 to X is r_w (i.e., the radius of the wells) while the distance from well 2 to X is $2l$ (assuming that $l \gg r_w$). Thus, the equation for well 1 (or well 2, if signs are flipped) is:

$$\frac{4\pi k_{h,eff} b}{q\mu}\left(p_{wb,1} - p_i\right) = \ln\left(\frac{r_w}{2l}\right)^2 \tag{4.7}$$

Equation 4.7 does not contain any reference to parameters at well 2 and, in fact, well 2 serves only as an "image" well and need not exist in the system [13]. Equation 4.7 forms the basis for the second step in the multi-well solution, which is the equation for the pressure of a well off-center in a constant-pressure circle. The geometry of this system is shown in Figure 4.6.
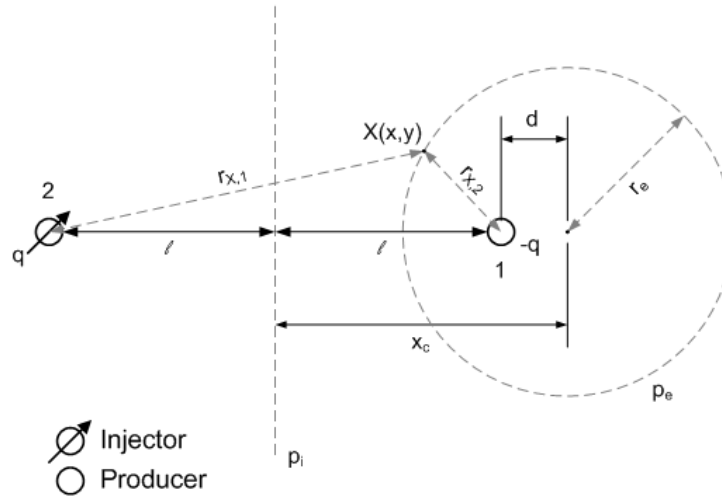
Figure 4.6. The doublet system used to define the pressure-flow relationship for a well located d units off center in the constant pressure circle defined by r_e, modified from Brigham [17].

To derive the equation for pressure at well 1 in terms of the pressure at r_e, the difference in pressure between the constant pressure circle (at p_e) and the constant pressure line (at p_i) must be derived. This result is then subtracted from the equation for the difference in pressure between the well and the constant pressure line (Equation 4.7).

Chapter 4: Modeling CO$_2$ Storage in Saline Aquifers

The solution for the pressure difference between any point on the constant pressure circle and the constant pressure line is in the form of Equation 4.6:

$$\frac{2\pi k_{h,eff} b}{q\mu}\left(p_e - p_i\right) = \ln\left(\sqrt{K}\right) \qquad (4.8)$$

Subtracting the equation for the constant pressure line (Equation 4.7) from Equation 4.8 and simplifying, we arrive at:

$$\frac{2\pi k_{h,eff} b}{q\mu}\left(p_e - p_{wb,1}\right) = \ln\left(\frac{2l\sqrt{K}}{r_w}\right) \qquad (4.9)$$

K must be eliminated from the above equation by writing the equation of the constant pressure circle of Figure 4.6 in terms of l and K. As defined in Equation 4.6, K can be written as the ratio of the square distances between point X (on the constant pressure circle) and the two wells:

$$K = \frac{(l-x)^2 + y^2}{(l+x)^2 + y^2}$$

This can then be manipulated to give the equation for the circle with radius r_e:

$$\left[x - \frac{l(1+K)}{(1-K)}\right]^2 + y^2 = \frac{4l^2 K}{(1-K)^2}$$

Therefore, the radius of the circle is:

$$r_e = \frac{2l\sqrt{K}}{1-K}$$

Writing d in terms of l and K, we get:

$$d = \frac{2lK}{1-K}$$

Taking the ratio of of r_e and d we can solve for K:

$$K = \frac{d^2}{r_e^2}$$

and, from the previous three equations:

$$\sqrt{K} = \frac{r_e}{2l}\left(1 - \frac{d^2}{r_e^2}\right)$$

Therefore, the equation for a well producing (or injecting, with a change of sign) off-center in a constant pressure circle is:

$$\frac{2\pi k_{h,eff} b}{q\mu}\left(p_e - p_{wb,1}\right) = \ln\left[\frac{r_e}{r_w}\left(1 - \frac{d^2}{r_e^2}\right)\right] \tag{4.10}$$

If $d = 0$, Equation 4.10 reduces to the commonly applied equation for a well on center in a constant pressure circle [13, 21]. This on-center equation can also be derived from the integration of the radial form of Darcy's law. A number of studies have used the on-center solution (Equation 4.10) to estimate aquifer injectivity in CO_2 storage [8, 9, 11, 22], and this solution will be used in the following sections as a comparison to the multi-well solution derived here.

The final step involves the extension of the single well off-center result to a multi-well system injecting into a constant pressure circle. This requires the estimation of the pressure effect of one well in the constant pressure circle on another. The geometry of the system is defined in Figure 4.7.
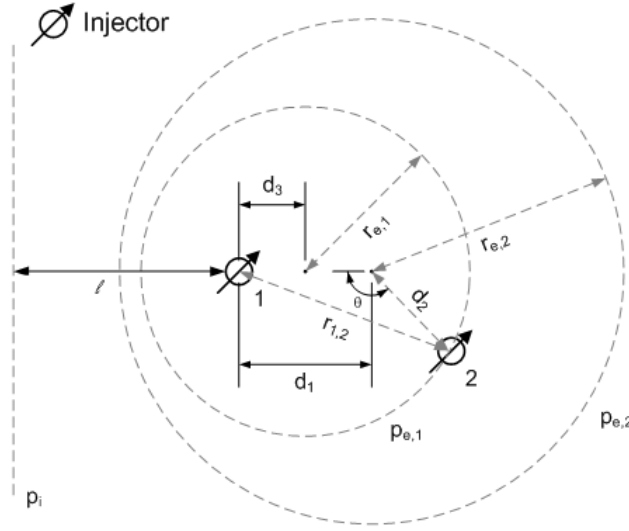
Figure 4.7. The geometry of the system used to develop the relationship pressure-flow relationship for multiple wells injecting into a constant pressure circle, modified from Brigham [17].

The equation for the effect of one well on another (i.e., well 2 on well 1) injecting in a constant pressure circle is derived by writing the pressure drop between the two constant pressure circles defined by $r_{e,1}$ and $r_{e,2}$, via two different approaches and solving for the logarithmic terms. From the geometry of the system in Figure 4.7 it is clear that well 2 can be anywhere on the circle defined by $r_{e,1}$.

The first two equations are for well 1, off center by d_3 in the circle formed by $r_{e,1}$ and off center by d_1 in the circle formed by $r_{e,2}$. These equations are written using the off-center result presented in Equation 4.10 (note that the sign of the left hand side has been flipped because well 1 is an injector):

$$\frac{2\pi k_{h,eff} b}{q\mu}\left(p_{wb,1} - p_{e,1}\right) = \ln\left[\frac{r_{e,1}}{r_w}\left(1 - \frac{d_3^2}{r_{e,1}^2}\right)\right]$$

$$\frac{2\pi k_{h,eff}b}{q\mu}\left(p_{wb,1}-p_{e,2}\right)=\ln\left[\frac{r_{e,2}}{r_w}\left(1-\frac{d_1^2}{r_{e,2}^2}\right)\right]$$

The result of subtracting the second equation from the first is:

$$\frac{2\pi k_{h,eff}b}{q\mu}\left(p_{e,2}-p_{e,1}\right)=\ln\left[\frac{r_{e,2}\left(r_{e,1}^2-d_3^2\right)}{r_{e,1}\left(r_{e,2}^2-d_1^2\right)}\right] \tag{4.11}$$

The second set of equations is for the pressure difference between the line of constant pressure at the center of the system and each of the circles (Equation 4.8), as:

$$\frac{2\pi k_{h,eff}b}{q\mu}\left(p_{e,1}-p_i\right)=\ln\left(\frac{r_{e,1}}{d_3}\right)$$

$$\frac{2\pi k_{h,eff}b}{q\mu}\left(p_{e,2}-p_i\right)=\ln\left(\frac{r_{e,2}}{d_1}\right)$$

Subtracting the second equation from the first results in a statement of the pressure effect of well 2 on well 1 (or vice versa):

$$\frac{2\pi k_{h,eff}b}{q\mu}\left(p_{e,1}-p_{e,2}\right)=\ln\left(\frac{r_{e,1}}{d_3}\frac{d_1}{r_{e,2}}\right) \tag{4.12}$$

Since neither $r_{e,1}$ or d_3 should appear in the solution, we would like to eliminate these terms from Equation 4.12. The left hand side of Equations 4.11 and 4.12 are equal, thus we can set the logarithmic terms equal, and isolate the ratio of $r_{e,1}$ to d_3:

$$\left(\frac{r_{e,1}}{d_3}\right)^2=\frac{r_{e,2}+d_3 d_1-d_1^2}{d_3 d_1}$$

The ratio $r_{e,1}$ to d_3 can also be written from the system geometry using the cosine law:

$$\left(\frac{r_{e,1}}{d_3}\right)^2 = \frac{d_1 d_2^2 + d_1(d_1 - d_3)^2 - (d_1 - d_3)(d_2^2 + d_1^2 - r_{1,2}^2)}{d_1 d_3^2}$$

Setting the two previous equations equal, solving for $d_1 d_2$, and back substituting results

in:

$$\left(\frac{r_{e,1}}{d_3}\right)^2 = \frac{d_2^2 d_1^2 + r_{e,2}^2\left(r_{e,2}^2 - d_2^2 - d_1^2 + r_{1,2}^2\right)}{r_{1,2}^2 d_1^2}$$

Substituting this relationship back into Equation 4.12, where the logarithmic terms are

squared and the logarithm is multiplied by ½ yields:

$$\frac{2\pi k_{h,eff} b}{q\mu}\left(p_{e,1} - p_{e,2}\right) = \frac{1}{2}\ln\left[\frac{d_2^2 d_1^2 + r_{e,2}^2\left(r_{e,2}^2 - d_2^2 - d_1^2 + r_{1,2}^2\right)}{r_{1,2}^2 r_{e,2}^2}\right] \quad (4.13)$$

This is final expression for the effect of well 2 on well 1 (or vice versa). Thus, for well 1

the sum of the effects of injecting off-center into a constant pressure circle and of well 2

on well 1 is:

$$\frac{2\pi k_{h,eff} b}{\mu}\left(p_{wb,1} - p_e\right) = q_1 \ln\left[\frac{r_e}{r_w}\left(1 - \frac{d_1^2}{r_e^2}\right)\right] + \frac{q_2}{2}\ln\left[\frac{d_2^2 d_1^2 + r_e^2\left(r_e^2 - d_2^2 - d_1^2 + r_{1,2}^2\right)}{r_{1,2}^2 r_e^2}\right] \quad (4.14)$$

Similarly for well 2, the above equation can be written:

$$\frac{2\pi k_{h,eff} b}{\mu}\left(p_{wb,2} - p_e\right) = q_2 \ln\left[\frac{r_e}{r_w}\left(1 - \frac{d_2^2}{r_e^2}\right)\right] + \frac{q_1}{2}\ln\left[\frac{d_2^2 d_1^2 + r_e^2\left(r_e^2 - d_2^2 - d_1^2 + r_{1,2}^2\right)}{r_{1,2}^2 r_e^2}\right] \quad (4.15)$$

where, in both of the above equations, $r_{e,i}$ and $p_{e,i}$ have been replaced with r_e and p_e,

respectively.

4.2.3   A General Multi-Well Model

Equations 4.14 and 4.15 form a linear system that allows the BHIP to be related to the system geometry, aquifer properties, and injection rates for the two-well example. This linear system can be extended to a generic system of n wells by writing the equation $\overline{A} \cdot \vec{x} = \vec{b}$, where:

$$\overline{A} = \begin{bmatrix} \alpha_1 & \beta_{1,2} & \cdots & \beta_{1,n} \\ \beta_{2,1} & \alpha_2 & \cdots & \beta_{2,n} \\ \vdots & \vdots & & \vdots \\ \beta_{n,1} & \beta_{n,2} & \cdots & \alpha_n \end{bmatrix} \tag{4.16}$$

$$\vec{x} = \begin{bmatrix} q_1 \\ q_2 \\ \vdots \\ q_n \end{bmatrix} \tag{4.17}$$

$$\vec{b} = \begin{bmatrix} \dfrac{2\pi kb}{\mu}\left(p_{wb,1} - p_e\right) \\ \dfrac{2\pi kb}{\mu}\left(p_{wb,2} - p_e\right) \\ \vdots \\ \dfrac{2\pi kb}{\mu}\left(p_{wb,n} - p_e\right) \end{bmatrix} \tag{4.18}$$

In equation 4.16, α_n is the off-center logarithm term written for well n (i.e. the term multiplied by q_1 in Equation 4.14 is α_1) and $\beta_{n,k}$ is the pressure effect of well k on well n (i.e., the term multiplied by q_2 in Equation 4.14 is $\beta_{1,2}$). It is clear from the two well system that $\beta_{n,k}$ is equal to $\beta_{k,n}$. Therefore, for a specified geometry, BHIP for each of n-wells, and aquifer properties, the injection rate for each of n-wells can be calculated by inversion of $\overline{A}$ followed by multiplication by $\vec{b}$ or a number of alternative methods, such as Gauss-Jordan elimination or LU-factorization with substitution [18].

The injectivity of the linear system as a function of the number of wells and system geometry can be generalized to any set of aquifer properties by using the dimensionless injectivity, i_d. For well n, the dimensionless injectivity is defined as [23]:

$$i_{d,n} = \frac{q_n \mu}{2\pi k_{h,eff} b (p_{wb,n} - p_e)}$$ (4.19)

If it is assumed that the BHIP, $p_{wb,n}$, at each injection well is equal—which appears to be the configuration that maximizes the sum of the $i_{d,n}$ for the n-well system—the dimensionless injectivity for each well can easily be calculated by setting each element of $\bar{b}$ (Equation 4.18) to 1 and solving for $\bar{x}$ (Equation 4.17), which now contains $i_{d,n}$. Figure 4.8 shows the average, minimum, and maximum dimensionless well injectivity in systems with 1 to 100 wells with 40-acre well spacing.
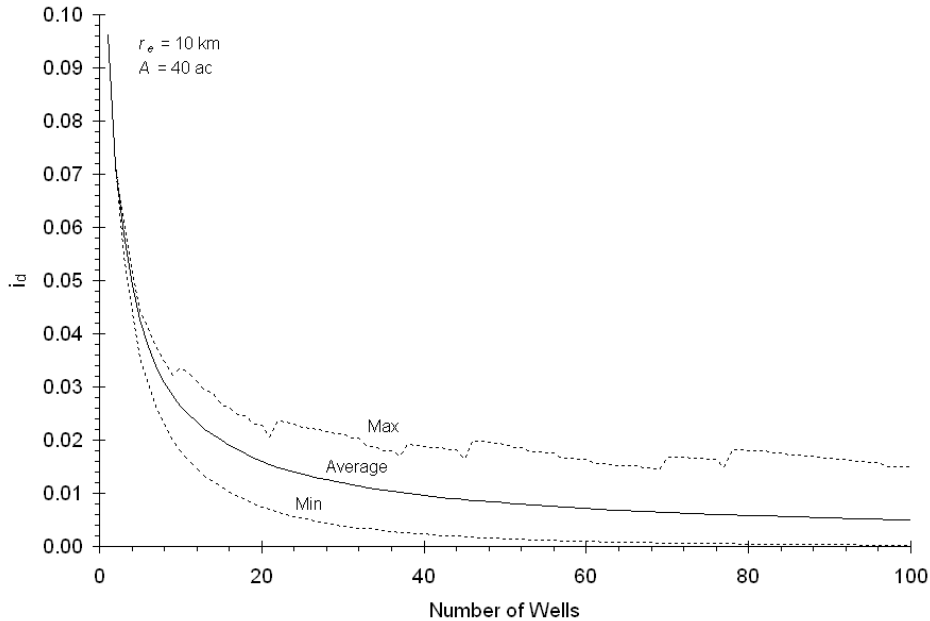
Figure 4.8. The average, minimum, and maximum injectivity for systems with 1 to 100 wells on 40 acre spacing, and a constant pressure radius where $p_e = p_i$ at 10 km.

This figure clearly shows that the addition of wells to the system decreases the average, minimum, and maximum well injectivity in the system. The well with the minimum injectivity is always the well at the center of the system, while the well with the maximum is always on the perimeter of the system. The decrease in the average injectivity of individual wells with the addition of more wells (Figure 4.8) means that the there are diminishing returns from adding wells to a system. Figure 4.9 shows the total (cumulative) injectivity of systems with 1 to 100 wells for three different well spacings.
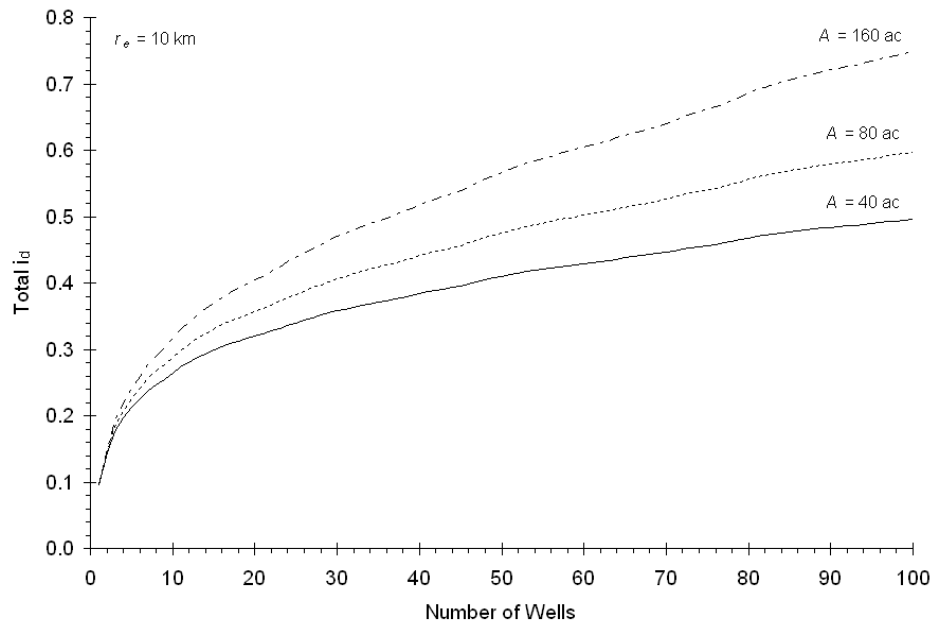
Figure 4.9. The total injectivity for systems with 1 to 100 wells on 40, 80, and 160 acre spacing with a constant pressure radius where $p_e = p_i$ at 10 km

The results shown in both Figure 4.8 and Figure 4.9 are based on a constant pressure radius, r_e, of 10 km. The selection of an appropriate value for r_e and the sensitivity of the injectivity to r_e are discussed in the following section.

4.2.4   Injectivity and Sensitivity to Boundary Conditions

Describing the behavior of a well injecting to a constant pressure circle containing other

injectors requires that the pressure (p_e) at radius (r_e) is known, as shown in Equation 4.14.

Typically, the pressure, p_e, is assumed to be the initial reservoir pressure, p_i, prior to

injection, in which case r_e is referred to as the drainage radius of the system. However,

this radius will increase with time [20] and the transient behavior of the system cannot be

derived from the steady-state solution presented in Section 4.2.1. Thus, Equation 4.4

must be solved numerically to arrive at a solution. A five-well system shown in Figure

4.10 is used to illustrate the numerical solution.
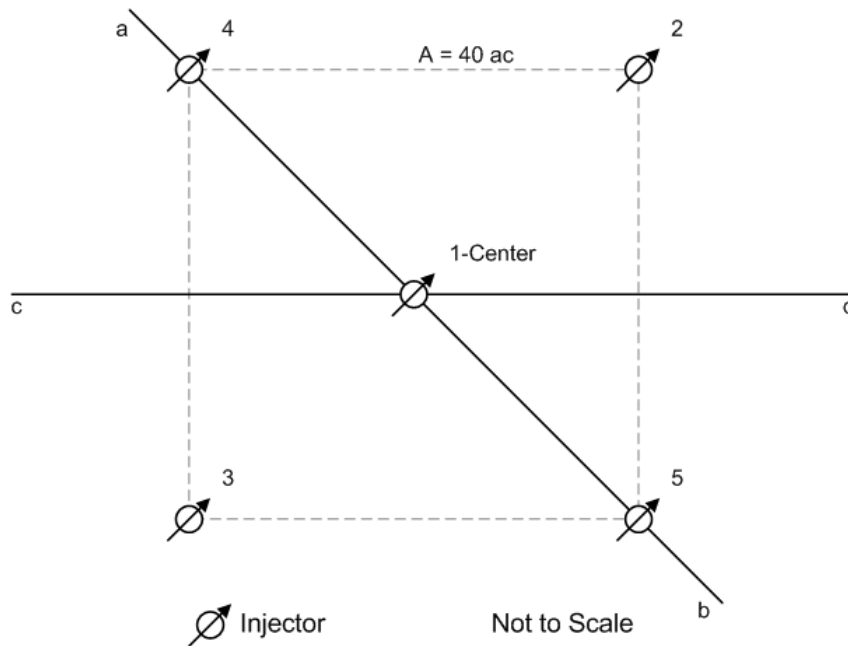
Figure 4.10. An illustrative 40-acre, 5-well injection pattern used to calculate the change
in pressure field with time.

The resulting pressure distribution is shown in Figure 4.11 for cuts a-b, and Figure 4.12

for cut c-d based on injection of 1 million tonnes of CO_2 per year. The aquifer parameters

are representative of a medium-permeability aquifer (k_h = 50 md), at a depth of

approximately 1000 m.
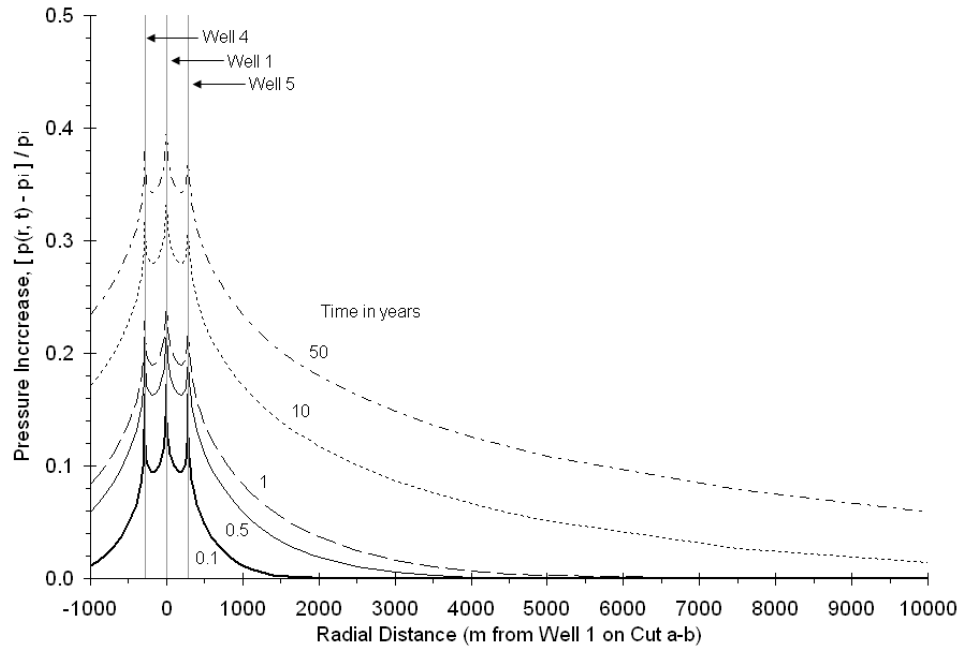
Figure 4.11. Pressure distribution in a confined aquifer for an illustrative set of parameters along cut a-b (shown in Figure 4.10) at times ranging from 0.1 years (i.e., 30 days) to 50 years.
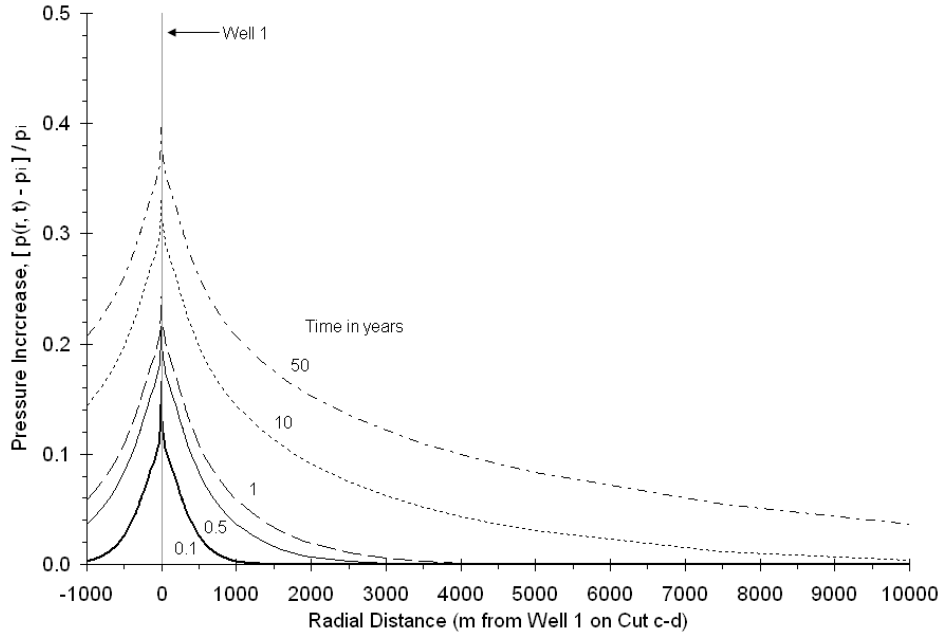
Figure 4.12. Pressure distribution in a confined aquifer for an illustrative set of parameters along cut c-d (shown in Figure 1.5) at times ranging from 0.1 years (i.e., 30 days) to 50 years.

Figure 4.11 and Figure 4.12 both show that over time the pressure at any given radius in the system increases over time for a case with a fixed injection rate. Note that over time the BHIP required to maintain the fixed injection rate increases. In this example, at 0.1 years (i.e., 30 days) the aquifer pressure is equal to the initial pressure at a radial distance of approximately 1,000 m (1 km). As time passes, the pressure transient moves further outwards, and the radial distance at which the current pressure equals the initial pressure increases.

The rate at which the pressure transient moves outwards will vary from system to system but the general behavior of every system will be the same, i.e., the pressure transient will move radially away from the well(s) over time. Nordbotten et al. [20] have shown that the rate at which the pressure transient moves outwards is proportional to the square root of time. Following Nordbotten et al. [20], the definition of *u* (Equation 4.3) can be

rearranged to calculate the radius at which the pressure is approximately equal to the initial pressure:

$$r_e = \sqrt{t\left(\frac{4k_{h,eff}u_c}{c\mu}\right)} \qquad (4.20)$$

where u_c is the cut-off value of u chosen such that the value of $W(u)$ is acceptably close to zero. If a truncated power series expansion with an even number of terms is used to approximate $W(u)$, as done here, the value for u_c at which $W(u) = 0$ can be calculated (see Figure 4.4). For the two-term expansion, this value of u_c is 0.5615. Thus, for a specified set of aquifer parameters the value of r_e can be calculated, as illustrated in Figure 4.13.
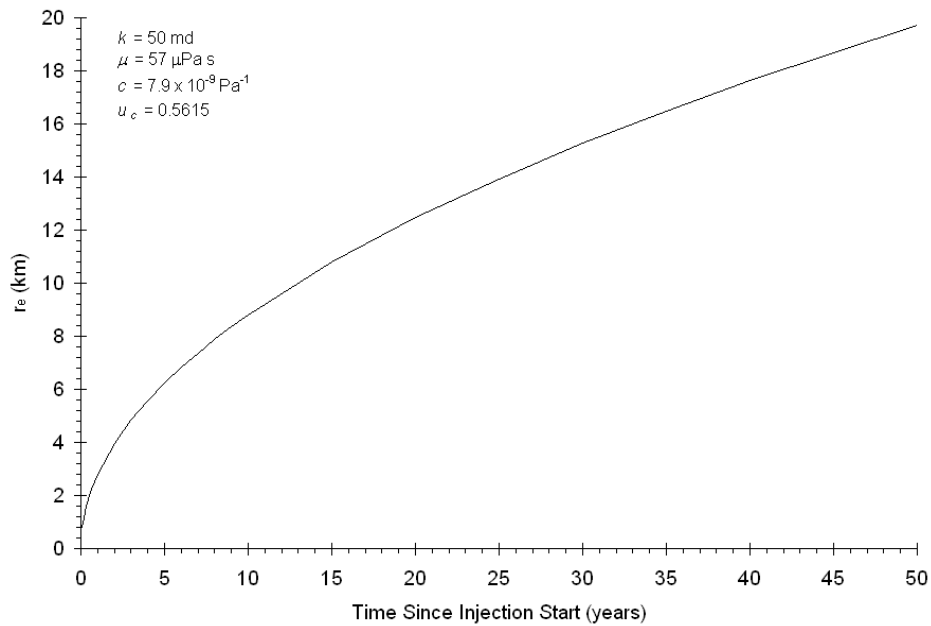
Figure 4.13. The radius at which $p = p_i$ for the example system above calculated using Equation 4.20

Based on these results, if the solution for injectivity were desired for a time of approximately 10 years, the appropriate value of r_e (where $p = p_i$) would be approximately 10 km. While these results suggest the magnitude of r_e, its exact value will

depend on parameter values for the aquifer of interest. Thus, it is of interest to determine whether a general result for r_e will suffice by examining the sensitivity of the simplified system (Equation 4.14) to r_e.

The sensitivity of $i_{d,n}$ is its derivative with respect to r_e, which is solved for via:

$$\vec{x}' = \overline{A}^{-1}\left(-\overline{A}'\vec{x}\right)$$

where $\overline{A}'$ represents $\dfrac{\partial}{\partial r_e}\overline{A}$ and $\vec{x}'$ represents $\dfrac{\partial}{\partial r_e}\vec{x}$.

For a five-well system with geometry corresponding to that show in Figure 4.10, Figure 4.14 shows clearly that the sensitivity of dimensionless injectivity to changes in r_e falls non-linearly with r_e. For example, an increase in r_e from 10 km to 11 km would result in a decrease to the dimensionless injectivity of approximately 2%, whereas the same increase at 20 km would result in an injectivity decrease of less than 1%.
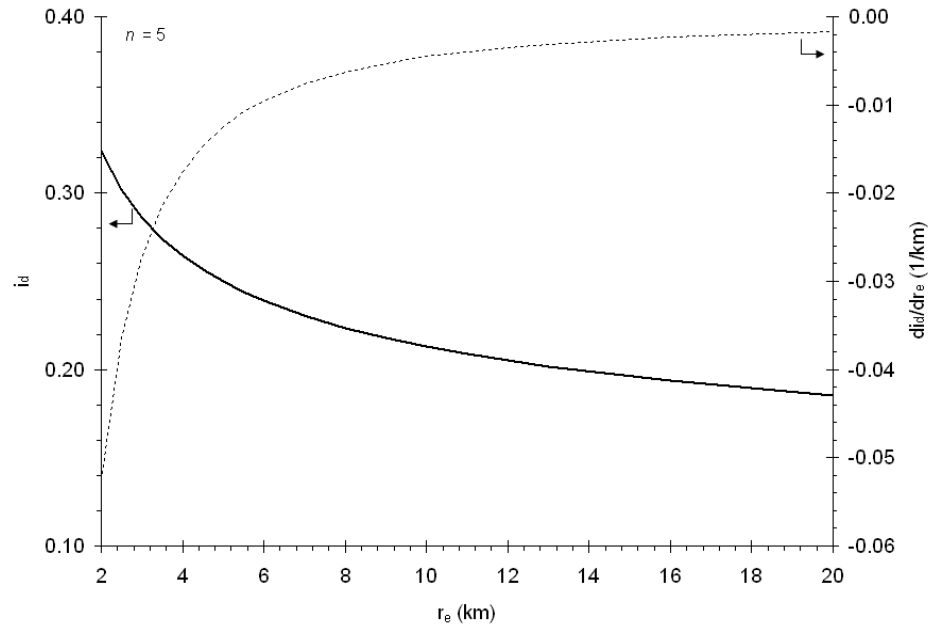
Figure 4.14. Dimensionless injectivity and its derivative with respect to the pressure boundary radius, r_e, for a 40 ac, five-well system of injectors.

Comparing the illustrative results shown in Figure 4.13 and the general results from Figure 4.14 suggest that for a planning horizon of 10 to 20 years in a CO_2 storage project, the appropriate drainage radius is between 10 and 20 km; and, the injectivity calculated with this assumptions will be relatively insensitive to r_e.

4.2.5   Establishing the BHIP—Flow in the Wellbore

Equation 4.14 shows that the injection rates in the system are a function of the wellbore pressure. Thus, knowledge of the BHIP is necessary to estimate the number of wells required for a specified injection rate.

The BHIP will be limited to some fraction of the reservoir fracture pressure, as it would be undesirable to fracture the wellbore environment in a CO_2 storage operation. In the absence of field data, the fracture pressure can be estimated from a correlation presented by Heller and Taber [24]:

$$G_f = \gamma - \beta e^{-\alpha d}$$
$$p_f = G_f d \qquad\qquad (4.21)$$

where, G_f is the fracture gradient (Pa/m); α, β and γ are coefficients with the values 4.36 $\times 10^{-4}$ m^{-1}, 9.24 kPa/m, and 22.62 kPa/m, respectively; and, p_f is the fracture pressure at depth (Pa).

Once the BHIP is known, the wellhead pressure needed to generate the BHIP can be calculated. The design of CO_2 injection wells for aquifer storage will likely be nearly identical to those designed for EOR, shown in Figure 3.5. Appendix C describes a numerical model that can be used to calculate the pressure gradient in a CO_2 injection well considering pressure changes due to hydrostatic head, friction losses, and heat transfer. However, as in the EOR performance model, the complexity introduced by such a model is undesirable in the context of an aquifer storage performance model. Thus, a response surface model (the same as that used for the EOR performance model) based on the full numerical model described in Appendix C is used to estimate the wellhead pressure in the aquifer storage performance model. The description in this section mirrors that in Section 3.2.2.

The response surface model assumes that the pressure gradient in the wellbore is a linear function of depth and, thus, that the BHIP can be written as:

$$p_{wb} = \frac{\Delta p}{\Delta L} L + p_{wh} \qquad\qquad (4.22)$$

where, p_{wb} is the BHIP pressure, p_{wh} is the wellhead pressure, and L is the wellbore length.

Chapter 4: Modeling CO$_2$ Storage in Saline Aquifers

Because Equation 4.22 can represent only pressure gradients linear with depth, it is valid only for flow rates below approximately 1 Mt CO$_2$ per year per well at temperatures less than 30°C and wellhead pressures greater than 8 MPa for the 3-inch (0.076 m) inside diameter tubing modeled. The form of the regression equation for pressure gradient is:

$$\frac{\Delta p}{\Delta L} = a_1 q^2 + a_2 \log(p_{wh})^2 \tag{4.23}$$

where, p_{wh} is the wellhead pressure (Pa), and q is the volumetric flow rate (m^3/d) at wellhead conditions.

Parameter estimates for the regression coefficients are given in Table 4.1. The complete set of parameters used to generate the dataset upon which the regression is based are listed in Appendix C. The regression model given in Equation 4.23 accounts for a large proportion of the variation in the set of 2895 data points generated by the numerical model, reflected by an adjusted-r^2 value of 0.99.

Table 4.1. Regression coefficient estimates for the pressure drop correlation, Equation 4.23, where standard errors are reported in parentheses.

Coefficient	Value
a_1	-7.008 × 10^{-4} ** (3.100 × 10^{-6})
a_2	1.812 × 10^{2} ** (2.692 × 10^{-1})

** Significant at the 1% level

The regression coefficients in Table 4.1 show that the wellbore pressure gradient is negatively correlated with the volumetric flow rate, and positively correlated with the square of the base-ten logarithm of pressure. In addition, wellhead temperature influences the pressure gradient predicted by Equation 4.23 through its effect on volumetric flow

161

rate. Figure 3.6 shows the pressure gradient predicted by Equation 4.22 using the coefficients listed in Table 4.1.

4.2.6   Describing Reservoir Heterogeneity

Equation 4.4 and the approximate solution for the multi-well system (e.g., for the two-well case, Equations 4.14 and 4.15) were derived for a reservoir with homogeneous permeability. This means that the permeability in the direction of flow--primarily horizontal—is spatially invariant. However, this is rarely the case in a real aquifer. The variation in permeability can be described by the Dykstra-Parsons coefficient, V_{DP}, which is defined as [25]:

$$V_{DP} = \frac{k_{0.5} - k_{0.16}}{k_{0.5}}$$ (4.24)

where $k_{0.5}$ is the median permeability and $k_{0.16}$ is the 16th percentile permeability based on the distribution of measured permeability values. A V_{DP} value of zero corresponds to a homogeneous reservoir and values approaching 1.0 correspond to increasingly heterogeneous reservoirs. Willhite concludes that the value of V_{DP} falls between 0.5 and 0.9 for most oil reservoirs [26].

Because V_{DP} describes the variation in the underlying distribution of permeability, if the mean permeability, k_{avg}, and distribution of permeability measurements are known, a number of reservoirs can be generated that have an equal prior probability of representing the actual aquifer. The definition of V_{DP} (Equation 4.24), however, does not imply any specific permeability distribution for k. Jensen et al. [27] conclude that permeability measurements tend to follow a power-normal distribution [28] and, in practice it is

commonly assumed that permeability measurements are log-normally distributed, which is a limiting case of the power-normal distribution.

The aquifer storage model developed here assumes that permeabilities are drawn from a log-normal distribution and that the aquifer can be represented by a series of horizontal layers, each with uniform permeability, k_i, and thickness, h_i (see Figure 4.15). Thus, given k_{avg}, V_{DP}, the aquifer net thickness (i.e. the thickness that available for fluid flow), b, and the number of layers in the formation, the model will generate the effective permeability, $k_{h,avg}$, that characterizes the aquifer. Figure 4.15 shows the generic layered aquifer generated by the model.
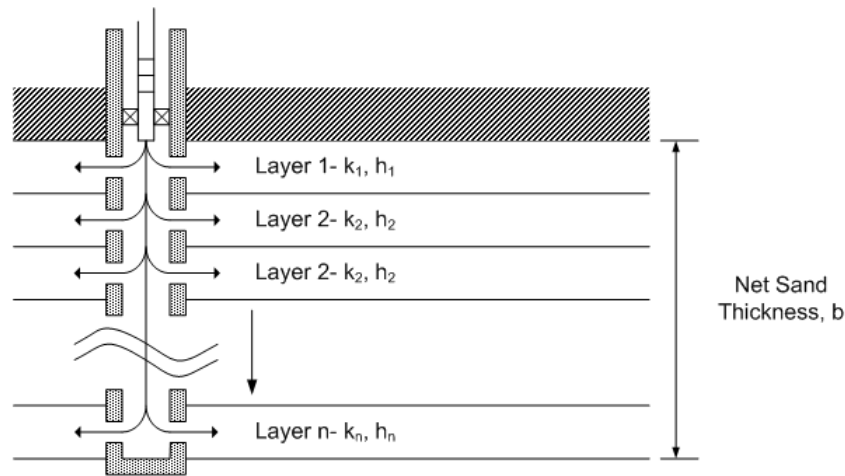
Figure 4.15. Generic layered aquifer model.

The effective permeability characterizing the formation shown in Figure 4.15 is given by [13]:

$$k_{h,eff} = \frac{\sum_{i=1}^{n} k_i h_i}{b} \tag{4.25}$$

where k_i and h_i are the permeability and thickness of layer i, and n is the number of layers in the system.

4.2.7   Generating the System Geometry for Multi-Well Scenarios

When more than two injection wells are required, the arrangement of these wells inside the constant pressure circle must be specified. Unfortunately, Equation 4.14 shows that the positioning of these wells relative to one another and to the drainage radius influences the injectivity of the system. To make the problem of positioning the wells manageable, the model assumes that the wells are located at the vertices of a square lattice. The lengths of the edges in the lattice are a function of the area associated with each injection well, referred to as the pattern spacing. Figure 4.16 shows the typical arrangement of wells in an n-well system.
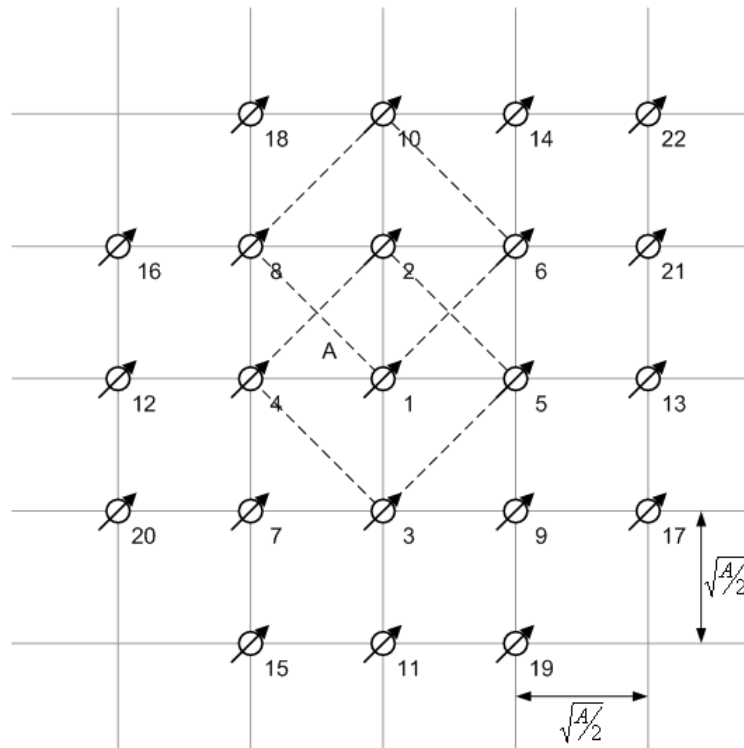
Figure 4.16. The arrangement of wells in an n-well system used by the model

Wells are added to the system at unoccupied lattice points in order of increasing radial distance from the center of the system, thus minimizing the surface area required for an *n*-well system.

4.2.8   *Illustrative Performance Model Results*

Results from the performance model have been generated for four illustrative cases. The Oklahoma North Purdy, Springer A and Alberta Joffre-Viking cases were used in Chapter 3 to illustrate the behavior of the CO_2-flood EOR model. These two oil fields are treated as aquifers with equivalent petrophysical properties for this case study. The Texas South Liberty-Frio and Alberta Lake Wabamun-Manniville cases have been identified as potential targets for large-scale geological sequestration [11, 29-31]. These four aquifers are all sandstone bodies, with depths greater than 1 km and *kh* values (i.e. the product of permeability and net sand thickness) from 4,500 to 940,000 md·ft. The performance inputs and other pertinent data have been collected from a number of sources [32-38], and are shown in Table 4.2. The parameters for the Mannville Aquifer were derived from an analysis of the datasets provided by the Alberta Geological Survey as part of their "Test Case for Comparative Modeling of CO_2 Injection, Migration and Possible Leakage—Wabamun Lake Area, Alberta, Canada" [38].

Table 4.2. Key performance model parameters for the four case study reservoirs

Parameter	Northeast Purdy Unit	Joffre Viking Pool	South Liberty	Lake Wabamun Area
Location	Oklahoma	Alberta	Texas	Alberta
Unit	Springer "A" Sandstone	Viking Aquifer	Frio Formation	Mannville Aquifer
Lithology	Sandstone	Sandstone	Sandstone	Sandstone
Well Spacing (acres)	80	80	80	80
CO$_2$ supply pressure (MPa)	10.3	10.3	10.3	10.3
P$_{wb,max}$ (% of p$_{frac}$)	90%	90%	90%	90%
r$_w$ (m)	0.15	0.15	0.15	0.15
Depth (m)	2,499	1,500	1,850	1,514
p$_{res}$ (MPa)	21.0	7.8	15.2	14.4
T$_{res}$ (K)	338	329	329	327
k$_h$ (md)	44	507	944	23
Net Sand (m)	91	30	300	59
ϕ (%)	13.0%	13.0%	27%	11.2%
x$_{brine}$ (ppm$_w$)	100,000	40,000	100,000	68,074
S$_{wc}$	0.20	0.30	0.30	0.66
k$_{rw,c}'$	1.00	1.00	1.00	0.80
k$_{rc,w}'$	1.00	1.00	1.00	0.12
V$_{DP}$	0.82	0.70	0.67	0.92

Each of the cases was evaluated with a project capacity factor (i.e. the percentage of the design capacity actually used on an annual basis) of 100% across a range of injection rates—3 Mt CO$_2$ per year being roughly equivalent to the amount of CO$_2$ captured from a 500 GW coal-fired power plant—with a time horizon of 10 years used to calculate the drainage radius as described in Section 4.2.4. The number of wells required for each of the illustrative cases is shown in Figure 4.17.
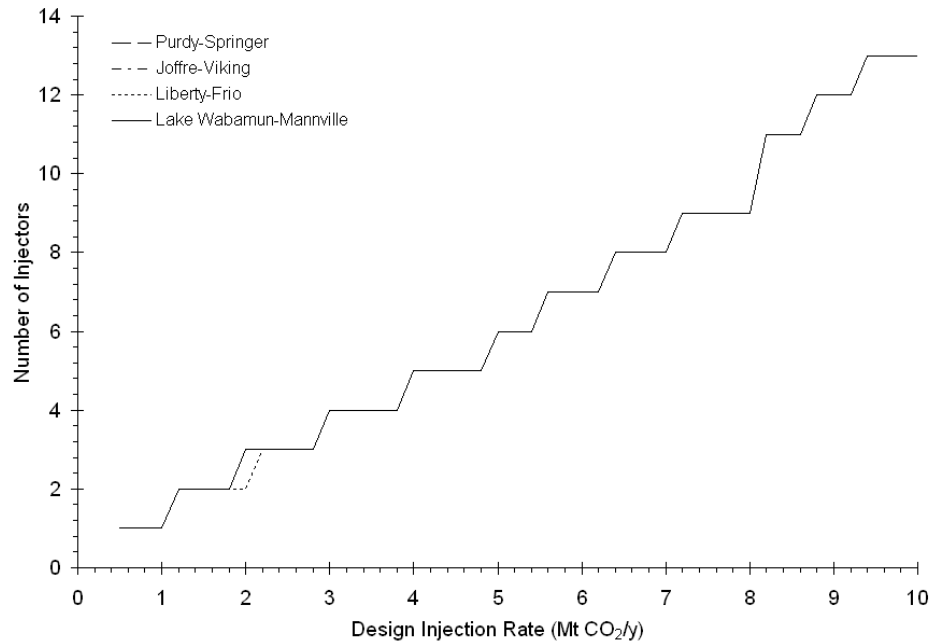
Figure 4.17. Number of wells required for each of the cases described in Table 4.2; note that the same number of wells is required across almost the entire range of injection rates for all four cases.

The number of injection wells predicted for each of the cases is the same despite the differing reservoir descriptions across the range of injection rates shown in Figure 4.17. This is not indicative of a broad trend that applies to all aquifers, as other sets of realistic aquifer parameters results in different numbers of wells being required than presented in Figure 4.17. However, at larger injection rates, the number of wells required for each of the sites begins to diverge. For example, for over 11 Mt CO_2 per year—comparable to the emissions from 2500 GW of pulverized coal capacity—the Lake Wabamun-Mannville site requires more injection wells than the other three sites. Nonlinearities in the number of injection wells are difficult to discern because of the 1 Mt CO_2 per year per well limit imposed by the wellbore model. Nonetheless, a second-order polynomial is the best fit curve to the data points in Figure 4.17.

The four cases are better differentiated by the required difference between the BHIP, p_{wb}, and initial aquifer pressure, p_i, required to match the specified injection rates, as shown in Figure 4.18. These results clearly show that to obtain the same injection rate, the pressure rise around the wellbore is highest for the Lake Wabamun-Mannville case—the aquifer with the lowest value of *kh*—and lowest for the Liberty-Frio case—the aquifer with the highest *kh*. In addition, the data points clearly show the non-linear interplay of pressure and injection rates in a multi-well system.
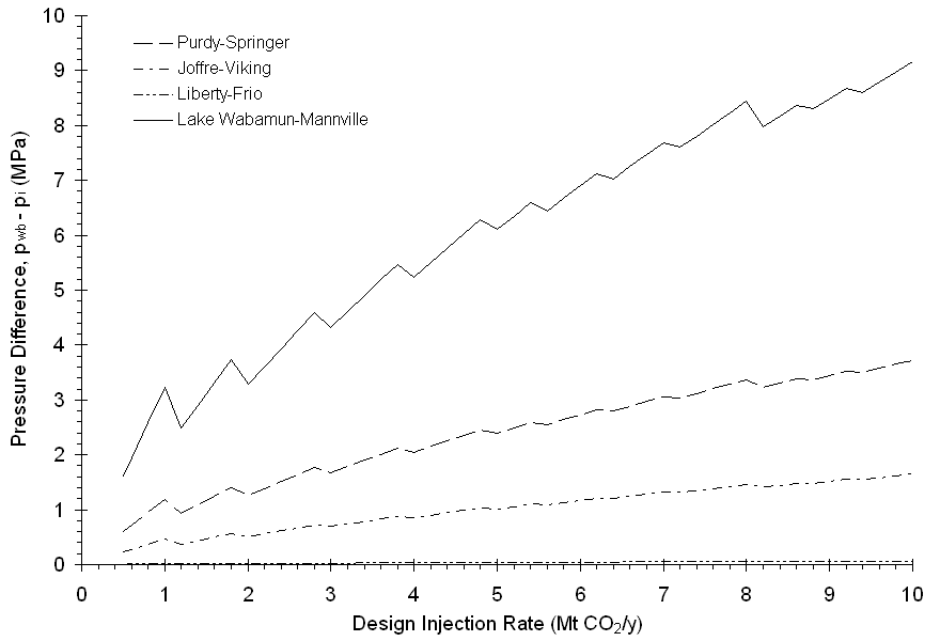
Figure 4.18. The difference between the BHIP, p_{wb}, and the initial aquifer pressure, p_i, for each of the cases across a range of design injection rates.

Figure 4.19 shows the required wellhead pressure estimated by the model for each of the cases across a range of injection rates. The wellhead pressure required by the Joffre-Viking case is lower than the minimum pressure allowable by the wellbore model, thus it is not shown in Figure 4.19. The relative order of the data points for a given flow rate reflect the required BHIP for each of the cases that were shown in the previous figure.

The discontinuous "saw tooth" curves shown in both Figure 4.18 and Figure 4.19 are the result of the model being able to add only integer number of wells. Only a small range of flow rates can be handled by a given number of wells and, within this range, the required BHIP and corresponding wellhead pressure increase with increasing flow rates until the maximum BHIP is reached, at which point the number of wells increases.
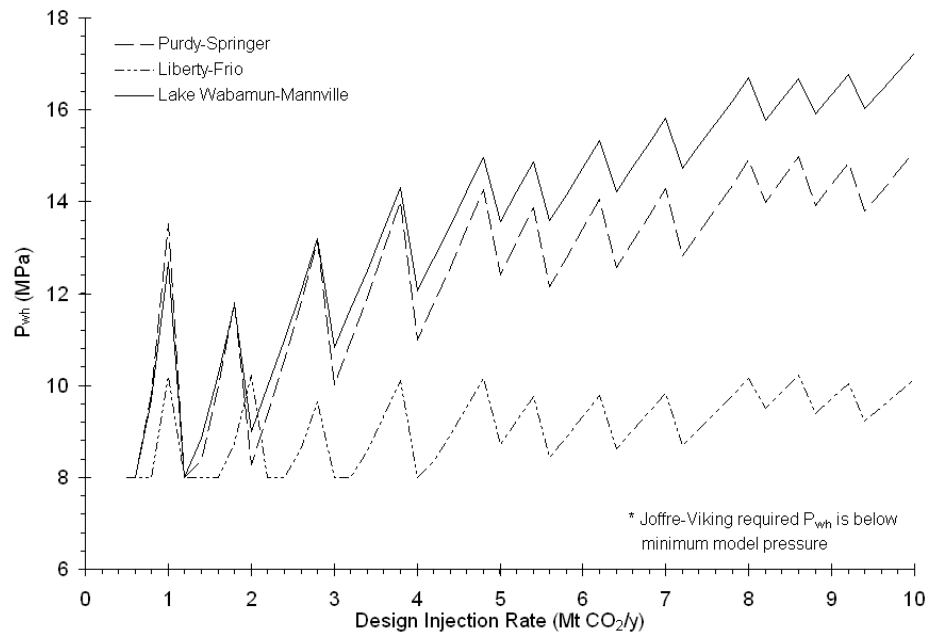
Figure 4.19. Wellhead pressure required to inject the CO_2 as a function of the design injection rate for each of the cases. Note that the wellhead pressure required for the Joffre-Viking case is not shown because it is below the minimum pressure of 8 MPa allowable in the wellbore model.

4.3 Saline Aquifer Storage Cost Model

The capital costs for saline aquifer storage consist of four elements: site characterization costs; project capital costs; operating and maintenance (O&M) cost; and, monitoring, verification, and closure costs.

The capital cost model structure, shown earlier in Figure 4.3, combines results from the performance model with specified cost factors to estimate the total capital cost of an

aquifer storage project reported as a levelized cost in 2004 US dollars per tonne CO$_2$. The capital cost of a storage project include the cost of any additional CO$_2$ compression (where necessary to increase the pressure of CO$_2$ prior to injection), the cost of surface equipment required for each well (e.g. the wellhead, CO$_2$ metering equipment, etc.), and the cost of drilling and completion of injection wells. The capital cost also includes a one-time cost of site characterization. Annual expenses include the costs of normal field operation and maintenance (including periodic well workovers), and compression of CO$_2$ prior to injection. The following sections describe how the costs associated with each of these categories were estimated.

4.3.1   Site Characterization Cost

The cost of site characterization is highly dependent on the requirements of the regulatory regime to which the project is subject. However, given that CO$_2$ should be isolated from the atmosphere for long timescales, it would be prudent to characterize the subsurface over the area which the injected CO$_2$ is likely to spread over a set time horizon to ensure that conduits to the surface, natural or otherwise, do not exist. Thus, the main factor affecting the cost of site characterization will be the area of review. Nordbotten et al. have proposed a method to estimate the aerial extent of plume spread in CO$_2$ storage [39] and, this method, described in Appendix E, is used to estimate the required area of review for a storage project over the specified planning horizon. Tombari suggests the approximate costs associated with characterizing this area to be: $100,000 per square mile (mi^2, $38,610 per km^2) for geophysical characterization (3-D seismic); $3,000,000 to drill and log a well; and an additional 30% of these total costs for data processing,

modeling, and other services [40]. One well would be required for every 25 mi^2 (65 km^2) of the review area [40].

4.3.2 Project Capital Costs—Drilling and Completion

The capital cost of an aquifer storage project can be classified into three main areas: well drilling and completion (D&C); injection equipment costs (e.g., wellhead, flow and control equipment, distribution piping, etc.); and, compression equipment costs. D&C costs are discussed in this section, while injection and compression equipment costs are described in Sections 4.3.3 and 4.3.4, respectively.

D&C costs include the cost of physically drilling an injection well, running casing, hanging tubing, and installing any downhole equipment (e.g., chokes and packers, as shown earlier in Figure 3.5). D&C costs are well documented by the annual Joint Association Survey (JAS) on Well Drilling Costs [41], which lists the average cost of oil and gas wells drilled and completed each year by depth interval and state. A regression model based on these costs was developed by Lewin & Associates [42], and updated to 2004 dollars in this research using the using the EIA Oil and Gas Lease Equipment and Operating Cost index [43]. This is the same regression model used to estimate D&C cost in the EOR model (Section 3.3.3), except that the regions have been aggregated to be consistent with those used in the injection equipment cost model by taking the highest state-level cost as representative of the region. The form of the Lewin & Associates cost model is:

$$C = a_1 e^{a_2 d} \qquad (4.26)$$

where C is cost in 2004 US dollars per well, a_1 and a_2 are regression coefficients and d is the well depth in feet. The value of the regression coefficients (where the a_1 parameter values have been updated to 2004 dollars) are listed by region in Table 4.3.

Table 4.3. Regression coefficients for use in Equation 4.26 for well drilling and completion (D&C) adapted from Lewin and Associates [42] and updated to 2004 US dollars.

Region	States	a_1	a_2
1	West Texas	43986	3.4×10^{-4}
2	South Texas	44041	3.5×10^{-4}
3	South Louisiana	44041	3.5×10^{-4}
4	Mid-Continent Region	42493	3.5×10^{-4}
5	Rocky-Mountain Region	80086	2.7×10^{-4}
6	California	70123	3.2×10^{-4}

The recent increase in oil prices has spurred a large increase in drilling activity. Thus,as with recent increases in injection equipment costs (driven by materials cost increases), D&C costs in years after 2004 can be expected to be considerably higher. D&C costs for future periods can be estimated using the EIA in the Oil and Gas Lease Equipment and Operating Cost [43].

4.3.3   *Project Capital Costs—Injection Well Equipment*

The cost of equipping injection wells for CO_2 for aquifer storage is assumed to be comparable to the cost of equipping wells for water injection. This assumption is consistent with those made by Bock et al. [9] to assess the cost of aquifer storage and by Advanced Resources International for the cost of CO_2-flood EOR [44]. The incremental cost of water injection equipment associated with adding new wells to a producing oil field in West Texas is estimated annually by the EIA for 2,000 ft (610 m), 4,000 ft (1219 m) and 8,000 ft (2438 m) deep wells [43]. A regression equation developed in this

research has the same form as Equation 4.26, with coefficients values described in Table

4.4.

The EIA cost for water injection wells has been extended to other regions by scaling the

West Texas incremental cost using the ratio of primary production equipment cost in the

region of interest to the cost in West Texas. The EIA estimates the cost of primary

production equipment for oil fields located in six regions: West Texas, South Texas,

South Louisiana, the Mid-Continent Region (i.e., Oklahoma, Kansas, Nebraska, Iowa,

Missouri), the Rocky-Mountain Region (i.e., Western New Mexico, Colorado, Wyoming,

Montana), and California [43]. The regression coefficients for the cost (in 2004 US

dollars) of equipping an incremental injection well in each of these regions is presented in

Table 4.4.

Table 4.4. Regression coefficients for use in Equation 4.26 for the incremental cost of equipping an injection well for CO_2 storage in 2004 US dollars.

Region	States	Injection Equipment	
		a_1	a_2
1	West Texas	31226	8.57×10^{-5}
2	South Texas	37040	3.54×10^{-5}
3	South Louisiana	39876	3.45×10^{-5}
4	Mid-Continent Region	39876	3.45×10^{-5}
5	Rocky-Mountain Region	29611	7.92×10^{-5}
6	California	38931	6.39×10^{-5}

The costs predicted by using the above regression are the cost of equipping an injection

well in a developed field. The EIA cost estimates are for the addition of eleven water

injection wells to a field with ten production wells. Thus, the costs derived from this data

should be scaled to represent the cost associated with projects where some infrastructure

already exists. In the case of a new aquifer storage project, no prior infrastructure would

exist. Thus, the average cost per well of installing n injection wells would be somewhat higher than the unit cost of installing $n+1$ injection wells. The scaling equation used in the aquifer model is based on a power-law scaling rule [45], where the exponent of 0.5 is from Bock et al. [9]:

$$C_{IE,n} = \begin{cases} C_{IE}\left(\dfrac{21}{n}\right)^{0.5} , n \le 21 \\ C_{IE}, n > 21 \end{cases}$$
(4.27)

where C_{IE} is the scaled average cost of injection well equipment cost for n-wells (\$ per well) and C_{IE} is the un-scaled average cost calculated from Equation 4.26 with coefficients from Table 4.4 (\$ per well). Equation 4.27 shows that maximum economies of scale are assumed to be reached by 21 wells—the total number of wells in the EIA cost estimate—after which it is assumed that the cost no longer scales with the number of wells.

4.3.4   Project Capital Costs—Compression Equipment

In the case where the pipeline pressure is insufficient for CO_2 injection, a compressor must be added at the storage site. The total capital cost of a reciprocating compressor station has been estimated by the International Energy Agency (IEA) in a European study of the pipeline transmission of CO_2 [46]. That compressor cost model was also used in earlier in the pipeline transport model (see Section 2.2.3), and is given by Equation 4.28:

$$C = 8.35P + 0.49$$
(4.28)

where, C is the compressor capital cost in millions of US dollars (2004) and P is the installed booster station power in MW. This correlation yields a unit cost of \$8,346 per kW of installed capacity.

4.3.5   Operating and Maintenance Costs

Operating and maintenance (O&M) costs for an aquifer storage project include expenses

for labor, chemicals, and other consumables, plus expenses for surface equipment and

subsurface equipment maintenance, including periodic well workovers. If CO_2

recompression is required, the cost of energy to operate the compressors is also and

O&M cost.

O&M costs for CO_2 injection are assumed to be comparable to the costs of water

injection for secondary oil recovery. This is consistent with the assumption made by

Bock et al. [9] to assess the cost of aquifer storage and by Advanced Resources

International for the cost of CO_2-flood EOR [44]. The O&M cost of water injection in

secondary oil recovery at a field in West Texas is estimated annually by the EIA for

2,000 ft (610 m), 4,000 ft (1219 m) and 8,000 ft (2438 m) deep wells [43]. The form of

the equation developed in this research to fit these data points again is given by Equation

4.26, shown earlier, with coefficient values given in Table 4.5.

The EIA O&M cost for water injection has been extended to other regions by scaling the

West Texas O&M cost using the ratio of primary production O&M cost in the region of

interest to the cost in West Texas. The EIA estimates the O&M cost of primary

production for oil fields located in six regions: West Texas, South Texas, South

Louisiana, the Mid-Continent Region (i.e., Oklahoma, Kansas, Nebraska, Iowa,

Missouri), and the Rocky-Mountain Region (i.e., Western New Mexico, Colorado,

Wyoming, Montana) [43]. The regression coefficients for the O&M cost (in 2004 US

dollars) in each of these regions is presented in Table 4.5.

Table 4.5. Regression coefficients for use in Equation 4.26 for O&M cost in 2004 US dollars per well.

Region	States	a_1	a_2
1	West Texas	26873	1.03×10^{-4}
2	South Texas	38954	9.60×10^{-5}
3	South Louisiana	38853	1.03×10^{-4}
4	Mid-Continent Region	26790	1.34×10^{-4}
5	Rocky-Mountain Region	32893	8.78×10^{-5}
6	California	29537	1.67×10^{-4}

4.3.6   Monitoring, Verification and Closure Costs

Like the cost of site characterization, the costs of monitoring and verification (M&V) and

site closure will be highly dependent on the requirements of a regulatory regime, which

has yet to be developed (e.g., see Wilson et al. [47]). Benson et al. [48] have estimated

the cost of M&V for two hypothetical scenarios. In both cases it was assumed that 258

million tonnes of CO_2 was injected into an aquifer over a 30 year period, and seismic

surveys are performed in the each of the first two years, the fifth-year, and every fifth

year thereafter for 80 years. One scenario assumed a low residual gas saturation, leading

to a large CO_2 plume; the second scenario, a high residual gas saturation, leading to a

small plume size. From these two scenarios Benson et al. [48] estimate the levelized cost

of site characterization, operational M&V, and post-closure M&V to be between $0.05

and $0.08 per tonne of CO_2 injected. If the effects of discounting are ignored, the

prorated share of the total cost estimated by Benson et al. [48] attributable to operating

M&V is approximately $0.02 per tonne CO_2.

Additional cost of site closure to the operator could range from zero— for example, if the

site performs as predicted and responsibility is transferred to the government—to many

times the original capital cost—for example, if the site does not perform as predicted and

responsibility for the stored CO_2 remains with the site owner or operator for an extended

period of time. The analysis by Benson et al. [48] implicitly assumed that the site

operator would be responsible for the cost of post-closure monitoring, and based on the

total levelized of $0.05 to $0.08 per tonne, the levelized cost of post-closure M&V is very

small. This suggests that a one-time charge (in real dollars) associated with closure could

be very small, particularly considering that the charge occurs at the end of the project life,

although there are no empirical basis for such estimates. Given these uncertainties, for

purposes of cost estimation the model allows for either a lump-sum (real dollar) charge

for the closure or a fee to be levied on each tonne of CO_2 injected that could be paid into

a fund over the operating life of the project to cover the closure cost. Default values for

both of these parameters are zero, but can be adjusted to explore other assumptions.

4.3.7   *Illustrative Cost Model Results*

Model Results for the cost of well drilling, completion and equipping for a project in

West Texas with up to 40 injection wells are illustrated in Figure 4.20 for depths between

1000 and 3000 m. As shown earlier by the illustrative performance model results, the

wellhead pressure (and thus the compressor power requirement) depends on depth and

other performance model results. Thus, the cost shown in Figure 4.20 does not include

the capital cost of compression equipment, which is shown in Figure 4.21, as a function

of the compressor power requirement, which is determined from the performance model.
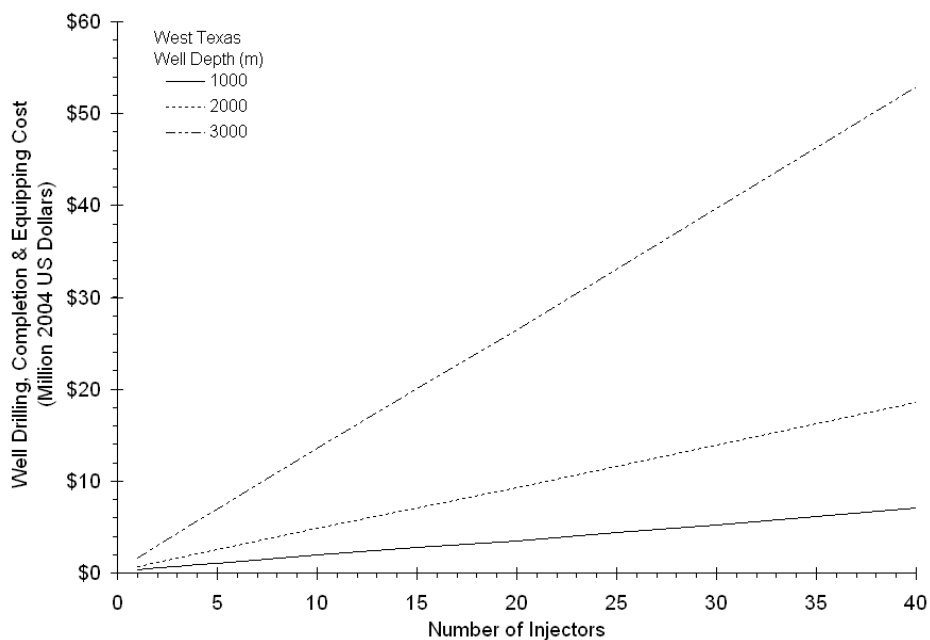
Figure 4.20. Capital cost of well drilling, completion, and equipping for a project located in West Texas with up to 40 injection wells for depths of 1000, 2000, and 3000 m.
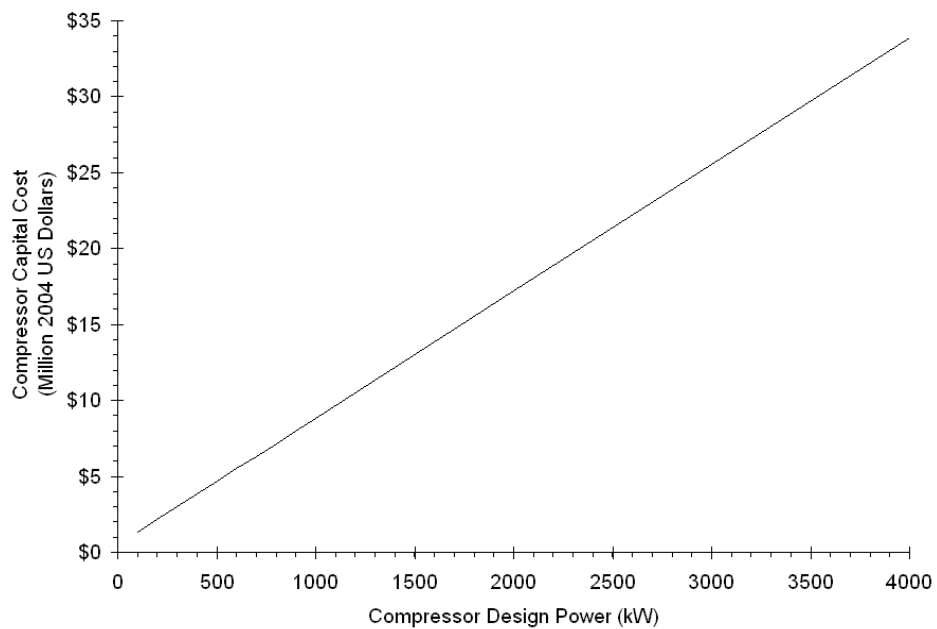
Figure 4.21. The capital cost of compression equipment as a function of the compressor power requirement.

The cost of site characterization is shown in Figure 4.22. The steps in cost at radii of approximately 4.5 and 6.5 km are caused by the addition of a well to the characterization requirements.
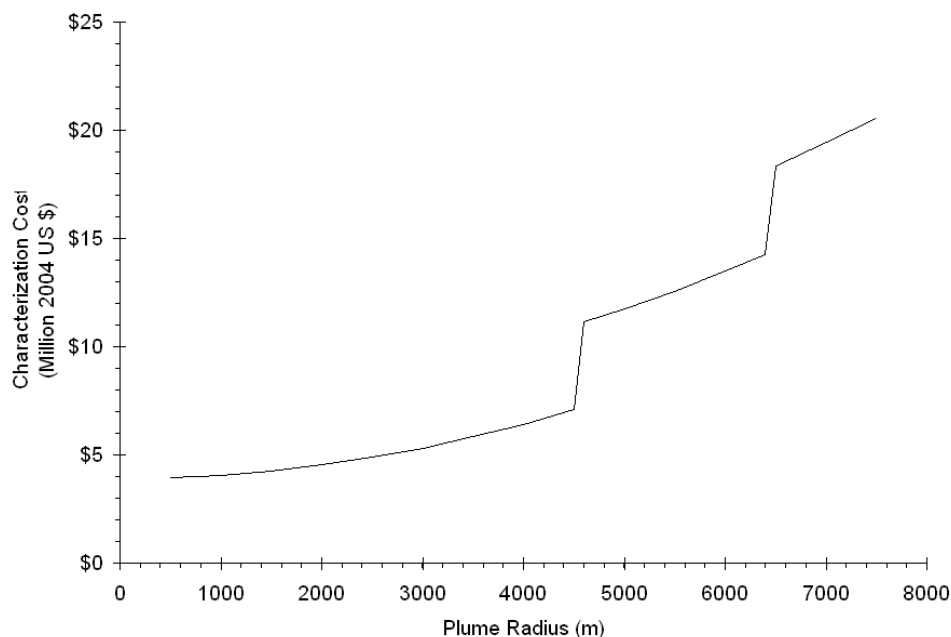
Figure 4.22. The cost of site characterization used in the model for plume radii between 0.5 and 8.0 km.

The site characterization cost found here are considerably larger than that of some prior estimates for aquifer storage, where the cost was only $1.7 million (2003) dollars [49], and applied without consideration of project size [9, 50]. However, the costs in Figure 4.22 are similar to a more recent estimate by Benson et al. [48].

The operating and maintenance cost for a West Texas project, excluding the cost of any additional energy associated with compression and any M&V costs, are shown in Figure 4.23. The additional annual cost of M&V and site closure would depend on the CO_2 injection rate, much as the site characterization cost depends on injection rate, as well as the unit cost of monitoring activities. Assuming an injection rate of 3 Mt CO_2 per year—

roughly equivalent to emissions from a 500 MW coal fired power plant—and a combined cost of \$0.03 per tonne CO_2 for M&V and site closure, the additional O&M cost would be approximately \$0.1 million per year.
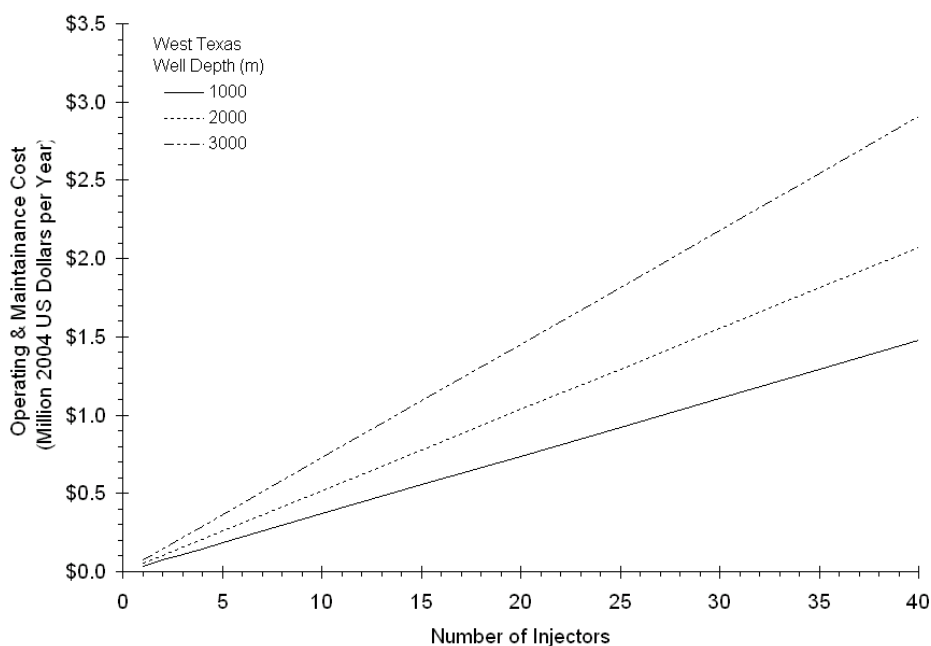
Figure 4.23. Operating and maintenance cost for a West Texas project, excluding the cost of any required compression energy and any M&V costs

4.4 Combining Performance and Cost

The performance model takes inputs from the user, as shown in Figure 4.3, and calculates the number of wells required for the specified geology, injection rate, and limits on the BHIP via the methods discussed in Section 4.2.1. The number of wells is then adjusted upwards if the resulting injection rate for any single well is greater than 1 million tonnes CO_2 per year, which is the limit for the wellbore flow model (Section 4.2.5). The adjusted number of wells, compressor power requirement (calculated via the method discussed in Chapter 2), and user inputs are used to estimate the capital cost of the project, as well as the O&M costs. Both capital and O&M costs are subject to capital cost escalation factors

(i.e., multipliers) that can be adjusted to change the capital costs estimated by the model. The levelized cost of CO_2 storage is estimated by dividing the sum of the annualized capital costs (arrived at using a capital recovery factor) and the annual O&M cost by the product of the capacity factor and the design flow rate and adding any additional M&V cost and injection fees associated with site closure.

4.5   Illustrative Case Studies

The reservoir descriptions used in the performance model for the four illustrative case studies are listed in Table 4.2 and were previously used to illustrate the behavior of the performance model. The cost model parameters used in the case study are listed in Table 4.6 and are the same for each case for ease of comparisons. The design CO_2 flow rate and the capital recovery factor will be varied parametrically as part of the analysis.

Table 4.6. Cost model parameter values used in the four case studies.

Project Parameter	Deterministic Value
Capital Recovery Factor (%)	15
O&M Costs	
Compression Energy Cost ($/MWh)	40
Operating Monitoring & Verification ($/tonne)	0.02
Injection Fee ($/tonne)	0
Closure Cost ($)	0
Site Characterization Cost	
Geophysical Cost ($/km2)	38,610
Test Well Spacing (km2/well)	65
Test Well Cost ($/well)	3,000,000
Consulting Services (% of Total)	30
Capital Cost Escalation Factors	
Drilling & Completion	1.0
Injection Well Equipment	1.0
Compression Equipment	1.0
O & M Cost	1.0

The levelized cost of CO_2 storage predicted by the aquifer storage model is presented in Figure 4.24 for the four cases across a range of mass flow rates. For a design injection rate of 5 Mt CO_2 per year, the levelized cost of CO_2 storage is $0.82 per tonne CO_2 for the Purdy-Springer case; $8.85 per tonne CO_2 for the Joffre-Viking case; $0.35 per tonne CO_2 for the Liberty-Frio case; and, $0.75 per tonne CO_2 for the Lake Wabamun-Mannville case. Figure 4.25 shows the same results on an expanded scale for the three lowest-cost sites.
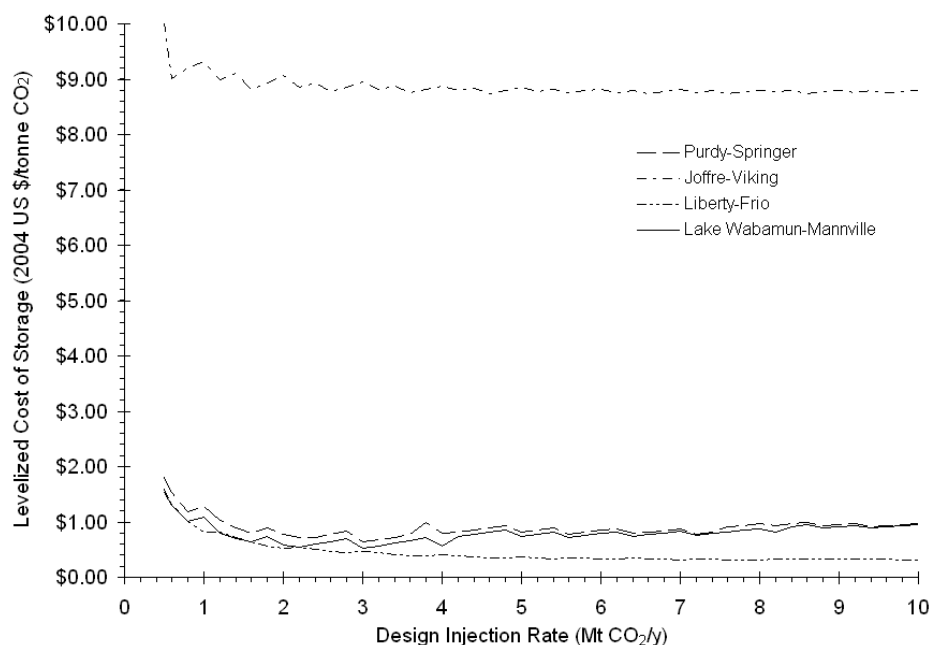
Figure 4.24. Levelized cost of CO$_2$ storage for the four cases across a range of design injection rates.
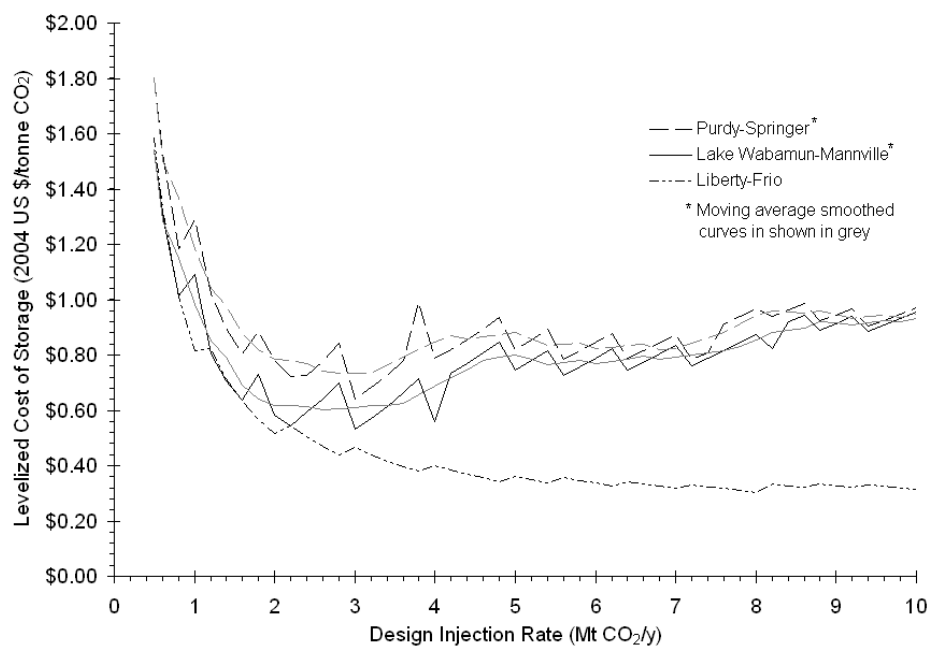
Figure 4.25. Levelized cost of CO$_2$ storage for the three low-cost cases shown in Figure 4.24 across a range of design injection rates. Smoothed curves are shown in grey for the Purdy-Springer and the Lake Wabamun-Mannville cases.

Several observations can be made from Figure 4.24 and Figure 4.25. First, the levelized cost of storage in the Joffre-Viking case is substantially higher than for any of the other cases. Second, the three "low-cost" cases show different behavior with increasing injection rates: the storage cost for the Liberty-Frio case continually declines over the range shown, whereas the cost for both Lake Wabamun-Mannville case and the Purdy-Springer case goes through a minimum at between 2 and 3 Mt CO_2 per year (shown most clearly by the smoothed curves). These differences in cost can be explained largely by examining the breakdown of total capital cost for each of the projects, shown in Figure 4.26 for 5 Mt CO_2 per year.
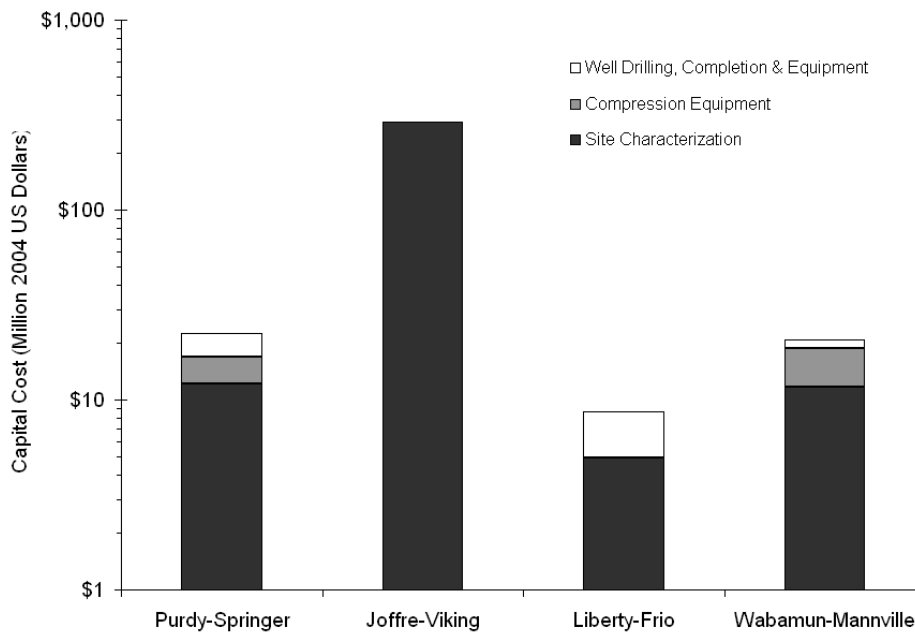
Figure 4.26. Breakdown of capital cost for each of the four cases at 5 Mt per year CO_2. Note the logarithmic scale.

For all four cases at 5 Mt CO_2 per year, Figure 4.26 shows that the capital cost of site characterization dominates the total capital cost. For the Joffre-Viking case the cost of site characterization represents nearly all of the capital cost because the aquifer properties

(i.e., underpressured, relatively thin net sand, and high porosity) results in an abnormally large footprint for site characterization (i.e., almost 2600 km^2). Conversely, the cost of site characterization for the Liberty-Frio site is much lower despite the high permeability of the Frio Sandstone because of the expansive net sand (i.e. aquifer net thickness), which translates into a relatively small footprint (i.e., less than 50 km^2).[2] The Purdy-Springer and Wabamun Mannville cases are intermediate between these two cases; the cost of compression equipment being a more significant factor. As the CO_2 injection rate increases, a trade-off between site characterization cost and compression cost (including resulting energy cost) occurs in the two intermediate cases, resulting in the minimums shown in Figure 4.25.

4.5.1   Model Sensitivity Analysis Results

To assess the sensitivity of the model to changes in multiple performance and economic parameters, uniform distributions were assigned to a number of parameters and the model was used to estimate the levelized cost of CO_2 storage over a Monte Carlo simulation for the Lake Wabamun-Mannville case. Uniform distributions were selected to represent uncertainty or variability because there is no prior information that would suggest choosing a more complex distribution (such as a triangular or lognormal distribution). Twelve performance model parameters and seven cost model parameters were assigned distributions; both the parameters and the distributions for the parameter values are listed in Table 4.7.

---

[2] This being said, the method used to estimate the aerial extent of the plume (see Appendix E) may not be appropriate for the Liberty-Frio case because the low velocity of the injected CO_2 means that buoyancy may be a large factor that can not be neglected [39]. Nordbotten et al [39] present a more complex alternative method that accounts for buoyancy which could be used in this scenario.

Table 4.7. The uncertainty distributions for parameters considered in the sensitivity analysis of the Lake Wabamun-Mannville case.

Model Parameter	Uncertainty Distribution
Performance Model Parameters	
Planning Horizon (years)	Uniform (10,30)
$P_{wb,max}$ (% of p_{frac})	Uniform (80,90)
Depth (m)	Uniform (1435,1580)[a]
G_p (MPa/km)	Uniform (7.93,10.63)[a]
G_T (K/km)	Uniform (20,30)[b]
Net Sand (m)	Uniform (35.5,74.2)[a]
ϕ (%)	Uniform (8,15)[c]
X_{brine} (ppm_w)	Uniform (53369,90639)[a]
Cost Model Parameters	
Geophysical Cost ($/km²)	Uniform (28958, 48263)[d]
Test Well Cost ($/well)	Uniform (2250000, 3750000)[d]
Capital Recovery Factor (%)	Uniform (10,20)
Energy Cost ($/MWh)	Uniform (40,20)
Operating Monitoring & Verification ($/tonne)	Uniform (0.01,0.03)[e]
Capital Cost Escalation Factors	
Escalation Factor for Drilling & Completion	Uniform(1.0,1.5)[d]
Escalation Factor for Injection Well Equipment	Uniform(1.0,1.5)[d]
Escalation Factor for O & M Cost	Uniform(0.75,1.25)[e]
Escalation Factor for Compression	Uniform(0.75,1.25)[e]

[a] Lower and upper bounds for distribution correspond to the 25th and 75th percentiles from the Lake Wabamun dataset [38]

[b] Typical geothermal gradients in the Alberta basin range from 20 ºC to 60 ºC/km [1]; the geothermal gradient implied by the depth and reservoir temperature in Table 4.2 is approximately 25 to 30 ºC depending on the assumed surface temperature.

[c] Lower and upper bounds for distribution correspond to the 25th and 75th percentiles from the Lake Wabamun dataset [38] for the Ellserslie Member of the Wabamun Group

[d] Given the recent increases in oil price and raw materials costs, the cost of D&C and injection well equipment would likely be higher than estimated by the regressions presented in Section 4.3

[e] Distribution bounds 25% above and below deterministic value (see Table 4.6)

The Dykstra-Parsons coefficient was used as discussed in Section 4.2.6 to generate

unique layered reservoirs for each of 1,000 Monte Carlo trials. The distributions for

depth, geothermal and pressure gradients (G_p and G_T, respectively), net sand, porosity

(ϕ), and total dissolved solids (X_{brine}) were derived from the Lake Wabamun dataset

provided by the Alberta Geological Survey [38]. From these 1,000 trials cumulative

distribution functions (CDF) were generated showing the breakeven CO_2 price, the net

CO_2 utilization, and the cumulative mass of CO_2 stored.

Figure 4.27 shows the CDF for the levelized cost of CO_2 storage. The median cost of CO_2

storage is $0.95 per tonne CO_2, with a 90% confidence interval of $0.55 to $1.81 per

tonne CO_2. Note that these results exclude 429 cases where the model could not meet the

required injection rate using fewer than 100 injectors. In such scenarios, a project

developer would likely look at other sequestration targets or use horizontal drilling to

reduce the number of wells required.
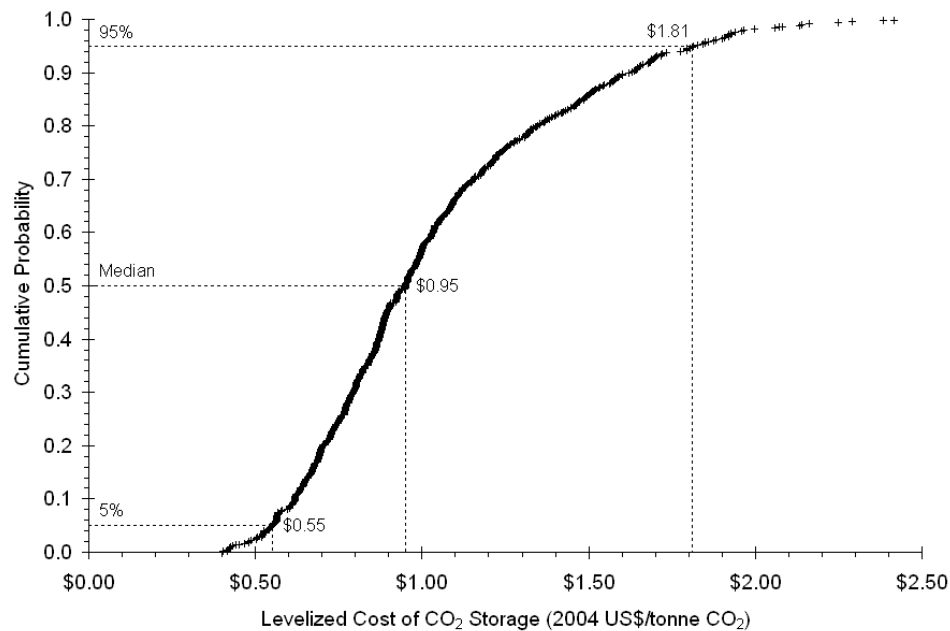
Figure 4.27. CDF for the levelized cost of CO_2 storage for the Lake Wabamun-
Mannville case.

Results of the Monte Carlo trials can also be used to assess the sensitivity of storage cost

to the model parameters assigned uniform distributions. The measure used to assess the

sensitivity is the Spearman rank-order correlation (r_s) [51]. The value of the rank order

correlation coefficient for each model parameter is shown in Figure 4.28. The dashed

vertical lines to the left and the right of the y-axis indicate the 5% significance level ($r_s =$ ±0.07); thus rank-order correlation coefficients smaller than this value are not statistically significant at the 5% level. Figure 4.28 shows that the strongest correlation with the levelized cost of CO_2 storage is the effect of the effective permeability ($r_s = $ -0.58) and, followed by the capital recovery factor ($r_s = 0.41$), planning horizon ($r_s = 0.21$), and porosity ($r_s = $ -0.19). Following these, other significant rank-order correlation coefficients (by decreasing magnitude) are net sand thickness and test well cost.
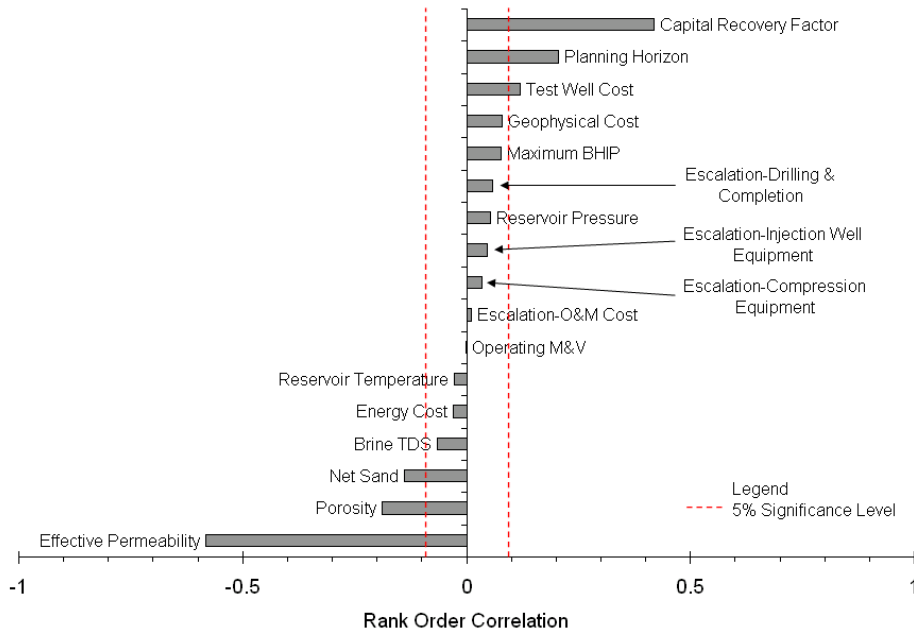
Figure 4.28. Rank-order correlation between the results of the Monte Carlo sensitivity analysis and the parameters assigned uniform distributions.

4.6   Comparison with Other Models

The IPCC Special Report on Carbon Capture and Storage (SRCCS) [7] cited three studies as the basis for their estimates of aquifer storage costs, which ranged from $0.2 to $6.2 per tonne CO_2 excluding monitoring, verification & closure costs. Of those studies, only Bock et al. present a method [9] that related cost to the geology of a target formation.

Bock et al. [9] used a correlation presented by Law and Bachu [11] to estimate the

number of wells required for a design flow rate. The correlation developed by Law and

Bachu [11] relates mass injection rate to reservoir permeability, k; net aquifer thickness,

h; pressure difference between the initial pressure, p_i, and the BHIP, p_{wb}; and, CO_2

viscosity. That correlation, however, did not account for interactions between injection

wells and, as Figure 4.1 shows, significantly overestimates the injectivity of a multi-well

system.
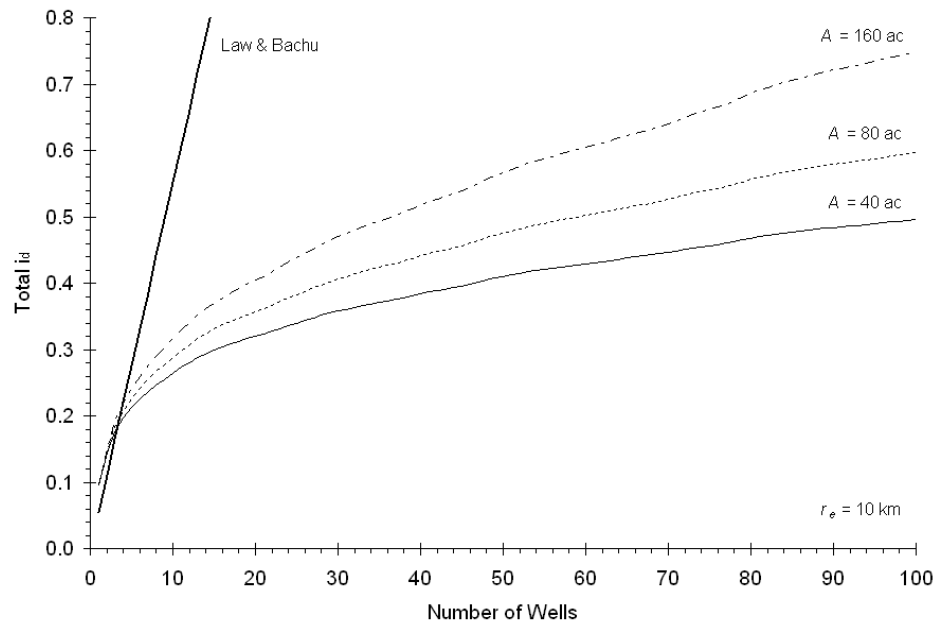
Figure 4.29. The total injectivity for systems with 1 to 100 wells on 40, 80, and 160 acre spacing with a constant pressure radius where $p_e = p_i$ at 10 km, compared with results of the correlation developed by Law & Bachu [11].

The costs used by the Bock et al. model [9] for well drilling and completion, and for

injection equipment are based on the same data used in the model presented here (i.e., the

EIA Oil and Gas Lease Equipment and Operating Cost index [43]); however, the cost of

site characterization used by Bock et al. [9] was a fixed value substantially smaller than

the values typically found here. Nor do Bock et al. report the stand alone values of

storage cost; rather, they report only a combined cost of CO_2 transport and storage, so that systematic comparisons are not possible.

Overall, the results presented here are generally similar to the IPCC cost ranges for onshore CO_2 storage in aquifers. However, the case studies used here to estimate the cost of aquifer storage are different than those used in the three publications cited by the IPCC. Based on those prior studies, however, the IPCC concluded that the largest component of the storage cost was the cost of well drilling, completion and equipping [7]. In contrast, the examples presented here show these to be the smallest portion of the total cost of storage when current site characterization costs are accounted for.

4.7   References

1.   Bachu, S., *Screening and ranking of sedimentary basins for sequestration of CO_2 in geological media in response to climate change.* Environmental Geology, 2003. **44**: p. 277-289.
2.   Bachu, S. and K. Haug, *In-Situ Characteristics of Acid-Gas Injection Operations in the Alberta Basin, Western Canada: Demonstration of CO_2 Geological Storage*, in *The CO_2 Capture and Storage Project (CCP) for Carbon Dioxide Storage in Deep Geologic Formations for Climate Change Mitigation*, S. Benson, Editor. 2004, Elsevier Science.
3.   Bachu, S. and W.D. Gunter. *Overview of Acid-Gas Injection Operations in Western Canada*. in *7th International Conference on Greenhouse Gas Control Technologies*. 2004. Vancouver, Canada: Elsevier Science.
4.   Papanikolau, N., et al., *Safe storage of CO_2: experience from the natural gas storage industry*, in *8th International Conference on Greenhouse Gas Control Technologies*. 2006, Elsevier Science: Trondheim, Norway.
5.   Benson, S.M., et al., *Lessons Learned from Natural and Industrial Analogues for Storage*. 2002, Lawrence Berkley National Laboratory: Berkley, CA.
6.   Keith, D.W., et al., *Regulating the Underground Injection of CO_2.* Environmental Science & Technology, 2005. **39**: p. 499A-505A.
7.   Benson, S., et al., *Underground geological storage*, in *IPCC Special Report on Carbon Dioxide Capture and Storage*, B. Metz, et al., Editors. 2005, Cambridge University Press: Cambridge, U.K.
8.   Hendriks, C.F., *Carbon dioxide removal from coal fired power plants*. 1 ed. 1994: Kluwer Academic Publishers.
9.   Bock, B., et al., *Economic Evaluation of CO_2 Storage and Sink Enhancement Options*. 2003, TVA Public Power Institute: Muscle Shoals, AL.

10. Allinson, W.G., D.N. Nguyen, and J. Bradshaw, *The Economics of Geological Storage of CO$_2$ in Australia.* APPEA Journal, 2003. **43**: p. 623-636.

11. Law, D.H.S. and S. Bachu, *Hydrogeological and Numerical Analysis of CO$_2$ Disposal in Deep Aquifers in the Alberta Sedimentary Basin.* Energy Conversion & Management, 1996. **37**(6-8): p. 1167-1174.

12. Wildenborg, T., et al. *Cost Curves for CO$_2$ Storage: European Sector.* in *7th International Conference on Greenhouse Gas Control Technologies.* 2004. Vancouver, Canada: Elsevier Science.

13. Craft, B. and M. Hawkins, *Applied Petroleum Reservoir Engineering.* 1st ed. Prentice-Hall Chemical Engineering Series. 1959, Englewood Cliffs, NJ: Prentice-Hall. 437.

14. Freeze, R.A. and J.A. Cherry, *Groundwater.* 1979, Englewood Cliffs, N.J.: Prentice-Hall. xvi, 604 p.

15. Bachu, S., et al., *CO$_2$ storage capacity estimation: Methodology and gaps.* International Journal of Greenhouse Gas Control, 2007. **1**(4): p. 430-443.

16. Chevron Australia, *Draft Environmental Impact Statement/Environmental Review and Management Programme for the Proposed Gorgon Development.* 2005, Chevron Austraila Pty Ltd: Perth, Australia.

17. Brigham, W., *Doublets and Other Allied Well Patterns.* 2000, Stanford University Petroleum Research Institute: Stanford, CA.

18. Press, W.H., *Numerical recipes in C : the art of scientific computing.* 2nd ed. 1992, Cambridge; New York: Cambridge University Press. xxvi, 994 p.

19. Selby, S.M., ed. *Standard Mathematical Tables.* 16th ed. 1968, The Chemical Rubber Co.: Cleveland, OH.

20. Nordbotten, J.M., M.A. Celia, and S. Bachu, *Analytical solutions for leakage rates through abandoned wells.* Water Resources Research, 2004. **40**(4).

21. Dake, L.P., *Fundamentals of reservoir engineering.* 1 ed. 1978: Elsevier.

22. Shafeen, A., et al., *CO$_2$ sequestration in Ontario, Canada. Part II: cost estimation.* Energy Conversion & Management, 2004. **45**: p. 3207-3217.

23. Pizarro, J.O.S. and L.W. Lake, *Understanding Injectivity in Heterogeneous Reservoirs*, in *SPE/DOE Improved Oil Recovery Symposium.* 1998, Society of Petroleum Engineers: Tulsa, OK.

24. Heller, J.P. and J.J. Taber, *Influence of Reservoir Depth on Enhanced Oil Recovery by CO$_2$ Flooding*, in *Permian Basin Oil & Gas Recovery Conference of the Society of Petroleum Engineers.* 1986, Society of Petroleum Engineers: Midland. TX.

25. Lake, L.W. and J.L. Jensen, *Review of heterogeneity measures used in reservoir characterization.* 1989, Society of Petroleum Engineers: Richardson, TX. p. 40.

26. Willhite, G.P., *Waterflooding.* SPE Textbook Series. 1986, Richardson, TX: Society of Petroleum Engineers. 326.

27. Jensen, J.L., D.V. Hinkley, and L.W. Lake, *A Statistical Study of Reservoir Permeability: Distributions, Correlations, and Averages.* SPE Formation Evaluation, 1987. **2**(4): p. 461-468.

28. Freeman, J. and R. Modarres, *Inverse Box-Cox: The power-normal distribution.* Statistics & Probability Letters, 2006. **76**(8): p. 764-772.

29.   Gunter, W.D., et al., *Aquifer Disposal of CO₂-Rich Gases: In the Vicinity of the Sundance and Genesee Power Plants*. 1993, Alberta Department of Energy: Edmonton, AB.

30.   Gunter, W.D., et al., *Central Alberta: CO₂ Disposal Into Alberta Basin Aquifers - Phase II*. 1994, Alberta Department of Energy: Edmonton, AB.

31.   Hovorka, S.D., *Optimal Geological Environments for Carbon Dioxide Disposal in Saline Aquifers in the United States*. 1999, Bureau of Economic Geology, University of Texas at Austin: Austin, TX. p. 63 p.

32.   Simlote, V.N. and E.M. Withjack, *Estimation of Tertiary Recovery by CO₂ Injection--Springer A Sand, Northeast Purdy Unit.* Journal of Petroleum Technology, 1981(May): p. 808-818.

33.   Stephenson, D.J., A.G. Graham, and R.W. Luhning, *Mobility Control Experience in the Joffre Viking Miscible CO₂ Flood.* SPE Reservoir Engineering, 1993(August): p. 183-188.

34.   Alberta Geological Survey. *Major Basin Units for CO₂ Sequestration*. 2005 [cited 2007 December 29]; Available from: http://www.ags.gov.ab.ca/website/co2_formation/viewer.htm.

35.   Hovorka, S.D., C. Doughty, and M.H. Holtz, *Testing Efficiency of Storage in the Subsurface: Frio Brine Pilot Experiment*, in *7th International Conference on Greenhouse Gas Control Technologies*. 2004: Vancouver, Canada.

36.   Hovorka, S.D., et al., *Evaluation of Brine-Bearing Sands of the Frio Formation, Upper Texas Gulf Coast for Geological Sequestration of CO₂*, in *First National Conference on Carbon Sequestration*. 2001, National Energy Technology Lab: Washington, DC.

37.   Holtz, M.H., et al., *Geologic Sequestration in Saline Formations: Frio Brine Storage Pilot Project, Gulf Coast Texas*, in *Fourth Annual Conference on Carbon Capture & Sequestration*. 2005: Alexandria, VA.

38.   Alberta Geological Survey. *Test Case for Comparative Modelling of CO₂ Injection, Migration and Possible Leakage - Wabamun Lake Area, Alberta, Canada*. 2006 May 1 [cited 2007 December 29]; Available from: http://www.ags.gov.ab.ca/activities/wabamun/wabamun_base.html.

39.   Nordbotten, J.N., M.A. Celia, and S. Bachu, *Injection and Storage of CO₂ in Deep Saline Aquifers: Analytical Solution for CO₂ Plume Evolution During Injection.* Transport in Porous Media, 2005. **58**: p. 339-360.

40.   Tombari, J., Schlumberger Limited. *RE: Site Characterization Costs for GS*. Personal Communication, 21 December 2007.

41.   American Petroleum Institute, *Joint Association Survey on Drilling Costs*. 2002, American Petroleum Institute: Washington, DC. p. 111.

42.   Lewin & Associates Inc., *Economics of Enhanced Oil Recovery*. 1981, Department of Energy: Washington, DC. p. 123.

43.   Energy Information Administration. *Oil and Gas Lease Equipment and Operating Costs 1988 Through 2006*. 18 June 2007 [cited 26 September 2007]; Available from: http://www.eia.doe.gov/pub/oil_gas/natural_gas/data_publications/cost_indices_equipment_production/current/coststudy.html.

44. Advanced Resources International, *Basin Oriented Strategies for CO$_2$ Enhanced Oil Recovery: Permian Basin*. 2006, US Department of Energy: Arlington, VA. p. 117.

45. Perry, R.H., D.W. Green, and J.O. Maloney, *Perry's chemical engineers' handbook*. 7th ed. 1997, New York: McGraw-Hill.

46. Woodhill Engineering Consultants, *Pipeline Transmission of CO$_2$ and Energy: Transmission Study - Report*. 2002, IEA Greenhouse Gas R&D Programme: Stoke Orchard, UK.

47. Wilson, E.J., S.J. Friedmann, and M.F. Pollak, *Research for deployment: Incorporating risk, regulation, and liability for carbon capture and sequestration.* Environmental Science & Technology, 2007. **41**(17): p. 5945-5952.

48. Benson, S.M., et al. *Monitoring Protocols and Life-Cycle Costs for Geologic Storage of Carbon Dioxide*. in *7th International Conference on Greenhouse Gas Control Technologies*. 2004. Vancouver, Canada: Elsevier Science.

49. Smith, L., et al., *Carbon Dioxide Sequestration in Saline Formations-Engineering and Economic Assessment Final Technical Report*. 2001, Battelle Memorial Institute: Columbus, OH. p. 93.

50. McCoy, S.T. and E.S. Rubin, *Models of CO$_2$ Transport and Storage Costs and Their Importance in CCS Cost Estimates*, in *Fourth Annual Conference on Carbon Capture and Sequestration*. 2005: Alexandria, VA.

51. Morgan, M.G., M. Henrion, and M. Small, *Uncertainty : a guide to dealing with uncertainty in quantitative risk and policy analysis*. 1990, Cambridge: Cambridge University Press. 332.

Chapter 5: Conclusions

In this thesis models have been developed to estimate the performance and cost of CO_2 transport by pipeline, CO_2 storage through enhanced oil recovery, and CO_2 storage in saline aquifers. Each of the models was used to estimate cost and performance for a range of cases involving CO_2 transport and storage. Moreover, the sensitivity of cost to input parameter changes was quantified using the probabilistic assessment capabilities of the models. Sections 5.1 through 5.3 summarize results from each of the models and discuss the implications of these results. Sections 5.4 and 5.5 review the limitations of the results and suggest several directions for future work.

5.1　Pipeline Transport of CO_2—Results and Implications

Figure 2.10 (reproduced below as Figure 5.1) summarizes results from the CO_2 pipeline transport model based on inputs listed in Table 2.3. This figure illustrates how the cost of pipeline transport varies with distance, design capacity, and region of construction. Economies of scale in CO_2 transport are clearly evident in Figure 5.1, suggesting that it may be more efficient to encourage hub-and-spoke transport systems rather than point-to-point systems to transport large amounts of CO_2. In either case, current regulations for CO_2 pipelines may have to be revised and expanded to effectively regulate a large infrastructure for transport of CO_2.
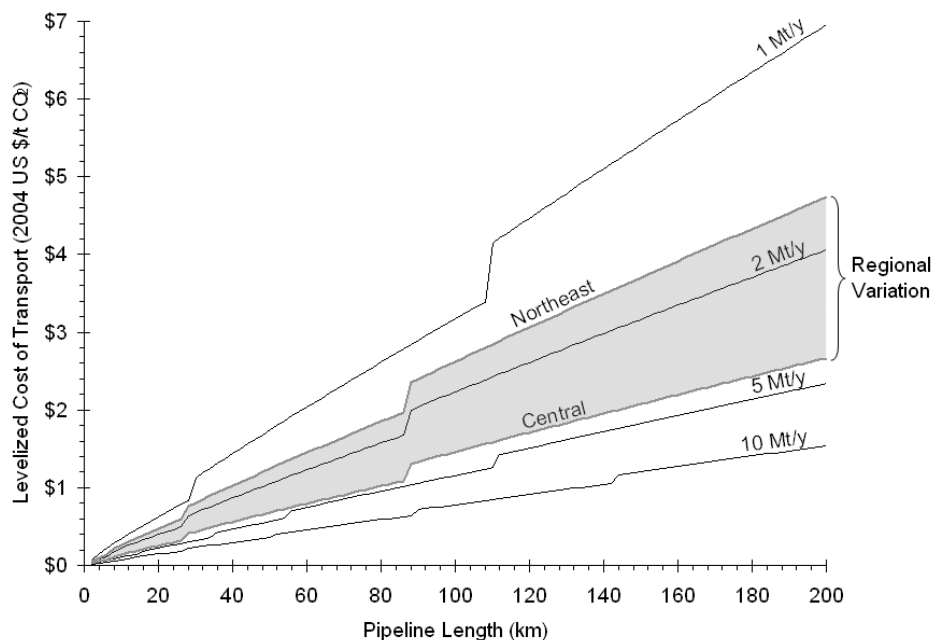
Figure 5.1. Illustrative results for the levelized cost of CO_2 transport (in constant 2004 US dollars) over a range of pipeline design capacities and pipeline distances.

5.2 CO_2 Storage through Enhanced Oil Recovery—Results and Implications

Unlike the cases of CO_2 transport or saline aquifer storage, it is not possible to estimate a meaningful levelized cost of CO_2 storage for CO_2-flood EOR. This is because the CO_2 storage function of this process has traditionally been a secondary effect of oil recovery—the main motivation for this process. However, the breakeven cost of CO_2 (i.e., the cost of CO_2 at which the project has a net present value of zero) can be interpreted as the highest price a CO_2-flood developer would be willing to pay for CO_2 delivered to the site based on the assumed benchmark oil price (and numerous other factors). The amount of oil produced, CO_2 stored, and the breakeven CO_2 prices for four cases examined with the EOR model are shown in Table 5.1.

Chapter 5: Conclusions

Table 5.1. Results for the four EOR case studies from Chapter 3 showing cumulative oil produced in million barrels (mmbbl), cumulative CO_2 stored, the CO_2 storage rate (tonnes per barrel), and the breakeven CO_2 price for two West Texas Intermediate (WTI) oil prices.

Field	Oil Produced (mmbbl)	CO_2 Stored (Mt)	CO_2 Storage Rate (t/bbl)	Breakeven CO_2 Price ($/tonne CO_2)	
				$50/bbl (WTI)	$100/bbl (WTI)
Northeast Purdy Unit	36	5.8	0.16	$83	$315
SACROC Unit, Kelly-Snyder Field	402	83.3	0.21	$120	$310
Ford Geraldine Unit	13	2.3	0.18	$34	$243
Joffre Viking Pool	23	3.3	0.14	$123	$392

Across the range of oil prices experienced over the last several years (since about 2004), the breakeven prices for CO_2 estimated from the case studies range from a low of $34 per tonne CO_2 ($1.79 per mscf CO_2) to a high of $392 per tonne CO_2 ($20.75 per mscf CO_2). These results emphasize the wide range of EOR project profitability and the wide range in the amount of CO_2 that can be stored through EOR projects—although it should be noted that projects like the SACROC Unit, with fairly large CO_2 storage capacity are the exception; most operating EOR projects have smaller CO_2 storage capacities. These results also suggest that there is ample profit incentive to early entrants who are able to provide CO_2 for new EOR projects because typical CO_2 capture costs (reviewed in Chapter 1) are much lower than the prices shown in Table 5.1.

The results from these case studies also highlight that, for many EOR projects, the rate of CO_2 storage and the total capacity for CO_2 storage are very small in relation to the rate and amount of CO_2 produced by a modern coal-fired power plant (i.e., 2 to 3 Mt CO_2 per year for 500 MW of coal fired capacity). This highlights that the viability of CO_2-flood EOR as a means to mitigate CO_2 emissions hinges on whether there are fields remaining

that are amenable to CO_2-flooding that can accept these large amounts of CO_2 at practical

rates. In a study of the Alberta and Williston Basins (Western Canada), Bachu and Shaw

found that the majority of EOR-related CO_2 storage capacity is in a very small fraction of

reservoirs and that when reservoirs with total capacities of less than 1 Mt CO_2 were

excluded, only 2% of reservoirs were suitable for CO_2 storage [1]. The results would

likely be similar for other sedimentary basins. Consequently, CO_2-flood EOR alone will

not be the solution for mitigating emissions on a large-scale.

In addition, the results of the case studies show that the CO_2 storage rate in tonnes per bbl

oil is relatively small compared to the CO_2 emissions produced from the consumption of

the oil. One typical barrel of light oil[1] contains approximately 0.11 tonnes C, which if

fully oxidized produces 0.42 tonnes of CO_2 (excluding emissions associated with the

additional energy used in oil refining, such as from hydrotreating). This compares to the

CO_2 storage rates in Table 5.1 of 0.14 to 0.21 tonnes CO_2 per barrel of oil produced.

Thus, CO_2 stored in any of the case study projects would not offset emissions from the

combustion of oil produced from the project. On the other hand, if the marginal barrel of

oil displaced by CO_2-flood EOR production were from a carbon-intensive source, oil

sands for example [2], CO_2-flood EOR would result in a net emissions reduction

compared with consumption of the marginal barrel. Thus, whether CO_2-flood EOR

results in a net emission of CO_2 is sensitive to the source of the hydrocarbon that EOR

production is assumed to displace on the supply curve.

---

[1] Assuming that one kilogram of oil contains 0.84 kilograms of carbon with a gravity of 35 to 40°API (equivalent to the carbon content of decane, $C_{10}H_{22}$).

5.3   CO$_2$ Storage in Deep Saline Aquifers—Results and Implications

Results of the aquifer storage case studies show a large range of variability in the cost per tonne of CO$_2$ stored, driven primarily by differences in aquifer geology and petrophysical properties. For a design injection rate of 5 Mt CO$_2$ per year, the levelized cost of CO$_2$ storage ranged from \$0.35 per tonne CO$_2$ for the Liberty-Frio case to \$8.85 per tonne CO$_2$ for the Joffre-Viking case. Considering only the costs of well drilling and completion, and injection equipment, the capital cost of all of the cases was relatively similar; however, inclusion of the cost of site characterization changed the results greatly. For all of the cases, the largest portion of the total levelized cost (ranging from 45% for Liberty-Frio to 98% for Joffre-Viking) was the cost of site characterization. The importance of assumptions regarding site characterization cost (and the implied methods of site characterization) to the levelized cost of CO$_2$ storage in saline aquifers has not been previously demonstrated.

The large contribution of site characterization cost to the levelized cost of storage implies that requirements for site characterization imposed by a regulatory framework should be carefully considered. Requirements for high-resolution characterization methods (e.g. 3D-seismic, as assumed here) or larger areas of review will increase the levelized cost of storage. However, the upfront cost requirements for characterization could be managed by, for example, limiting the area of review to the area impacted for a specified time horizon (e.g., the planning horizon for a project), with provision for further characterization prior to extension of the operation past the original planning horizon.

5.4   Limitations of These Results

The results for CO_2 transport and storage costs presented here are based on a limited number of illustrative case studies. While the models can be applied to a wider range of cases, caution must be exercised when applying the results presented here to different situations. For example, the effect of pipeline routing on transport cost is not considered by the pipeline transport model. Thus, it is entirely possible that the cost of a pipeline in a nominally high-cost region (e.g., Northeast US) could be lower than the cost of a particular pipeline in a generally lower-cost region (e.g., Central US) depending on the pipeline routing because of factors such as complex terrain, river crossings, and high population densities. Other tools are available that allow such details of pipeline routing to be considered (e.g., Zhang et al. [3]), and can be used in conjunction with this model to develop more accurate cost estimates. Thus, cost differences between regions should be interpreted only as being broadly representative.

Similarly, the illustrative cases for both EOR and aquifer storage were selected based on available data. While descriptions of a large number of CO_2-flood EOR projects have been published, particularly in *Society of Petroleum Engineers* journals, the data available on saline aquifers suited to CO_2 injection are much sparser. Consequently, the four EOR cases represent a range of typical projects based on those that have been developed to date, while the two additional aquifer storage cases may not cover as broad a range of potential projects. Thus, it is possible that some storage projects, particularly aquifer storage projects, could exhibit considerably different cost behavior.

In addition, the CO_2-flood EOR model was developed to answer questions about the cost of EOR storage in cases where a reservoir-specific answer is desired but limited

information is available; or, where an answer is desired with minimal effort and cost. Far more accurate estimates can be made using more advanced models [4], particularly if a history-matched model of the reservoir is available. Such estimates are far more time-consuming and costly to obtain, but, are necessary to support investment decisions on EOR projects. Conversely, where there is inadequate information to even apply the less-complex model presented here, rule-of-thumb based methods are more appropriate (e.g., see Bock et al. [5]). Similarly, the aquifer storage model presented here fills the niche where adequate data is available to apply the model, but the insufficient to support analysis using more complex simulators (e.g. see Pruess et al. [6]).

5.5   Future Work

All of the models developed here are suitable for use in addressing a variety of questions related to policies and projects for carbon capture and storage. Perhaps the most pressing need for future work, however, concerns the development of data needed to estimate CO_2 storage costs. Given the necessary geological data to allow storage cost from site to site to be differentiated, the models developed here could be used to perform source-sink matching and to generate regional cost curves. However, data characterizing aquifers at the project-level scale appropriate for use of the screening model developed here are not widely available. While the US Department of Energy (DOE)—though its Regional Carbon Sequestration Partnerships—has produced a "Carbon Sequestration Atlas of the United States and Canada," [7] the data in that atlas are too small-scale for use in the type of model developed here. Thus, it is currently difficult to estimate the practical capacity available for CO_2 storage at local scales [8], or to generate reliable cost curves (i.e., the cost of storing increasing amounts of CO_2) on a national scale. Thus, collection,

aggregation, and application of the model to this required data is a significant area for future research.

The CO_2 transport and storage models presented here can also be used to assess the impact of regulatory requirements on the cost of CCS. Future work could analyze a number of alternative regulatory scenarios to examine their impact on cost. This type of analysis could be used as part of a benefit-cost analysis, or a cost-effectiveness analysis, of proposed regulations for CO_2 capture and storage. The models developed here would be valuable tools to help evaluate different proposals.

5.6   References

1.   Bachu, S. and J. Shaw, *Evaluation of the CO_2 sequestration capacity in Alberta's oil and gas reservoirs at depletion and the effect of underlying aquifers.* Journal of Canadian Petroleum Technology, 2003. **42**(9): p. 51-61.

2.   Brandt, A.R. and A.E. Farrell, *Scraping the bottom of the barrel: greenhouse gas emission consequences of a transition to low-quality and synthetic petroleum resources.* Climatic Change, 2007. **84**(3-4): p. 241-263.

3.   Zhang, H., W. Li, and H. Herzog, *MIT CO_2 Pipeline Transport and Cost Model.* 2007, Massachusetts Institute of Technology: Carbon Capture and Sequestration Technologies Program: Boston, Massachusetts.

4.   Gerritsen, M.G. and L.J. Durlofsky, *Modeling fluid flow in oil reservoirs.* Annual Review of Fluid Mechanics, 2005. **37**: p. 211-238.

5.   Bock, B., et al., *Economic Evaluation of CO_2 Storage and Sink Enhancement Options.* 2003, TVA Public Power Institute: Muscle Shoals, AL.

6.   Pruess, K., et al., *Numerical Modeling of Aquifer Disposal of CO_2,* in *SPE/EPA/DOE Exploration and Production Environmental Conference.* 2001, Society of Petroleum Engineers: San Antonio, TX.

7.   National Energy Technology Lab, *Carbon Sequestration Atlas of the United States and Canada.* 2007, Pittsburgh, PA: US Department of Energy. 86.

8.   Bachu, S., et al., *CO_2 storage capacity estimation: Methodology and gaps.* International Journal of Greenhouse Gas Control, 2007. **1**(4): p. 430-443.

Appendix A: Estimation of Physical Properties

Physical properties are the attributes of a substance that can be measured directly or indirectly through experimentation, such as density, enthalpy, and viscosity. Estimation of the physical properties of CO_2 and CO_2-containing mixtures is of critical importance in the design of transport and injection systems for carbon capture and storage as well as the behavior of injected CO_2 in the subsurface. Additionally, in the case of enhanced oil recovery (EOR), it is necessary to know the physical properties of crude oils at reservoir conditions. This appendix discusses the methods employed to estimate physical properties of both CO_2 and CO_2-containing mixtures and crude oils in the models developed in this thesis.

A.1 Physical Property Estimation for Pure Fluids and Fluid Mixtures

Fluids are a phase of matter, capable of flowing under an applied shear stress (i.e., they will flow from high pressure to low pressure) and can be either gaseous or liquid. A pure fluid consists of only one substance (e.g., Hg or CO_2). Conversely, a fluid mixture, such as acid gas, contains more than one substance (e.g., in the case of acid gas, H_2S, CO_2, and other minor constituents) and its physical properties are a function of composition. While crude oils are fluid mixtures, they contain on the order of hundreds of hydrocarbon components, as well as non-hydrocarbon impurities, and can not easily be treated in the same way as a pure fluid or simple fluid mixture. Consequently, they are treated separately in Section A.2. The following sections discuss pressure-volume-temperature relationships (PVT) for pure fluids and simple fluid mixtures, thermodynamic property

Appendix A: Estimation of Physical Properties

and transport property estimation for these mixtures, and finishes by comparing the accuracy of different calculation methods.

A.1.1   *Pressure-Volume-Temperature Relationships*

Equations of state (EOS) relate the pressure, volume and temperature of pure fluids and fluid mixtures. The relationship between pressure, p, molar volume, v, and temperature, T, can be expressed by the compressibility, Z:

$$Z = \frac{pv}{RT} \tag{A.1}$$

where R is the universal (or ideal) gas constant. When $Z = 1.0$, Equation A.1 reduces to the familiar ideal gas law. However, for real gases (or liquids) Z is generally less than 1, and near the critical point Z changes rapidly with pressure and temperature. Thus for a typical single-phase, real-gas system where pressure and temperature are fixed, Equation A.1 shows that the compressibility must be estimated to calculate the density of the system (or vice versa).

To describe both liquids and gases, an EOS must be at least cubic in V and to be analytically tractable must be no greater than quartic in V [1]. An EOS that fits these requirements was proposed by van der Waals over a century ago and was the first cubic EOS [2]. To date, there are over 400 parameterizations of the cubic EOS proposed in literature [2], however, only small number of these equations are commonly used.

A generalized cubic EOS can be written [1]:

$$p = \frac{RT}{v-b} - \frac{\Theta(v-\eta)}{(v-b)(v^2 + \delta v + \varepsilon)}$$

Appendix A: Estimation of Physical Properties

For all of the parameterizations of the cubic EOS discussed here, $\eta = b$, thus this generalized equation reduces to Equation A.2.

$$p = \frac{RT}{v - b} - \frac{\Theta}{v^2 + \delta v + \varepsilon} \qquad (A.2)$$

In Equation A.2, b, δ, ε, and Θ are fluid specific parameters that vary depending on the parameterization used.

To solve the cubic EOS analytically for compressibility using the cubic equation, it must be rewritten in terms of Z, and set equal to zero:

$$Z^3 + (\delta' - B' - 1)Z^2 + [\Theta' + \varepsilon' - \delta'(B' + 1)]Z - \varepsilon'(B' + 1) + \Theta'B' = 0$$

where the dimensionless parameters are defined:

$$B' = \frac{bp}{RT} \qquad \delta' = \frac{\delta p}{RT} \qquad \Theta' = \frac{\Theta p}{RT} \qquad \varepsilon' = \varepsilon\left(\frac{P}{RT}\right)^2 \qquad (A.3)$$

The parameterizations available in the models are listed in Table A.1, Table A.2, and Table A.3. These parameterizations represent a range from those commonly used in the process and reservoir engineering fields, such as Soave, 1972 (commonly referred to as SRK) or Peng and Robinson, 1976, to more recent and less commonly used parameterizations, such as Twu et al, 1995. In the remainder of this discussion, the custom of referring to different parameterizations as EOS will be followed. For example, the Peng and Robinson parameterization will be referred to as the Peng and Robinson EOS.

Appendix A: Estimation of Physical Properties

Table A.1. The seven cubic EOS available in the models developed for this thesis.

EOS	δ	ε	Θ
Redlich & Kwong (1949)	b	0	$a\alpha(T_r)$
Wilson (1964)	b	0	$a\alpha(T_r)$
Soave (1972)	b	0	$a\alpha(T_r)$
Peng & Robinson (1976)	$2b$	$-b^2$	$a\alpha(T_r)$
Soave (1984)	$2c$	c^2	$a\alpha(T_r)$
Patel, Teja & Valderrama (1990)	$b+c$	$-bc$	$a\alpha(T_r)$
Twu et al. (1995)	$2b$	$-b^2$	$a\alpha(T_r)$

Table A.2. The temperature-dependent attractive terms for the cubic EOS available in the models developed for this thesis.

EOS	$\alpha(\omega,T_r)$
Redlich & Kwong (1949)	$1/T_r^{1/2}$
Wilson (1964)	$\left[1+(1.57+1.62\omega)(1/T_r-1)\right]T_r$
Soave (1972)	$\left[1+\left(0.48+1.574\omega-0.176\omega^2\right)\left(1-\sqrt{T_r}\right)\right]^2$
Peng & Robinson (1976)	$\left[1+\left(0.37464+1.54226\omega-0.2699\omega^2\right)\left(1-\sqrt{T_r}\right)\right]^2$
Soave (1984)	$\left[1+\left(0.4998+1.5928\omega-0.19563\omega^2+0.025\omega^2\right)\left(1-\sqrt{T_r}\right)\right]^2$
Patel, Teja & Valderrama (1990)	$\left[1+\left(0.46283+3.58230\omega Z_c+8.19417\omega^2 Z_c^2\right)\left(1-\sqrt{T_r}\right)\right]^2$
Twu et al. (1995)	$T_r^{-0.171813}e^{\left[0.125283\left(1-T_r^{1.77634}\right)\right]}+...$ $...\omega\left\{T_r^{-0.607352}e^{\left[0.511614\left(1-T_r^{2.20517}\right)\right]}-T_r^{-0.171813}e^{\left[0.125283\left(1-T_r^{1.77634}\right)\right]}\right\}$

The $\alpha(\omega,T_r)$ term listed in Table A.2 is referred to as the attractive term of the cubic EOS, and is the only temperature dependent term in the equations of state presented here. However, the attractive term is dependent on the reduced temperature, T_r, which is the temperature relative to the fluid critical temperature, T/T_c. In addition, the attractive term is a function of the Pitzer acentric factor, ω, which relates to the vapor pressure of a pure species measured at a fixed T_r.

Appendix A: Estimation of Physical Properties

Table A.3. Coefficients for the cubic EOS listed in Table A.1.

EOS	$\dfrac{ap_c}{(RT_c)^2}$	$\dfrac{bp_c}{RT_c}$	$\dfrac{cp_c}{RT_c}$
Redlich & Kwong (1949)	0.42748	0.08664	-
Wilson (1964)	0.42748	0.08664	-
Soave (1972)	0.42748	0.08664	-
Peng & Robinson (1976)	0.45724	0.0778	-
Soave (1984)	0.42188	0.08333	0.04167
Patel, Teja & Valderrama (1990)	$0.66121 - 0.76105Z_c$	$0.02207 + 0.20868Z_c$	$0.57765 - 1.87080Z_c$
Twu et al. (1995)	0.457236	0.0778	-

All of the parameters for the cubic EOS discussed thus far have been in terms of pure component properties—ω, T_c, and P_c. To accommodate fluid mixtures, mixing rules must be used that define the cubic EOS parameters based on the pure fluid parameters. While there are a number of more modern mixing rules available, many of which are reviewed by Valderrama [2], simple van der Waals-type rules [1, 3] have been used here:

$$b_m = \sum_{i=1}^{n} y_i b_i$$

$$\Theta_m = \sum_{i=1}^{n} \sum_{j=1}^{n} y_i y_j \Theta_{ij} \qquad (A.4)$$

$$\Theta_{ij} = \begin{cases} \Theta_i, & \text{if } i = j \\ \sqrt{\Theta_i \Theta_j}\,(1 - k_{ij}), & \text{if } i \neq j \end{cases}$$

Where y represents the mole fraction of the component, and n is the number of components in the system.

Appendix A: Estimation of Physical Properties

A.1.2 Estimation of Real Fluid Thermodynamic Properties

Thermodynamic properties or potentials are a measure of the amount of energy stored in a system. In this context, properties of interest are the enthalpy, H, entropy, S, heat capacity at constant pressure, C_p, and at constant volume C_v. With the exception of ideal-gas heat capacity, C_p^{ig}, these properties are not directly measurable; rather they are derived from pressure-volume-temperature relationships. Moreover, excepting C_p, it is not possible to estimate absolute values of these properties; only differences can be defined. These properties are referred to as state properties.

For ease of calculation, these state properties are estimated as departures from the ideal gas value. For any generic thermodynamic state property, M, the departure function is defined as:

$$M^d = M^{ig} - M \tag{A.5}$$

where M^{ig} is the ideal gas value of the thermodynamic property and M is the real gas value.

The departure functions for enthalpy and entropy are generated from the departure function for Gibbs free energy, G^d. It can be shown that [3]:

$$d\left(\frac{G^d}{RT}\right) = \frac{v^d}{RT}dp - \frac{H^d}{RT^2}dT$$

Thus at constant temperature:

$$d\left(\frac{G^d}{RT}\right) = \frac{v^d}{RT}dp$$

Appendix A: Estimation of Physical Properties

The departure function for volume is simply defined:

$$\frac{v^d}{RT} = \frac{(1-Z)}{p}$$

and, making the appropriate substitution:

$$\frac{G^d}{RT} = \int_0^p (1-Z)\frac{dp}{p}$$

The enthalpy departure function can then be derived:

$$\frac{H^d}{RT} = -T\left[\frac{\partial\left(G^d/RT\right)}{\partial T}\right]_p$$

$$= -T\left\{\frac{d}{dT}\left[\int_0^p (1-Z)\frac{dp}{p}\right]\right\}_p$$

$$= T\int_0^p \frac{dZ}{dT}\bigg|_p \frac{dp}{p}$$

And, from the definition of Gibbs free energy:

$$\frac{S^d}{R} = T\int_0^p \frac{dZ}{dT}\bigg|_p \frac{dp}{p} - \int_0^p (1-Z)\frac{dp}{p}$$

Therefore, based on Equation A.2:

$$\frac{G^d}{RT} = -\frac{\Theta}{RT\left(\delta^2 - 4\varepsilon\right)^{1/2}}\ln\left[\frac{2v + \delta - \left(\delta^2 - 4\varepsilon\right)^{1/2}}{2v + \delta + \left(\delta^2 - 4\varepsilon\right)^{1/2}}\right] + \ln\left[Z\left(1 - \frac{b}{v}\right)\right] - Z + 1 \qquad (A.6)$$

$$\frac{H^d}{RT} = \frac{T\,d\Theta/dT - \Theta}{RT\left(\delta^2 - 4\varepsilon\right)^{1/2}}\ln\left[\frac{2v + \delta - \left(\delta^2 - 4\varepsilon\right)^{1/2}}{2v + \delta + \left(\delta^2 - 4\varepsilon\right)^{1/2}}\right] - Z + 1 \qquad (A.7)$$

Appendix A: Estimation of Physical Properties

$$\frac{S^d}{R} = -\frac{d\Theta/dT}{R(\delta^2 - 4\varepsilon)^{1/2}} \ln\left[\frac{2v + \delta - (\delta^2 - 4\varepsilon)^{1/2}}{2v + \delta + (\delta^2 - 4\varepsilon)^{1/2}}\right] + \ln\left[Z\left(1 - \frac{b}{v}\right)\right] \qquad (A.8)$$

The derivative of Θ is the product of a and the derivative of the attractive term, α. Table A.4 shows the first derivatives of the attractive term for all of the equations of state discussed here. The $f(\omega)$ term present in several of the derivatives represents the polynomial term containing the Pitzer acentric factor and can be identified by comparing the results with those in Table A.2.

Table A.4. Derivatives of the attractive term used in the estimation of thermodynamic properties

EOS	$\partial\alpha/\partial T$
Redlich & Kwong (1949)	$-\dfrac{1}{2TT_r^{1/2}}$
Wilson (1964)	$\dfrac{\alpha}{T} - \dfrac{f(\omega)}{T}$
Soave (1972)	$-f(\omega)\sqrt{\dfrac{\alpha}{TT_c}}$
Peng & Robinson (1976)	$-f(\omega)\sqrt{\dfrac{\alpha}{TT_c}}$
Soave (1984)	$-f(\omega)\sqrt{\dfrac{\alpha}{TT_c}}$
Patel, Teja & Valderrama (1990)	$-f(\omega, Z_c)\sqrt{\dfrac{\alpha}{TT_c}}$
Twu et al. (1995)	$\dfrac{T_r^{-0.171813}}{T_c} e^{[0.125283(1 - T_r^{1.77634})]}\left(\dfrac{0.171813}{T_r} + 0.222545 T_r^{0.77634}\right)(\omega - 1) - ...$ $...\omega\dfrac{T_r^{-0.607352}}{T_c} e^{[0.511614(1 - T_r^{2.20517})]}\left(\dfrac{0.607352}{T_r} + 1.12820 T_r^{1.20517}\right)$

The equation for heat capacity at constant volume can be integrated following substitution of Equation A.2 to arrive at the departure function for C_v:

210

Appendix A: Estimation of Physical Properties

$$C_v^d = T \int_v^\infty \left[\left(\frac{\partial^2 p}{\partial T^2} \right)_v \right]_T dv$$

$$= \frac{T \, d^2\Theta \big/ dT^2}{\left(\delta^2 - 4\varepsilon \right)^{1/2}} \ln \left[\frac{2v + \delta - \left(\delta^2 - 4\varepsilon \right)^{1/2}}{2v + \delta + \left(\delta^2 - 4\varepsilon \right)^{1/2}} \right]$$

(A.9)

At ideal gas conditions, the difference between C_p and C_v simplifies to the ideal gas constant, R. This relationship is written fully as [1]:

$$C_p = C_v - T \left(\frac{\partial p}{\partial T} \right)_V^2 \Big/ \left(\frac{\partial p}{\partial V} \right)_T$$

Rewriting the above relationship in terms of departure functions results in the relation below, which can be integrated with the substitution of Equation A.2 for p:

$$C_p^d = R + T \int_v^\infty \left[\left(\frac{\partial^2 p}{\partial T^2} \right)_v \right]_T dv + T \left(\frac{\partial p}{\partial T} \right)_V^2 \Big/ \left(\frac{\partial p}{\partial V} \right)_T$$

$$= R + \frac{T \, d^2\Theta \big/ dT^2}{\left(\delta^2 - 4\varepsilon \right)^{1/2}} \ln \left[\frac{2v + \delta - \left(\delta^2 - 4\varepsilon \right)^{1/2}}{2v + \delta + \left(\delta^2 - 4\varepsilon \right)^{1/2}} \right] - T \frac{\left(\dfrac{R}{v - b} - \dfrac{d\Theta \big/ dT}{v^2 + \delta v + \varepsilon} \right)^2}{\dfrac{RT}{\left(v - b \right)^2} - \dfrac{\Theta \left(2v + \delta \right)}{\left(v^2 + \delta v + \varepsilon \right)^2}}$$

(A.10)

Solving Equations A.10 and A.9 to arrive at the constant volume and pressure heat capacity requires the second derivative of the attractive term of the cubic equation of state. The second derivatives are given in Table A.5.

Appendix A: Estimation of Physical Properties

Table A.5. Second derivatives of the attractive term used in the estimation of heat capacity.

EOS	$\partial\alpha/\partial T$
Redlich & Kwong (1949)	$-\dfrac{3}{4T^2 T_r^{1/2}}$
Wilson (1964)	0
Soave (1972)	$\dfrac{f(\omega)}{2T}\left(\dfrac{f(\omega)}{T_c}+\sqrt{\dfrac{\alpha}{TT_c}}\right)$
Peng & Robinson (1976)	$\dfrac{f(\omega)}{2T}\left(\dfrac{f(\omega)}{T_c}+\sqrt{\dfrac{\alpha}{TT_c}}\right)$
Soave (1984)	$\dfrac{f(\omega)}{2T}\left(\dfrac{f(\omega)}{T_c}+\sqrt{\dfrac{\alpha}{TT_c}}\right)$
Patel, Teja & Valderrama (1990)	$\dfrac{f(\omega,Z_c)}{2T}\left(\dfrac{f(\omega,Z_c)}{T_c}+\sqrt{\dfrac{\alpha}{TT_c}}\right)$
Twu et al. (1995)	$\dfrac{(\omega-1)}{TT_c}e^{\left[0.125283\left(1-T_r^{1.77634}\right)\right]}\left(0.096298T_r^{0.604527}-0.049526T_r^{2.38087}-...\right.$ $...\,0.201333T_r^{-1.171813}\left.\right)+\omega\dfrac{e^{\left[0.511614\left(1-T_r^{2.20517}\right)\right]}}{TT_c}\left(0.010754T_r^{0.597818}+...\right.$ $...\,1.27283T_r^{2.80299}+0.976228T_r^{-1.607352}\left.\right)$

To calculate thermodynamic properties of mixtures, the mixing rules presented as Equation A.4 have to be expanded to include the first and second derivatives of the attractive parameter. The mixing rule for the first derivative of T is given as Equation A.11, while the second derivative is listed as Equation A.12.

$$\frac{d\Theta_m}{dT}=\sum_{i=1}^{n}\sum_{j=1}^{n}y_i y_j\frac{d\Theta_{ij}}{dT}$$

$$\frac{d\Theta_{ij}}{dT}=\begin{cases}\dfrac{d\Theta_i}{dT}, & \text{if } i=j\\[2ex]\dfrac{(1-k_{ij})}{2\sqrt{\Theta_i\Theta_j}}\left(\Theta_i\dfrac{d\Theta_j}{dT}+\Theta_j\dfrac{d\Theta_i}{dT}\right), & \text{if } i\neq j\end{cases} \qquad (A.11)$$

Appendix A: Estimation of Physical Properties

$$\frac{d^2\Theta_m}{dT^2} = \sum_{i=1}^{n}\sum_{j=1}^{n} y_i y_j \frac{d^2\Theta_{ij}}{dT^2}$$

$$\frac{d^2\Theta_{ij}}{dT^2} = \begin{cases} \dfrac{d^2\Theta_i}{dT^2}, & \text{if } i = j \\[2ex] \dfrac{(1-k_{ij})}{2\sqrt{\Theta_i\Theta_j}}\left(\Theta_i\dfrac{d^2\Theta_j}{dT^2} + \dfrac{d\Theta_j}{dT}\dfrac{d\Theta_i}{dT} + \Theta_j\dfrac{d^2\Theta_i}{dT^2}\right) - \cdots \\[2ex] \cdots \dfrac{(1-k_{ij})}{4\Theta_i\Theta_j\sqrt{\Theta_i\Theta_j}}\left(\Theta_i\dfrac{d\Theta_j}{dT} + \Theta_j\dfrac{d\Theta_i}{dT}\right)^2, & \text{if } i \neq j \end{cases}$$

(A.12)

A.1.3 *Estimation of Ideal Gas Properties*

As discussed in Section A.1.2, thermodynamic properties of real fluids are calculated as departures from the ideal gas behavior. Thus, this section briefly identifies the methods used to calculate the ideal-gas values of enthalpy, entropy, and constant pressure heat capacity.

Aly and Lee [4] proposed a set of accurate self-consistent equations for to calculating enthalpy, entropy and heat capacity. The form of the Aly and Lee equations have been adopted by many organizations, such as the AIChE sponsored DIPPR® 801 project, which maintains a database of critically evaluated process design data. The equations for heat capacity, enthalpy, and entropy are reproduced below for convenience.

$$C_p^{ig} = A + B\left[\frac{C/T}{\sinh(C/T)}\right]^2 + D\left[\frac{(E/T)}{\cosh(E/T)}\right]^2$$

(A.13)

$$H^{ig} = \int_0^T C_p^{ig}\, dT$$

$$= AT + BC\coth\left(\frac{C}{T}\right) - DE\tanh\left(\frac{E}{T}\right) + HCON$$

(A.14)

Appendix A: Estimation of Physical Properties

$$S_{ig} = \int_0^T \frac{C_p^{ig}}{T} dT - \ln \frac{p}{p_\circ}$$

$$= A\ln(T) + B\left\{\frac{C}{T}\coth\left(\frac{C}{T}\right) - \ln\left[\sinh\left(\frac{C}{T}\right)\right]\right\} - ...$$ (A.15)

$$...D\left\{\frac{E}{T}\tanh\left(\frac{E}{T}\right) - \ln\left[\cosh\left(\frac{E}{T}\right)\right]\right\} + SCON - \ln\frac{p}{p_\circ}$$

In Equations A.13, A.14, and A.15, tabulated constants are represented by variables A through E, and $HCON$ and $SCON$ are integration constants, the value of which depends on the reference enthalpy and entropy chosen. The tabulated constants can be found in a number of different data compilations such as the DIPPR® 801 database or National Institute of Standards and Technology TRC publications.

A.1.4   Estimation of Transport Properties

Estimation of transport properties is important for understating flow and heat transfer processes, such as those encountered in CO_2 pipelines and injection strings. Transport properties of interest in this context are viscosity and thermal conductivity. The methods used to estimate viscosity and thermal conductivity of real gases in this work were proposed by Chung et al., [5] and modified for high pressure application by Reid, Prausnitz, and Poling [1]. However, the details of the calculation methods will be not be reproduced here as, while being relatively simple to implement, the calculation of thermal conductivity and viscosity involve over a dozen equations each.

A.1.5   Comparison of Cubic EOS

Designing CO_2 transport and injection systems requires most accurate properties data available. Thus, the best cubic EOS for design applications will be the most accurate across the range of conditions that are encountered in transport and injection systems. As

Appendix A: Estimation of Physical Properties

discussed in Chapter 2, CO_2 pipeline systems operates at pressures between

approximately 8 MPa and 15 Mpa at roughly atmospheric temperatures. In the CO_2

injection string, similar ranges of pressure would likely be encountered, but the

temperatures will range from atmospheric to temperatures on the order of 100^oC.

The accuracy of the EOS described here was assessed by comparing physical properties

of pure-CO_2 calculated by the parameterizations against the same properties calculated by

the EOS of Span and Wagner[6] and the transport property correlations of Vesovic et al.

[7]. The EOS of Span and Wagner is considered the "reference" EOS for pure CO_2 and is

estimated to be within ±0.03% to ±0.05% of the true value for compressibility. Similarly,

the correlations of Vescovic et al. are the reference correlations for viscosity and thermal

conductivity, and are estimated to have an error of less than 2% in range of conditions

considered.

The physical properties compared for each cubic EOS in Figure A.1 are, from left to

right, the compressibility, enthalpy, entropy, heat capacity (at both constant pressure and

constant volume), viscosity, and thermal conductivity. Each parameterization was

assessed across the same range of pressure—7 MPa to 15 MPa—and the same range of

temperature—between 270 K and 370 K.

Appendix A: Estimation of Physical Properties
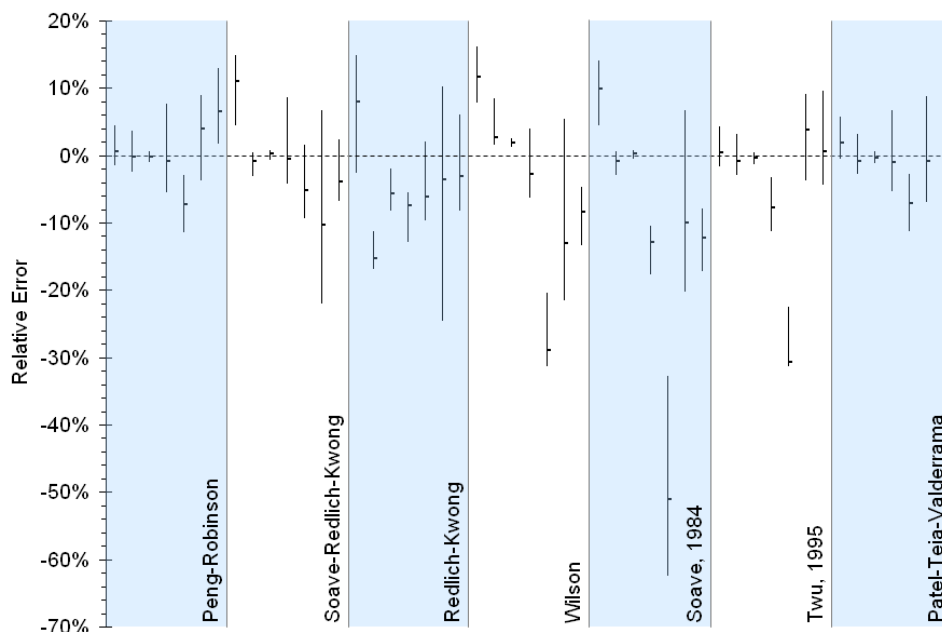
Figure A.1. Relative error (i.e., the difference between the estimated and actual values, divided by the actual value) for seven parameters, estimated with the seven cubic EOS presented here. For each EOS, the seven lines correspond to (from left to right) Z, H, S, C_p, C_v, η, and λ. The upper end of each line corresponds to the first quartile; the lower end to the third quartile; and, the dash-mark to the median.

The measures compared in Figure A.1 are the medial, 25th percentile, and 75th percentile relative errors. The 25th and 75th percentile errors have been chosen as a basis for comparison as opposed to the minimum and maximum errors for two reasons: the range of temperatures includes the critical point where all EOS are notoriously inaccurate, and; the enthalpy crosses zero in this range of conditions, and thus is subject to extremely large relative errors (as the relative error is normalized to the absolute value of the enthalpy). Table A.6 presents the numerical results in more detail.

Table A.6. The median, first and third quartile relative error for seven estimated parameters for all seven cubic EOS presented here.

Parameter	Measure	PR	SRK	RK	W	S84	T95	PTV
	Median	0.5	11.0	8.0	11.7	9.9	0.5	1.8
Z Error	Q1	-1.5	4.4	-2.6	7.8	4.4	-1.7	-0.5
	Q3	4.4	14.9	14.9	16.2	14.0	4.2	5.8
	Median	-0.3	-0.9	-15.4	2.7	-0.8	-0.8	-0.8
H Error	Q1	-2.5	-3.1	-16.9	1.5	-3.0	-3.0	-2.8
	Q3	3.7	0.4	-11.4	8.4	0.6	3.1	3.2
	Median	-0.2	0.2	-5.7	1.9	0.3	-0.4	-0.3
S Error	Q1	-1.1	-0.7	-8.2	1.3	-0.6	-1.3	-1.2
	Q3	0.5	0.7	-1.9	2.6	0.8	0.4	0.6
	Median	-0.9	-0.5	-7.5	-2.8	-12.9	-7.8	-1.1
C_P Error	Q1	-5.5	-4.3	-12.8	-6.4	-17.7	-11.3	-5.3
	Q3	7.7	8.6	-5.4	4.0	-10.5	-3.3	6.7
	Median	-7.3	-5.2	-6.1	-28.9	-51.0	-30.7	-7.2
C_V Error	Q1	-11.5	-9.4	-9.7	-31.3	-62.5	-31.4	-11.3
	Q3	-2.3	1.6	2.1	-20.5	-32.8	-22.6	-2.8
	Median	4.0	-10.4	-3.6	-13.0	-10.0	3.8	-0.8
η Error	Q1	-3.8	-22.0	-24.6	-21.5	-20.3	-3.7	-6.9
	Q3	9.0	6.7	10.2	5.4	6.7	9.2	8.7
	Median	6.5	-3.9	-3.1	-8.4	-12.2	0.7	5.7
λ Error	Q1	1.8	-6.8	-8.2	-13.3	-17.3	-4.4	1.0
	Q3	12.9	2.4	6.0	-4.7	-7.9	9.6	9.8

Based on this analysis, the EOS proposed by Peng and Robinson (PR) is the most accurate, followed closely by the Patel-Teja-Valderamma (PTV) EOS. This agrees with general process engineering industry practice, in which the Peng-Robinson EOS is the standard. Thus, while all seven of the equations of state are available in each model developed in this thesis, all of the models default to using the PR EOS, and all of the results presented here are based on properties predicted with the PR EOS.

A.2   Properties of Crude Oils

Crude oils are complex mixtures of hydrocarbons, ranging from light ends (e.g., CH_4 and C_2H_6) to polyaromatic hydrocarbons (e.g., pyrene), organometalic compounds (e.g.,

porphyrins), and heteroatomic compunds (e.g. thiophene). While advances have been

made in lumping large groups of constituents into pseudocomponents, and modeling

crude oils using cubic EOS [2], this requires assay results for the specific oil. The

alterative to using EOS is to use generic correlations for crude oil properties.

In the modeling work performed in this thesis, only two crude oil properties are of

interest: oil viscosity and oil formation volume factor. Density of the crude oil (i.e., the

API gravity), and the gas-oil ratio must be known to asses these properties.

A.2.1   *Estimation of Oil Viscosity*

Crude oil is categorized as "live" or "dead" depending on whether the oil contains gases

in solution. At initial reservoir conditions, oil is considered to be live and, thus, contains

light ends that are liberated as the reservoir pressure falls and oil is brought to the surface.

Correlations for live-oil viscosity are based on the dead-oil viscosity, which is a

correlated with temperature and API gravity. Live oil viscosity is then a function of the

dead oil viscosity and the gas-oil ratio, R_s (i.e., the ratio of produced gas to produced oil).

The correlations tested for the dead-oil viscosity are listed in Table A.7, including the

region of the oils used in developing the correlation. Typical results from at each

correlation at two temperatures for a range of API gravities are shown in Figure A.2.

Table A.7. The correlations tested for dead-oil viscosity and the valid temperature and API gravity ranges for these correlations.

Correlation	Oil Region	Temperature Range (^{o}F)	API Gravity Range
Beal [8]	California	100 – 220	10.1 – 52.2
Beggs & Robinson [9]	N/A	70 – 295	16 – 58
Glaso [10]	North Sea	100 – 300	20.1 – 45.8
Egbogah & Ng [11]	N/A	41 – 176	5 – 58
Labedi [12]	African	100 – 306	32.2 – 48.0
Kartoatmodjo & Schmidt [13]	Worldwide	75 – 320	14.4 – 58.9
Petrosky & Farshad [14]	Gulf of Mexico	114 – 288	25.4 – 46.1
Elsharkawy & Alikhan [15]	Middle East	100 – 300	19.9 – 48.0
Naseri et al. [16]	Iran	105 – 295	17 – 44
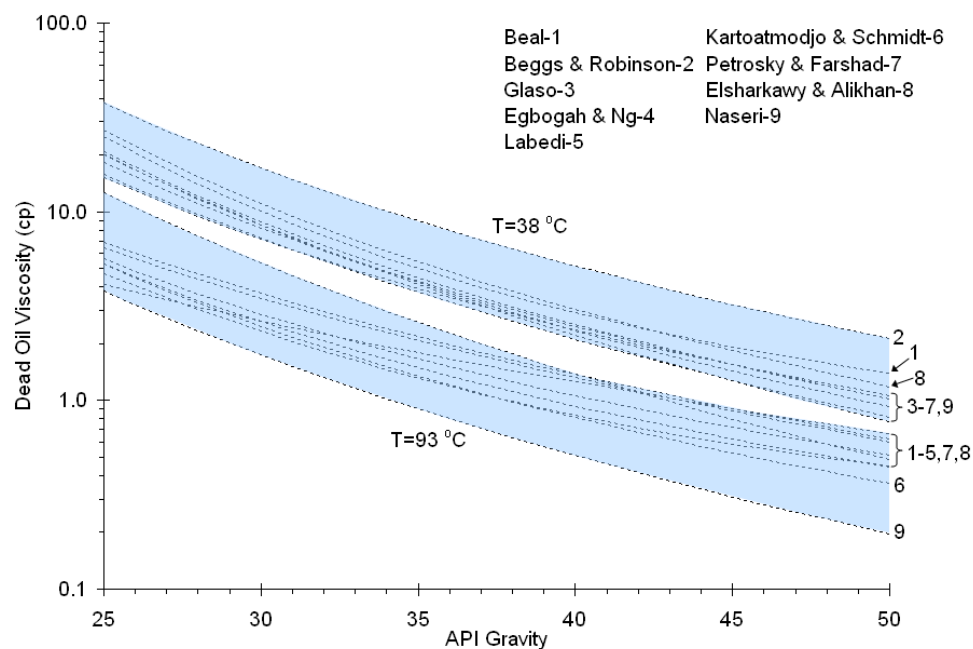
Figure A.2. Typical results for the dead-oil viscosity correlations available in the models, showing the range of possible viscosities depending on the correlation chosen, the API gravity, and the system temperature.

The viscosity estimated with these correlations is strongly dependent on both the system temperature and the type of crude oil used to develop the correlation, as can be seen in

Appendix A: Estimation of Physical Properties

Figure A.2 (note the logarithmic scale). However, even when these factors are known, the estimated dead-oil viscosity can only be considered an order of magnitude estimate [17].

Correlations for live-oil viscosity are listed in Table A.8, including the region of the oils used in developing the correlation and the valid range of gas-oil ratios for the correlation (in industry standard units of standard cubic feet, scf, per stock-tank barrel, STB). Typical results from each correlation for two temperatures and a range of gas-oil ratios are shown in Figure A.3.

Table A.8. The correlations tested for live-oil viscosity and the valid temperature and API gravity ranges for these correlations.

Correlation	Number	Region	R_s Range (scf/STB)
Chew & Connally [18]	1	California	51 – 3544
Beggs & Robinson [9]	2	N/A	20 – 2,070
Kartoatmodjo & Schmidt [13]	3	North Sea	0 – 2,890
Petrosky & Farshad [14]	4	Middle East	21 – 1,885
Elsharkawy & Alikhan [15]	5	African	10 – 3,600
Dindoruk & Christman [19]	6	Worldwide	133 – 3,050
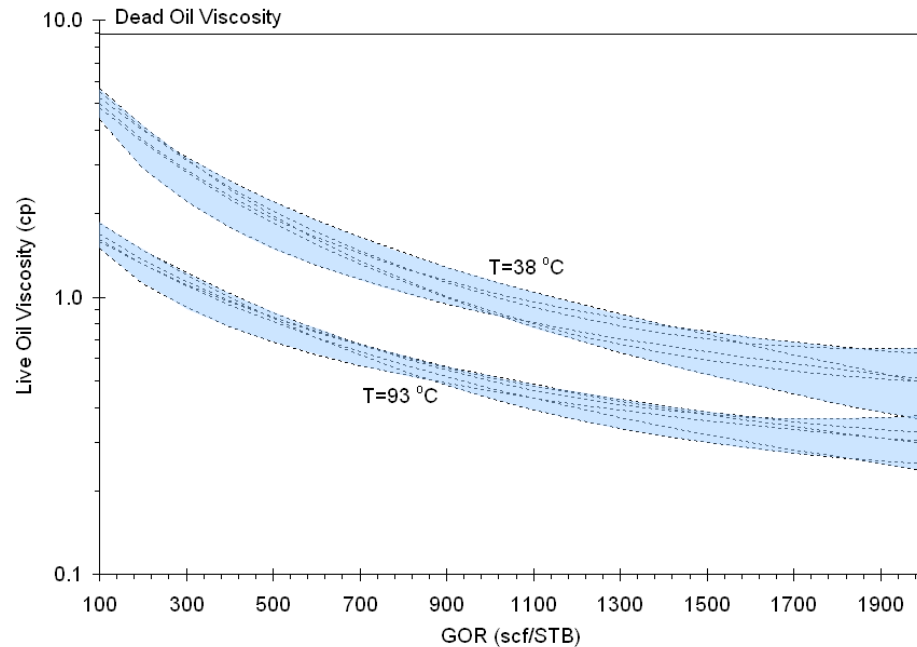
Figure A.3. Typical results for the live-oil viscosity correlations available in the models, showing the range of possible viscosities depending on the correlation chosen, R_s, and the system temperature.

For a given dead oil viscosity and gas-oil ratio, variation in the predicted live-oil viscosity between correlations is much smaller than the corresponding variation for the dead-oil viscosity. Moreover, the large difference between dead-oil viscosities (for a given API gravity) estimated by the different correlations shown in Figure A.2 is reduced somewhat in the calculation of the live-oil viscosity. For example, at 38 ^{o}C, a 30° API crude oil could have a viscosity ranging from 17 cp to 7 cp depending on the correlation used. Under saturated conditions, the same oil with a gas-oil ratio of 1100 scf/STB would have a live-oil viscosity between 1.6 cp and 0.7 cp, depending on the live-oil correlation chosen.

Appendix A: Estimation of Physical Properties

A.2.2   Estimation of Oil Formation Volume Factor

As discussed previously, oil at reservoir conditions contains dissolved gas (in proportion

to the gas-oil ratio). At the surface, where the oil is under near-atmospheric pressures and

temperatures (i.e., stock-tank conditions), gas is liberated from solution, and the volume

of oil decreases relative to the volume at reservoir conditions. The ratio of oil volume at

reservoir conditions to volume at stock-tank conditions is known as the formation volume

factor, B_o.

The correlation for the formation volume factor used in this work is the Standing

correlation (reproduced in [17]). Using the gas-oil ratio, R_s, the gas and oil specific

gravities, γ_g and γ_o, respectively, and the reservoir temperature in °F, T_F, the formation

volume factor at or below the bubble point, B_{ob}, can be predicted:

$$B_{ob} = 0.9759 + 12\left(10^{-5}\right)C_{Bob}^{1.2}$$
$$C_{Bob} = R_s\sqrt{\frac{\gamma_g}{\gamma_o}} + 1.25T_F$$

$$(A.16)$$

At pressures above the bubble point, the formation volume factor can be estimated from

Equation A.16 using:

$$B_o = B_{ob}\exp\left[\kappa_o\left(p_b - p\right)\right]$$

$$(A.17)$$

Where, p_b is the bubble point pressure in psia, and κ_o is the isothermal compressibility of

the oil (psia^{-1}).

When bubble point pressure and isothermal compressibility are not known, they can be

calculated using Equations A.18 and A.19, developed by Standing, and Vazquez and

Beggs [17].

Appendix A: Estimation of Physical Properties

$$p_b = 18.2(C_{pb} - 1.4)$$

$$C_{pb} = 10^{(0.00091T_F - 0.0125\gamma_{API})}\left(\frac{R_s}{\gamma_g}\right)^{0.83} \quad \text{(A.18)}$$

$$\kappa_o = \frac{(-1443 + 5R_s + 17.2T_F - 1180\gamma_g + 12.61\gamma_{API})}{10^5 p} \quad \text{(A.19)}$$

The estimated bubble point is estimated to and accuracy of approximately 15%, while the estimated isothermal compressibility may be in error by as much as 50% at high pressures (i.e., approaching the maximum pressure of the correlation, which is 9500 psia or 66 MPa) [17].

A.3   References

1.   Poling, B.E., J.M. Prausnitz, and J.P. O'Connell, *The Properties of Gases and Liquids*. 5 ed. 2001: McGraw-Hill Book Company.
2.   Valderrama, J.O., *The State of the Cubic Equations of State.* Industrial and Engineering Chemistry Research, 2003. **42**(8): p. 1603-1618.
3.   Smith, J.M., H.C. van Ness, and M.M. Abbott, *Introduction to Chemical Engineering Thermoynamics*. 6 ed. 2001, New York, NY: McGraw-Hill Higher Education. 660.
4.   Aly, F.A. and L.L. Lee, *Self-consistent equations for calculating the ideal gas heat capacity, enthalpy, and entropy.* Fluid Phase Equilibria, 1981. **6**(3-4): p. 169-179.
5.   Chung, T.H., et al., *Generalized Multiparameter Correlation for Nonpolar and Polar Fluid Transport Properties.* Industrial and Engineering Chemistry Research, 1988. **27**: p. 671-679.
6.   Span, R. and W. Wagner, *A New Equation of State for Carbon Dioxide Covering the Fluid Region from the Triple Point Temperature to 1100K at Pressures up to 800 Mpa.* Journal of Physical and Chemical Reference Data, 1996. **25**(6): p. 1509-1596.
7.   Vesovic, V., et al., *The Transport-Properties of Carbon-Dioxide.* Journal of Physical and Chemical Reference Data, 1990. **19**(3): p. 763-808.
8.   Beal, C., *The Viscosity of Air, Water, Natural Gas, Crude Oil and Its Associated Gases at Oil Field Temperatures and Pressures.* Transactions of the American Institute of Mining and Metallurgical Engineers, 1946. **165**: p. 94-115.
9.   Beggs, H.D. and J.R. Robinson, *Estimating the Viscosity of Crude Oil Systems.* Journal of Petroleum Technology, 1975: p. 1140-1141.
10.   Glaso, O., *Generalized Pressure-Volume-Temperature Correlations.* Journal of Petroleum Technology, 1980: p. 785-795.

11. Egbogah, E.O. and J.T. Ng, *An improved temperature-viscosity correlation for crude oil systems.* Journal of Petroleum Science and Engineering, 1990. **5**: p. 197-200.

12. Labedi, R., *Improved correlations for predicting the viscosity of light crudes.* Journal of Petroleum Science and Engineering, 1992. **8**: p. 221-234.

13. Kartoatmodjo, T. and Z. Schmidt, *Large data bank improves crude physical property correlations.* Oil and Gas Journal, 1994. **92**(27): p. 51-55.

14. Petrosky, G.E. and F.F. Farshad, *Viscosity Correlations for Gulf of Mexico Crude Oils*, in *Production Operations Symposium*. 1995, Society of Petroleum Engineers: Oklahoma City, OK.

15. Elsharkawy, A.M. and A.A. Alikhan, *Models for predicting the viscosity of Middle East crude oils.* Fuel, 1999. **78**: p. 891-903.

16. Naseri, A., M. Nikazar, and S.A. Mousavi Dehghani, *A correlation approach for prediction of crude oil viscosities.* Journal of Petroleum Science and Engineering, 2005. **47**: p. 163-174.

17. McCain, W.D., *Reservoir-Fluid Property Correlations-State of the Art.* Society of Petroleum Engineers Reservoir Engineering, 1991: p. 266-271.

18. Chew, J.N. and C.A. Connally, *A Viscosity Correlation for Gas-Saturated Crude Oils.* Transactions of the American Institute of Mining and Metallurgical Engineers, 1959. **216**: p. 23-25.

19. Dindoruk, B. and P.G. Christman, *PVT Properties and Viscosity Correlations for Gulf of Mexico Oils.* Society of Petroleum Engineers Reservoir Evaluation and Engineering, 2004: p. 427-437.

Appendix B: Oil Recovery Methods

Oil recovery methods can be grouped into conventional and enhanced methods. Conventional recovery involves production of oil through natural reservoir pressure caused by gas expansion (i.e., gas drive) or water influx (i.e., waterdrive), through pumping (i.e., artificial lift). Conventional recovery also encompasses waterflooding, where water is injected into the reservoir to maintain reservoir pressure and displace residual oil. Conventional recovery ceases when the oil production rate is too low to offset the cost of operating the field. At this point, typically 40% to 60% of the original oil in place (OOIP) remains trapped in the reservoir [1].

Enhanced oil recovery (EOR) methods allow additional oil to be economically extracted from the reservoir above that extracted via conventional production, and can generally be categorized into three broad classes: thermal, chemical, and gas [2]. Thermal methods include steam and hot water injection, and in-situ combustion. Chemical recovery methods include polymer and surfactant flooding. Gas methods include injection of both miscible and immiscible gases, such as light hydrocarbons (e.g., propane, butane), CO_2, and flue gases.

CO_2 can be used in two distinct EOR processes: immiscible and miscible flooding. In the immiscible CO_2-flood process, the CO_2 acts to improve oil recovery by dissolving in the oil, causing it to swell, and reducing both density and viscosity of the oil [2]. In the miscible CO_2-flooding process, reservoir pressure is high enough to cause the CO_2 to become completely miscible with the reservoir oil, greatly increasing displacement efficiency in areas contacted by the displacing fluid [2, 3].

Appendix B: Oil Recovery Methods

Under field conditions, miscible CO_2-flooding allows an additional 10 to 15% of the OOIP to be recovered [1]. Immiscible CO_2-flooding does not increase recovery efficiencies to the same extent as miscible flooding and, to date, has been employed infrequently [4]. However, the miscible CO_2-flooding process can only be implemented on reservoirs that meet a number of screening criteria. Table B.1, describes screening criteria suggested by a number of authors.

For miscibility to develop between the reservoir oil and injected CO_2, the reservoir pressure must be greater than the minimum miscibility pressure (MMP) for the reservoir oil. This criteria is explicitly addressed by the criteria proposed by the National Petroleum Council [5] and Shaw and Bachu [5]. All of the other authors criteria presented in Table B.1 imply that MMP must be greater than reservoir pressure. In addition to MMP, oil density (reflected by the API gravity) and residual saturation to waterflooding, S_{or}, are important screening criteria.

A large number of papers discuss methods to estimate MMP (e.g. Holm and Josendal [6], Yellig and Metcalfe [7], Wang and Orr [8]). Additionally, an overview of miscibility, laboratory measurement of MMP, and MMP predictive methods can be found in monographs by Stalkup [3] and Green and Willhite [2].

Table B.1. Proposed screening criteria for miscible CO_2-flooding compiled by Shaw and Bachu [9], modified to include criteria proposed by Stalkup [3] and Kovscek [10], as well as a more recent NPC report [5].

Criterion	Geffen (1973)	Lewin et al. (1976)	McRee (1977)	Iyoho (1978)	OTA (1978)	Carcoana (1982)	Stalkup (1983)	Taber & Martin (1983)	NPC (1984)	Taber et al. (1997)	Shaw & Bachu (2001)	Kovscek (2002)
Crude Oil Criteria												
ρ (°API)	>30	>30	>35	30-45	i) <27 ii) 27-30 iii) >30	>40	>27	>26	>25	i) 22-27.9 ii) 28-31.9 iii) 32-39.9 iv) >40	27-48	>22
μ (mPa s)	<3	<12	<5	<10	<12	<2	<12	<15		<10		
Reservoir Criteria												
T (°C)						<91					31-120	
p (MPa)	7.6	10.3				8.3						
G (kPa/m)												<17.4
k (md)			>5	>10		>1						
d (m)		>914	>607	>762	i) >2195 ii) >1676 iii) >762	< 2987		>607		i) >1219 ii) >1006 iii) >853 iv) >762		
S_{or}	>0.25	>0.25	>0.25	>0.25		>0.30	>0.20	>0.30		>0.20	>0.25	
C (kg/m³)												>10
kh (m³)												>10^{-14}
$S_o\Phi$												>0.05
p/MMP									>1		>0.95	

B.1 References

1. Blunt, M.F., F.J. Fayers, and F.M. Orr, *Carbon Dioxide in Enhanced Oil Recovery.* Energy Conversion & Management, 1993. **34**(9-11): p. 1197-1204.
2. Green, D.W. and G.P. Willhite, *Enhanced Oil Recovery*. SPE Textbook Series. 1998, Richardson, TX: Society of Petroleum Engineers. 545.
3. Stalkup Jr., F.I., *Miscible Displacement*. 1983, Dallas: Society of Petroleum Engineers. 204.
4. Moritis, G., *CO$_2$ injection gains momentum.* Oil & Gas Journal, 2006. **104**(15): p. 37-41.
5. National Petroleum Council, *Enhanced Oil Recovery*. 1984.
6. Holm, L.W. and V.A. Josendal, *Mechanisms of Oil Displacement by Carbon Dioxide.* Journal of Petroleum Technology, 1974(December): p. 1427-1438.
7. Yellig, W.F. and R.S. Metcalfe, *Determination and Prediction of CO2 Minimum Miscibility Pressures.* Journal of Petroleum Technology, 1980: p. 160-168.
8. Wang, Y. and J.F.M. Orr, *Analytical calculation of minimum miscibility pressure.* Fluid Phase Equilibria, 1997. **139**(1-2): p. 101-124.
9. Shaw, J. and S. Bachu, *Screening, evaluation, and ranking of oil reservoirs suitable for CO$_2$-flood EOR and carbon dioxide sequestration.* Journal of Canadian Petroleum Technology, 2002. **41**(9): p. 51-61.
10. Kovscek, A.R., *Screening Criteria for CO$_2$ Storage in Oil Reservoirs.* Petroleum Science and Technology, 2002. **20**(7-8): p. 841-866.

Appendix C: Numerical Modeling of the Wellbore Environment

Estimating the pressure drop across a CO_2 injection well (or any segment of an injection well) begins with a total energy balance on the flowing fluid, which can be written:

$$dH + \frac{g}{g_c}dh + \frac{u}{g_c}du = dQ + dW \qquad (C.1)$$

In Equation C.1: H is the fluid enthalpy; h is height relative to the well bottom; g is acceleration due to gravity; g_c is a conversion factor for converting force units (in SI, equal to unity); u is fluid velocity; Q is heat transfer; and, W is flow work.

Because there is no flow work being done (i.e., pump or turbine work) and the kinetic energy change is negligible, both dW and du can be eliminated. Thus, Equation C.1 accounts for pressure-volume work (dH), changes in potential energy (dh), and heat transfer. Equation C.1 can then be integrated in the direction of flow (i.e., from point 1, upstream, to point 2, downstream) to yield:

$$H_2 - H_1 + \frac{g}{g_c}\left(h_2 - h_1\right) = Q \qquad (C.2)$$

Pressure does not appear explicitly in Equation C.2; however, enthalpy is a function of pressure and temperature. Since the upstream pressure and temperature are known, the upstream enthalpy can be calculated (see Appendix A for the analytical relationship between enthalpy, pressure, temperature). Thus, assuming the heat transfer term is known, Equation C.2 can be rearranged to solve for the enthalpy of the downstream fluid.

Because the downstream enthalpy is a function of pressure and temperature, a second energy balance must be used to determine the downstream pressure. Equation C.3 shows

Appendix C: Numerical Modeling of the Wellbore Environment

the differential form of this mechanical energy balance. Equation C.3 accounts for

changes in kinetic energy, pressure-volume work, changes in potential energy, and

energy loss due to skin friction in a flow system.

$$\frac{c}{g_c v} du + \frac{1}{v} dp + \frac{g}{g_c v^2} dh + \frac{2 f_F c^2}{g_c D_i} dL = 0 \qquad (C.3)$$

In Equation C.3: c is a constant equal to the product of density, ρ, and fluid velocity, u; g

is acceleration due to gravity; g_c is the conversion factor converting force units (in the SI

system of units, this is equal to unity); v is the specific volume of fluid; p is pressure; f_F is

the fanning friction factor; D_i is the pipeline diameter; and L is tubing length.

Following the derivation in Section 2.1.2, Equation C.3 is simplified (i.e., assuming

kinetic energy changes are negligible and average compressibility), and solved for

downstream pressure resulting in:

$$p_2 = \sqrt{p_1^2 - \frac{2g p_{ave}^2 M (h_2 - h_1)}{g_c Z_{ave} R T_{ave}} - \frac{64 Z_{ave} R T_{ave} f_F \dot{m}^2 \Delta L}{g_c \pi^2 D_i^5 M}} \qquad (C.4)$$

where: p_{ave} is average pressure; T_{ave} is average temperature; R is the ideal gas constant; M

is the fluid molecular weight; Z_{ave} is the fluid compressibility calculated at p_{ave} and T_{ave};

$\dot{m}$ is the mass flow rate; and, ΔL is the tubing segment length.

The average temperature, T_{ave}, required in Equation C.4 is calculated using Equation C.5.

Because pressure varies non-linearly along the pipeline, the average pressure, P_{ave}, is

calculated using Equation C.6 [1].

$$T_{ave} = \frac{T_1 + T_2}{2} \qquad (C.5)$$

Appendix C: Numerical Modeling of the Wellbore Environment

$$P_{ave} = \frac{2}{3}\left(p_2 + p_1 - \frac{p_2 p_1}{p_2 + p_1}\right) \qquad (C.6)$$

Using Equation C.4, the downstream pressure can be calculated following the iterative method described in Section 2.1.2. Thus, both pressure and enthalpy are known at the well bottom, and temperature can therefore be estimated using a root finding algorithm (e.g., van Wijngaarden-Deker-Brent) on Equation C.5.

As noted previously, the heat transfer term in Equation C.2 must also be calculated to arrive at the BHIP. The heat transfer calculations follow the approach outlined by Willhite [2] with the solution for transient radial heat transfer to the surrounding rock proposed by Ramey [3]. Figure C.1 shows the important parameters relevant to the heat transfer problem over a cross-section of the wellbore.

As Figure C.1 shows, the wellbore is simplified to: tubing, containing the flowing fluid; an annulus between the casing and tubing, filled with brine; cement between the formation and the sandface; and, the surrounding rock. Resistance to heat transfer from the tubing and casing is ignored, as the conductivity of the steel used in the tubing and casing is at least an order of magnitude larger than any other conductivity in the system.
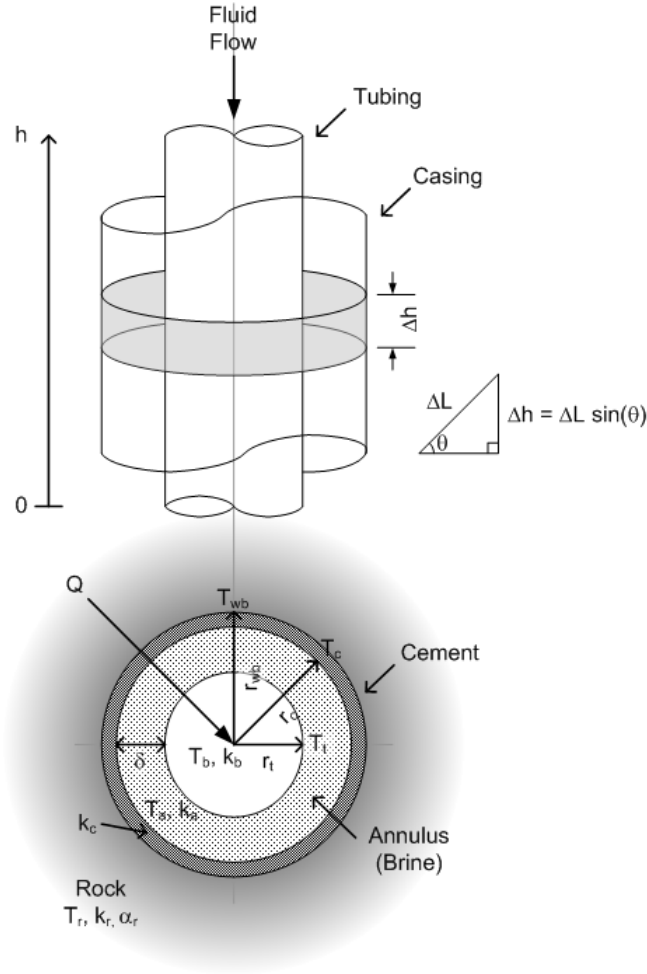
Figure C.1. Cross-section of the wellbore showing important parameters relevant to the wellbore heat transfer problem.

If only radial heat transfer is considered, the heat transfer between the flowing fluid and the wellbore can be written as:

$$Q = \frac{(T_r - T_b)}{\sum R_{th}} \qquad \text{(C.7)}$$

In Equation C.7, T_b is the bulk temperature of the flowing fluid, T_r is the temperature of the undisturbed rock, and R_{th} is resistance to heat transfer. In this case, the bulk temperature of the flowing fluid is calculated as the average of the upstream and

Appendix C: Numerical Modeling of the Wellbore Environment

downstream temperatures (i.e, Equation C.5). If the temperature of the rock is higher than

the temperature of the flowing fluid, energy is transferred to the fluid, and q is greater

than zero.

The temperature of the undisturbed rock at depth, d, is calculated using the geothermal

gradient, G:

$$T_r = T_s + Gd \qquad (C.8)$$

where, T_s is the surface temperature and G is typically approximately 25 $^{\circ}$C per kilometer

[4, 5].

Neglecting radiative heat transfer between the tubing and casing, the expression for

resistance to heat transfer needed in Equation C.7 is derived by Willhite as [2]:

$$\sum R_{th} = \frac{1}{\pi \Delta L k_b N u_D} + \frac{\ln(r_c/r_t)}{2\pi \Delta L\, k_a N u_\delta} + \frac{\ln(r_{wb}/r_c)}{2\pi \Delta L\, k_c} + \frac{f(t)}{2\pi \Delta L\, k_r} \qquad (C.9)$$

where: k is the thermal conductivity of the bulk tubing fluid (b), annulus fluid (a),

concrete (c), and rock (r); Nu is the Nusselt number with characteristic length of the

tubing diameter (D) and tubing-annulus gap (δ); r are the radii defined in Figure C.1; and,

$f(t)$ is the time function developed by Ramey [3].

From left to right, the terms in Equation C.9 account for heat transfer between the

flowing fluid and the tubing (via forced convection), across the annular space (via natural

convection), and across the cement into the formation (via conduction). The Nusselt

number for forced convection is calculated using the correlation of Sieder & Tate [6] and

the for natural convection, using the correlation of MacGregor & Emery [7]. Properties of

the casing fluid, required to calculate the annular Nusselt number, are estimated using the correlations of Batzle & Wang presented by Adams & Bachu [8].

The BHIP and bottomhole temperature are calculated using a finite-difference method: the wellbore is broken into n segments, and the pressure and temperature are calculated at the bottom of each segment (starting from the wellhead conditions) using Equations C.2, C.4, C.7. Because the heat transfer term (Equation C.7) is a function of the flowing bulk fluid properties, which are related by temperature and pressure to the downstream enthalpy calculated from Equation C.2, an iterative solution method is required for each segment. The iteration scheme is illustrated is Figure C.2

Appendix C: Numerical Modeling of the Wellbore Environment

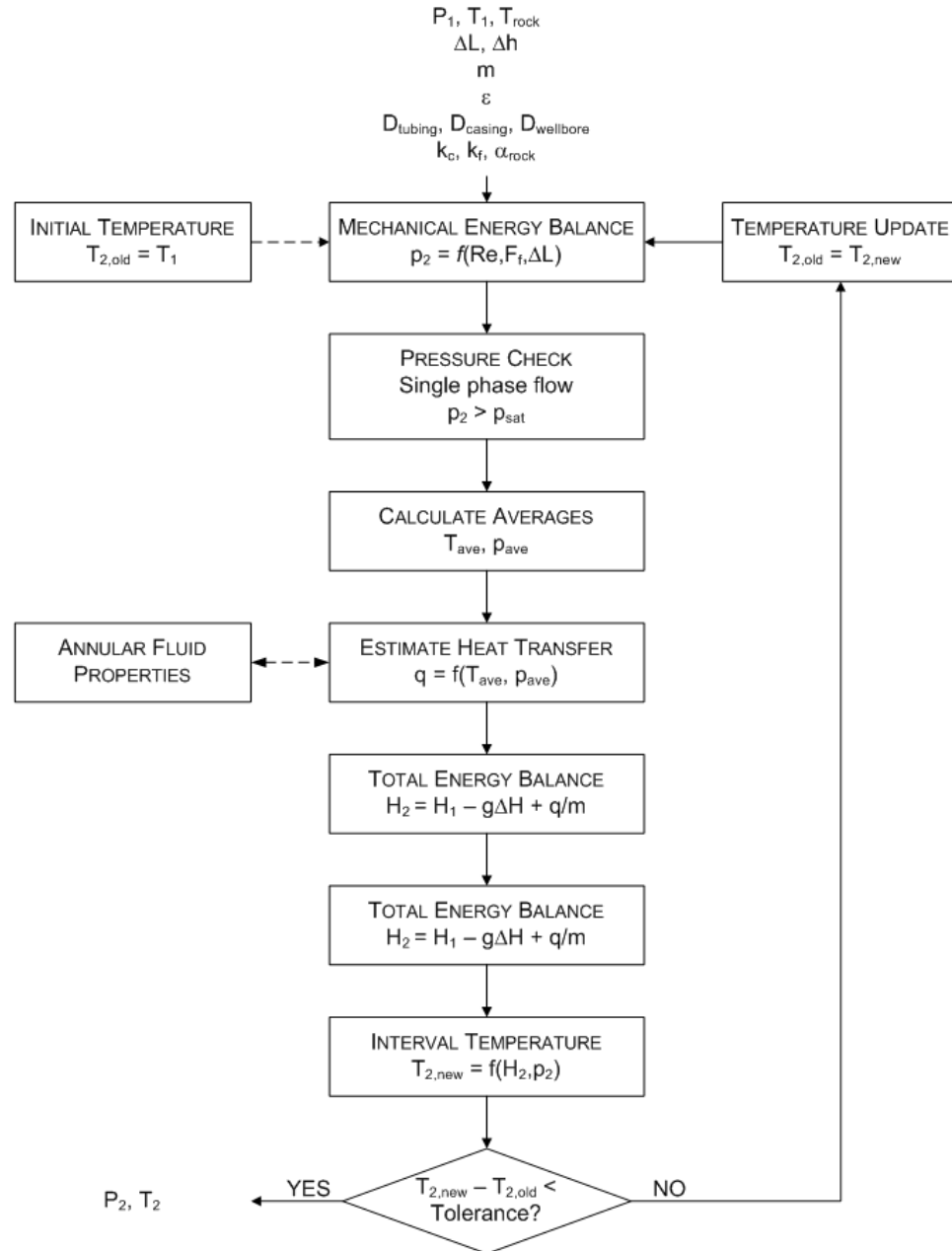**Figure C.2.** The iteration scheme used to solve for the downstream pressure over a segment of the wellbore.

Thus, Equations C.2, C.4, C.7 and the iteration scheme presented in Figure C.2 combine

to for the wellbore flow model. Using the wellbore flow model with the illustrative

parameter values presented in Table C.1 for different mass flow rates generates the

pressure distribution shown in Figure C.3.

Appendix C: Numerical Modeling of the Wellbore Environment

Table C.1. Illustrative values for the wellbore flow model parameters.

Model Parameters	Deterministic Value
Well Completion	
Wellbore Length (m)	1000
Wellbore Angle (θ)	90
Tubing Diameter (m)	0.076
Casing Diameter (m)	0.152
Wellbore Diameter (m)	0.254
Pipe Roughness (mm)	0.0457
Annulus Salt Concentration (ppm_w)	100000
Cement Thermal Conductivity (W/m K)	0.87
Geological	
Ground Temperature (^oC)	13.79
Geothermal Gradient (^oC)	10.3
Rock Thermal Conductivity (W/m K)	2.6
Rock Thermal Diffusivity (m^2/d)	0.09
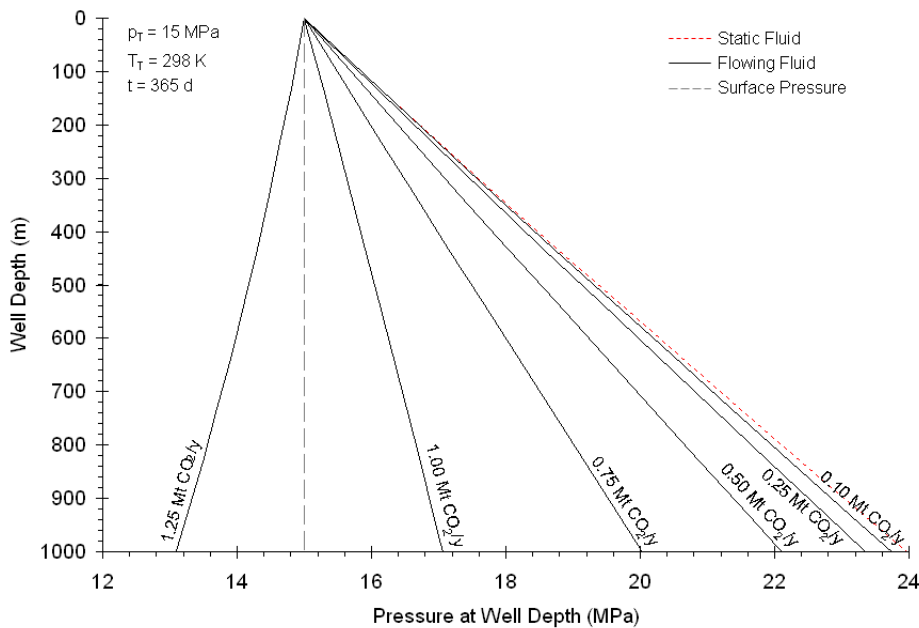
Figure C.3. Results from the wellbore flow model for pressure as a function of depth for mass flow rates between 0.1 Mt CO_2 per year and 1.25 Mt CO_2 per year.

The results in Figure C.3 show that increasing the mass flow rate reduce the bottom hole

pressure for all well depths at fixed wellhead conditions. At flow rates between 1 and

Appendix C: Numerical Modeling of the Wellbore Environment

1.25 Mt per year of CO_2 injected, the pressure gradient becomes negative, resulting in

BHIP lower than the wellhead pressure. At the other extreme, flow rates less than 0.1 Mt

CO_2 per year result in flowing pressure losses so small that the BHIP is nearly the same
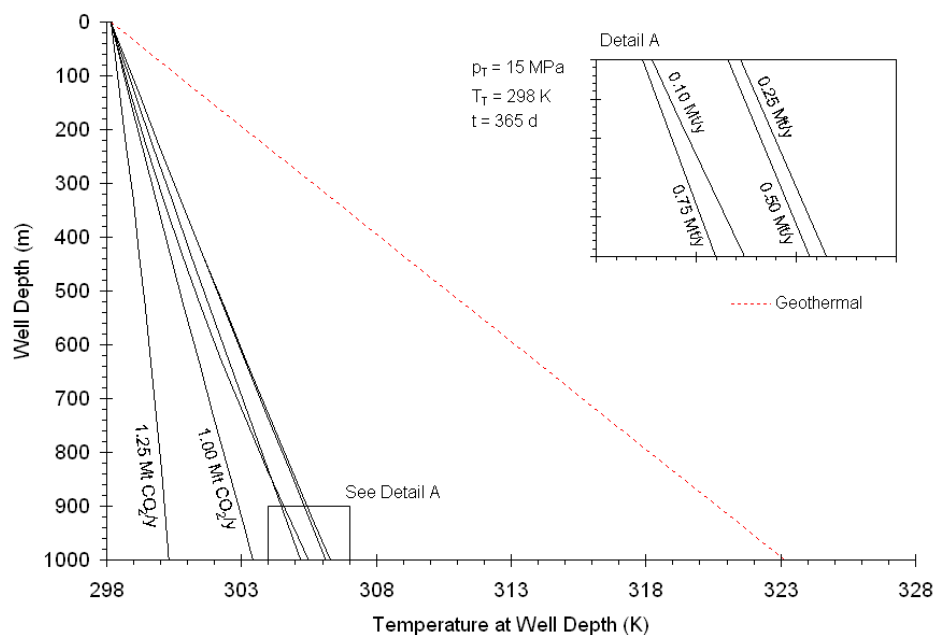
as hydrostatic fluid pressure.

Figure C.4. Results from the wellbore flow model for temperature as a function of depth for mass flow rates between 0.1 Mt CO_2 per year and 1.25 Mt CO_2 per year.

While the relationship between pressure and mass flow rate is monotonic, the relationship

between temperature and mass flow rate is more complex, as Figure C.4 shows. At flow

rates between 1 Mt CO_2 per year and 1.25 Mt CO_2 per year, bottomhole temperature

decreases with increasing flow rates. At lower mass flow rates, temperature passes

through a maximum between 0.5 Mt CO_2 per year and 0.25 Mt CO_2 per year.

Because of the strong dependence of injection rates on BHIP, the pressure is much more

important than temperature in the context of the EOR performance model developed

here. Thus, it is important to know how the well completion and geological parameters

affect the BHIP. Figure C.5 presents the results of a sensitivity analysis on heat transfer related parameters in the wellbore flow model, where parameter value differences are relative to the base values listed in Table C.1, with a mass flow rate of 0.5 Mt CO_2 per year, time of 365 days, wellhead pressure of 15 MPa, and wellhead temperature of 298 K.
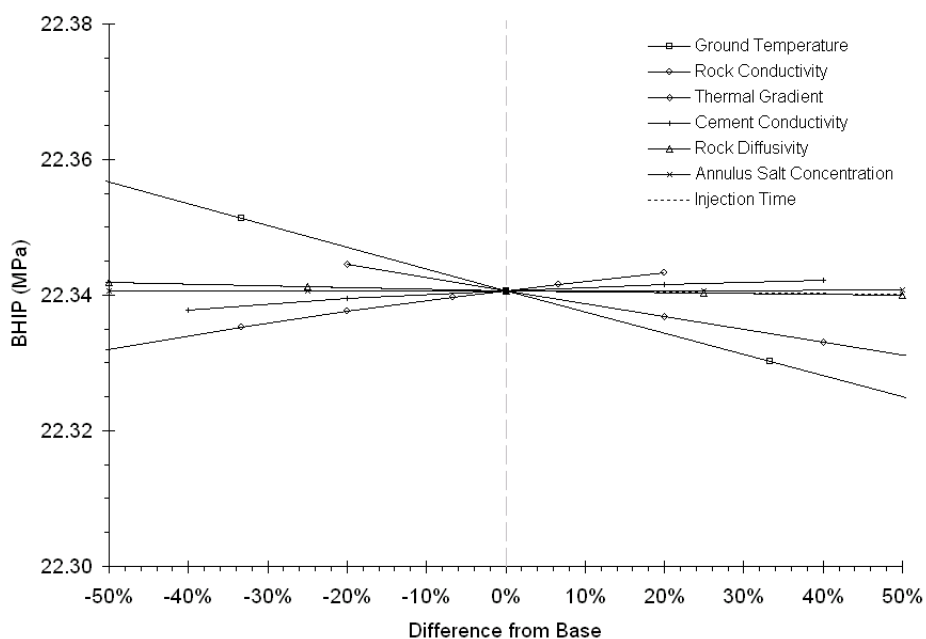

Figure C.5. Sensitivity of BHIP to changes in the heat transfer related input parameter values listed in Table C.1, where the difference from the base parameter value is calculated as $(x-x_{base})/x_{base}$.

Parameters included in Figure C.5 do not include the tubing, casing and wellbore diameters, as they are not independent parameters (e.g., smaller tubing means smaller casing can be used). Figure C.5 shows that changes to the parameters related to the heat transfer calculation (Equation C.7) have a very small influence on the calculated BHIP. For example, a 50% change in the surface temperature changes the calculated BHIP by only 16 kPa. Moreover, the BHIP is less sensitive to changes in all other heat transfer related parameters.

Appendix C: Numerical Modeling of the Wellbore Environment

Figure C.6 shows the sensitivity of BHIP to changes in wellbore flow model non-heat transfer related parameter values, where base values are defined in Table C.1. Of the parameters considered in Figure C.6, BHIP is least sensitive to materials roughness—200 kPa for a 50% change—and most sensitive to surface pressure—9 MPa for a 50% change. The sensitivity of BHIP to changes in heat transfer related parameters is at least an order of magnitude smaller than the sensitivities shown in Figure C.6. Thus relatively speaking, BHIP is nearly insensitive to changes in heat transfer related parameter values.
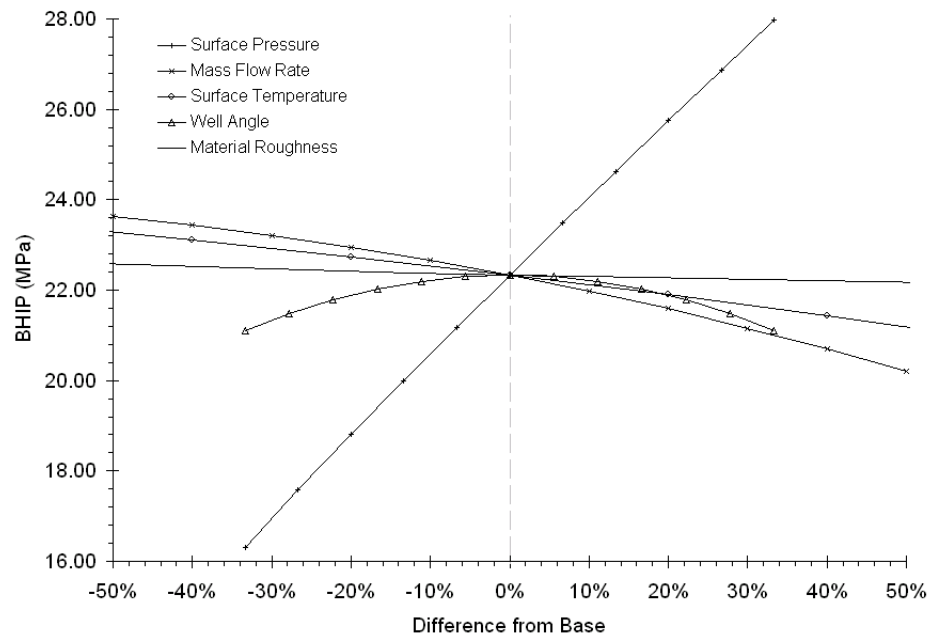
Figure C.6. Sensitivity of BHIP to changes in non-heat transfer related input parameter values listed in Table C.1, where the difference from the base parameter value is calculated as $(x\text{-}x_{base})/x_{base}$.

C.1   References

1. Mohitpour, M., H. Golshan, and A. Murray, *Pipeline Design & Construction*. 1st ed. 2003, New York, NY: ASME Press.
2. Willhite, G.P., *Over-all Heat Transfer Coefficients in Steam and Hot Water Injection Wells*. Journal of Petroleum Technology, 1967(May): p. 607-615.
3. Ramey, H.J., *Wellbore Heat Transmission*. Journal of Petroleum Technology, 1962(April): p. 427-435.

4. Bachu, S., *Screening and ranking of sedimentary basins for sequestration of CO$_2$ in geological media in response to climate change.* Environmental Geology, 2003. **44**: p. 277-289.

5. Holloway, S. and D. Savage, *The Potential for Aquifer Disposal of Carbon Dioxide in the UK.* Energy Conversion & Management, 1993. **34**(9-11): p. 925-932.

6. Holman, J.P., *Heat Transfer.* 9th ed. 2002, New York, NY: McGraw-Hill.

7. Macgregor, R.K. and A.F. Emery, *Free Convection through Vertical Plane Layers - Moderate and High Prandtl Number Fluids.* Journal of Heat Transfer, 1969. **91**(3): p. 391.

8. Adams, J.J. and S. Bachu, *Equations of state for basin geofluids: algorithm review and intercomparison for brines.* Geofluids, 2002. **2**(4): p. 257-271.

Appendix D: Arial Extent of CO_2 Plume Size in Aquifer Injection

Methods to estimate the aerial extent of a CO_2 plume were developed by both Saripalli and McGrail [1] and Nordbotten et al [2]. Both these methods are extensions of the Buckley-Leverett equation [3], describing the immiscible displacement of one fluid by another, solved for a radial system. However, these authors make different assumptions about the displacement of brine by CO_2. Saripalli and McGrail [1] implicitly assume that the displacement is stable (i.e. the endpoint mobility ratio, *M*, is less than one) while Nordbotten et al [2] assume that the displacement is unstable, and significant viscous fingering occurs. Assuming equal endpoint relative permeabilities (k_{rw} and k_{rc} for brine and CO_2, respectively), the mobility ratio in displacement of brine by CO_2 will be much greater than ten. Thus, the approach taken by Nordbotten et al [2] is more appropriate for this type of displacement.

While the results obtained by Nordbotten et al [2] agree broadly with Buckley-Leverett theory, their derivation is difficult to follow and does not follow typical conventions in the reservoir engineering field. For convenience, their result is derived here using the similar assumptions—namely, effects of capillary pressure are negligible, fluids are incompressible, and the reservoir petrophysical properties are homogeneous—using arguments analogous to those used by Dake [3] for an unstable, horizontal displacement.
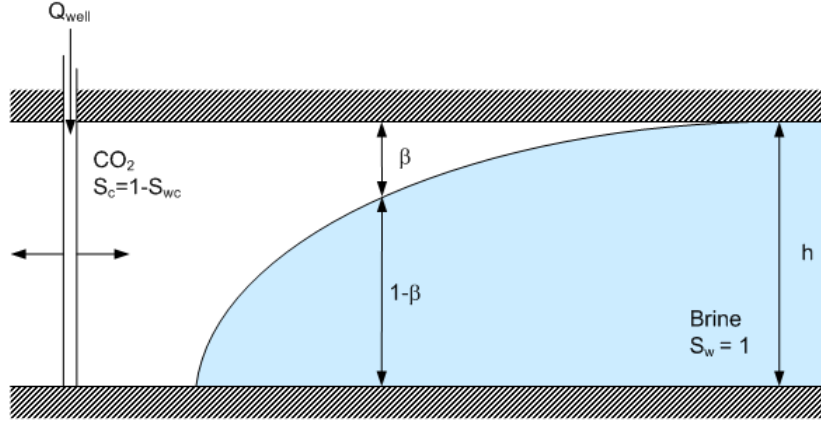
Appendix D: Arial Extent of CO_2 Plume Size in Aquifer Injection

Figure D.1. Geometry of a system where CO_2 is displacing brine.

The system modeled is illustrated in Figure D.1. For a differential cylindrical volume of this system, the volumetric balance on the CO_2 phase can be written:

$$\varphi \frac{\partial \bar{S}_c(r,t)}{\partial t} + \nabla \cdot q_c(r,t) = 0 \tag{D.1}$$

where: $\bar{S}_c$ is the vertically averaged saturation of CO_2, φ is the reservoir porosity, q_c is the flux of CO_2, r represents radial distance from the injection well, and t is time. Assuming drainage (i.e., CO_2 is displacing brine in a brine-wet reservoir), the vertically averaged saturation of CO_2, $\bar{S}_c$, is defined as:

$$\bar{S}_c = \beta(1 - S_{wc}) \tag{D.2}$$

Darcy's law for the brine and CO_2 phases can be written as:

$$q_c = -K\beta\lambda_c \nabla p_c \tag{D.3}$$

$$q_w = -K(1 - \beta)\lambda_w \nabla p_w \tag{D.4}$$

242

Appendix D: Arial Extent of CO_2 Plume Size in Aquifer Injection

In equations D.3 and D.4 K is the intrinsic permeability of the reservoir, β is the fraction of the reservoir thickness invaded by the CO_2 plume, λ is the phase mobility (k_r/u), and ∇p is the pressure gradient.

Since the fluids are incompressible ($\nabla \cdot q = 0$), the flux into the system equals the flux out of the system and the total apparent flux, q_t, is:

$$q_t = \frac{Q_{well}}{A} = q_c + q_w$$

where: Q_{well} is the injection rate of CO_2 into the system and A is the area across which the flux occurs. Assuming capillary pressure is negligible and, therefore $\nabla p_c = \nabla p_w = \nabla p$ and substituting equations D.3 and D.4, we arrive at:

$$\frac{Q_{well}}{A} = -K\left[\beta\lambda_c + (1-\beta)\lambda_w\right]\nabla p \tag{D.5}$$

Solving equation D.5 for pressure gradient, results in:

$$\nabla p = -\frac{Q_{well}}{KA\left[\beta\lambda_c + (1-\beta)\lambda_w\right]}$$

which can then be substituted into equation D.3, to arrive at the flux of the CO_2 phase as a function of the injection rate.

$$q_c = \frac{\beta\lambda_c}{\beta\lambda_c + (1-\beta)\lambda_w}\left(\frac{Q_{well}}{A}\right) = f_c\frac{Q_{well}}{A} \tag{D.6}$$

In equation D.6, the term referred to as f_c is the fractional flow of the carbon dioxide phase in the system. Substituting this equation into the volumetric balance, D.1, yields:

Appendix D: Arial Extent of CO_2 Plume Size in Aquifer Injection

$$\varphi \frac{\partial \overline{S}_c}{\partial t} + \nabla \cdot \left(f_c \frac{Q_{well}}{A} \right) = 0$$

Writing the divergence operator for a cylindrical coordinate system gives:

$$\varphi \frac{\partial \overline{S}_c}{\partial t} + \frac{1}{r} \frac{\partial}{\partial r} \left(r f_c \frac{Q_{well}}{2\pi r h} \right) = 0$$

Simplifying results in:

$$\varphi \frac{\partial \overline{S}_c}{\partial t} + \frac{Q_{well}}{2\pi r h} \frac{\partial f_c}{\partial r} = 0 \tag{D.7}$$

Applying the chain rule to the fractional flow equation, the $\partial f_c / dr$ can be rewritten:

$$\frac{\partial f_c}{dr} = \frac{\partial f_c}{\partial \overline{S}_c} \times \frac{\partial \overline{S}_c}{\partial r} = f_c' \frac{\partial \overline{S}_c}{\partial r}$$

Upon substitution into D.7, we arrive at a statement of the Buckley-Leverett equation for a radial system:

$$\frac{\partial \overline{S}_c}{\partial t} + \frac{Q_{well} f_c'}{2\pi r h \varphi} \frac{\partial \overline{S}_c}{\partial r} = 0 \tag{D.8}$$

This equation was solved by Woods and Comer [4] for the boundary conditions, $r = r_w$ at $t = 0$, resulting in:

$$r(\overline{S}_c) = \sqrt{\frac{f_c' Q_{well} t}{\pi h \varphi} + r_w^2} \tag{D.9}$$

If vertically averaged saturation of the CO_2 phase was not assumed (i.e., D.2), determination of f_c' would require an assumption of the shape of the relative permeability curves for the CO_2-brine system and particular reservoir rock. However, because we are

244

Appendix D: Arial Extent of CO_2 Plume Size in Aquifer Injection

operating under the assumption that saturation is a linear average of phase saturations

(i.e., D.2), f_c' can be expressed via the chain rule as:

$$f_c' = \frac{df_c}{d\beta} \times \frac{d\beta}{d\bar{S}_c} = \frac{\lambda_w \lambda_c}{[\lambda_w + \beta(\lambda_c - \lambda_w)]^2} \left(\frac{1}{1 - S_{wc}}\right)$$

Substituting this into the above equation, we arrive at an expression for the radial

distance as a function of the fraction of the formation height invaded by the CO_2 plume:

$$r(\beta) = \sqrt{\frac{\lambda_w \lambda_c Q_{well} t}{\pi h \varphi (1 - S_{wc})[\lambda_w + \beta(\lambda_c - \lambda_w)]^2} + r_w^2} \qquad \text{(D.10)}$$

Assuming that the injection well radius is much smaller than the radius of the CO_2 plume,

the maximum extent of the CO_2 plume occurs at $\beta = 0$:

$$r_{max} = \sqrt{\frac{\lambda_c Q_{well} t}{\pi h \varphi \lambda_w (1 - S_{wc})}} \qquad \text{(D.11)}$$

With the residual water saturation in the invaded area, S_{wc}, set to zero, equation D.11 is

the same as that presented by Nordbotten et al [2]. As concluded by Nordbotten et al [2],

this equation is a reasonably accurate estimate of the maximum extent of plume spread

under conditions where buoyancy caused by the density difference between CO_2 and

brine is relatively small in relation to viscous and pressure forces.

D.1 References

1.   Saripalli, P. and P. McGrail, *Semi-analytical approaches to modeling deep well injection of CO_2 for geological sequestration.* Energy Conversion & Management, 2002. **43**: p. 185-198.
2.   Nordbotten, J.N., M.A. Celia, and S. Bachu, *Injection and Storage of CO_2 in Deep Saline Aquifers: Analytical Solution for CO_2 Plume Evolution During Injection.* Transport in Porous Media, 2005. **58**: p. 339-360.
3.   Dake, L.P., *Fundamentals of reservoir engineering.* 1 ed. 1978: Elsevier.

4.   Woods, E.G. and A.G. Comer, *Saturation Distribution and Injection Pressure for a Radial Gas-Storage Reservoir.* Journal of Petroleum Technology, 1962(December): p. 1389-1393.

Appendix E: CO$_2$ Price Conversion Table

Table E.1. Conversions between CO$_2$ price metrics used in this thesis

\$/mscf	\$/tonne CO$_2$	\$/tonne C
\$0.50	\$9.45	\$34.63
\$0.53	\$10.00	\$36.64
\$1.00	\$18.90	\$69.27
\$1.50	\$28.35	\$103.90
\$2.00	\$37.81	\$138.54
\$2.50	\$47.26	\$173.17
\$3.00	\$56.71	\$207.81
\$3.50	\$66.16	\$242.44
\$4.00	\$75.61	\$277.08
\$4.50	\$85.06	\$311.71
\$5.00	\$94.52	\$346.35
\$5.29	\$100.00	\$366.44